

Berichte aus der Biomedizinischen Technik 6
Publisher: Univ.-Prof. Dr. rer. nat. G. rau

Thorsten Sieß

Systems Analysis and Development of Intravascular Rotation Pumps for Heart Support

Helmholtz-Institut
for Biomedical Technology
at the RWTH university of applied sciences, Aachen

Shaker Verlag publishers
D 82 (Diss. RWTH, Aachen)

Systems Analysis and Development of Intravascular Rotation Pumps for Heart Support

Dissertation

Approved by the Faculty of Mechanical Engineering

At the Rheinisch-Westfälische Technische Hochschule [university of applied sciences] of Aachen

For obtaining the academic degree of

Doctor in the Engineering Sciences

Submitted by

Diplom-Engineer Thorsten Sieß

From Bielefeld

Advisor: Univ.-Prof. Dr. rer. Nat. Günther Rau

Co-Advisor: Univ.-Prof. Dr.-Ing. Dr. h.c. Heinz E. Gallus

Date of the oral examination: June 24, 1998

Die Deutsche Bibliothek - CIP Standard Record

Siess, Thorsten,

Systemanalyse und Entwicklung Intravascularer Rotationspumpen zur Herzunterstützung/ Thorsten Siess. -

Als.Ms.gedr. -

Aachen, Shaker, 1999

(Berichte aus der Biomedizinischen Technik [reports from biomedical technology], vol. 6)

Dissertation at Aachen, Technische Hochschule [university of applied sciences], 1998

ISBN 3-8265-6150-3

Copyright Shaker Verlag 1999

All rights, including the right of reprinting of excerpts, of full or partial representation, of storage in data processing media, and of translation reserved.

Printed as a manuscript. Printed in Germany

ISBN 3-8265-6150-3

ISSN 1430-7316

Shaker Verlag GmbH * P.O. box 1290 * 52013 Aachen, Germany

Phone: +49 2407 95 96-0, Fax: +49 2407 95 96-9

Internet: www.shaker.de * e-mail: info@shaker.de

Preface

At the beginning of the present project there was initially only an idea and the uncertainty of its implementability. On the laborious road to its successful implementation, many people made a personal direct or indirect contribution.

For the fantastic working environment, I would particularly like to thank Univ.-Prof. Dr. rer. Nat. Günther Rau at this point, the director of the Helmholtz-Institut, as well as Prof. Dr.-Ing. H. Reul, the head of the Biomechanics workgroup. I have received from them material suggestions, freedom, and the ability to work independently and creatively.

For taking on the co-advisorship, and the professional supervision of the work, I particularly wish to thank Univ.-Prof. Dr.-Ing. Dr. h.c. H.E. Gallus

Many student and post-graduate researchers as well as assisting students have contributed their share to this project by working out the details and by being so engaged. My special thanks go out to all of them, as well as to my predecessor, Dr. med. dent. Dipl.-Ing. N. Rosarius, as well as the hope that the interdisciplinary work has meant as much to them on a professional and human level, and has been as enjoyable to them, as it has to me.

My particular gratitude with respect to the implementation goes out to all the employees at the mechanical workshop. Often, a drawing had to be converted from a scale of 10:1 or 20:1 to a scale of 1:1, because it was only at such scales that the components could be drawn. I would therefore like to thank the staff at the mechanical workshop for their excellent work on the one hand, and for picking up the challenge of pushing the limits of what can be manufactured through precision-engineering. Without the excellent implementation and the indication of the technical limits, the realization of the idea of a miniature pump with an integrated high-performance drive in a functional lab sample would not have succeeded.

Furthermore, the extensive financing of the project by the Deutsche Forschungsgesellschaft over a period of four years, the possibility of using the excellent infrastructure of the Helmholtz-Institut, and finally, the third-party financing by the American Guidant Corporation were a material condition for the expensive development of the individual components of the pump system.

For the initial clinical tests, I would particularly like to thank Prof. W. Flameng and Prof. B. Meyns of the Katholieke Universiteit Leuven, who have consistently believed in the project, and who also successfully performed the first test of the diagonal pump systems, developed by me in parallel, for middle- and long-term heart support.

My particular gratitude also goes to all employees of the Helmholtz-Institut for their far-reaching support and for the friendly atmosphere in which I have had the great pleasure to work.

Without the understanding for the many weekends spent working and the moral support of my dear wife Claudia, and the help in the form of mental distraction by our sons Eric and Quint, the present project would not have been possible.

Bardenberg, June 1998

*To my dear wife Claudia
And our sons
Eric and Quint*

Table of Contents

1. Introduction

2. Intravascular heart support systems according to rotary pump principle

2.1 The Hp Hemopump system

2.1.1 Further development of Hemopump system: Hp31, Hp14

2.1.2 Clinical testing of Hp21

2.2 Description of capacity and applicability of intravascular heart support systems according to the rotary pump principle

2.3 Final review of the Hemopump system

2.4 Derived system parameters for Helmholtz micro-axial pumps

3. Analysis of possible design concepts and choice of concept

3.1 Pump with an integrated magnetic clutch

3.1.1 Magnetic clutch

3.1.2 Bearings in blood

3.1.3 Pump concept with an integrated magnetic clutch

3.2 Pump with through-shaft

3.2.1 Sealing concepts

3.2.1.1 Hydrodynamic capacity:

3.2.1.2 Hydrostatic seal:

3.2.1.3 Magnetic fluid seal:

3.2.1.4 Frictional connection seals:

3.2.2 Pump concept

3.3 Concept comparison and choice

4. Drive concepts, design and testing

4.1 Assessment of required capacity

4.2 Drive concepts

4.2.1 Hydraulic drives

4.2.2 Electrical drives

5. Fluid mechanics design

5.1 General considerations on the working principle of hydrodynamic pumps

5.2 General considerations on blade design and description of the system of actions

5.3 Parameters and requirements derived from the medical applications

5.4 Assessment of losses

5.5 Assessment of the optimum rotation speed: Cordier vs. cavitation border

5.6 Rotor entrance angle

5.7 Transformation of hub diameter

5.8 Speed distribution and calculation of the angles in the rotor exit

5.8.1 Specific blading work

5.8.2 Method of radial balance

5.8.3 Choice of a proper angular momentum distribution

5.8.4 Viscosity effect

5.8.5 Continuity equation

- 5.8.6 Subsequent calculation of the total specific blading work
- 5.8.7 Angle excess and blade structure angle β_2
- 5.9 Calculation of the guide wheel angle
- 6. Creation of the blading components**
- 6.1 Determination of the axial enthalpy distribution and CAD/CAM creation of the blading components
- 6.2 Production aspects and process parameters
- 7. Experimental Flow Visualization in Micro-Axial Pump Blade System**
- 7.1 Experimental Flow Visualization in Micro-Axial Pump Blade Systems
 - 7.1.1 Light section and tracer methods
 - 7.1.2 Particle tracking
 - 7.1.3 Washing method
 - 7.1.4 Explicit current filament method
 - 7.1.5 Color injection method
 - 7.1.6 Laser-Doppler anemometry
 - 7.1.7 Recording media and their suitability for documentation purposes
- 7.2 Secondary Flows
- 7.3 Flow Analysis in an Enlarged 10:1 Model
 - 7.3.1 The test rig and the 10:1 model
 - 7.3.2 Flow results in the enlarged model
 - 7.3.3 Discussion of the informative value of the enlarged model
- 7.4 Flow Analysis in the Original Size
 - 7.4.1 Test construction for flow visualization
 - 7.4.2 Test construction for flow visualization
 - 7.4.3 Analysis of the results and evaluation of the methods
- 8. Method for Examining Pump-Induced Blood Damage**
- 8.1 Assessment of Pump-Induced Hemolysis
 - 8.1.1 Method and simplifying assumptions for determining pump-induced blood damage
 - 8.1.2 Execution of the method
- 8.2 Effect of design parameters on blood damage
- 9. Hydraulic and Mechanical *In-Vitro* Tests on Lab Samples**
- 9.1 Hydraulic Properties of the Blade System Components
 - 9.1.1 Test structure and measuring technology
 - 9.1.2 Results for select blade systems
- 9.2 Impact of the Design Parameters on Performance, Efficiency Rates, and Pump Characteristics
 - 9.2.1 Impact of the induced total enthalpy on the performance characteristics
 - 9.2.2 Impact of the channel height on internal losses
 - 9.2.3 Impact of the internal losses on the pump characteristics
- 9.3 Impact of flow control on inlet and outlet sides under the conditions of application
- 9.4 Mechanical research of the drive integrated into the pump
- 10. Pump-ventricle interaction and pump function control**
- 10.1 Test set-up
- 10.2 Pump characteristics in pulsating environment
- 10.3 Volume unloading of the ventricle and risk of suction
- 10.4 Volume flow calculation and avoidance of suction phases
- 11. Experimental in vitro research of blood damages**

- 11.1 Blood compatibility of the pump
- 11.2 In vitro blood compatibility research
 - 11.2.1 Test parameters and limit values
 - 11.2.2 Test set-up and performance
 - 11.2.3 Results
- 12. First in vivo experiments**
- 12.1 Animal model
- 12.2 Test performance and results
- 13. Perspectives**
- 14. Summary**

List of references

Formulas and abbreviations used

Symbol	Meaning	Unit
1. Latin characters		
A	Area	m ²
A	Constant	m/s
A	Constant	m/s; 1
a	Acceleration	m/s ²
a	Distance from the pressure side	m
a	Specific energy	m ² /s ²
B	Induction	H
B	Constant	m ² /s, 1
C	Constant	1/s
c	Specific heat capacity	kJ/kg/K
c	Absolute speed	m/s
\bar{c}	Mean absolute speed	m/s
D	Diameter	m
d	Diameter	M
d()	Infinitesimal quantity	[]
f	Frequency	1/s
f	Lens focal length	m
f	Factor	1
F	Force	N
F	Optical correction factor	1
g	Gravitational acceleration	m/s ²
h	Specific enthalpy	m ² /s ²
h	Magnet distance	M
h	Level height	M
\bar{h}	Arithmetically averaged duct height	M
H	Enthalpy	kg * m ² / s ²
\dot{H}	Enthalpy flow	kg * m ² / s ²
i	Control variable	1
I	Flow	A
j	Specific dissipation	m ² /s ²
k	Control variable	1
K	Constant	Nm
l	Length	m
L	Angular momentum	kg * m ² / s
L	Free jet length	m
L	Axial grid length	m
\dot{m}	Mass flow	kg/s
M	Torque	Nm
n	Rotation speed	1/s
n	Exponent	1
n	Number	1
P	Power	W
P	Pressure	bar; Pa; mmHg

p		Pressure	bar; Pa; mmHg
	\dot{Q}	Heat flow	W
	\bar{Q}	Internal leakage flow	m ³ /s
r		Radius	m
τ		Arithmetically averaged radius	m
\bar{r}		Area-standardized radius	m
\bar{r}		mean lever	m
R		Largest component radius	m
R		Resistance	Ω
s		Particle track length	m
s		Feed length	m
s		Component of particle location	m
s		Specific entropy	m ² / (s ² * K)
s		Tube length	m
s		Blade thickness	m
s		Chord length	m
S		Duct length	m
S		Particle location in Cartesian coordinates	m, m
\bar{S}		Stress tensor	N/m ²
T		Temperature	K
t		Time	s
t		Division	m
per.		Peripheral speed of the rotor blades	m/s
U		Voltage	V
V		Volume	m ³
	\dot{V}	Volume flow	m ³ /s
v		Flow speed	m/s
w		Speed in the relative rotor system	m/s
y		Specific flow energy	m ² /s ²
z		number	1
z		geodetic height	m

2. Greek characters

α		Flow and blade construction angle of the stator	degrees
α		Convective heat transfer value	W/mK
β		Flow and blade construction angle of the rotor	degrees
δ		Diameter parameter	1
δ		Angle overstatement	degrees
δ		Boundary layer thickness	m
δ_2		Impulse loss thickness	m
γ		Flow angle	degrees
γ		Arc of contact	degrees
	$\dot{\gamma}$	Shear rate	1/s
η		Dynamic viscosity	Pa • s
η		Efficiency	1
ϕ		Twisting angle	degrees
λ		Diffusive thermal conductivity value	W/mK
λ		Resistance rate	-

μ	Angle overstatement factor	-
ν	Kinematic viscosity	m^2/s
ρ	Density	kg/m^3
σ	Rotation speed parameter	1
σ	Compressive stress	N/m^2
τ	Degree of reaction	1
τ	Shear stress	N/m^2
ϑ	Temperature	K
ω	Angular speed	rad/s
ζ	Loss coefficient	1

3. Operators

$\frac{d ()}{d ()}$	Total differential
$\frac{\delta ()}{\delta ()}$	Partial differential
$\int_a^b () d ()$	Integral within the limits a, b
Δ	Difference

4. Special signs

\varnothing	diameter	m
O_2	molecular oxygen	-
%	percent	1
®	registered trademark	-
∞	infinite	-

5. Abbreviations

CI	Cardiac Index	$1 / (\text{min} \cdot \text{m}^2)$
Fr	Froude number	-
Hb	Hemoglobin	$\text{g}/100 \text{ mL whole blood}$
Hp14	femoral 14-french hemopump	
Hp21	femoral 24-french hemopump	
Hp31	femoral 24-french hemopump	
Hk	Hematocrit	1
IABP	Intra-Aortal Balloon Pump	
IH	Index of Hemolysis	-
IT	Index of Thrombolysis	-
LDH	Cytoplasmic enzyme from thrombocytes	
LAP	Left-Atrial Pressure	mmHg
LV-	Left-Ventricular	
LVWI	Left-Ventricular Work Index	$\text{g} \cdot \text{mm} / (\text{m}^2 \cdot \text{min})$
MAP	Mean Atrial Pressure	mmHg
Nu	Nusselt number	-
PCWP	Pulmonary Capillary Wedge Pressure	mmHg

Pr	Prandtl number	-
Re	Reynolds number	-
RV	Right-Ventricular	
s	safety	1
VAD	Ventricular Assist Device	

Indices and Superscripts

0	Starting conditions
0	inlet-side position of the rotor blade outside of the rotor blade duct
1	inlet-side position of the rotor blade inside of the rotor blade duct
2	outlet-side position of the rotor blade outside of the rotor blade duct
3	outlet-side position of the rotor blade inside of the rotor blade duct
4	a position at the inlet level of the stator
5	a position at the outlet level of the stator
a	outside
a	axial
A	outside
Ao	aorta
downstream	in reference to the fluid stream
outflow	on the outflow side
ax	axial
AX	axial
B	relating to an acceleration
B	outer scope of a rotor
Bernoulli	relating to dynamic pressure reduction
cal	calculated
D	dissipation
D	outlet side
Diffusor	relating to the diffusor of the radial pump
Diss	relating to dissipation
E	for inflow losses
inflow	inflow
req.	required
exp.	relating to the exposed time
exp.	experiment
extern	external
Friction	loss due to friction
avg	average
H	hydraulic
hyd	hydraulic
i.	inside, at the hub
i.	running parameter
intern	internal
Interval	relating to an interval size
local	relating to a specific location
L	for flow acceleration
Lauftrad	relating to the rotor

lam.	laminated
local	relating to local parameters
LV	in the left ventricle
m	in the meridian plane
m	mean
mm	median
max	maximum value
M	specific machine parameter
torque	transmittable torque of a magnetic coupling
mech.	mechanical
mf	mean/average flow
normal	in the normal direction
use.	useable part
particle	relating to particles
proj.	relating to a projected measurement
R	for tube friction losses
r	radially
rel.	relatively
rGG	calculated via the equation of radial equilibrium
rot.	in the rotational direction
S	gap
blade	relating to the blades
hose	hose
rel.sp.	relating to relative speed
blade	relating to blades
chord	relating to chords
gap	relating to the gap between the rotor and the housing
t	total
turb.	turbulent
u	in the peripheral direction
V	in the ventricle
V	loss
loss	loss, or relating to loss
x	at the hub inlet level
x	coordinates in the axial direction
yM	specific machine parameter

1. Introduction

An acute heart failure with the resulting decrease of pumping capacity is mostly attributable to reduced heart muscle contraction. The latter generally comes as the result of insufficient provision of the heart muscle due to reduced blood flow through the coronary vessels. Other causes, such as heart muscle disease or anatomic defects are less frequent, but just as grave.

In such cases, targeted and timely use of mechanical circulation support systems can not only ensure blood flow through the peripheral organs, but most importantly, provide mechanical heart support, which immediately reduces the work required from the heart. It reduces oxygen volume required by the heart muscle and increases blood flow in the heart vessels, due to augmented perfusion pressure, so that the heart can recover due to these measures, if there is a reversible cause of heart failure.

Small mechanical heart support systems are more preferable than the larger, mostly extra-corporeally located systems due to their minimally invasive placement, if they provide sufficient hydraulic capacities.

The intra-aortal balloon pump (IABP), the first clinically available pump that can be inserted into the human vessel system, can only support the left heart, which is most often affected, to a limited extent of about 10%. It was first in 1989 that the catheter pump "Hemopump" introduced by Richard Wampler and based on the rotary pump principle became a clinically available intravascular blood pump, which can substantially relieve the left heart.

The Hemopump ultimately demonstrated that a quickly rotating rotary pump only damages blood within physiologically reasonable limits, despite the high shear rate inherent to the pump type. The prevailing perception that non-pulsating blood propelling could only be properly done with slow radial pump with relatively large impellers had to be re-considered.

In 1994, the Hemopump micro-axial pump system intended solely to support left heart completed its first clinical testing. This caused immediate euphoria of discovery of a universal pump concept for heart support, which disregarded reasonable assessment of the capacities and system specific restrictions. The extensive use of the pump in the clinical practice was prevented by the drive of the pump head through a flexible and damageable shaft, as well as the currently available insufficient delivery capacity of some 2.5 l/min, the pump head diameter of 7.4 mm being too large to bring the pump through the peripheral vessels, along with the long start-up times.

Based on these drawbacks and limitations of the Hemopump system described in the sources, the Helmholtz Institute for Biomedical Technology in Aachen is now pursuing an improved concept on intravascular micro-axial blood pumps for temporary heart support.

An important feature different from Hemopump is the integration of an intra-corporeal drive directly connected to the pump unit. It allows to avoid the flexible shaft with its drawbacks, in particular, the start-up time of 10 to 30 minutes associated therewith.

Not just one pump size, but a pump family with external diameters of 5.4 mm, 6.4 mm and 8.0 mm for left and right heart support is developed due to widely varying clinical requirements, and receive a new hydraulic design. These systems, whose capacity exceeds that of the Hemopump, cover the capacity range most important for clinical treatment at physiological pressures, and have volume flow rates of 2 l/min to 7 l/min.

A higher hydraulic capacity must generally be achievable for a pump unit by means of a short, no longer than 80 mm long, inlet or outlet hose. The total length of the rigid pump unit cannot exceed 30 mm, since otherwise an excessively long, stiff part of the system makes impossible passage of the pump unit through the small vessel radii and to the immediate vicinity of the heart valve.

In the course of this work, a pump family consisting of impeller versions 5.8 and 4.8 in diameter is developed for systems, which can be peripherally inserted. These systems are limited in their hydraulic capacity to pure heart support due to their small dimensions, i.e. they can substantially substitute the heart function only short term at the very best. However, if a direct access with open thorax is chosen for an intravascular pump system, then the diameter of the system can be increased. This work will deal with a respectively enlarged pump in the form of a 7.2 mm impeller version parallel to the primarily considered 5.8 mm system.

The improved intravascular micro-axial pumps improved in this work with respect to their capacity and user friendliness represent a promising concept in the area of minimally invasive surgery. For example, systems, which are able to take over the entire heart minute volume for a short time, can be used intraoperatively. In such case a heart-lung machine would be unnecessary, which can mean improved recovery for the patient due to reduced surgery trauma.

Then the provided documentation shows, supported by a thorough research of sources and system analysis of Hemopump system (Chapter 2), alternative designs with integrated shaft (Chapters 3 and 4).

Based on these conclusions and the design discussed in great detail in Chapter 5, flow behavior is researched in Chapters 7 through 10 on chosen versions of blading components with respect to high hydraulic capacity and delivery characteristic dependent upon the design parameters.

The first results available in vitro and in vivo for the whole system provide in Chapters 11 and 12 final assessment of the produced design concept of a miniature impeller pump with integrated drive.

2. Intravascular heart support systems according to rotary pump principle

Before developing our own intravascular micro-axial pump, we would like to provide a description of the commercially available Hemopump system. It will consist of the description of the original Hemopump HP21 system, which is inserted through the leg artery (arteria femoralis), its clinical trial and the obtained results, which led to further development of Hp14 and Hp31.

Based on these results, we will derive the system parameters for the Helmholtz micro-axial pump and present it in Chapter 2.4. They will serve as a basis for further development of a micro-axial pump with integrated drive.

2.1 The Hp Hemopump system

Development of the Hemopump system intended to support the left heart has been performed in stages, with the basic design of the pumps being identical, except for their sizes. The original Hp21 system, which was to be inserted through the periphery, is shown on Figure 2.1, and consists from miniature rotor pump, essentially with axial flow and one stage, with rotor (7) and stator (4),

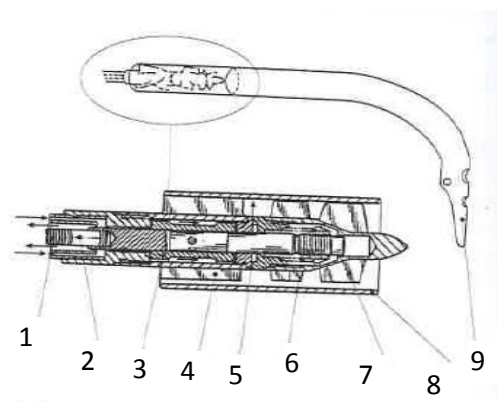


[Figure 2.1 Scheme of Hp21]

both located in a housing (8), 7 mm in diameter and 18 mm long. The flexible suction tube (9) located upstream from the pump is about 200 mm long, and is pre-curved to improve placing and location, which extends from the ventricle over the aorta ascendens, aortic arch up into aorta descendens. The drive of the pump head is performed by a flexible shaft (2), which is located in a coaxial guiding catheter (1), 3.2 mm in diameter, which is connected to a drive located outside of the body. All bearings (3), the flexible shaft (2) and the seal (5) in the pump head are oiled and flushed with a bio compatible 40% glucose water based solution /Butler 1988; Rutan 1989/. The amount is regulated by two roll pumps operating as a unit, one of which forwards the impressed flow through the capillaries into the guiding catheter (1) in the direction of the pump head, while the other one intakes a given smaller flow through the central lumen in which the flexible shaft (2) runs. The difference between the incoming and outgoing glucose flow gets through the plain bearing (3) in the pump head and the connected hydrostatic axial seal (5) into blood. The sealing gap between rotor (7) and stator (4) is kept narrow by the compression spring (6) integrated in the rotor hub, and is kept free of blood by the targeted leakage flow from inside. Blood may not get into the sealing gap at any point, because otherwise fibrin deposits accumulate in the gap, make it wider, and the fixed leakage flow results in significant drop of flushing pressure. This lets more blood penetrate through the gap and the plain bearing (3), and immediately causes pump failure. That is why a pressure censor is integrated in the inlet part of the flashing unit, so that when pressure in the flushing liquid drops to the minimum of about 500 mmHg, the blood pump can be operated. Prior to that point, the console does not allow the system to start up. The so-called pressurizing takes, depending upon the previous ventilation, 10 to 30 minutes /Johnson & Johnson 1988, 1994/.

2.1.1 Further development of Hemopump system: Hp31, Hp14

Based on the initial experience with Hp21, Hp14 was developed as femoral, percutaneously placed pump, and Hp31 as a sternotomy pump (used on open chest). Due to the placement problems with a system 7.4 mm till 8 mm in diameter (Hp21, Hp31), such large systems are rather not place peripherally.

Hp14, with the diameter of 4.6 mm and a rigid length of 30 mm, is a system, which must be introduced by percutaneous instruments without dissection of the vessel. The hydraulic capacity is definitely lower than that of Hp21, despite the short and straight suction tube, due to the small pump diameter, and equals 2.3 l/min at the pressure difference of 70 mmHg. The system can be used during high risk angioplasties /Figulla 1994; Loisanca 1990a, 1990b; Scholtz 1990, 1991/, according to /Aboul-Hosn 1995/, as support system in fetal operations, and as a true alternative to IABP. The hemolysis of this system plays an important role in its current version.

A sternotomy Hp31, 8 mm in diameter, with a short, straight suction tube, represents a hydraulically developed Hp21, which is clearly more effective than Hp21 at identical dimensions of the blading parts, and produces 4.2 l/min at the pressure difference of 100 mmHg. This pump can be used during open heart surgeries or for heart support for several days, the drawback of the system is the repeated surgery, which is always required for removal.

2.1.2 Clinical testing of Hp21

The intravascularly placed /Duncan 1989; Frazier 1990, 1991/ micro-axial pump system Hemopump was found to be helpful for temporary left heart support /Wampler 1988, 1991a, 1991b, 1993, 1994/. When the first commercially available system Hemopump Hp21 was used clinically, systematic complications were discovered resulting primarily from the drive by means of a flexible extra-corporeally driven shaft and the

relatively large external diameter of the pump. Despite placement of Hp21 in aorta descendens with the resulting straight line shaft movement, shafts were broken in 10% of all cases. The external diameter of the pump unit of 7.4 mm also made impossible the clinical use of the pump in at least 25% of all cases due to sclerotic changes or stenosis of arteria femoralis /Flameng 1991; Scholz 1990; Wampler 1991a; Waldenberg 1994/, and increased the risk of endothelium injuries and leg ischemia as the result of shifted calcification. In those instances when Hp21 was successfully applied, the volume flow of about 2-2.5 l/min could be achieved at middle arterial pressures of 60-90 mmHg, which is clearly below the described design point of 3-3.5 l/min at counter pressure of 100 mmHg. The reason is, among other things, the position of the pump before the aortic arch and the resulting suction tube, whose flow resistance alone requires the minimum capacity of about 0.5 l/min – 1 l/min.

Besides, the insufficient control of this pump function and position turned out to be problematic in clinical use /Löhn 1997; Meyns 1996; Siess 1996/.

The system specific blood damages based on a group of 145 patients /Aboul-Hosn 1995/ is in mostly cases clinically tolerable.

	Pre-operative	During the surgery	Post-operative
Thrombocyte count [1,000/mm ³]	(n=81) 207 ± 11.9	(n=69) 122 ± 7.1	(n=59) 116 ± 8.1
Plasma hemoglobin [mg/dl]	(n=47) 18.5 ± 3.4	(n=65) 44.9 ± 6.9	(n=51) 35 ± 7.9
Total hemoglobin [g/dl]	(n=87) 11.5 ± 0.24	(n=75) 10.4 ± 0.17	(n=61) 10.4 ± 0.2

Table 1: Blood damage from Hp21 according to /Aboul-Hosn 1995/.

However, in certain cases the hemolysis was so high, that the total hemoglobin dropped significantly as the result of the pump application (pump induced anemia). This group of patients also had the lowest survival rate.

It is also very noticeable that the thrombocyte count always fell significantly during the pump use. Therefore, the thrombolysis is clearly increased in comparison to hemolysis (see in this regard Chapter 8.1.2viii and Chapter 8.2).

2.2 Description of capacity and applicability of intravascular heart support systems according to the rotary pump principle

The on-going clinical testing of the Hemopump systems (Hp21, Hp31, Hp14) produced results with respect to the indication spectrum and further applicability of intravascular micro-axial pump systems / Deeb 1990; Flameng 1991; Frazier 1990a, 1990b, 1991; Loisanse 1990; Waldenberger 1994; Wampler 1988, 1991a, 1991b, 1993, 1994/;

- Although the intravascular micro-axial pump Hp21 is much more effective than the intra-aortal balloon pump (IABP) / Frazier 1990; van Ommen 1990/, the volume flow of < 2.5 l/min, which can be achieved on average, is mostly not enough for the large, out of body heart support systems, such as membrane and centrifugal pumps. Therefore, the overall circulation can only be substantially supported in exceptional cases during a transient complete heart failure /Deeb 1990; Jegaden 1991/.

A further benefit of the system compared to IABP is the genuine volume relief of the heart, which does not even require synchronization of the pump with the heart activity. The drawback compared to IABP is the large diameter, so that on some occasions placement becomes difficult or impossible.

- The important part of this minimally invasive pump system (Hp21, Hp14) compared to the generally accepted assist systems is the relatively fast and gentle placement without thoracotomy, so that that it can also be used by cardiologists with sufficiently reduced pump, such as in case of H14, and heart support can be provided already at an early stage of heart failure.

However, because of its start-up time described in Chapter 2.1, which is caused by the flushing unit, the hemopump system cannot be used as a true emergency system (cf. Chapter 2.4).

- The experience tells that heart support systems as still used as an instrument of last resort, which in many cases significantly reduces the chances of the natural heart to cure due to the delayed application. To the contrary, if the treating cardiologists or heart surgeons have systems at their disposal, which can be quickly placed and are easy to use, when counter indications are taken into account, then the heart can be supported upon the first signs of failure, which is extremely important for cure.

In studies of fibrillating hearts and hearts in cardiogenic shock, hemodynamic values were achieved using micro-axial pumps, which were sufficient for cure of myocardium and sufficient perfusion of peripheral organs. For example, early heart support with increased blood flow can preserve a large part of ischemic myocardium /Deeb 1990; Flameng 1991; Merhige 1989; Scholz 1991, 1994b; Smalling 1992; Wampler 1991a; Wouters 1991/ in case of grave myocardial infarction /Jegaden 1990/ due to reduction of the required O₂ volume of the heart muscle with the concurrently improved blood flow.

- Prophylactic use of pump can also reduce the risk of tachycardia or heart flutter during angioplasties on coronary vessels /Figulla 1994; Loisanse 1990a, 1990b; Scholz 1994a/.
- If the intra-operative use is the primary target, then the hydraulic capacity of a micro-axial pump system can be increased for a short time by increasing the rotation speed above the designed level. Although this increases the pump induced hemolysis, it can only be tolerated for up to about an hour.

Under these conditions, an intra-arterial and biventricular pump system can replace the heart-lung machine during bypass surgeries on heart with reduced pulse. This can significantly reduce the morbidity associated with the heart-lung machine by eliminating the large plastic surface and avoiding the ischemia surgery phase. According to /Aboul-Hosn 1995/, it must be assumed that the time patients spend in a hospital, and especially in intensive care, can be significantly reduced.

Below is the list of clinical indications described so far, physiological use criteria, counter-indications and system specific complications. They are based solely on the application cases, which remain rare, of Hemopump Hp14, Hp21, Hp31 and, in absence of long term experience, must be considered preliminary /Aboul-Hosn 1995; Deeb 1990; Flameng 1991; Frazier 1990a, 1990b, 1991; Loisanse 1990; Waldenberger 1994; Wampler 1988, 1991a, 1991b, 1993, 1994/.

Indications:

- acute rejection reaction upon a successful heart transplant;
- if unexpected complications take place during a catheter examination with possible dilatation of a narrowed coronary vessel; prophylactic use during high risk dilatations;
- if a heart muscle contracts insufficiently (transient heart failure; cardiomyopathy) upon surgery (for example, a bypass surgery);

- the heart cannot wean from cardiopulmonary bypass (heart-lung machine) (low cardiac output);
- acute infarction: if upon an infarction the left ventricle, which mostly gets affected, reduces its pumping capacity to the level that puts the patient's life in danger, and myocardium must regenerate to the extent of reversibility of cardiogenic failure (cardiogenic shock); an early application of an intravascular pump could significantly minimize the area affected by infarction (ischemic area);
- in some cases, as a temporary measure for immediate performance of causal therapy;
- surgeries on hearts without cardiopulmonary bypass.

Physiological use criteria:

- pulmonary capillary wedge pressure [PCWP] (\equiv LAP) > 18 mmHg;
- mean arterial pressure [MAP] < 90 mmHg;
- cardiac index [CI] < 2 liter/(min x m²);
- left ventricular work index [LVWI] < 1,500 g x mm/ (m² x min);
- \rightarrow LVWI = (PCWP + MAP) x CI x 13.6

It takes into account all significant physiological indications, and turned out to be an important criterion of successful application of Hemopump: at LVWI < 1,500 mmg/ m²/min the survival rate drops below 40%;

- no positive reaction on medication or volume therapy, as well as the use of IABP.

Counter-indications:

- arteriosclerosis;
- implantation problems due to physiological vessel dimensions, stenosis, calcification of intima or other diseases of aortal wall;
- pulmonary hypertension (for the left ventricular hemopump system);
- biventricular heart failure (for the left ventricular hemopump system);
- hypertrophic ventricle with poor hemodynamic due to reduced filling of the ventricle in case of irregular pump operation;
- disease in final stage (non-regenerative heart insufficiency);
- grave stenosis or insufficiency of aortic or pulmonary valve;
- valve prosthesis, which prevents inserting and sealing of suction tube;
- blood anomalies with the risk of increased blood damage;
- mural thrombus in atrium/ventricle.

Potential risks inherent to the system:

- hemolysis;
- thrombolysis;
- bleedings;
- cavitation;
- embolism due to a high hemolysis rate and thrombus appearance;
- vascular damages, up to vessel dissection;
- placement problems (for example, retrograde shifting, valve passage, position of cannula in the ventricle);
- in at least 25% of patients, placement of Hp21 is impossible, because the pump is too large for peripheral vessels;
- infection and sepsis;

- misplacement of suction tube in aorta ascendens upon tube ejection;
- valve damages by high relative movement of suction tube towards the valve door or by suction of the pump to the valve apparatus;
- endocardial damages by pump suction;
- forward displacement of heart;
- leg ischemia up to amputation based on misplaced deposits or shifting of vessels by guiding catheter;
- pump failure (for example, shaft breakdown in Hp21 – Johnson & Johnson; seal failure);
- pump dependence.

2.3 Final review of the Hemopump system

The concept of a drive with a flexible shaft and external drive, inherent to all Hemopump systems, is a significant drawback, despite the improved service life and the possibility at this time to place the shaft beyond the aortic arch. In addition to the still existing risk of shaft breakdowns, the required flushing unit of the seal with integrated shaft oiling represents a systematic drawback due to the required start-up time of 10 to 30 minutes, and increases the risk of septic complications. Hp14 was specifically designed as an emergency system, and should be able to start quickly. If the patient collapses in a catheter laboratory, the patient must be immediately stabilized hemodynamically, so that Hp14 must sometimes be prepared for operation prophylactically. If the application is unsuccessful, it results in significant additional costs (about 10,000 DM), which is unacceptable due to the increased cost pressure in the health industry.

The principal drawback of the Hemopump system is irregular operation. Neither control of the current pump function /Mees 1991/, nor the positioning can be performed without additional equipment. Furthermore, irregular operation can lead to cyclical suction phases with the risk of cavitation in the pump and heart rhythm defects.

It its current form, the Hemopump system cannot be used as the right heart support system.

2.4 Derived system parameters for Helmholtz micro-axial pumps

Based on the experience with the Hemopump system, we can summarize below the medical requirements and technical goals for a new concept of an intravascular micro-axial pump. The basic quality of the system is the maximum possible hydraulic capacity, in order to be prepared to all scenarios. Since the heart support system has a maximum capacity $V < 2 \text{ l/min}$ at physiological pressures, and has a limited indication spectrum, such volume flow is defined as hydraulic lower limit.

Since capacity and placement ability depend upon the size of the respective pump, a pump family will be developed as a left and right heart support system, consisting of the diameters of 5.4 mm, 6.4 mm and 8.0 mm.

Boundary conditions for percutaneously inserted system:

Diameter of a pump inserted through the periphery cannot significantly exceed 6 mm. Besides, the length of the rigid pump part must be limited to about 30 mm, in order to enable introduction of the pump through the curved peripheral vessels.

To avoid the drawbacks caused by the flexible shaft, the drive should be integrated directly into the pump.

If such a system is developed with a seal between the rotating and stationary part, then there should be no flushing of the seal and bearing parts due to the start-up times and the technical efforts associated with it. This way the new pump system can be used as an emergency system.

Based on these basic requirements, a 6.4 mm pump hydraulically comparable to Hp31 will be developed in the course of this work. The 5.4 mm version developed in addition to it is hydraulically stronger than the comparable Hp14 due to the pump diameter larger than that of Hp14.

Figures 2.2 and 2.3 show examples of a peripheral placement for the left (LV Assist) and right heart support (RV Assist).

It is precisely during the use of an intravascular system for right heart support with reversed flow that it becomes clear how short the rigid pump part must be. Otherwise it is practically impossible to insert the tube end through two valve doors.

Alternatively to the presentation in Figure 2.3, an RV pump can also be placed in the right atrium, so that the extended and possibly bent pressure tube stretches through the ventricle into the pulmonary artery (truncus pulmonaris).

If LV is used according to Figure 2.2, placement of the pump in aorta ascendens with short and straight suction tube is a prerequisite of a high capacity system, since otherwise, as discussed with regard to Hp21, the hydraulic losses in the long tube will additionally reduce already limited capacity.

Boundary conditions for a transthoracic placement system:

If the pump is introduced not through the periphery, but into the vessel system in the vicinity of the heart, then the nominal system diameter can be increased to 7 mm -8 mm. This enables volume flows of up to 6 l/min under physiological conditions. The length of the total system created to this end with an 8.0 mm pump with integrated drive should not exceed 40 mm in this case, so as not to make its use in the vessel system unnecessarily difficult.

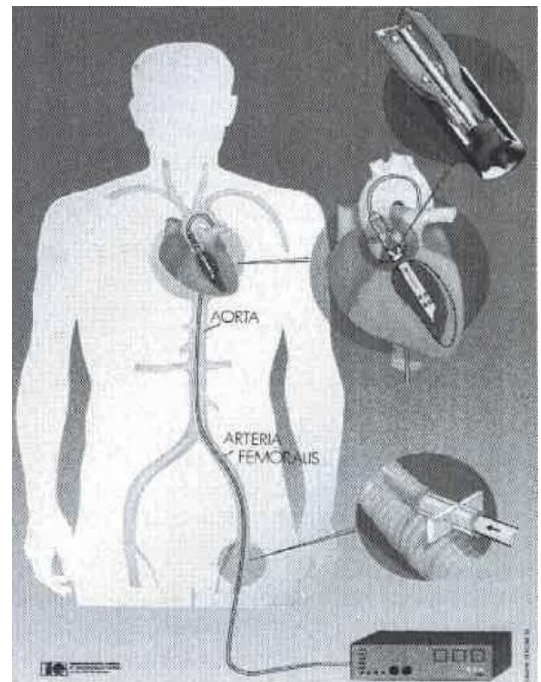


Figure 2.2 Scheme of a left side heart support with an intra-arterial micro-axial pump

Requirements to location:

Passage through the native valve apparatus is common for all intravascular systems for short and medium term heart support; it prevents a hydraulic by-pass between the pressure and suction sides. This requires a tube connected to the pump, according to Figures 2.2 and 2.3, for both the right and left side heart support. It free end must be able to pass through the valve apparatus, and should have an suction protected tip for the LV system according to Figure 2.10. Even with the minimal wall thickness, the tube must be soft, flexible and collapse protected, which can be achieved with an integrated spiral reinforcement.

The total system consisting of the pump, drive, tube and guiding catheter must be visible by means of a diagnostic procedure (X-rays, ultrasound), and can optionally be placed through a guiding chord.

Requirements to integrated sensors:

For exact information on the current pump function, sensors integrated into the pump head are indispensable. It should provide information on the pump position and the current flow, as well as allow for obstruction or suction control required due to bending or blockage of the tube.

The required sensors should also allow locating the system without X-rays or ultrasound, and should also be usable for description of heart activity.

The respective research is presented in Chapter 10.

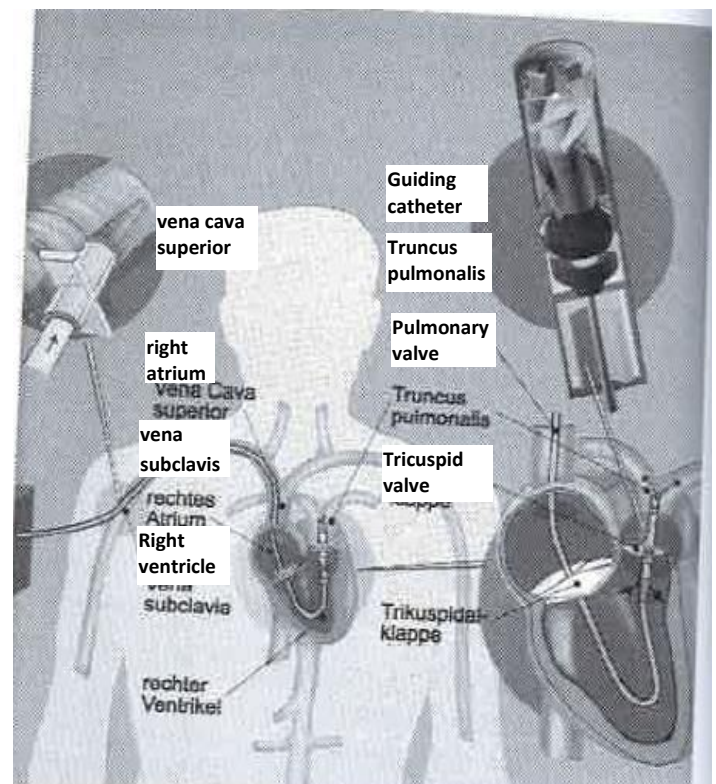


[Figure 2.3 Scheme of a right side heart support with an intra-arterial micro-axial pump with reversed flow]

3. Analysis of possible design concepts and choice of concept

Quickly rotating heart support systems built according to the rotary principle have the highest hydraulic capacity density available, so that no other principle of propelling can be considered, if the purpose is to achieve maximum capacity with the minimum space. The external diameter of the intravascular pumps in question is limited even stronger than the total length of the rigid pump system, due to the intended placement through the peripheral vessels. Therefore, we will limit our research to a peripherally placeable system with the diameter under 6.4 mm, based on the experience with Hemopump Hp21. At this point it cannot be determined for sure to which extent the sufficient placement can be achieved in this manner.

If we consider a system 6.4 mm in diameter and take into account the results from Chapter 9.2.2 on the internal pressure loss as a function of achievable flow cross sections, it becomes clear that nesting of the drive and pump with a drive located in the hub or in the pump casing is wrong for hydraulic reasons, and is also technically unfeasible due to the required drive capacity, as described in Chapter 4.

A reasonable solution can be found in axial arrangement of system components with the resulting diameter to length ratio of $\approx 1:6$, with the drive located behind the pump due to the improved convective heat removal, and logically in the flow direction. For the case of the left heart support according to Figure 2.2, this is, in principle, possible, while with the required flow reversal for the right heart support according to Figure 2.3, liquid can in principle only be sucked away by a motor.

If we also take into account the requirement that the liquid, which needs to be pumped, i.e. blood, cannot get into the mechanical parts of the pump and drive, since otherwise the system will immediately fail, we are left with two possible approaches according to Figure 3.1, which can be split into two main groups, according to the energy transfer between the shaft and the pump.

Energy in this case can be transferred magnetostatically and positively, which requires different bearing and sealing concepts. In case of magnetostatic energy transfer, there is a physical barrier between the input and output sides, so that separate bearings are required for the drive and pump sides. In case of positive transfer, the pump is driven directly. The latter case requires, however, a dynamic seal on the drive shaft.

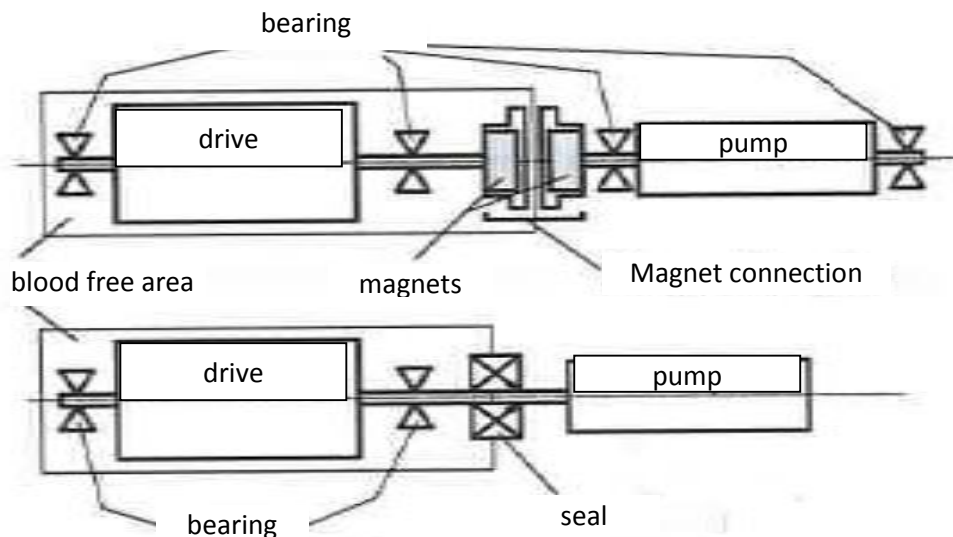


Figure 3.1: Bearing and sealing concepts for a micro-axial pump with integrated drive

3.1 Pump with an integrated magnetic clutch

Before we start developing a general concept of a pump with magnetostatic energy transfer, we would like to provide a description of development of an operable magnetic clutch. In addition to the determination of the design type, another central issue is the provision of torque that can be transferred through the clutch, which enables rotor operation at the design point of the pump with a security of about 2.

We will then discuss the bearing forms, which can be used for the work of rotor in blood.

3.1.1 Magnetic clutch

Concept:

As far as the transfer principle is concerned, magnetic clutches can be split into the categories of synchronous and hysteresis clutches. Hysteresis clutches, where one of the sides is made of a segmented magnet, and the other one of a magnetic hysteresis material with high remanence and permeability, and low coercive force, display mostly constant transferrable torque at small slip of the output side to the input side. Similarly constructed eddy current clutches, where the hysteresis disc is replaced by a combination of a copper and soft iron discs, have a torque proportional to slip. Due to the relative movement, significant temperatures in excess of 100°C can be achieved in both clutch forms, so that they are not an option for integration in blood pumps not only because of their 10 per cent lower torque compared with synchronous clutch /Thyssen AG 1992, Westphal 1994/, but also because of the thermal aspects.

In synchronous clutches, the input and output sides have the same, even number of permanent magnets, arranged in mirror symmetry for disc clutches and in rotation symmetry for concentric rotary clutches. Both designs are similar with respect to the transferrable torque, assuming comparable magnet volumes and strengths, since identical torque transferring diameter d_{moment} can be achieved.

While the diameter d_{moment} for concentric rotary clutch equals to the external diameter of the centrally arranged magnet port plus the gap heights, in case of disc clutch it can be well approximated by the

$$d_{Moment} = \sqrt{\frac{D_a^2 + D_i^2}{2}}$$

analogy of a centroid of an area at the point of load as in Figure 3.2, where D_a is the external rotating and D_i is the inner rotating magnet diameter. The benefit of a concentric rotary clutch over a disc

clutch is, as shown in Figure 3.2, the simple structure with a generally plane parting surface and level magnets. The disc clutch, to the contrary, produces axial forces, which result from the attracting magnet forces and must be captured from the bearing components of the drive and pump, while a concentric rotary clutch remains virtually free of force with perfectly concentric structure. Figure 3.2 illustrates the design principle of both clutch types.

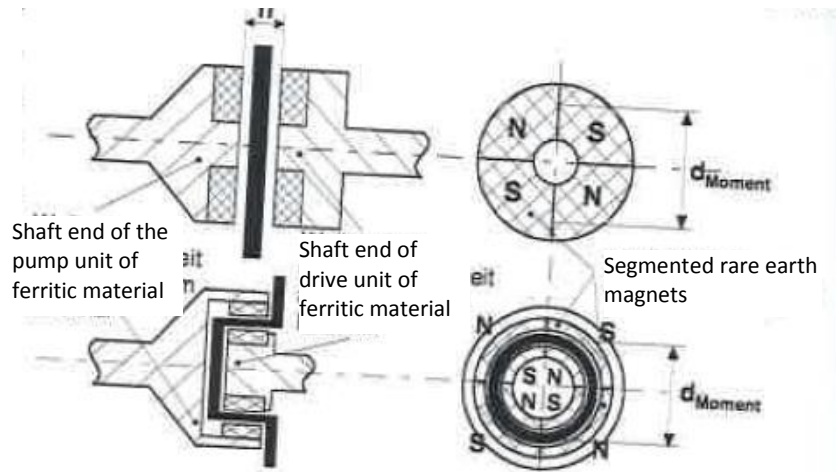


Figure 3.2 Synchronous clutches: - magnet – disc clutch –concentric rotary clutch

Implementation and testing:

For research of the transferrable torque performed within the scope of this work, the disc clutch turned out to be preferable due to its simple structure and the possibility to assess the torque as a function of the magnet distance h . For use in axially arranged blood pumps, the disc coupling also has another benefit, namely that the fluid gap is also level due to the simple parting disc, so that flushing of the axial gap can be ensured by proper flow direction better than in a concentric rotary clutch.

For a four segment disc clutch with the arrangement according to Figure 3.2, the transferrable torque and axial forces were measured as a function of the axial magnet distance h and the twisting angle between the input and output magnet halves, and are presented in Figure 3.3 together with the minimum required torque for transfer of 3W of mechanic capacity at the rotation speed of $n = 30,000$ turns/min.

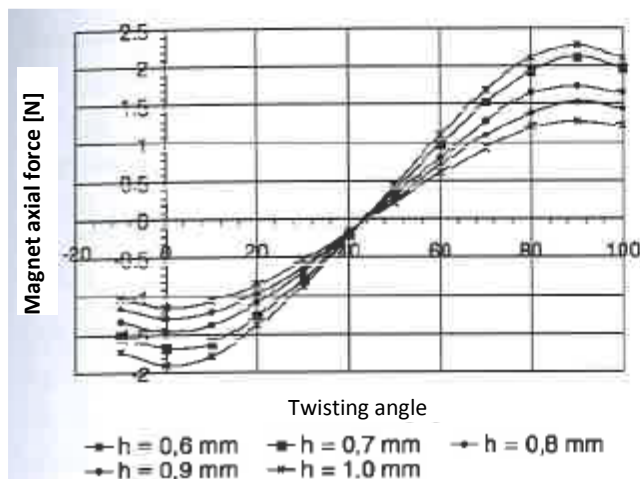


Figure 3.3a: Axial force of a magnet disc clutch with a diameter of 5.8 mm

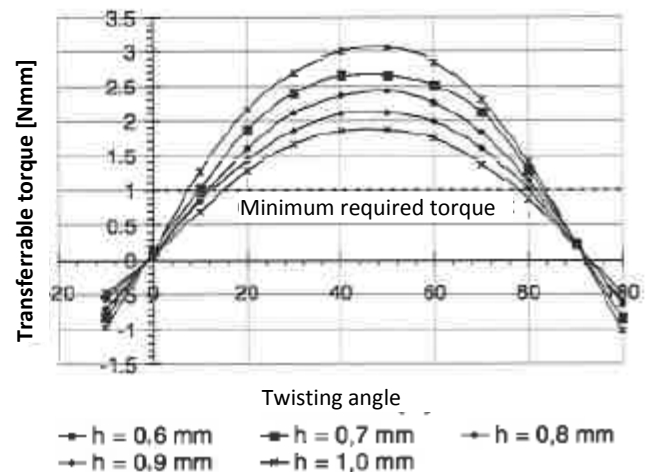


Figure 3.3b: Torque transfer of a magnet disc clutch with a diameter of 5.8 mm

Assessment:

The clutch measured in this case with the diameter of 5.8 mm, and 6.0 mm long including the air gap and partition disc, can transfer according to the performed measurements at the realistic magnet distance of $h \approx 0.7 \text{ mm} - 0.9 \text{ mm}$ the minimum required torque with the security of $s \approx 2.4$. This demonstrates the principal function of a magnetic clutch in the available space.

3.1.2 Bearings in blood

Concept:

To implement a pump with a physically separate input part, it is necessary to provide a rotor bearing in blood similarly to Figure 3.1, since an additional encapsulated bearing is unacceptable due to its dimensions and the required additional friction. According to the explanations provided in Chapter 11.1 on blood induced bearing breakdown due to high local temperatures, implementation of bearings, whose concept involves blood passage through narrow gaps, must be accompanied by effective heat removal. There may also not be any obvious bearing gaps, which would allow a thrombus growing inside the bearing to grow into the flow channel. Based on the experience with the rotary blood pumps developed in the Helmholtz institute for chronic heart support, an initial thrombus growth can be diminishing, if the thrombus in the border area is deprived of chemically active substances due to high flow speeds, so that thrombocytes are not accumulated any longer. This can be done by a roller trace bearing /Westphal 1994/, as well as the plain bearing versions presented in Figure 3.4 and based on mixed friction.

In both cases, the smooth transfer between the rotating and stationary part ensures that no significant thrombus can grow from the gap into the blood flow, provided there is sufficient surrounding flow. Besides, the rotating bearing diameter is chosen in both design examples as little as possible, in order to keep the relative speed and the associated dissipation in the bearing at a low level. For the inner plain bearing of version b, this results in a separate sealing gap on the shaft circumference, in order to minimize the hemline towards the blood flow. This sealing gap is also very low, in order to keep low the induced additional friction and blood shearing.

Testing and assessment:

Extensive research of rotary blood pumps, which are developed for chronic organ perfusion at the Helmholtz institute, is currently conducted in connection with the whole area of bearings in blood. The experience with the implemented bearings make it clear that all bearing versions, which come into immediate contact with blood, demonstrate high thrombogenicity.

3.1.3 Pump concept with an integrated magnetic clutch

The description of the pump concepts presented below is provided as a review with a short system assessment.

Concept I: Version with maximum distance of rotor bearing /Rosarius 1994/:

The pump unit for left heart support shown in Figure 3.5 has primarily axial current, as all concept examples presented below, and the fluid resulting from the drive located directly behind the blades, whose external diameter is the same as that of the pump unit, is drained diagonally through the rotating pump shaft (5).

The pump unit is spatially separated from the drive unit by a disc (14) made of bio compatible thermoplastic or ceramics, so that the power transfer is performed magnetostatically by the already described magnet disc clutch (13) from Figure 3.2. The infeed star wheel located axially and radially with respect to the pump housing (2) consists of a central inlet funnel (1), which is centered to the pump housing (8) over no more than three bridges (2). In the funnel, there is either a ball holder (3), if the bearing is made as a full roller trace bearing, or the space for a radial plain bearing (4), as shown in Figure 3.4b. The rotor (6) is connected to the pump shaft (5) in a torsion-resistant way, and is axially placed in such way that a minimal axial clearance of the starting disc (17) can be chosen among the rotor (6), stator (7) and shaft (5). The function of the starting discs is to minimize the back current between the stator and shaft against the main flow with low frictional connection. The stator itself consists of a hollow hub with three blades arrange on the top of it, and is fixed at the pump cover (8) over the frictional connection of the external blade edges.

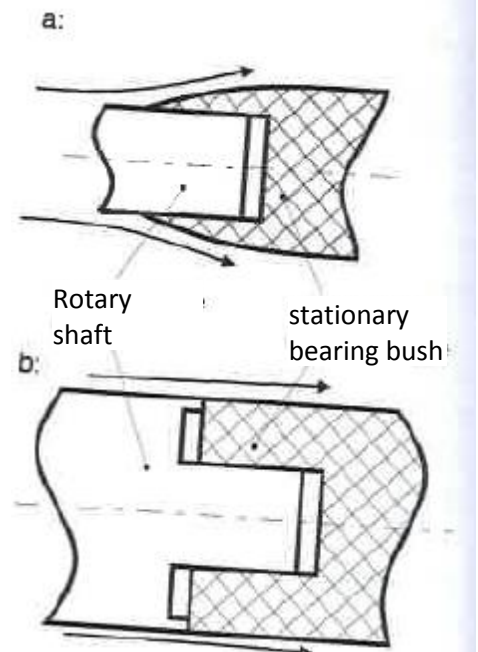


Figure 3.4: Plain bearing in blood flow
a: located externally
b: located internally

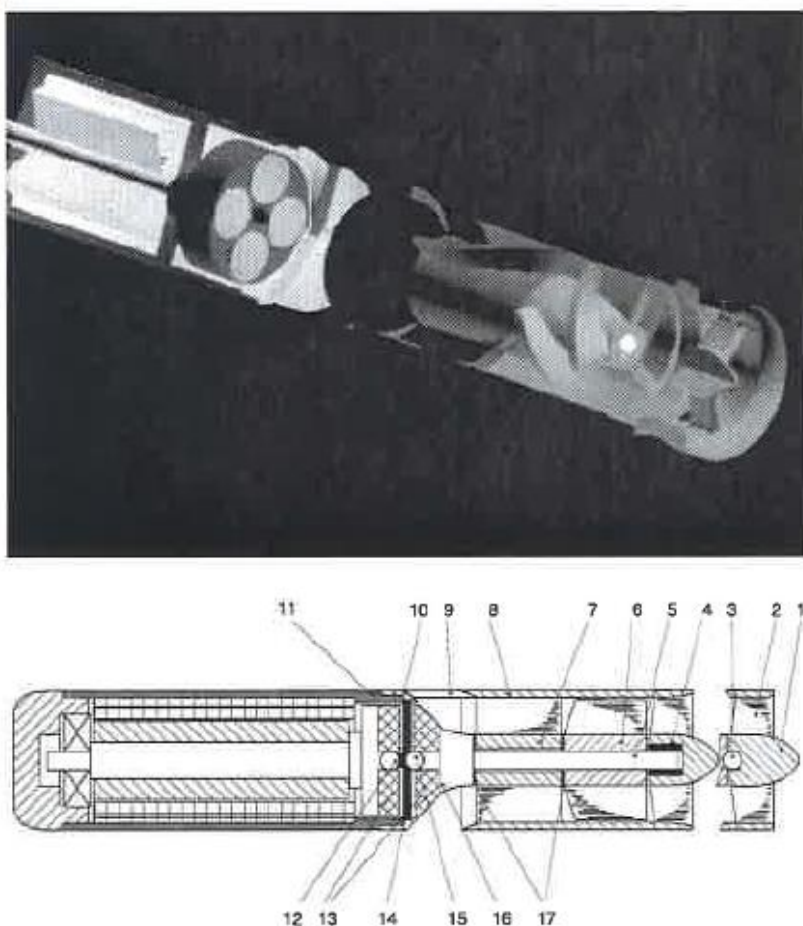


Figure 3.5 Concept with maximum distance of rotor bearing

At the end of the back portion of the pump shaft (16), which expands radially, there is a pump side coupling unit and the back part of the roller trace bearing (15) consisting of calotte in the parting disc (14) and a ball connected with the shaft.

This form of the roller trace bearing did not work well during the testing, because either friction torque between the ball and calotte was too high, with the respective axial pretension, or the centralizing effect was too low with the low pretension, so that an occasional contact of the rotor blades with the pump covering could not be prevented. A better option is the already described combined bearing of the roller trace bearing and radial plain bearing, which does not require axial pretension. The axial force of the magnets reduced by the axial thrust of the rotor is sufficient for the back centering of the ball in the calotte.

The pump covering (8) is connected with the thin bridges (9) over the diagonal fluid discharger, and through the ring-shaped end (10) with the drive housing (11), and centered to the latter. On the inner side of the of the covering there is a fix with supporting edge to which the parting disc is both radially centered and arranged level with the drive housing part.

Figure 3.5 illustrates a micro electromotor, which will be discussed in more detail in Chapter 4.2.2. We only need to mention at this point the front bearing (12), which makes the axial force of the coupling magnets be received directly in the center on the thin parting disc (14), so that specifically if thermoplastic materials are used, the disc is not axially deformed by these forces as a membrane.

The described concept is mechanically feasible in the version with combined bearing, but turns out to be hydraulically ineffective. The star wheel located at the intake works as a cover, and results, with the identical blading, in a significant 1.0 l/min capacity reduction compared to the pump version described below, which does not require a star wheel.

Concept II: Version with central plain bearing:

The concept presented here with a central stator plain bearing is based on Concept I, so that we will only describe here significant differences.

The bearing of the rotor shaft (5) is performed without an inlet ring through a combination of a radial plain bearing (16) located in the stator, similarly to version b in Figure 3.4, and an axial bearing (15), which corresponds to a deformed roller trace bearing based on a ball running against an even surface. This type of combined bearing is based on the use of the axial force in the drive direction resulting from the magnet attraction reduced by the axial thrust of the rotor (6), so that an axial drop is only required in the area of the magnet disc clutch (13). This form of bearing guarantees a reliable centering of the rotor shaft with low friction losses, while compensation of the axial force inherent to the disc clutches can still take place directly in the center of the parting disc (14).

If a central rotating coupling (18) is alternatively integrated according to Figure 3.6b, then the axial drop in the coupling area becomes unnecessary. Instead, the plain bearing (16) centrally placed in the stator also serves as axial bearing (17) on the coupling side in order to receive the axial thrust of the rotor (6). The central part of the central rotating coupling (19) is located on the blood side due to the smaller rotating diameter and the resulting lower shearing.

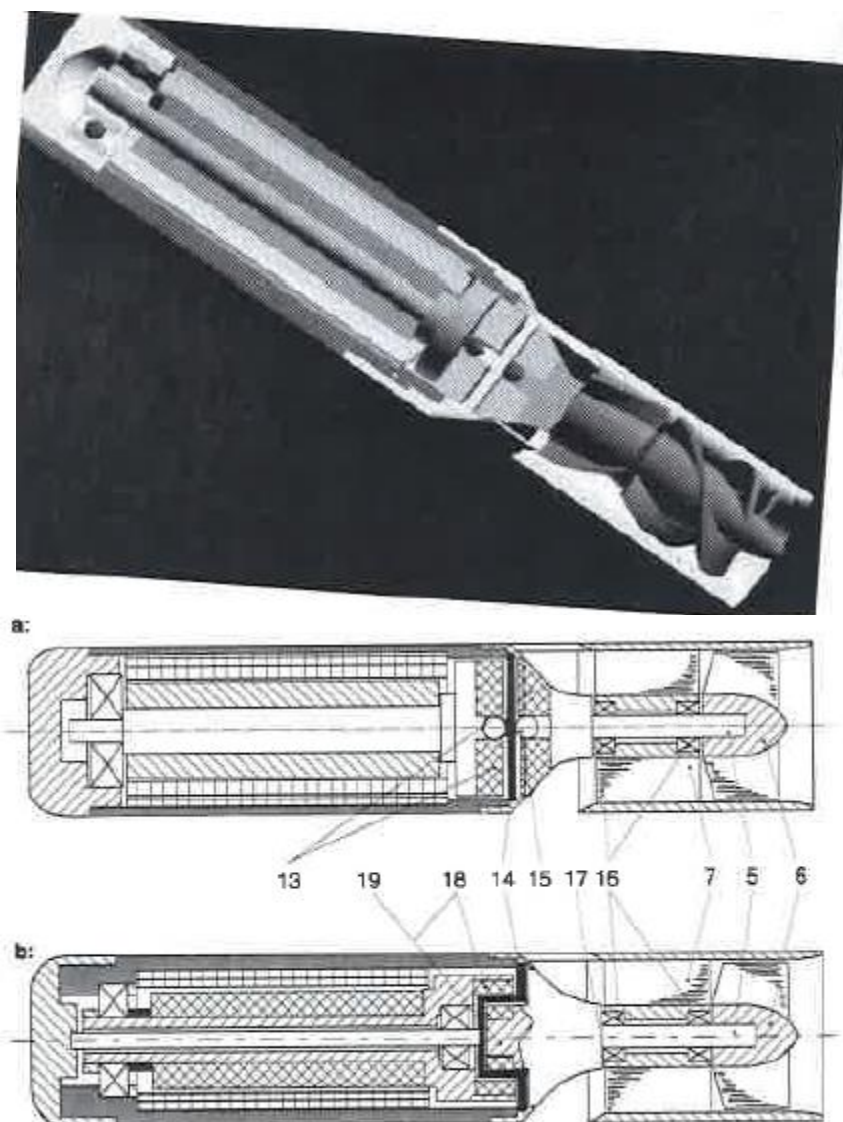


Figure 3.6: Concept with central plain bearing in stator:

a: with disc clutch

b: with central rotating coupling

Concept III: Version with inverse plain bearing:

Since Concept II presented in Figure 3.6 is based on a bearing located in stator, it cannot be used in this form for a pump without a stator. Figure 3.7 shows an example of a similarly structured system with inversely arranged bearing (20) centrally located in the rotor (6). In this embodiment, the coupling magnets (13) and the parting disc (14) are spherically curved on both sides, the center of the curve being located in the roller trace bearing (20). This ensures a constant distance between the magnets with additional magnetic centering of the hanging and oscillating rotor based on the axial magnet forces. To ensure sufficient stability of the bearing shaft (21), the latter is centrally located at the back drive cover (22) and in the parting disc (14). To this end, the drive must be designed as a hollow shaft motor (23).

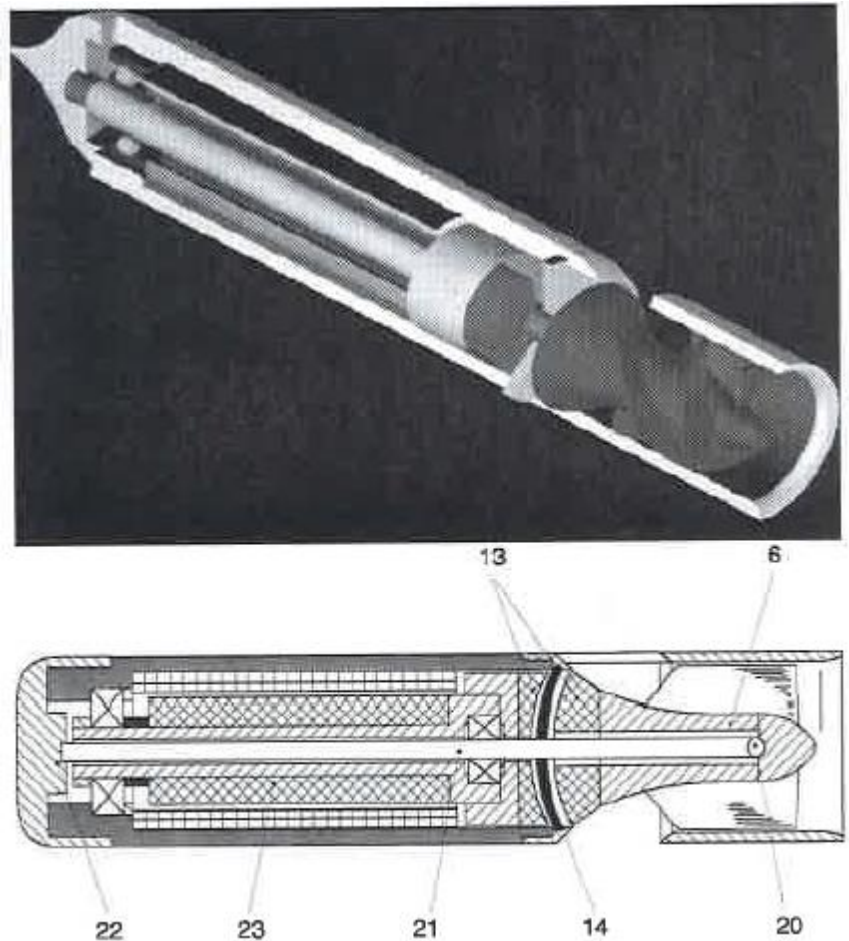


Figure 3.7: Concept with central plain bearing in rotor

3.2 Pump with through-shaft

The concept of a pump with a central shaft according to Figure 3.1 requires a dynamic seal of the drive part against the flow of fluid. This can only be done with seals, which are compact and have a small dissipated capacity $P_{\text{Friction}} < 1 \text{ W}$.

Below we will discuss various sealing concepts, their function and the choice of the concept of a pump with a through-shaft.

3.2.1 Sealing concepts

The possible seals can be split into the categories of fluid and frictional connection seals. Fluid seals include hydrodynamic and hydrostatic seals, as well as magnetic fluid seals. Compared to the frictional connection seals, they do not have any dry friction, if properly dimensioned, and are consequently durable. Depending upon the fluid viscosity, the dissipated capacity in the seal can be significantly lower than $P_{\text{Friction}} < 1 \text{ W}$.

3.2.1.1 Hydrodynamic capacity:

Since the seal may not leak, no labyrinth seals can be used. The only possible system is the one with a fluid-proof stop, as shown in Figure 3.8, in which the disc moving with the shaft in a respective

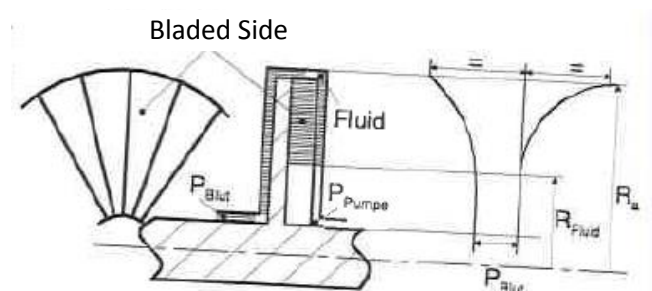


Figure 3.8 Working principle of a dynamic stop according to /Trutnovsky 1981/

compartment is bladed on one side. Radially increasing pressure can build up on the bladed side as the result of centrifugal force, so that depending upon the rotation speed, the fluid pressure P_{Blut} can be higher than the pressure P_{Pumpe} inside the pump, and yet a fluid ring with the inner radius of R_{Fluid} forms on the bladed side. A calculation of the seal capacity for a seal 4 mm in diameter, which is thus still can be integrated in the vicinity of the hub of a micro axial pump stator, resulted in the maximum useful pressure of $\Delta P_{\text{Nutz}} = P_{\text{Blut}} - P_{\text{Pumpe}} = 13.16 \text{ kPa}$ (100 mmHg) at the rotation speed of $n = 30,000 \text{ turns/min}$ in full bladed cased with a loss capacity of $P_{\text{Verlust}} = 0.008 \text{ W}$ /Trutnovsky 1981/. However, up to small rotation speeds, the resulting pressure decreases over proportionally, so that physiological pressures can no longer be sealed in this case.

Assessment:

In view of the fact that the dynamic seal must be, for safety reasons, combined with a further static seal, in this case specifically for start-up of the pump, and that blood is unfit as sealing liquid due to its aggregation tendency, this type of seal will not be pursued any further.

3.2.1.2 Hydrostatic seal:

In this type of seal, leaking sealing liquid is pumped through a narrow gap with high pressure into the medium, which is to be sealed off. This form of active flushing can ensure that no blood gets into the narrow gap in this case. This form of seal is known to work in micro axial pumps (see axial seal in Hemopump system). The drawback here is that there must be an additional flushing liquid, which must be forwarded into blood with targeted pressure. Furthermore, for the sealing function and minimization of the flushing flow volume, the gap must be kept very narrow, which requires active pressing of the rotating and stationary parts. This results in a complex design of the gap and high starting torque, which cannot be provided at the time the pump starts by the micro motor, which needs to be integrated in this case.

3.2.1.3 Magnetic fluid seal:

Concept:

Another version of a fluid seal is a magnetic fluid seal /Ferrofluidics Corp; USPat. Re32573; Rosensweig 1985/ in conjunction with a small axial gap between the stator and rotor, as shown on the scheme in Figure 3.9.

In this version, there are a centrally located magnet and a pole piece, in which a non-ferrous stator housing is located in such way, that the magnetic field lines are always perpendicular to the shaft bridges. Along the field lines, in an about $10 \mu\text{m}$ wide gap, the colloidal magnet particles of the magnetic fluid orientate and even remain in the magnetic field when there is a pressure difference across the bridge. The width capacity of each stage is estimated at 45 mmHg, so that an eight stage seal would theoretically be able to withstand pressures of up to $\Delta P = 360 \text{ mmHg}$.

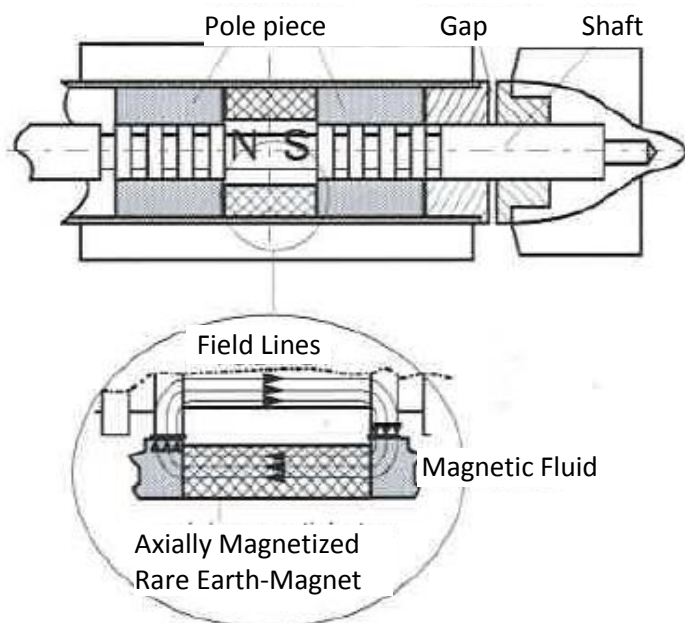


Figure 3.9 Scheme of a miniature magnetic fluid]

However, the experiments show that the maximum pressure capacity does not exceed 160 mmHg, which is caused by the extremely small size of the seal, so that general calculations are only applicable to a limited extent.

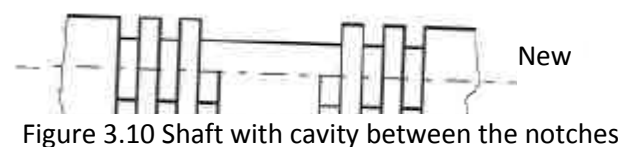
The narrow axial gap in Figure 3.9 between the stator and rotor affects rotation of the fluid in the gap due to the rotation of the shaft and rotor according to the Stokes' law, which causes build-up of radial pressure of about 8÷ 12 mmHg. In addition to this intended effect that the hydrodynamically functioning seal creates a pressure difference between the inner and outer radius of the stator hub, and thereby relieves the magnetic fluid seal, another effect is that the fluid exchange at the border surface between the pumped medium and magnetic fluid is reduced, so that the sealing losses due to magnetic fluid erosion with time are minimized.

Implementation and testing:

The concept of magnetic fluid seal was researched separately in a testing facility developed for this purpose. In addition to the pure tightness, the capacity dissipated in the seal could also be measured.

The tightness research has clearly shown that the local mixed friction, as well as too high eccentricity in the gap between the pole piece and grooved shaft must be absolutely avoided, since the magnetic fluid in both cases is either mechanically wiped off or dynamically pumped away from the seal area based on convergent gap. In this case, the seal gets visible leaky already upon short working time of about 5 minutes and low pressures of up to 50 mmHg. Therefore, stringent requirements are imposed on the form and location tolerances of the shaft with respect to the pole piece. The eccentricity must be no more than half the width of the gap, which, in its turn, is limited to 10 µm through 20 µm for optimal tightness. If such requirements are fulfilled, then tightness improves, but after a short time again starts leaking a mixture of water and glycerin, due to the mixing of the magnetic fluid with the liquid, which is supposed to be sealed off, i.e. blood or, in this case, water. The resulting emulsion build-up from sealing liquid and the medium, which is to be sealed off, becomes more obvious with the increase of the eccentric position of the shaft with respect to the pole piece. The resulting convergent and divergent gap results in fast mixing of the sealing liquid with the medium, which is to be sealed off. This dilution results in gradual loss of the magnetic qualities of the liquid vital for the sealing function. Finally, the cushion of the magnetic fluid can no longer resist the pressure of the liquid, which is sealed off, and gets washed away.

Figure 3.10 shows the way to resist this dilution resulting from the working principle; an additional cavity is created between the affected areas, from which stored magnetic fluid can be added to the sealing area, once the liquid is washed away.



A further problem is the assembly and insertion of the magnetic fluid. When the shaft is inserted, the notches filled with the magnetic fluid are pulled by the magnetized pole piece. It cannot be guaranteed in this case that a portion of the fluid does not leave its designated position and become no longer available for the sealing function. Therefore, each experiment must be preceded by sufficient start-up time for the sealing fluid to settle in the magnetic field and excessive amount to exit the sealing area.

If in addition to that the whole notch area in Figure 3.10 is filled with the magnetic fluid, this causes divergence and significant reduction of the magnetic field in the gap between the shaft and pole piece related to the sealing. During the start-up time, excessive amounts of magnetic fluids are driven away from the seal, so that afterwards the sealing liquid is not only placed in the proper location, but also available in

an amount sufficient for proper sealing. However, this step becomes unnecessary if magnetizing of the central ring magnet takes place upon installation, as it is usually done in the commercially available sealing systems.

The magnetic fluid seals considered here were tested in the combination presented in Figure 3.11, with the system consisting of a pump, sealing and bearing was operating in order to measure capacity, first externally, and after that with an integrated drive. The latter version also went through a 6 hour in-vitro blood experiment, in order to test the mixing propensity of blood at the phase boundary to the sealing liquid. Based on the preliminary experiments, the seal consists of four sealing stages on each side of the centrally arranged ring magnet, since each further stage linearly increases the maximum achievable seal pressure.

In order to slow down the mixing at the phase boundary, the seal is preceded by an area, which minimizes on-going mixing in the border area due to the narrow gap between the sleeve and shaft. The tightness experiments were performed in a testing facility similar to that shown in Figure 9.1a, and the design operation point of the pump was fixed at $n = 30,000$ turns/minute at 100 mmHg. The mechanics of the pump remains open to the external pressure through the back opening, so that the total pressure difference of the pump concerns the seal.

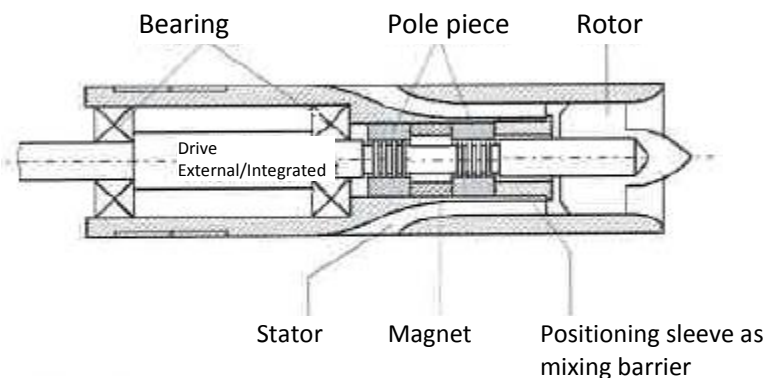


Figure 3.11 integrated magnetic fluid seal

The magnetic fluid on the basis of hydrocarbon by Ferrofluidics was used and resulted in the seal service life of up to 90 minutes. The dissipated capacity in the seal was between 1.0 W and 1.5 W. Such a high loss capacity results from a relatively high basic viscosity of the syrupy carrier fluid ($\eta \approx 240$ mPas at 40°C) and viscosity increasing effect of the Lorentz force due to the ferromagnetic particles moving in the magnetic field.

For safe operation, temperature of the sealing liquid must be verified due to high dissipation capacity; according to the manufacturer's instructions, its carrier fluid achieves steam pressure of one atmosphere at 150°C. Temperature of the sealing liquid can only be calculated. The following simplifying assumptions have been made:

- the total dissipated capacity from dry friction and fluid shearing is transformed into heat in magnetic field;
- heat loss through the shaft is negligibly small;
- the entire magnetic field has the same temperature;
- the temperature at the bottom of the pole piece corresponds to the magnetic field temperature;
- due to high convective heat loss resulting from the high flow speed, the entire pump stator has the fluid temperature on its surface facing the pump;
- the entire heat is transferred through the pole piece, and not through the shaft as well, as it is actually the case.

Therefore, the fluid temperature can be assessed from the equation for the heat flow:

$$\dot{Q} = P_{\text{verl.}} = +2 \cdot \pi \cdot \lambda \cdot L \cdot \frac{\vartheta_{\text{Ferrofluid}} - \vartheta_u}{\ln(d_2/d_1)} = +2 \cdot \pi \cdot \lambda \cdot L \cdot \frac{\Delta \vartheta_{\text{Ferrofluid}}}{\ln(d_2/d_1)} \quad (\text{Gl.3.1})$$

With the assumed boundary conditions of $P_{\text{Verl.}} = 2.5 \text{ W}$ as a maximum value, $\lambda = \lambda_{\text{Stahl}} \approx 50 \text{ W/mK}$, and $\vartheta_u = 25^\circ\text{C}$, as well as the geometric distances $d_1 = 4 \text{ mm}$, $d_2 = 2 \text{ mm}$ and $L = L_{\text{polschuh}} = 4.8 \text{ mm}$, we arrive at the temperature increase in the magnetic fluid of $\Delta \vartheta_{\text{Ferrofluid}} = 1.1^\circ\text{C}$. This temperature is below the critical blood temperature of 42°C .

The maximum seal service time of up to 10 hours was produced by the experiments with a magnetic fluid by NSK on the hydrocarbon basis, which has a clearly lower viscosity of the carrier fluid ($\eta \approx 70 \text{ mPas}$ at 40°C) even at stronger coercive field than the Ferrofluid produced by Ferrofluidics, which was used afterwards, and a lower propensity to fluid mixing at phase boundary. Unfortunately, this result cannot be reproduced at will with the available seal quality. Instead of that, the seal service time can vary from 30 minutes to the achieved 10 hours with identical protocol. The cause of failure has always been penetration, sooner or later, of the sealed medium into the sealing liquid. For example, the pump cleared a 6 hour in vitro blood test with constant motor capacity during the test, but when the facility was taken apart, there was hardly any magnetic fluid in the seal area. Instead, it had already been largely substituted with blood. An important cause of this repeated mixing is the production quality, which could not be achieved at the lab scale. The required form and location tolerances in the area of $< 1\text{-}2 \text{ }\mu\text{m}$ can only be achieved after the assembly of the pole piece, magnets and the front sleeve together by a subsequent processing with jig grinding for openings, since it allows to get rid of alignment errors and eccentricities.

Assessment:

It can now be established that a magnetic fluid seal can in principle be used for short term support. However, it imposes very high production requirements, which are sometimes very difficult to implement. In particular, in this case the used miniature ball bearings cannot be arranged on both sides of the seal, so that the bearing clearance of $6 \text{ }\mu\text{m}$ typical in such cases causes eccentricity of $3 \text{ }\mu\text{m}$ already in the seal, and of $6 \text{ }\mu\text{m}$ at the end of the sleeve. This results in an eccentricity of the shaft to the pole piece, which is already close to the upper limit. A further problem is poor reproducibility of the results, which are all based on washing of the magnetic fluid away. In these cases, although most of the fluid gets inside the pump, a small part of it also gets into the pumped medium. Although these amounts are in the area of 0.001 ml , if this fluid is based on hydrocarbon, it can cause if not health problems, than at least certification issues.

3.2.1.4 Frictional connection seals:

Concept:

In all frictional connection seals, a pre-stressed sealing lip is frictionally connected to a counter surface. In operation with sealing against fluid, this causes mixed friction in the concerned area, since some very small penetration of fluid into the concerned area, be it due to capillary forces or micro grooving, cannot be prevented. Due to the mixed friction, the loss capacity can be small, $P_{\text{Friktion}} < 1 \text{ W}$, if the rotating diameters are small, even with a seal of this type.

If deemed necessary due to significant thrombus development, radial shaft seals can also be operated hydrostatically, since there already is a very narrow gap between the shaft and seal. The gas is flushed in this case with an isotonic and biocompatible solution from inside to the outside. The electrolytic balance of the flushing liquid is required in order to prevent penetration of pure blood into the gap due to osmotic

pressure, and in order to ensure low leakage into blood. This type of seal implies that drive runs in the flushing liquid, which is possible with a brushless synchronous motor described in Chapter 4.2.2.

Implementation and testing:

Of all the commercially available seal types in axial or radial form, most cannot be used because of the materials they are made of or their available sizes.

Due to its large rotating diameter, the axial form causes relative speeds of up to 5 m/s, which is far beyond the limit values of realistic friction combinations for operations that last hours or days.

Solely radial seals with very small rotating diameters of the PTFE or UHdPE basis can be considered for the dynamic load due to the demonstrated biocompatibility. To this end, the profile of unfilled PTFE shown in Figure 3.12 was tested against an unhardened, ferritic, non-rusting shaft.

The tested wiper shown in Figure 3.12 consists of a sealing element and a conic sealing lip. The dynamic sealing is performed by a sealing lip in the radial direction on the shaft, while a light press fit maintains a rather surface than purely line contact due to the elastic form of the lip.

With a rotating diameter of 2 mm, friction torque of merely 0.3 Nmm was measured in water/glycerin, which causes the friction capacity of $P_{\text{Verlust}} = 0.94 \text{ W}$ at the rotation speed of $n = 30,000$ turns/minute. This dynamic friction capacity is even slightly below the loss capacity of a magnetic fluid seal. The sealing capacity achievable in this manner was equal in the short term to up to 300 mmHg.

Operation during several hours caused leaking due to visible shaft wear. The tests with assembly performed days in advance also showed early collapse of the seal due to relaxing qualities /Michaeli 1992/ of the seal material. PTFE, as any other thermoplastic, causes material relaxation under pretension. The pretension resulting from the press fit between the shaft and sealing lip is not counteracted by any external force, with the exception of the tension resulting from the elastic deformation of plastic. However, this tension gradually goes away due to the relaxation effect (tendency to creep) in the plastic.

This process can be compensated by using a spring working in a radial direction. Figure 3.13 shows a commercially available miniature radial shaft seal with integrated sealing lip pretension. Experiments with this seal using a shaft covered with a thin layer in PVD process resulted in service times of up to many days.

There is an issue of sensitivity of such seal to misalignments resulting from rigidity of the sealing lip. This prevents the system from compensating radial misalignment of the shaft to the seal. A slightly eccentric position already causes significant increase in friction torque and early collapse of the seal, sometimes after

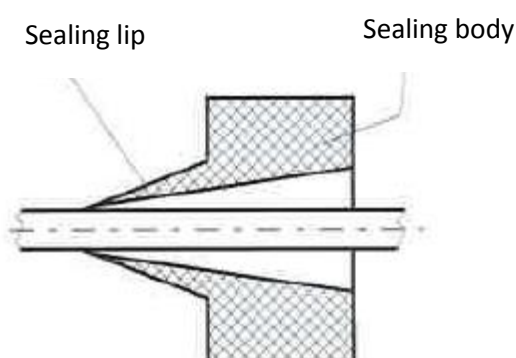


Figure 3.12 Radial shaft seal with thin lip

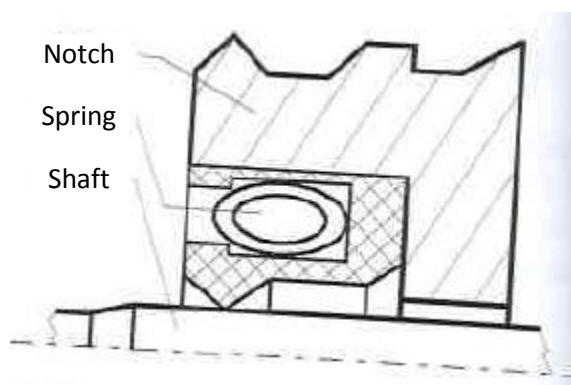


Figure 3.13: Radial shaft seal on PTFE basis with spring pretension

several minutes. This problem can be solved by additionally using the seal as radial plain bearing. The experiments demonstrated that the appearing radial forces can be accumulated without visible seal wear. As the result of this structural modification, the service times of up to 7 days have been achieved, and the only limitation was wear of the thin layer on the shaft.

Another issue with this type of seal is the initial static friction torque, which must be applied when micro electric motor starts and can be very high, depending on the tolerances. If the fit between the shaft and sealing ring is at the lower limit of the recommended tolerance range with an excess of only 10 μm to 30 μm , then the starting procedure is unproblematic and reproducible. Already upon an initial start-up time of merely 30 seconds, the friction torque between the shaft and seal remains stable and low. A new start can be repeated as necessary and does not affect the sealing capacity, as long as the shaft and sealing ring are not manipulated manually with respect to each other in the course of a new assembly.

Assessment and summary:

The relatively simple design of frictional connection seal compared to all other discussed sealing options, together with the achievable low frictional losses $P_{\text{Friction}} < 1 \text{ W}$, makes it preferable for short time pump use of up to several days.

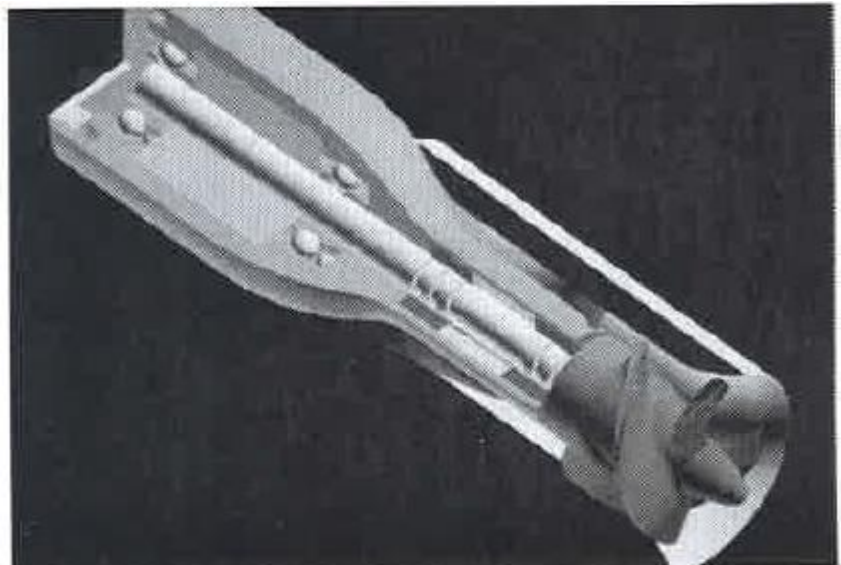
3.2.2 Pump concept

Concept IV: Version with central shaft:

Contrary to Concepts I to III presented so far, this concept is based on direct force transfer with a central shaft with both motor anchor and pump motor attached to it. The following picture shows the system in its constructive form.

Bearing (24), whether floating or fixed, is performed by a miniature ball bearing, which is positioned inside the structure using the principle of space minimization and highest possible bearing distance. Important aspects of the function of the drive and integrated seal (25, 27) are concentricity with allowed eccentricity $e < 8 \mu\text{m}$, which can be achieved with the chosen bearing.

Contrary to the previously discussed concepts, there is no



CAD Graphics of a Pump with Ferric fluid seal

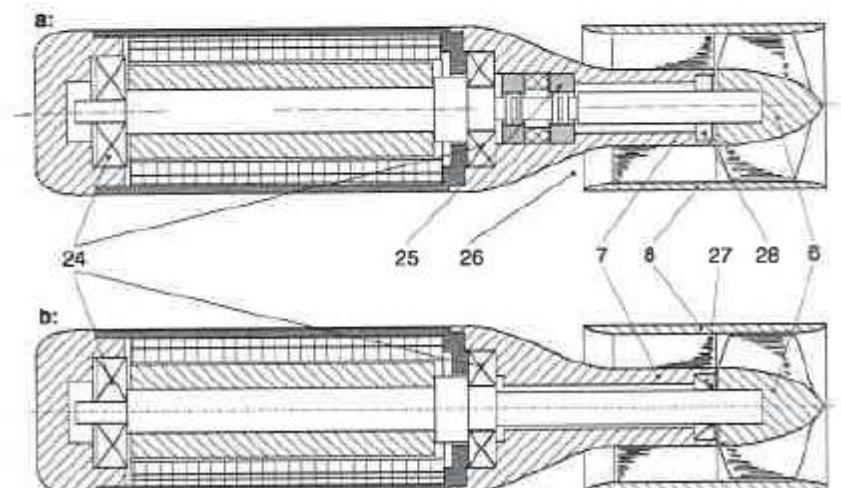


Figure 3.14: Concept with a central shaft and seal

A: Ferric Fluid seal
B: Ferric fluid seal
ABIOMED Ex. 1044

further liquid gap between rotor and stator, except for the bearing clearance, in which pure blood could be sheared and could agglomerate.

The flood at the inlet is directed axially without an inlet ring, and then similarly to the already presented versions, with exit diagonally (26) through a stationary notch.

The embodiments presented in Figures 3.14a,b can be immediately converted into versions without a stator by removing it. In such case, the pump cover (8) is no longer attached to stator (7) over frictional connection, but similarly to the magnetic clutch versions, through bridges to the drive housing.

3.3 Concept comparison and choice

Finally, we provide a comparison in the table form of the discussed micro-axial pump concepts I through IV, and choose a system fit for short time left heart support. The same criteria apply to an RV pump with reverse flow direction.

	Concept I	Concept II	Concept III	Concept IV
Blading: - rotor + stator - rotor	possible possible	possible impossible	impossible possible	possible possible
Right heart support	possible	possible to limited extent	possible	possible
Flow guidance for left heart support	with infeed star wheel; diagonal outflow over rotary shaft through slot in pump cover	axial; diagonal outflow over rotary shaft through slot in pump cover	axial; diagonal outflow over rotary shaft through slot in pump cover	axial; diagonal outflow over diagonal notch part
Fluid gap	between rotor shaft and stator; in the area of the magnetic clutch; two pump bearings	in the plain bearing between rotor shaft and stator; in the area of the magnetic clutch	in inverse plain bearing; in the area of the magnetic clutch	axial gap between rotor and stator
Coupling	magnetostatic	magnetostatic	magnetostatic	none
Seal	none	none	none	see Chapter 3.2.1
Bearing: - in blood - in drive	2 bearings 2 bearings	2 bearings 2 bearings	1 bearing 2 bearings	0 bearings 2 bearings
Frictional losses	medium: through fluid gap and four bearings	medium: through fluid gap and four bearings	medium: through fluid gap and three bearings	medium to high: through seal and two bearings
Flow losses	high: through infeed star wheel and bridges in the outlet; losses of about 1.2 l/min compared to IV	low: through bridges in the outlet; losses of about 0.2 l/min compared to IV	low: through bridges in the outlet; losses of about 0.2 l/min compared to IV	low: since there are no additional flow obstacles in the channel
Thrombogenicity	very high: through bearing in the infeed star	high: through bearing in blood, high	medium: through bearing in blood, medium	medium: through seal

	wheel, high number of fluid gaps	number of fluid gaps	number of fluid gaps	
Duration of use: (assessed) - acute - medium - chronic	- - -	0 0 -	0 + +	+ 0 -
Complexity	high	medium	medium	high for (magnetic fluid seal); low for lip seal
Minimal design length with micro electric motor with respect to Version IV	+ 10 mm (infeed star wheel and coupling)	+ 6 mm (coupling)	+ 6 mm (coupling)	size comparison: minimal design length = 32 mm as a 6 mm pump without a stator

Table 2: Concept comparison

Summary:

Concept IV is the best option for short time use, since it is the shortest system in terms of design with the highest hydraulic capacity and lowest complexity (lip seal).

For the following experiments with blading and the system in general, we will only use the lab sample according to Concept IV, Figure 3.14b, with frictional connection miniature radial shaft seal according to Figure 3.13.

4. Drive concepts, design and testing

Before discussing the choice and design of a drive fit to be integrated into a micro-axial blood pump under Concept IV from Chapter 3.2.2, we will present an assessment of the required capacity based on the blading types available so far. Similarly to Chapters 7 through 12, we will only consider 6 mm drives, whose results can be transferred onto the 5 and 7 mm systems.

4.1 Assessment of required capacity

To characterize the hydraulic power consumption of blading as a function of the rotation speed, we will first present the capacity curve for the ideal case of congruent speed triangles in rotor with different rotation speeds.

The principle of angular momentum says that the sum total of all torque interacting in the system in question (in our case, rotor) with the flow is equal to the change of the angular momentum L_u itself, which lets us calculate the driving torque M_u :

$$M_u = \frac{d}{dt}(L_u) \stackrel{r_1, r_2, c_{u1}, c_{u2} = \text{constant}}{=} \dot{m} \cdot (r_2 \cdot c_{u2} - r_1 \cdot c_{u1}) \stackrel{c_{u1}=0 \text{ (for flow free of angular momentum)}}{=} \dot{m} \cdot r_2 \cdot c_{u2} \quad (\text{equation 4.1})$$

From the simplified requirement of rotation speed invariant congruent speed triangles, the following approximation can be derived for the volume flow, respectively mass flow with respect to the conditions in the design point:

$$\dot{V} = \frac{n}{n_0} \cdot \dot{V}_0 \quad \text{with } \dot{m} = \dot{V} \cdot \rho \stackrel{\rho = \text{constant}}{\text{be derived (already in the previous sentence for grammatical reasons)}}$$

(equation 4.2)

Taking into account the flow angle α_2 constant for blade, we can calculate the required capacity $P_{\text{rot}}(n)$ as:

$$P_{\text{rot}}(n) = M_u \cdot \omega = \frac{n^3}{n_0^2} \cdot \frac{2 \cdot \dot{V}_0^2 \cdot \rho \cdot r_2}{(r_2^2 - r_1^2) \cdot \tan(\alpha_2)} = \frac{n^3}{n_0^2} \cdot K \quad (\text{equation 4.3})$$

with $K = 3.8 \text{ Nmm}$ for the rotor in question. This means that the required capacity increases cubically with the rotation speed.

In a testing facility shown in Figure 9.1a, the blades identical for calculation purposes were tested with respect to hydraulic and capacity aspect. Figure 4.1 shows the measured and calculated performance. Both must be interpreted exclusive of the assumed mechanical loss of 0.5 W, which does not event exceed the 0.5 W assumed for the 4 bearing version of the pump according to Concept I. The additional capacity needed under Concept IV and caused by inclusion of frictional connection seals is disregarded here.

If we compare the measurement with the calculated capacity need, we can see a good qualitative correlation.

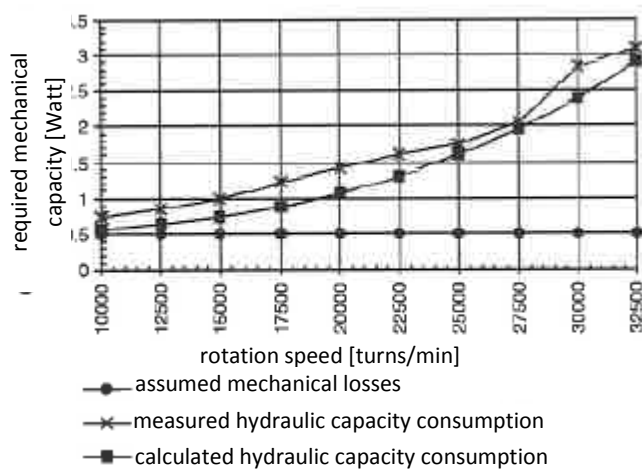


Figure 4.1 Initial assessment of required capacity

Based on the results, a mechanic capacity of about 3W is required for operation of moderate blading at the design point of $n = 30,000$ turns/min, which must at least be provided by the following drives in the available space. Figures 9.3b-9.5b in Chapter 9.1.2 show that the required capacity can strongly exceed these minimum requirements, depending upon the blading.

The minimum requirements to the drive of a 6 mm LV pump are listed below:

required drive capacity:	$P_{\text{mech}} \geq 3 \text{ W}$
design rotation speed:	$n = 30,000 \text{ turns/min}$
maximum permitted external diameter:	$D_{\text{Amax}} \leq 6.4 \text{ mm}$
maximum permissible length:	$L_{\text{AXmax}} \leq 20 \text{ mm}$

4.2 Drive concepts

If the mechanical energy transfer principle with flexible shaft and extra-corporeal drive of the Hemopump concept is supposed to be substituted by an energy transformer in the immediate proximity of the pump, then the available options are electromechanical and hydraulic-mechanical transformers. Pneumatically driven systems are excluded due to the risk of air embolism, since otherwise system pressures of up to 10 bars are required for intra-aortal balloon pumps for a pneumatically driven energy transformer, so that even the smallest gaps cause large leaks into blood.

For the sake of providing an overview, the description of the drive systems considered in this work is followed by the discussion of experiments and results.

4.2.1 Hydraulic drives

Contrary to an electromechanical transformer with its systematic problems of the size (about 6.4 mm in diameter, 20 mm length) and heat loss that needs to be removed ($P_{\text{Verlust}} > 2 \text{ W}$), a hydraulic drive can be more compact with theoretically the same output capacity /Backe 1988/, and has an inner cooling due to energy transfer by incoming and outgoing working fluid. Besides, hydraulic motors allow for determined leakage of the drive fluid, so that it is unnecessary to have a seal between the rotor and

stator, if the working fluid is a water-based biocompatible solution, and leak into blood does not exceed 100 ml/h.

Requirements to a hydraulic drive concept:

In addition to the maximum permissible external diameter of 6.4 mm, the design length of the drive should be significantly below 20 mm, so that the total system consisting of a pump and drive could be better placed within about 25 mm. This limits the length of the hydraulic motor to about 10 to 15 mm. Furthermore, the diameter of the hose through which the working fluid is added may not exceed 4 mm, since otherwise the peripheral vessels through which the system is supposed to be introduced get too narrow in the cross-section, which causes insufficient blood flow (ischemia) in the peripheral organs. Depending upon the motor displacement, this results in very high pressure losses in the hydraulic catheter of 4 bar at the assumed displacement of 0.6 l/min of the motor and a distance of 2 m for the direct and reverse catheter lumen. The upper limit for system pressure was set at 10 bar, so that taking into account a pressure reserve of 2 bar, the working pressure in the hydraulic motor is set at 4 bar.

Concept of hydraulic motor:

The stringent requirements with respect to the very small displacement, relatively high working pressure and small dimensions leave us with just one motor according to the positive displacement principle. Hydrodynamic systems with inherently high volume flows and low system pressures are automatically dismissed /Karassik 1985/.

Various positive displacement principles for pistons, tooth and wings were researched for hydraulic motor for feasibility /Backe 1988, Vetter 1990/. The only principle that looks realistic in production in the given dimensions is the rotary slide motor. It consists of a further simplified, single-acting vane motor with only two wings in the form of a rotary slide. The benefit of this structure is that the rotor and slide structure is easier to produce than a version with multiple wings. The resulting pulsation is taken into account.

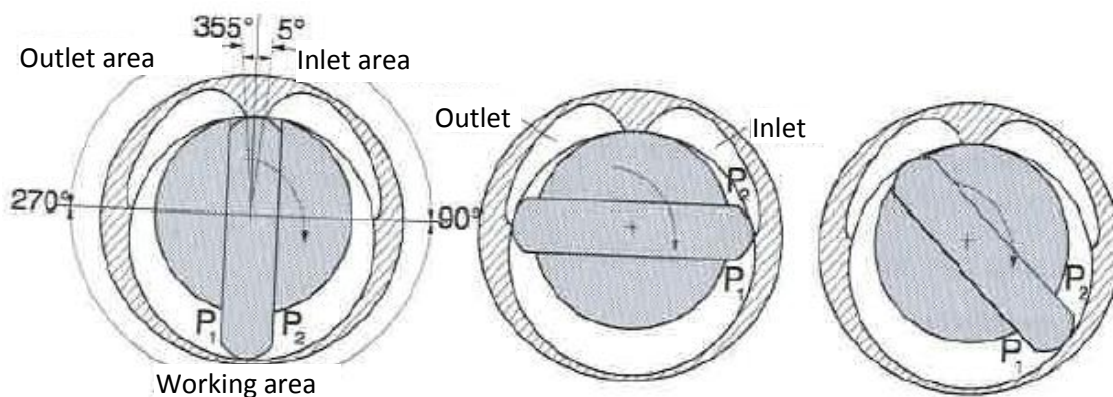


Figure 4.2 Scheme of rotary slide motor (fluid area is in white)

In order to keep the number of the required parts low and further simplify the production, the hydraulic motor should only have one slide and no springs in order to reduce the radial leakage gap. The slide is double-acting, and is pushed along the external contour of the working space eccentrically to the rotation axis. The working fluid is added and removed axially through the system catheter on the back side of the hydraulic motor, due to the limited external diameter.

The working principle of the motor is illustrated in Figure 4.2 and can be described as follows.

The working liquid is brought into the back side of the hydraulic motor axially through the inlet tube, and then forwarded in such way that it flows into the working space tangentially at the angle from 5° to 90° . The actual working area consists of a half-circle from 90° to 270° , in which the lever arm and, correspondingly, the area affected by pressure change. Then the fluid is discharged tangentially at the angle from 270° to 355° , and is again forwarded into the axial direction. Between 355° and 5° there is a sealed area from the shaft/housing wall or slide/housing wall. This sealed area eliminates the by-pass between the pressure and suction areas.

Figure 4.3 shows the inlet and outlet channels, in which the working fluid is forwarded into and out of the working space, as described above, as smoothly as possible. Both channels shown as nets are located in the front of the working space shown in Figure 4.2. The inlet and outlet pressure channels are connected to the round openings.

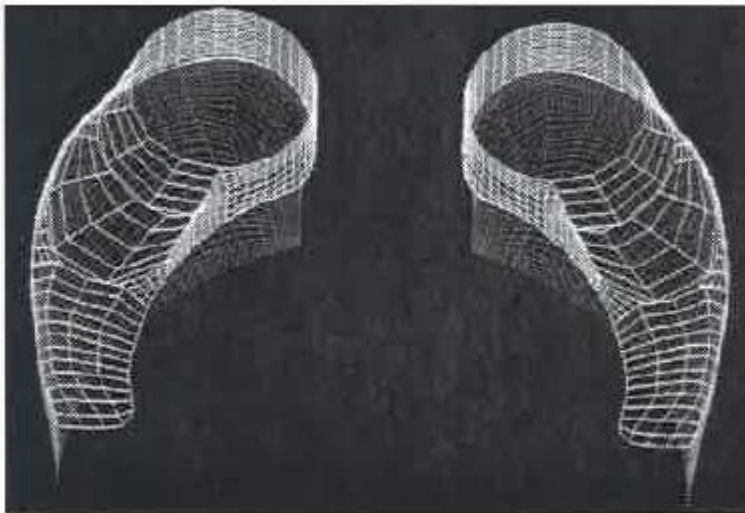


Figure 4.3 CAD graphical net representation of the inlet and outlet flow channels

Testing and discussion:

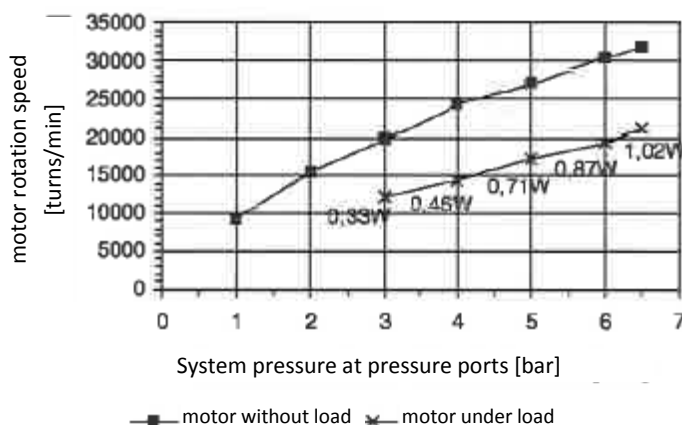


Figure 4.4 Capacity data of the most powerful 6.4 mm hydraulic motor

A special testing facility was developed for testing of hydraulic motor, which can be connected to the micro-axial testing facility according to Figure 9.1a. This way we can measure the hydraulic capacity, which is received by the hydraulic motor, as well as its capacity loss indirectly through the hydraulic diagram, which has already been built elsewhere for the integrated blading. The achievable rotation speed with and without load for the so far most powerful hydraulic motor is shown in Figure 4.4 as a

function of the system pressure at pressure ports of the motor. The maximum achievable capacity so far of $P = 1.02 \text{ W}$ at the rotation speed of $n = 21,270 \text{ turns/min}$ is much lower than the minimal required capacity. This comes as the result of high internal leakages in motor between the high and low pressure sides.

According to the calculations, the front gap height between the rotary slide and housing must be $< 5 \text{ }\mu\text{m}$, and between the shaft and slide $< 10 \text{ }\mu\text{m}$, in order to minimize the leaks, which cannot be implemented with the available manufacturing methods. For this reason, and in view of the fact that production at a later time point is always hardly possible within the required tolerances, the development of a usable hydraulic drive did not go beyond a pure study of options, despite the small size of the total system consisting of a pump and drive.

Figure 4.5 compares the smallest hydraulic motor with a pump and a hydraulically comparable micro electromotor version.

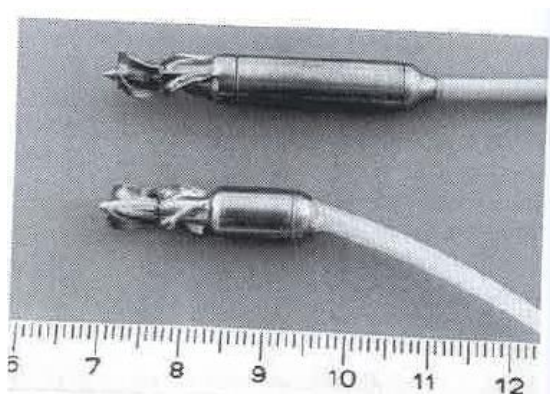


Figure 4.5 Pump with hydraulic motor, 6.4 mm in diameter, compared to a 6.4 mm pump with micro electromotor

4.2.2 Electrical drives

Electrical machines are electromechanical energy transformers. They use the force exercised by electromagnetic fields on moving charge carriers /Skudelny 1989/.

Requirements to an electromechanical drive concept:

Without getting into details of the functioning and differences between electromagnetic energy transformers in the form of synchronous, asynchronous and direct current machines, the energy transformer principles can be roughly filtered based on requirements to the system. They cover:

- simple structure: windings must be feasible;
- minimum dimensions: elongated form with the length to diameter ratio of 3:1;
- high rotation speed: if at all possible, no windings in rotor;
- highest possible power density;
- simple regulation of rotation speed and torque;
- solid structure: no mechanical commutation.

Concept description of a usable electromechanical drive concept:

Asynchronous machines must be disregarded, in particular, due to their size, and classic direct current machines due to the mechanical commutation. A viable option is an electronically commutated

synchronous machine, which is also known as brushless direct current motor. Stationary windings are located in the motor stator, in which magnetic field circulates according to the respective wiring. This magnetic field is followed by a rotating magnet rigidly connected to the drive shaft, while the angle between the magnet field of the winding and that of the magnet, similarly to the synchronous machine, cannot exceed a particular value, because otherwise the motion of the drive is disturbed.

The transmittable torque M of a conductor loop of the length l affected by the current I , which is located at the angle φ to induction B and radius r to the rotation center, can be calculated as $M = 2 \cdot r \cdot l \cdot B \cdot I \cdot \sin \varphi$. Due to the action and reaction principle, it does not matter, whether the winding or the magnet rotates.

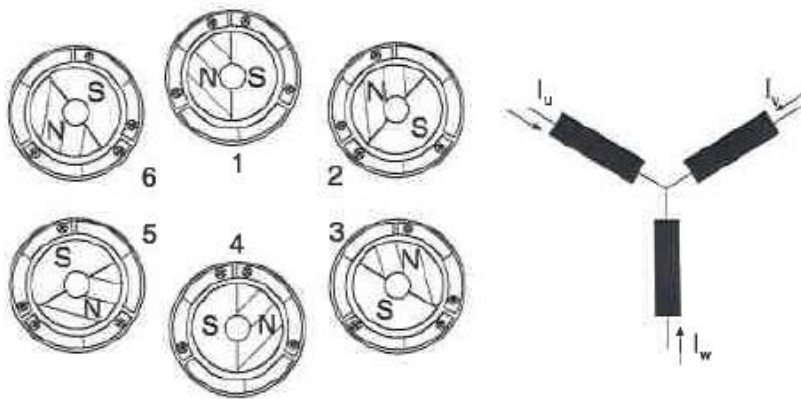


Figure 4.6 Principle of functioning and connection of a three phase synchronous machine /Stemme 1994/

Figure 4.6 illustrates the principle of functioning of a complete three phase drive with a diametrically magnetized, two pole magnet. Two of three phases of the stator winding are under current, according to the illustration, each current direction being shown by an arrow. The appearing stator field now depends on the current direction and current strength I . Due to the interconnection between the stator magnetic field and that of the permanent magnet, the magnet orientates and tries to follow the stator field, even against the external torque M . The presented stator configuration can generate 6 stator fields, so that the resulting magnet field has a spatial dissipation of 60° . Figure 4.7 illustrates a block commutation which corresponds to the three currents in Figure 4.6. To better identify the pulse width modulation, the applicable current curve is shown for I_u in dotted line.

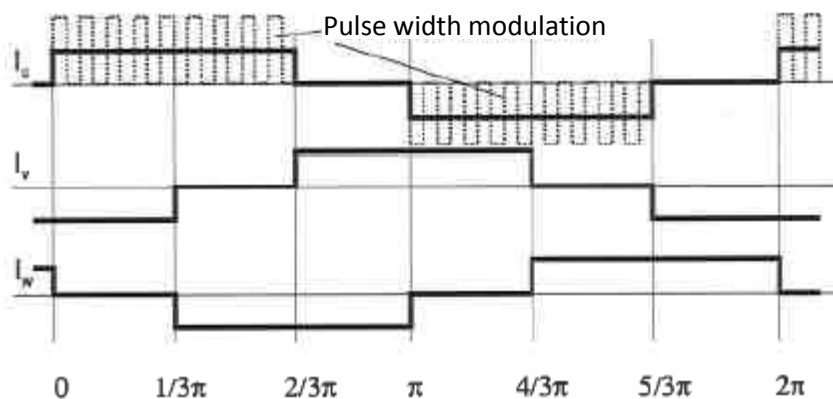


Figure 4.7 Phase current of a three phase synchronous machine

Knowledge of the relative angle position of the permanent magnetic rotor is a prerequisite for the additional current at proper time, as shown in Figure 4.7. With the required size, the position of the circulating magnet can no longer be identified with a Hall sensor. Instead, the induced voltage is measured in the winding, which is not part of the field structure and short circuited in a high resistance manner for measuring. The current position of the magnet can be identified from the time curve and, in this particular case, zero penetration of voltage in this winding. If too large an angle is detected between the magnetic field and the winding, then current in the windings affected by the field can be increased to obtain a constant rotation speed. This is performed by pulse width adjustment, similarly to Figure 4.7. Once the pulse width corresponds to the total phase length, the current is increased by increasing the phase voltage up to the impressed current limit, which serves as winding protection.

Creation of an electronically commutated synchronous machine:

As we are about to develop an electrical motor fit to operate a pump unit, we must mention that a motor with the required power density is not commercially available.

Under these conditions, a motor was designed in cooperation with the Department of Electrical Engineering of Eindhoven University and Kinetron. According to the datasheet, it was supposed to accumulate electrical power of about 3 W and provide mechanical capacity of about 1 to 1.5 W, which is far below the required capacity.

A new design of an electronically commutated DC motor by Prof. Jufer of the Ecole Polytechnique Federale de Lausanne provided the capacity within the range provided in Chapter 4.1, so that a first motor could be developed and produced in cooperation with ETEL S.A of Motiers, Switzerland.

Figure 4.8 illustrates a produced toothless lab drive, showing all further developments of an 8.00, 6.4 and 5.4 drive.

1 \equiv non-magnetic motor covering of titan with functional interface for pump stator and cap

2 \equiv mostly hysteresis free, magnetic closed circuit of multiple Co-Fe discs

3 \equiv 3 copper windings with rotating magnet field

4 \equiv diametrically magnetized rare earth permanent magnet adjusted to the winding with an air gap of about 0.1 mm

5 \equiv ferritic, non-corroding shaft glued to the magnet

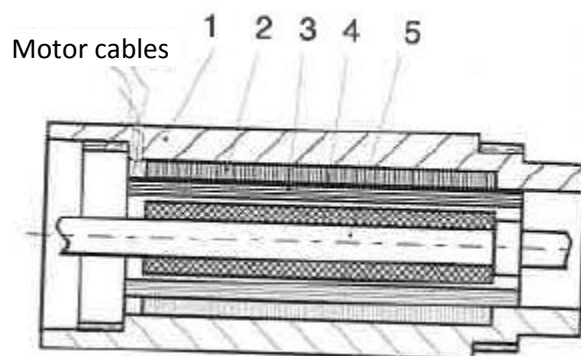


Figure 4.8 Micro electromotor

The drive consists of a titan motor housing (1) with a magnetic closed circuit consisting of multiple Co-Fe soft iron discs (2) glued inside it. Three axial windings (3) made of 0.1 mm thick, hexagonally formed copper wire are glued inside, similarly to Figure 4.6. The diametrically magnetized permanent magnet (4), which is fixed to the drive shaft (5), is positioned with an air gap of 0.1 mm to the stationary winding.

When the lab drive was constructed, it was ensured that the structure is modular to make sure that all functional parts of any pump version can be integrated. Therefore, threads and fits were integrated into the motor covering, which increase the external diameter from 6.5 mm to 8.5 mm for the magnetic closed circuit. The motor cables come on the side of the motor housing. It is first in the final version that the motor cables go in the housing directly to the guiding catheter, by-passing the back bearing.

Testing of the first lab drives of an electronically commutated synchronous machine

The laboratory drive shown in Figure 4.8 was researched in detail in combination with the chosen blading. It was verified to which extent the motor with its capacity is able to operate the chosen blading at the design point and, possibly, beyond it.

Furthermore, it was demonstrated theoretically and experimentally that the measured surface temperature does not exceed the maximum permissible temperature of 42°C.

Contrary to the first assumptions of electrical efficiency of up to 75%, the constructed motors had electrical efficiency of < 55%, which was caused by both high losses of copper due to strong currents and the principal type of winding. A rhombic winding, nominally with efficiency up to 20% higher, could not be constructed for technical reasons.

It could not be determined at this point whether and to which extent this form of winding is better than the axial winding, since the nominal benefit of a rhombic winding in the force flow comes at the cost of extensive winding at the ends with respectively high losses of copper. Therefore, it is quite possible that the effects compensate each other.

- **Assessment of maximum possible heat loss through the motor surface:**

Due to extremely capacity requirements to the micro motors with the actual electrical efficiency staying < 55%, there are non-negligible power losses of copper and iron. These power losses of up to 12 W can only go into the carrying medium, i.e. blood, at diffusive heat transport is insufficient due to the amount of power that needs to be removed. In this case, due to the active overflow of the shaft through the pump, we have forced convection, where inertia and friction forces are much higher than the lifting force caused by temperature change. Therefore, the Nusselt number required to identify the heat transfer coefficient α only depends upon the Reynolds and Prandtl numbers /Renz 1990; VDI Wärmeatlas [Heat Atlas] 1994/.

According to the results of the current visibility described in Chapter 7.4.2 and assessment of Figures 7.31 – 7.32, the middle axial fluid speed along the winding length, which is about 20 mm for all the motors, could be identified as $v_{\text{Freistrah}}=1.0$ m/s at design conditions.

For the estimate of the maximum removable heat amount, the moto surface can be treated as an even surface due to the direct flow and the border layer thickness being small compared to the motor diameter. The permissible surface temperature of the motor is limited to 42°C, so that at the normal body temperature a temperature difference of $\Delta\vartheta = 5\text{K}$ can be utilized.

Below we will calculate to this case a laminar heat transfer based on middle axial open jet speed, and a turbulent heat transfer, which is based on the initial axial outflow speed $v_{\text{Abstrom}}=2.76 \text{ m/s}$.

Therefore, it can be assumed for approximation purposes that the actual heat transfer takes place within the interval from 9.2 W to 17.0 W determined by it.

Based on this assessment of heat, which needs to be removed, which assessment was well supported by the measurement results presented below, it can be assumed that the surface temperature of the shaft itself remains uncritical even with the maximum heat transfer of about 12 W.

$$Re = \frac{\rho \cdot v_{\text{Freispirahl}} \cdot L}{\eta} \stackrel{\text{here}}{=} 5878 - 16223$$

$$Pr = \frac{\eta}{\lambda / c_p} \stackrel{\text{here}}{=} 24,16$$

$$Nu = \frac{\alpha \cdot L}{\lambda}$$

$$Nu_{\text{lam.}} = 0,664 \cdot Re^{1/2} \cdot Pr^{1/3} \stackrel{\text{here; } Re=5878}{=} 147,2$$

$$Nu_{\text{turb.}} = 0,0296 \cdot Re^{0,8} \cdot Pr^{0,43} \stackrel{\text{here } Re=16223}{=} 272$$

$$\dot{Q} = A \cdot \alpha \cdot (v_{\text{Motor}} - v_{\text{Fluid}})$$

$$\Rightarrow \dot{Q}_{\text{max}} = A \cdot \frac{Nu \cdot \lambda}{L} \cdot (v_{\text{Motor}} - v_{\text{Fluid}})_{\text{max}}$$

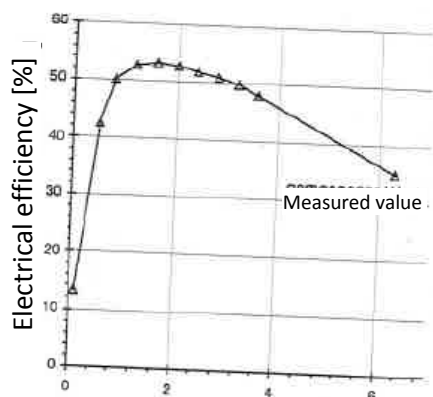
$$\stackrel{\text{here}}{=} 9,2W \left(\text{mit } \alpha_{\text{lam.}} = 4583 \frac{W}{m \cdot K} \right)$$

$$\text{bis } 17W \left(\text{mit } \alpha_{\text{turb.}} = 8468 \frac{W}{m \cdot K} \right)$$

- **Measurement of the surface temperature:**

The power density required in the shaft to operate the chosen blading can only be achieved by high convective heat transport to the blood surrounding the motor.

When motor is operated in the air with the respective power loss, the motor very quickly exceeds the permissible winding temperature of 60°C. This is caused by the low electrical efficiency compared to large motors and too high mechanic power loss.



Mechanical power [W]

—▲— Electrical efficiency of a 6.5 mm motor stator

Figure 4.9 Simulated efficiency (Jufer/ETEL) at $n=30,000$ turns/min extrapolated to 6.4 W

Figure 4.9 show the electrical efficiency of a lab shaft at the design rotation speed of $n=30,000$ turns/min as a function of provided mechanical power. Until the provided power of $P_{\text{mech}} = 3.6$ W, the efficiency is calculated and extrapolated to a comfortably measurable maximum value.

A power loss of 1.7 W to 11.7 W must therefore be expected in the respective power range, which must be completely transferred to blood with the surface temperature being limited to 42°C .

Upon the performed assessment of the expected surface temperature and the maximum removable heat power, we will now verify and validate the electromechanical shaft concept experimentally /Siess 1995/.

To this end, the initially constructed drive was integrated into a plexiglass tube, which has a diameter of 24 mm similar to that of an average aorta, according to Figures 7.31 and 7.32, together with the blading chosen when the motor capacity was identified.

The choice of an amorphous polymer is beneficial due to the available transparency, so that the outflow behavior described in Chapter 7.4.2 can be researched. Besides, the heat conductivity is low in comparison to other materials. Therefore, the measurements of the surface temperature during the contact of motor with the tube in the contact area result in the highest possible temperatures. Compared to tissue with flow of blood, this provides rather an over- than under-estimate of the temperature, which makes this estimate even more reliable.

On the suction side, the pump is axially fixed and hydraulically sealed through a flexible seal, similarly to a native heart valve. To measure the surface temperature, the position can be chosen centrally in the tube or linearly next to the tube. In the critical areas on the motor cover, thermic elements made of copper-constantan wire, 0.1 mm in diameter are positioned and fixed with heat conducting paste and a thin rubber ring. The latter isolates the measurement point from the surroundings, so that the surface temperature is measured, and not that of the surroundings. The temperature was measured on the so-called hotspots, which include the center of the motor winding as the center of the heat source (position 1) and the end of the winding (position 2) with the thickest temperature border layers due to their length.

Figures 4.10 through 4.12 illustrate the temperature curves for the operating states, which are deemed relevant. They include operating the pump at nominal rotation speed in central and eccentric positions, and in the latter case the temperature measurement is performed exactly in linear contact between the motor housing and the tube.

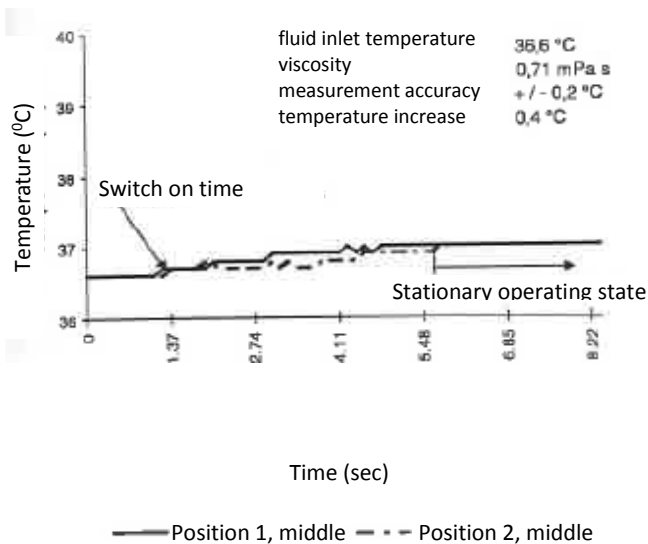


Figure 4.10 Temperature increase during central operation at $n = 30,000$ turns/min

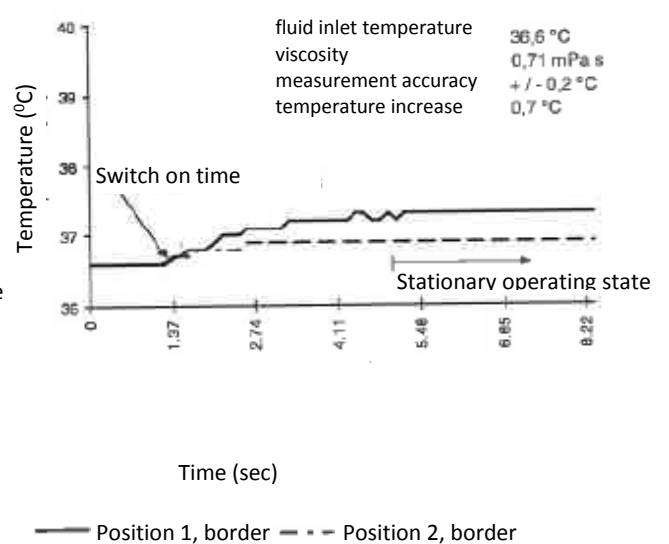


Figure 4.10 Temperature increase during wall contact and operation at $n = 30,000$ turns/min

The operation was again conducted at the nominal rotation speed in order to identify the worst possible operating state of the pump in this position; however, the inlet was occluded and the heating was measured at strongly reduced convection. The measurements demonstrate that the temperature achieves the new stable operating state within several seconds (about 4 seconds) of the motor start, if the pump is operated normally. A simple curve can also be seen in Figure 4.12, where a quasi-stationary temperature is achieved immediately following the full occlusion, with the temperature slightly rising afterwards, only as the result of the fluid heating in the measuring space, until the equilibrium of heat added through the motor and that removed through the heat conductor to the surroundings is also achieved here after about 240 seconds.

Based on these measurements, the heating of the motor surface during the operation of the initially constructed pump remains far below the limit values, and the power loss is assessed to be 2-3 W.

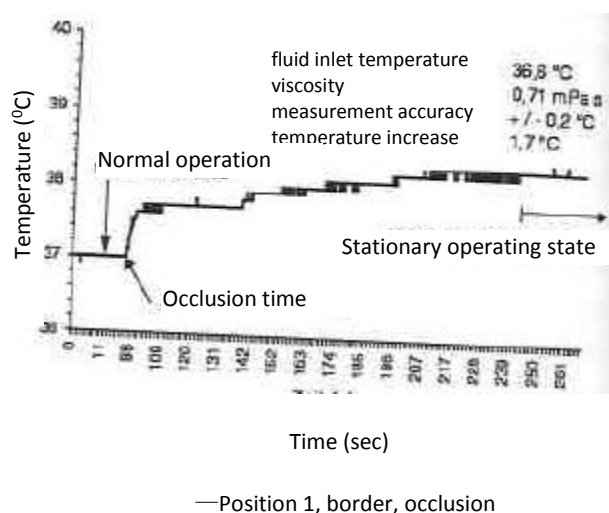


Figure 4.12 Temperature increase during full occlusion of the pump and operation at $n = 30,000$ turns/min

A comparable experiment was again conducted upon successful capacity increase of the motor in order to ensure that the motor can produce the maximum required capacity, at least for a short period of time, without causing critical temperatures. For this purpose, the blading from Figure 9.5a-c was

integrated, and the motor was operated at the upper limit of capacity. At the released mechanical power of 6.5 W, this resulted in the heat power of 11.5 W, which had to be released into the fluid. The temperature increase, which could now be measured, depending upon the arrangement of the thermic element, equaled $\Delta v = 2K - 2.8K$, so that even under such extreme full load conditions the surface temperature stayed $< 40^{\circ}C$, if the patient had a normal body temperature of $37^{\circ}C$. However, in such case a full occlusion of the pump would certainly need to be avoided, since otherwise temperatures are likely to get too high. The way to avoid such imaginable and unfavorable operating condition is discussed in Chapter 10.4.

- **Achievable power density:**

Based on the blading described below in Chapter 9.1.2 for a 6 mm LV pump, we will consider the power characteristic of the 8.5 mm lab drive and the 6.4 mm in vivo drive developed and thoroughly tested for our case.

It is impossible to describe the drive regardless of the respective blading in absence of the respective testing facility, which could sense torque of up to 0.1 Nmm at the rotation speed of up to $n = 40,000$ turns/min. It is only possible to measure the power indirectly by operating blading specifically for the required capacity over the motor, and this way reporting the limit rotation speed up to which the respective blading can be operated.

Figure 4.13 shows the required power for the rotation speed of the blading described in Chapter 9.1.2 and Pictures 9.3a-c through 9.5a-c. This blading characterized by its middle rotor exit angle $\beta_2[^{\circ}]$ covers the relevant power range.

While the blading with $\beta_2 = 44.2^{\circ}$ marks the lower limit of the required power, $\beta_2 = 94.5^{\circ}$ marks the upper limit. If we compare these curves with the initially calculated power curve of an 8.5 mm motor, it becomes obvious that even disregarding the bearing and seal induced losses, the blading with $\beta_2 = 54.2^{\circ}$ can only be operated barely above the design rotation speed of $n = 30,000$ turns/min. The required motor power is only achieved when the permissible motor current is increased to $I_{\text{phase}} = 0.9$ A, which makes it possible to cover the relevant power range, which covers a rotation safety of about 5,000 turns/min above the design rotation speed.

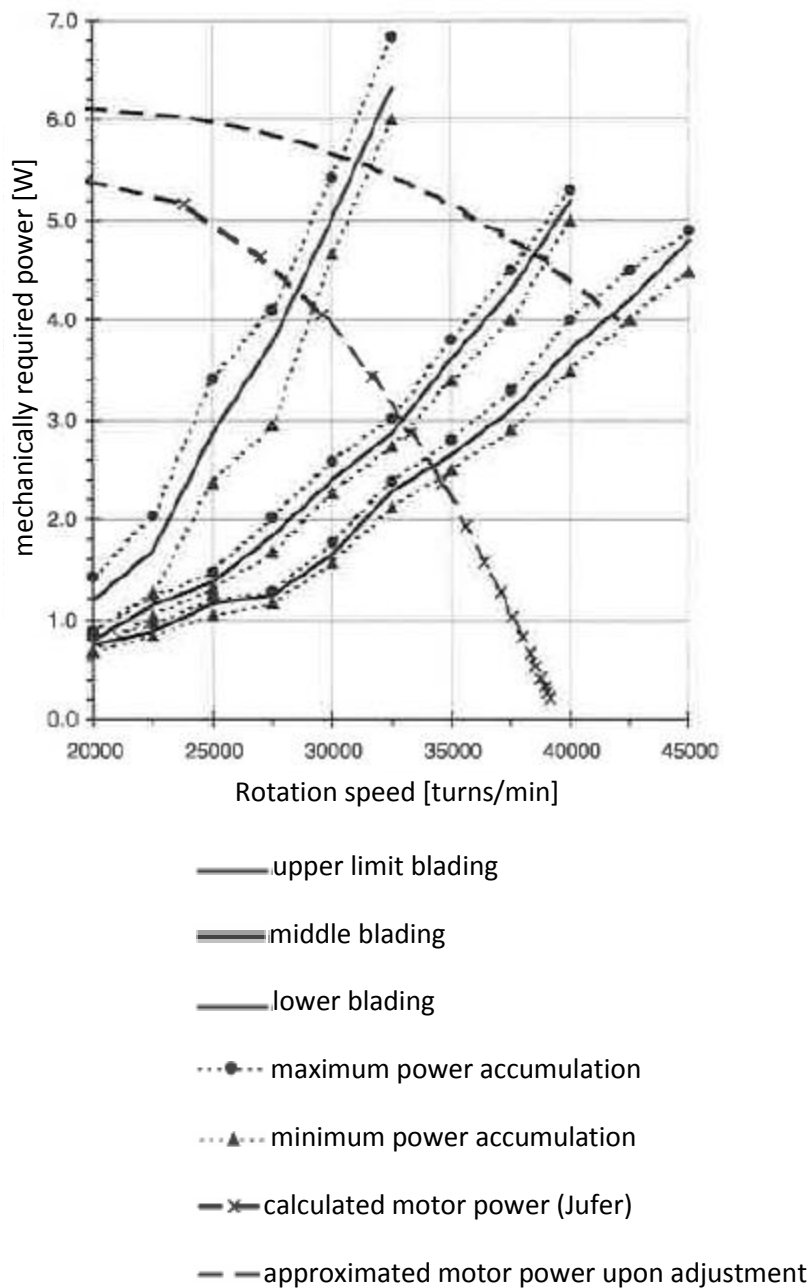


Figure 4.13 Comparison of power consumption to motor power output for a 6.5 mm stator (≅ 8.5 mm motor)

However, here the motor goes, as shown in Figure 4.14, into an early saturation stage, so that a rotation speed proportional to the control voltage can no longer be achieved. The provided curves show the motor characteristics prior to the increase of the current limit from the original 0.6 A to 0.9 A, since the saturation area is easier recognizable in this range.

The rotation speed cannot be regulated with the sensorless control beyond the control voltage respectively proportional to the rotation speed, since the motor is already subject to current limitation. Rotation speed can only be increased beyond that point by progressive increase of control voltage, so that no constant rotation speed independent of load can be guaranteed here. It is rather necessary to regulate control voltage separately to achieve the required rotation speed.

As further illustrated in Figure 4.13, the extreme blading with $\beta_2 = 94.5^\circ$ can also only be operated barely above its design rotation point in the power adjusted motor version, so that there is no more reserve for additional friction losses in the mechanical parts or short time increases of hydraulic capacity.

While it is impossible to further increase the motor power by increasing voltage due to the limit values for implantable systems, the current can also not be reasonably increased beyond the already obtained motor currents, since the current density already goes up to 70 A/mm^2 . A further increase merely causes copper losses and no actual capacity increase.

To summarize the above said, the power with the maximum power density of $\rho_{\text{mech}} = 10 \text{ W/ml}$ achievable here for a 6.5 mm motor stator can be taken as the measure of what is currently technically realistic.

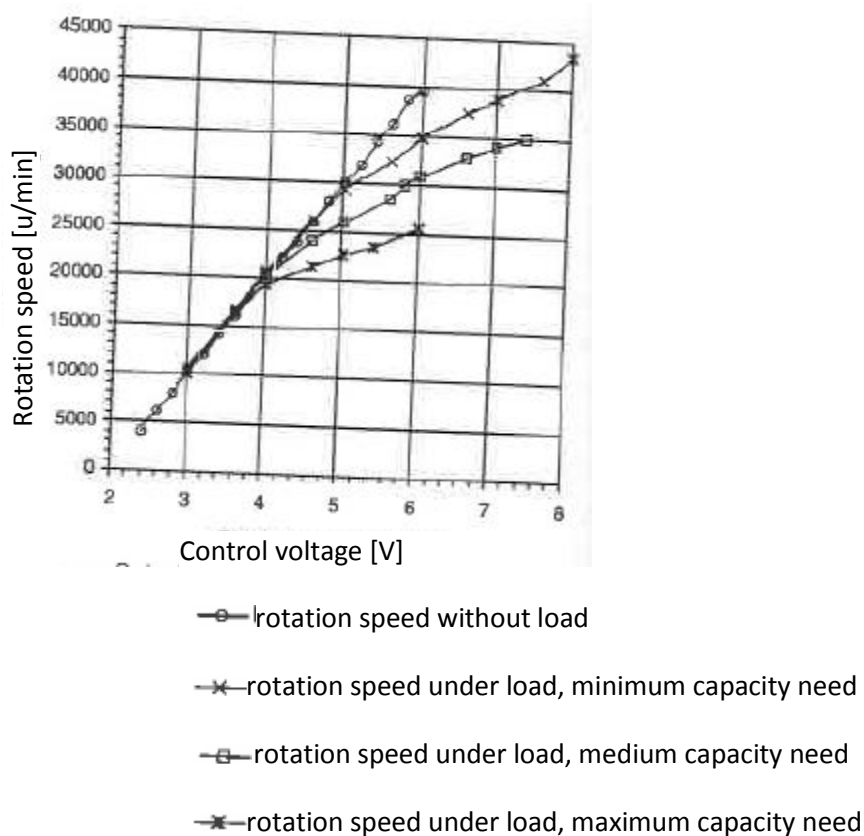


Figure 4.14 Functional connection of control voltage and rotation speed depending upon last for a 6.5 mm stator

Assessment:

The drive capacity, which can be achieved with the 6.5 mm motor stator of the first lab drive, is sufficient to operate all blading options at the design point without achieving physiologically critical surface temperatures.

Therefore, the electronically commutated miniature synchronous machine researched above is fit to be integrated into Concept IV of a micro-axial pump presented in Chapter 3.

Chapter 5. Fluid mechanics design

In Chapter 5 we will present a procedure for design of smallest axial pumps. This procedure proved itself for blading diameter of 6.0 mm. The underlying system of actions will then be described in detail, so that it can be used as a basis for further design of smallest pumps in medium viscous fluids (η : 3.0 – 4.0 mPa).

5.1 General considerations on the working principle of hydrodynamic pumps

Chapters 5.4 through 5.9 will describe the principle of the design procedure for an axial cascade according to the relevant parameters chosen according to the indications; at this point we will consider the working principle of rotary pumps based on simple considerations to answer the question why a rotary pumps or can build up pressure.

Based on one-dimensional theory for an adiabatic and non-stator stage, there is an achievable pressure difference Δp in the impeller /Gallus 1992/:

$$\Delta p_{\text{Laufrad}}^{\text{radial impeller}} = \rho \cdot \eta \cdot \left(\frac{u_2^2 - u_1^2}{2} + \frac{w_1^2 - w_2^2}{2} \right) \quad \text{or} \quad \Delta p_{\text{Laufrad}}^{\text{axial impeller}} = \rho \cdot \eta \cdot \left(\frac{w_1^2 - w_2^2}{2} \right).$$

Already this simple description, taking into account hydraulic limits for delay from w_1 to w_2 , makes it clear that the radial impellers can build up a much higher pressure than axial impellers due to the different peripheral speeds of the impeller from the entrance u_1 to the exit u_2 .

The following description illustrates an example of the working principle of rotary pump beyond the generally accepted theories. If we assume, for the sake of simplification, that a radial impeller is located in a centrifugal pump housing with an externally located ring diffuser, which impeller is under centrifugal flow, and fluid accelerates from the central entrance up to the exist located at periphery, without spills and in the periphery direction, then for blades with a radial exit angle the fluid has angular momentum at the time it leaves the impeller, which corresponds to its local peripheral speed. From the inside of the impeller and up to the external area, the fluid goes through a spiral-formed path, which approximates in its radial movement a circle at the time of exit, provided there was a sufficient number of rounds. The very fact that the fluid is kept in a circular path causes a radial pressure increase in the impeller of $p_{\text{Laufrad}}(r) \approx \rho/2 \cdot c_u^2(r)$. If we additionally assume that the angular momentum c_u in diffuser is completely transferred into a static pressure increase $p_{\text{Diffusor}} \approx \rho/2 \cdot c_u^2(R)$, then a radial blood pump with the peripheral speed at the impeller exit of $c_u = 10$ m/s can build up a maximum pressure with closed exit of

$$p_{\text{max}} \approx p_{\text{Laufrad}} + p_{\text{Diffusor}} \approx \rho \cdot c_u^2(R) \stackrel{\text{here}}{=} 1,058 \cdot 10^5 \text{ Pa (804 mmHg)}$$

In a purely axial pump with a radial flow, this radial aspect is lacking entirely, so that the working principle of an axial rotor must be described differently. We can use here a very simplified assumption that the axial grid of the impeller is a moving inclined plane. Depending upon the given radius r of the cylinder cover surface, on which the fluid should ideally be located, the inclined plane moves at constant angle speed of the rotor with a peripheral speed $c_{y\text{-Kontur}} = \omega_{\text{Rotor}} \cdot r$. Furthermore, if the angle β_1 in equation 5.15b of the inclined plane is chosen in such way that the fluid particle dm smoothly enters into the affected area of the plane, then the particle will pass the affected area of the plain without interactions in absence of friction and delay. In this perfect case the fluid particle is neither affected by

angular momentum, nor is the pressure built up between the entrance and exit. This case describes an ideal inducer, whose progress corresponds to a line or an inclined plain due to the constant blade angle.

If we now modify the inclined plane in its form so that the fluid particle still enters the affected area without interactions, but the entrance angle β_1 of the plane is continuously transformed in the axial direction into the rotor exit angle β_2 , then due to the inertia even in absence of friction the particle is affected by the acceleration force, which has an axial and tangential component according to Figure 5.1. Furthermore, if in the first approximation the axial speed of the particle between entrance and exit is kept constant, this causes pressure increase in rotor. At the same time, the fluid is affected by angular momentum, which, in its turn, can be transferred into a further pressure increase in the next stator, with minimal loss.

Below we will calculate the pressure increase and angular momentum impact generated in the rotor in absence of friction and leaks, with ideally simplified flow, on an example of a 6 mm rotor (see Chapters 7-8). To this end we will use the linear enthalpy distribution described with respect to production, based on Chapter 6, for which the rotor entrance angle is linearly transformed into the exit angle with mostly constant curvature according to equation 6.1. The given constant curvature implies a uniform movement of a particle with constant acceleration at a right angle to the contour, provided the particle path is congruent for blades.

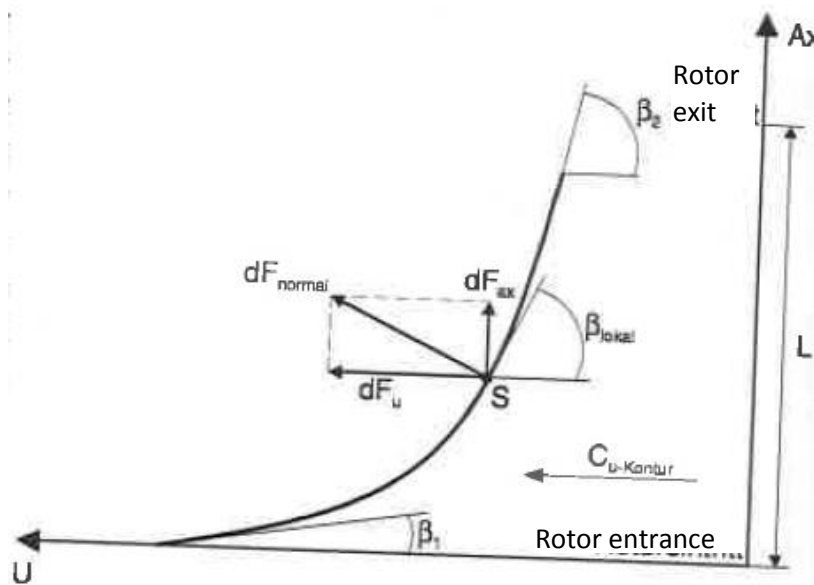


Figure 5.1 Axial grid of the rotor as "moving curved plane"

Correspondingly, in each point S the particle with the mass dm is affected by the forces dF_{ax} and dF_u due to the existing acceleration in the ax and u directions a_{ax} , a_u . The movement equations of the particle in the ax and u directions can be formulated as follows.

In ax direction:

$$\begin{aligned} a_{ax} &= a_{normal} \cdot \cos(\beta_{lokal}) = \text{constant} \\ c_{ax} &= a_{ax} \cdot t + c_{ax,0} (\equiv \text{Entrance speed}) \\ s_{ax} &= \frac{a_{ax}}{2} \cdot t^2 + c_{ax,0} \cdot t + s_{ax,0} (\equiv 0) \end{aligned}$$

In u direction:

$$\begin{aligned} a_u &= a_{normal} \cdot \sin(\beta_{lokal}) = \text{constant} \\ c_u &= a_u \cdot t + c_{u,0} (\equiv 0; \text{flow free of angular momentum}) \\ s_u &= \frac{a_u}{2} \cdot t^2 + c_{u,0} \cdot t + s_{u,0} (\equiv 0) \end{aligned}$$

Since a_{ax} and a_u depend upon the local angle $\beta_{\text{lokal}} = \beta(t)$, the movement equations are solved in discrete steps:

$$s_{ax}(t_{i+1}) \equiv \frac{a_{\text{normal}} \cdot \cos \beta(t_i)}{2} \cdot (t_{i+1} - t_i)^2 + c_{ax}(t_i) \cdot (t_{i+1} - t_i)$$

$$s_u(t_{i+1}) \equiv \frac{a_{\text{normal}} \cdot \sin \beta(t_i)}{2} \cdot (t_{i+1} - t_i)^2 + c_u(t_i) \cdot (t_{i+1} - t_i)$$

The local blade angle required here can be calculated for the particle movement congruent for blades at a local point S with $s_{ax}(\Delta t)$ and $s_u(\Delta t)$, where the latter movement must be considered with respect to $s_{u-\text{Kontur}}(\Delta t)$:

$$\beta_{\text{lokal}}(t_{i+1}) = \arctan \left(\frac{s_{ax}(t_{i+1}) - s_{ax}(t_i)}{s_u(t_{i+1}) - s_u(t_i) - c_{u-\text{Kontur}} \cdot (t_{i+1} - t_i)} \right)$$

A particle movement congruent for blades only exists when the local angle β_{lokal} of the particle trace corresponds to the local contour angle β_{Kontur} at identical ax coordinate. Below is the iteration in the ax direction for each discrete time value.

$\beta_{\text{Kontur};i}$	$s_{ax;i}$	$c_{ax;i}$	$\beta_{\text{lokal};i} (s_{ax;i}, s_{ax;i+1}, s_{u;i}, s_{u;i+1})$
$\beta_{\text{Kontur};i+1}$	$s_{ax;i+1}(\beta_{\text{Kontur};i}, c_{ax;i})$	$c_{ax;i+1}(s_{ax;i}, s_{ax;i+1})$	$\beta_{\text{lokal};i+1} (s_{ax;i+1}, s_{ax;i+2}, s_{u;i+1}, s_{u;i+2})$

The iteration is performed until the local blade angle corresponds to the particle trace at the identical time step with the absolute accuracy < 0.0002 .

In a calculation example considered here in detail, an operating point thoroughly documented in Chapters 7 and 8 of a 6 mm rotor with $V = 3.1$ l/min and $n = 30,000$ turns/min is considered, at which point in the immediate vicinity of the wall the entrance speed of the fluid at $c_{ax,0} = 2.06$ m/s and the exit speed according to Figure 8.2 at $c_{ax,2} = 4$ m/s and $c_{u,2} = 2.1$ m/s are calculated. The blade construction angle $\beta_1 = 15.1^\circ$ and $\beta_2 = 37.2^\circ$ together with the grid length $L = 4.2$ mm and the rotating diameter $D = 5.8$ mm, which results in the contour speed in peripheral direction of $c_{u-\text{Kontur}} = 9.1$ m/s, describe this blading to the extent required in at this point. Figure 5.2a demonstrates for this case, with time discretion of $\Delta t = 0.0005$ s between single support points, the speed as a function of current direction, as well as in Figure 5.2b the development of the curved plane together with the contour conform path curve of the particle from the view of a stationary and moving observer.

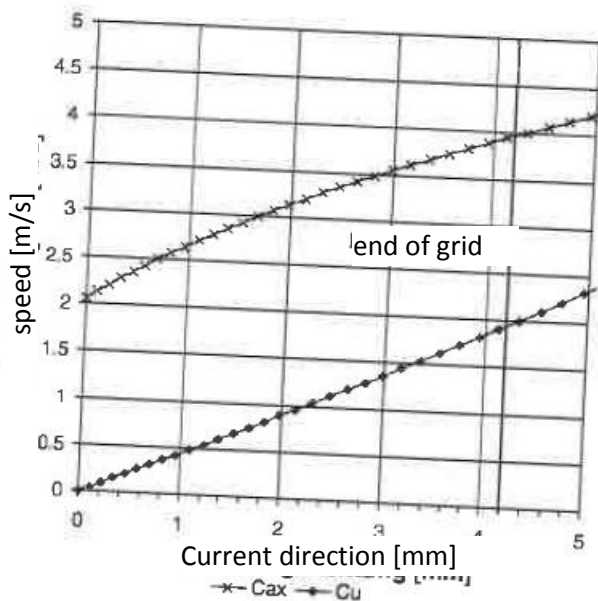


Figure 5.2a Particle speeds

for $a_{\text{normal}} = 800 \text{ g}$

and $a_{\text{ax-Verzögerung}} = 465 \text{ g}$

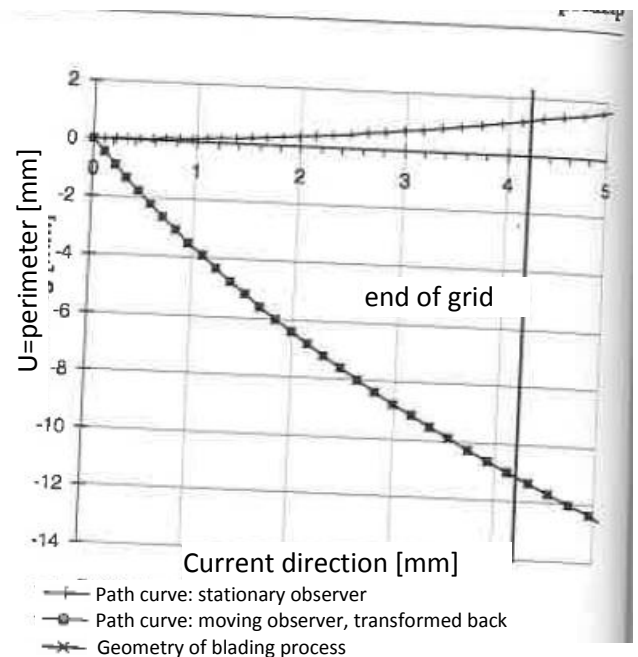


Figure 5.2b Particle movement

for $a_{\text{normal}} = 800 \text{ g}$

and $a_{\text{ax-Verzögerung}} = 465 \text{ g}$

To obtain the required speed and angle, an acceleration of 800 g acting along the normal is required. To obtain the required exit speed $c_{\text{ax},2} = 4 \text{ m/s}$, the acceleration affecting the particle in the axial direction is reduced by the acceleration designated as $a_{\text{ax-Verzögerung}}$. This delay portion causes increasing pressure Δp_{ax} in the axial flow direction, which can be calculated from the movement equation as follows:

$$dF_{\text{ax}} = dm \cdot a_{\text{ax-Verzögerung}} = \rho \cdot A \cdot dL \cdot a_{\text{ax-Verzögerung}}; \quad dp_{\text{ax}} = \frac{dF_{\text{ax}}}{A}$$

$$\Rightarrow \Delta p_{\text{ax}} = p_2 - p_1 = \rho \cdot a_{\text{ax-Verzögerung}} \cdot \int_{L=0}^L dL = \rho \cdot a_{\text{ax-Verzögerung}} \cdot L \stackrel{\text{hier}}{=} 20,6 \text{ kPa (157 mmHg)}$$

This pressure increase in rotor calculated for friction free and ideal flow process is quite realistic, considering the actual pressure increase with all the losses according to Chapter 9.2.2.

Based on the above described observations, it becomes clear, similarly to the one-dimensional theory for adiabatic and no-stator stage, that an axial grid can build up a much smaller pressure than a radial grid at comparable peripheral speeds. A mixed flow grid, through which the flow can go diagonally, is located between these two options.

5.2 General considerations on blade design and description of the system of actions

To provide blading for all pump versions constructed in the course of this work, we have chosen a one-stage design, since it has a much lower hemolysis than the respective multi-stage version can be expected to have due to very short areas of high shearing stress and small blading surface. The trade-off is that a one-stage design can build up much lower pressures than a comparable multi-stage design, which is primarily applicable to the left ventricular systems.

This inherent drawback can be compensated by designing the rotor as a half-diagonal grid and additionally increasing the operating rotation speed. Due to the half-diagonal design of the left ventricular rotors with diagonal hub and constant external diameter, the medium rotating diameter increases between the entrance and exit, which in itself creates additional pressure increase compared to a purely axial impeller /Gallus 1992/.

Despite the high speeds resulting from the high rotation speed of the blading edges, and the respective shearing stress, the hemolysis rate can be contained in tolerable range. This comes mostly as the result of the extremely short time $t \approx 0.003$ s that pure blood stays in the area of high shearing stress.

The geometry of the rotors is based on the targeted benchmarks at the design point according to Chapter 5.3. Despite this stringent capacity requirement, which applies to all pump options, the resulting grid load in the rotors may not cause any detachment on the blading due to high counter pressure, as the “rotating stall”, as well as cavitation on the blading tips.

To implement a pressure difference of, say, 100 mmHg and a curve stable against counter pressure, more than three blades seem to be required on the perimeter of the hub. However, the experience shows that already two to three blades provide a good balance for flow control and dragging friction losses within the micro-axial pumps in question at η : 3.0 – 4.0 mPa at 37°C in relatively high viscous fluid compared to water with η : 1.0 mPa at room temperature.

For these reasons, the stator in the LV pump has three blades and a pure axial flow. Its design length is relatively big, in order to ensure outflow with as little angular momentum as possible and a maximum pressure increase.

The channel flow in the hydraulic turbo machines in question is incompressible, affected by friction, not stationary, periodic and turbulent. Since at this point there is no final and generally accepted theory for calculation of turbulence, we will not consider this in detail. Turbulence and viscosity effect, and the resulting border layers can only be assessed qualitatively due to the lack of basis for design of turbo machines in the size in question on the basis of the known border layer theories.

The flow diagram presented in Figure 5.3 below illustrates the principle of actions in the course of design /Gallus 1989, 1992; Krause 1988; Schlichting 1965; Truckenbrodt 1980/.

The design of flow mechanics is provided in Chapter 5 on the example of one-stage pumps with and without stator, and will be performed corresponding to the flow diagram in Figure 5.3. The back arrows show iterative actions, i.e. if the result of a calculation step turns out to be unsatisfactory, then the respective steps must be repeated.

The following design process proved itself for one-stage grids with nominally axial flow with the diameters of 4.8 mm through 7.2 mm.

Medical requirements (Δp , V, Da)	See: Chapter 5.3
Loss assessment (constructive draft, Re)	Chapter 5.4
Assessment of the optimum rotation speed (γ , δ_{YM} , Cordier diagram, σ_M , n)	Chapter 5.5
Determination of the hub diameter control (channel geometry, axial acceleration $\rightarrow D_i(z)$)	Chapter 5.7

Calculation of the rotor entry angle taking into account the border layer effect	Chapter 5.6
Required specific blade work (efficiency factor assessment based on experimental data)	Chapter 5.8.1
Choice of proper angular momentum distribution $c_u(r)$	Chapter 5.8.3
Method of the radial balance taking into account the border layer effect in meridian flow direction and continuity equation → radial distribution of the flow values $c_3, w_3, \alpha_3, \beta_3$ (manufacturing problems, flow process)	Chapter 5.8.2 Chapter 5.8.4 Chapter 5.8.5
Repeated calculation of the total specific blade work (Δh integrated over the mass flow for capacity control taking into account the experimentally reported efficiency rate η)	Chapter 5.8.6
Rotor blade geometry (angle excess, α, β, t)	Chapter 5.8.7
Guiding blade geometry (α)	Chapter 5.9

Figure 5.3 Principle of actions in design of flow mechanics

Since the stator and no-stator designs of a one-stage pump with axial flow are treated according to the same theoretical assumptions, the calculation can also be performed in a largely similar way. Only the calculation of the hub diameter and stator is performed solely for the pumps designed for the left ventricular support. In the right ventricular case a stator is in principle unnecessary due to the low delivery head. The hub of the rotor is designed here in a purely axial way, without meridian acceleration, due to the reversed flow direction.

Following the design, it must be checked to which extent a no-stator system can be produced for the left ventricular case as well (see Chapter 9.2.3 with Figure 9.15). If the available delivery head is sufficient, then the total length of pump system, the required production efforts and thrombogenicity could be reduced.

5.3 Parameters and requirements derived from the medical applications

Benchmarks for the design were taken from the medically required and technically feasible qualities. These are the required volume flow, the required pressure difference between the respective ventricle and the vessel letting out fluid, as well as the maximum external diameter of the pump, and thus the open width of the housing.

The pressure difference between the left ventricle and aorta equals for the left heart support (LV pump):

$$\Delta p_{\text{nutz}} = 80 \text{ mmHg}_{\text{für } \varnothing 5\text{-Pumpe}} / 100 \text{ mmHg}_{\text{für } \varnothing 6 \text{ u. } \varnothing 7,4\text{-Pumpe}} = 10526 \frac{\text{N}}{\text{m}^2} \text{ bis } 13158 \frac{\text{N}}{\text{m}^2}$$

as well as between the right ventricle and pulmonary artery for the right heart support (RV pump):

$$\Delta p_{\text{nutz}} = 30 \text{ mmHg} = 3947 \frac{\text{N}}{\text{m}^2}.$$

For the pumps with the impeller diameters in question (4.8 mm/ 5.8 mm/ 7.2 mm), the total volume flow was chosen as

$$\dot{V} = 2,5 \frac{1}{\text{min } \varnothing 5\text{-Pumpe}} / 4,0 \frac{1}{\text{min } \varnothing 6\text{-Pumpe}} / 6,0 \frac{1}{\text{min } \varnothing 7,4\text{-Pumpe}} = 4,17 \cdot 10^{-5} \frac{\text{m}^3}{\text{s}} / 6,67 \cdot 10^{-5} \frac{\text{m}^3}{\text{s}} / 1,0 \cdot 10^{-4} \frac{\text{m}^3}{\text{s}}$$

as well as the inner diameter of the housing as

$$D_a = 5 \text{ mm} / 6 \text{ mm} / 7,4 \text{ mm} = 5 \cdot 10^{-3} \text{ m} / 6 \cdot 10^{-3} \text{ m} / 7,4 \cdot 10^{-3} \text{ m}$$

To ensure a safe placement and impeccable operation of the pumps, a sufficiently long tube must be available at the side looking away from the drive. For the LV pump the required suction tube length is 60 mm, and for the RV pump the required pressure tube length is 50 mm. These tubes must be taken into account in assessment of losses, as shown in Chapter 5.4.

The blood values were taken from the following data /Thews 1988/:

dynamic viscosity $\eta = 3.6 \cdot 10^{-3} \text{ Pa} \cdot \text{s}$, thickness $\rho = 1059 \text{ kg/m}^3$.

In this case, blood is deemed to be a Newtonian, incompressible fluid /Lambert 1989/, i.e. not only the density in the considered area is independent of pressure, but also the viscosity can be assumed to be constant due to the high shearing rate. Viscous and elastic flowing qualities and border shearing stress, which are typical for blood with low shearing rate, can be disregarded. Instead, due to the high shearing rate it must be made sure that blood damages do not exceed the acceptable level.

Hemolysis and thrombus formation are two important forms of blood damage, which can be caused by artificial systems in physiological blood circulation. Hemolysis can be triggered by both a border shearing stress of erythrocytes in shearing field and by their contact with foreign, raw or non-biocompatible surfaces, as well as by pressing of blood corpuscles in narrow gaps between parts moving with respect to each other.

Thrombocytes can also be activated by the above said causes and agglomerate into stagnation regions. Besides, ADP released from erythrocytes during hemolysis also affects activation of thrombocytes, so that both blood damages must always be considered in mutual context.

The construction targets of a heart support system derived from these conditions are, respectively, the minimization of the time that blood stays in voltage field, which is in the range from 1 to 5 ms for a 6 mm micro-axial pump due to the high flow speeds, a low dissipation in fluid, as well as avoidance of stagnation regions by effective flow control. The latter is of particular interest, since the experiments have shown that, despite the existing blood damage, thrombus formation is not necessarily triggered. This first happens when the damaged blood has low dilution, low shearing rate and long staying time, which in the systems in question only happens in re-circulation areas /Wurzinger 1985/.

5.4 Assessment of losses

The hydraulic efficiency rate of the pumps in question is defined as follows:

$$\eta_{hyd} = \frac{\Delta p_{nutz} \cdot \dot{V}}{P_{mech}} \quad \text{(Equation 5.1)}$$

P_{mech} is the mechanical power added to the rotor shaft. The experience with the 6 mm and 5 mm micro-axial pumps developed at HIA provided measured hydraulic efficiency rate, which had a lower limit of $\eta_{hyd} = 0.2$ and an upper limit of $\eta_{hyd} = 0.4$, and was thus much lower than it would have to be expected according to the existing calculations from the turbomachine design, where the calculated value was $\eta_{hyd} = 0.7$. The discrepancy results mostly from the dimensions of the pumps in question coupled with a relatively high viscosity of the fluid. Further research of the losses (i-v) listed below is provided in Chapter 9. The measurements underlying the above said efficiency rates were made without a tube preceding or following the pump. The resulting efficiency rate decrease due to additional pressure loss in the tube will be assessed, and the efficiency rate obtained in such manner will be used to calculate the required blade work in absence of analytically quantifiable losses.

The total pressure loss, which must be produced by the pump in addition to the actually measurable delivery head, consists of the following components:

- i. static pressure loss, which is required for acceleration of the flow to the speed at the rotor entrance, or rotor and stator exit, respectively (it is assumed that the flow speed in ventricle is close to zero, and the kinetic energy at the pump exit is not transformed into pressure, but is transformed into heat by dissipation in outflowing open jet);
- ii. channeling friction losses in the tube in the created flow;
- iii. for LV/RV pumps, additional inlet losses by dissipation at the time the speed profile is formed in the suction/ pressure tube;
- iv. outlet losses due to the jet contraction at the beginning of the tube of the LV pump, or at the centripetal fluid inlet through the inlet gap of the RV pump;
- v. internal pump losses: in the curved channels of the pumps, thrust losses at the beginning and at the end of each grid, secondary flow effects, internal leakage flows, effect of rigidity due to relatively high viscosity of the fluid coupled with the roughness of walls and low channels etc.

If we consider the above listed losses, and use the measured hydraulic efficiency rates (equation 5.1) for the calculation of the required blade work, then all loss components, except for the losses in the tube (ii-iii), are taken into account due to the lab structure.

The following efficiency rates have shown a good correlation of the design point and the actually measured operating point:

$$\eta_{hyd \text{ } \varnothing 6 / \varnothing 7,4 - \text{Pumpe}} = 30\%, \quad \eta_{hyd \text{ } \varnothing 5 - \text{Pumpe}} = 20\%.$$

Based on the above considerations, the total required pressure increase of the pumps Δp_{pumpe} must contain, in addition to the useful pressure increase between the ventricle and arterial vessel, the pressure loss in the tube (ii-iii). Below are all the loss components at the inlet and outlet of the pumps:

$$\Delta p_{\text{pumpe}} = \Delta p_{\text{nutz}} + (p_v - p_0)_{\text{Einlauf}} + P_{D-\text{Auslauf}} \quad \text{(Equation 5.2)}$$

Calculation of the pressure losses is performed according to /Truckenbrodt 1980/, volume 1.

For the **LV pump**, the total pressure loss in the suction tube is expressed as:

$$p_v - p_x = (\zeta_L' + \zeta_R + \zeta_E) \cdot \frac{\rho}{2} \cdot \bar{c}_x^2$$

(Equation 5.3)

Here, according to Figure 5.4, p_v is the pressure in the left ventricle, p_x is the pressure in the hub entrance plane, and c_x is the average speed in such plane. The respective loss coefficients ζ take into account, in this order, acceleration of the flow (\equiv static pressure reduction in the tube together with the dissipation appearing during the transformation of the flow profile from piston profile to laminar/turbulent profile), channeling friction losses, as well as the inlet losses at the time the fluid enters the tube.

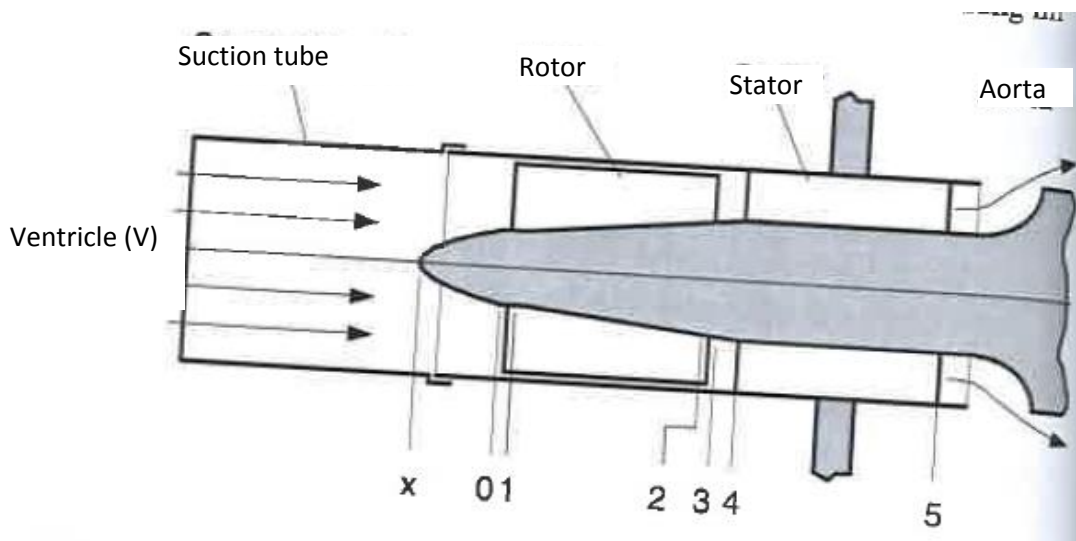


Figure 5.4 Cross-section description on the example of an LV pump

The average speed in the suction tube is determined as:

$$\bar{c}_x = \frac{4 \cdot \dot{V}}{\pi \cdot D_a^2}$$

(Equation 5.4)

The Reynolds numbers of all pump sizes Re' in the suction tube are as follows:

$$Re' = \frac{\bar{c}_x \cdot D_a}{\nu} = 3100_{\varnothing 5-Pumpe} / 4200_{\varnothing 6-Pumpe} / 5100_{\varnothing 7,4-Pumpe}$$

(Equation 5.5)

The critical Reynolds number for the turbulent transition in smooth tubes with round cross-section equals 2,300 /Schlichting 1965/, so that in good approximation there is a turbulent flow in the pumps of all sizes in the vicinity or immediate surrounding of the transition area. According to /Truckenbrodt 1980 page 259/, ζ_L'' is determined as:

$$\zeta_L'' = 1 + \zeta_L' \left(\frac{s'}{Re'} \right) \text{ with } \frac{s'}{Re'} = \frac{\frac{s}{D_a}}{\frac{\bar{c}_x \cdot D_a}{v}}$$

$$\zeta_L'' = 1,65_{\varnothing 5-Pumpe} / 1,5_{\varnothing 6-Pumpe} / 1,4_{\varnothing 7,4-Pumpe}$$

(Equation 5.6)

The flow is located solely for the 5.0 mm pump in the vicinity of the laminar-turbulent transition area, which leads to the assumption of a high pressure loss coefficient $\zeta_L'' = 1.65$; for the 6.0 mm pump $\zeta_L'' = 1$ was determined experimentally according to Chapter 9.3, so that purely turbulent flow in the tube must be assumed for this pump size, as well as the 7.4 mm pump. For a turbulent flow, i.e. for large Reynolds numbers $> 10^4$, this loss value is in the range from 1.058 to 1.076 (/Truckenbrodt 1980/, page 259, Table 3.5), which is well supported by the experimental data:

$$\zeta_L'' = 1,0_{\varnothing 7,4-Pumpe} / 1,06_{\varnothing 6-Pumpe}$$

The channeling friction loss ζ_R can be calculated as follows for the hydraulically smooth tube in the turbulent flow:

$$\zeta_R = \lambda(Re) \cdot \frac{s}{D_a} \text{ with } \frac{1}{\sqrt{\lambda}} = 2,0 \cdot \lg(Re \cdot \sqrt{\lambda}) - 0,8$$

$$\zeta_R = 0,431_{\varnothing 5-Pumpe} / 0,393_{\varnothing 6-Pumpe} / 0,302_{\varnothing 7,4-Pumpe}$$

(Equations 5.7 a,b)

For the LV pumps, the inlet loss ζ_E must also be taken into account. In order to do this, we can consider the suction tube going into the ventricle as a Borda outlet (/Truckenbrodt 1980/, page 206, 271-272), which results in a loss coefficient of $\zeta_E = 0.6 - 1.5$ for all pumps. The value cannot be determined more exactly based on the available literature, since the actual loss coefficient significantly depends upon the sharpness of edges of the inlet opening and the resulting jet contraction. The research according to Chapter 9.3 produces for a 6.0 mm tube a loss coefficient of $\zeta_E = 1$, which can be assumed for all inlet geometries for all pumps, unless a really round inlet opening with a diameter ratio of the largest inlet diameter to the tube diameter of 2 can be implemented.

If we apply all the values to equation 5.3, then the pressure difference between the ventricle and the hub entrance plane becomes:

$$p_V - p_x = 7339 \text{ Pa (56 mmHg)}_{\varnothing 5-Pumpe} / 7214 \text{ Pa (55 mmHg)}_{\varnothing 6-Pumpe} / 6584 \text{ Pa (50 mmHg)}_{\varnothing 7,4-Pumpe}$$

For the total pressure loss, we must now also take into account the acceleration of the flow from the hub entrance to the rotor entrance based on the cross-section reduction through the hub:

$$p_V - p_0 = (p_V - p_x) + (p_x - p_0) = (p_V - p_x) + \frac{\rho}{2} (\bar{c}_0^2 - \bar{c}_x^2) \text{ with } \bar{c}_0 = \frac{4 \cdot \dot{V}}{\pi \cdot (D_a^2 - D_{i,0}^2)} \quad (\text{Equation 5.8})$$

Here, $D_{i,0}$ is the diameter of the hub at the impeller entrance. According to the experience with design of micro-axial pumps, the following hub-diameter ration is chosen:

$$\frac{D_{i,0}}{D_a} = \frac{1}{3} \quad \text{and} \quad \frac{1}{3,7}$$

This gives, according to equation 5.8, the additional pressure loss, here assumed to be the total loss, of the system consisting of the pump and suction tube:

$$P_V - P_0 = 7972 \text{ Pa (61 mmHg)}_{\text{Ø5-Pumpe}} / 7847 \text{ Pa (60 mmHg)}_{\text{Ø6-Pumpe}} / 7052 \text{ Pa (54 mmHg)}_{\text{Ø7,4-Pumpe}}$$

Due to the meridian acceleration in the LV rotor resulting from the hub getting thicker in the flow direction, the fluid leaves the pump with an increased speed as a free jet, even in absence of angular momentum. This additional portion is eventually fully dissipated and is designated as $p_{D\text{-Austritt}}$:

$$p_{D\text{-Austritt}} = \frac{\rho}{2} \cdot (\bar{c}_{s-a}^2 - \bar{c}_0^2) \quad \text{(Equation 5.9)}$$

$$= 2100 \text{ Pa (16 mmHg)}_{\text{Ø5-Pumpe}} / 2000 \text{ Pa (15 mmHg)}_{\text{Ø6-Pumpe}} / 1000 \text{ Pa (8 mmHg)}_{\text{Ø7,4-Pumpe}}$$

Therefore, we ultimately get, according to equation 5.2, the sought pressure increase of the pump:

$$\Delta p_{\text{pumpe}} = 20600 \text{ Pa (157 mmHg)}_{\text{Ø5-Pumpe}} / 23000 \text{ Pa (175 mmHg)}_{\text{Ø6-Pumpe}} / 21200 \text{ Pa (162 mmHg)}_{\text{Ø7,4-Pumpe}}$$

If we take into account that all pumps are designed with a maximum admissible peripheral speed $c_{u\text{-max}} = 10 \text{ m/s}$, which is the limit value in terms of blood damage, then it becomes clear that the blading grid bears the highest load in the 6 mm system. However, all pumps are located in a small range, so that we can conclude already at this point that the volume flow with at the corresponding pump size and assumed physiologically required differential pressure is well adjusted to the respective pump size.

Inherent structural differences must be taken into account in **RV pumps**:

The inlet losses are not taken into account by the structure of the flow profile, since the flow gets into the rotor already shortly behind the pump entrance. Inlet losses through the gaps spread along the perimeter of the pump housing, whose area is by 20% larger than that of the respective connected pump cross section, are assessed for the LV pumps as $\zeta_E = 1$. The hub diameter of the pump is limited by the structural consideration. It results from the diameter of the respective frictionally locked seal, and is kept constant in the blading area. In the right ventricle/ atrium there is a condition $c_v \approx 0$. Thus, the pressure loss in the inlet of the RV pump from acceleration of the flow and inlet losses is:

$$\Delta p_{D\text{-Einlauf}} = (\zeta_L (=1) + \zeta_R (=0) + \zeta_E (=1)) \cdot \frac{\rho}{2} \cdot \bar{c}_0^2_{\text{Ø5,Ø6,Ø7,4-Pumpe}} \quad \text{with} \quad \bar{c}_0 = \frac{4 \cdot \dot{V}}{\pi \cdot (D_a^2 - D_i^2)} \quad \text{(Equation 5.10)}$$

$$= 10100 \text{ Pa (77 mmHg)}_{\text{Ø5-Pumpe}} / 11500 \text{ Pa (87 mmHg)}_{\text{Ø6-Pumpe}} / 8600 \text{ Pa (65 mmHg)}_{\text{Ø7,4-Pumpe}}$$

The Reynolds number in the pressure tube has the same value as in the suction tube of the respective LV pump, since both volume flow and diameter, as well as rigidity of the medium are the same. This means that the average speed and the channeling friction coefficient λ are identical. The length of the

pressure tube is chosen according to the length of the respective suction tube. The channeling friction coefficient λ can be calculated as follows:

$$\Delta p_{D-Auslauf} = \lambda(Re) \cdot \frac{s}{D} \cdot \frac{\rho}{2} \cdot \bar{c}_x^2 \quad (\text{Equation 5.11})$$

$$= 1000\text{Pa}(7,6\text{mmHg})_{\varnothing 5\text{-Pumpe}} / 1150\text{Pa}(9\text{mmHg})_{\varnothing 6\text{-Pumpe}} / 860\text{Pa}(6,5\text{mmHg})_{\varnothing 7,4\text{-Pumpe}}$$

Therefore, the total pressure difference, which is to be built up by the pumps, is equal to:

$$\Delta p_{\text{pumpe}} = \Delta p_{\text{nutz}} + \Delta p_{D\text{-Einlauf}} + \Delta p_{D\text{-Auslauf}} \quad (\text{Equation 5.12})$$

$$= 15050\text{Pa}(114\text{mmHg})_{\varnothing 5\text{-Pumpe}} / 16600\text{Pa}(126\text{mmHg})_{\varnothing 6\text{-Pumpe}} / 13400\text{Pa}(102\text{mmHg})_{\varnothing 7,4\text{-Pumpe}}$$

If we compare the required additional pressure of the RV pumps with that of the respective LV pumps, it will become clear that no stator is required for the RV operation (reaction rate in stator is $\tau \leq 40\%$), especially as the dissipated pressure in RV inlet tends to be overestimated with the inlet loss coefficient of $\zeta_E = 1$.

The total pressure built up by the pumps is illustrated in the following figure, split into the useful, dissipated and fluid accelerating components. The latter is also classified as the dissipated pressure component due to the conditions in the outflow from the pump.

The relatively small additional pressure required for the 7.4 mm pump results from the capacity requirement, which is low with respect to the pump size.

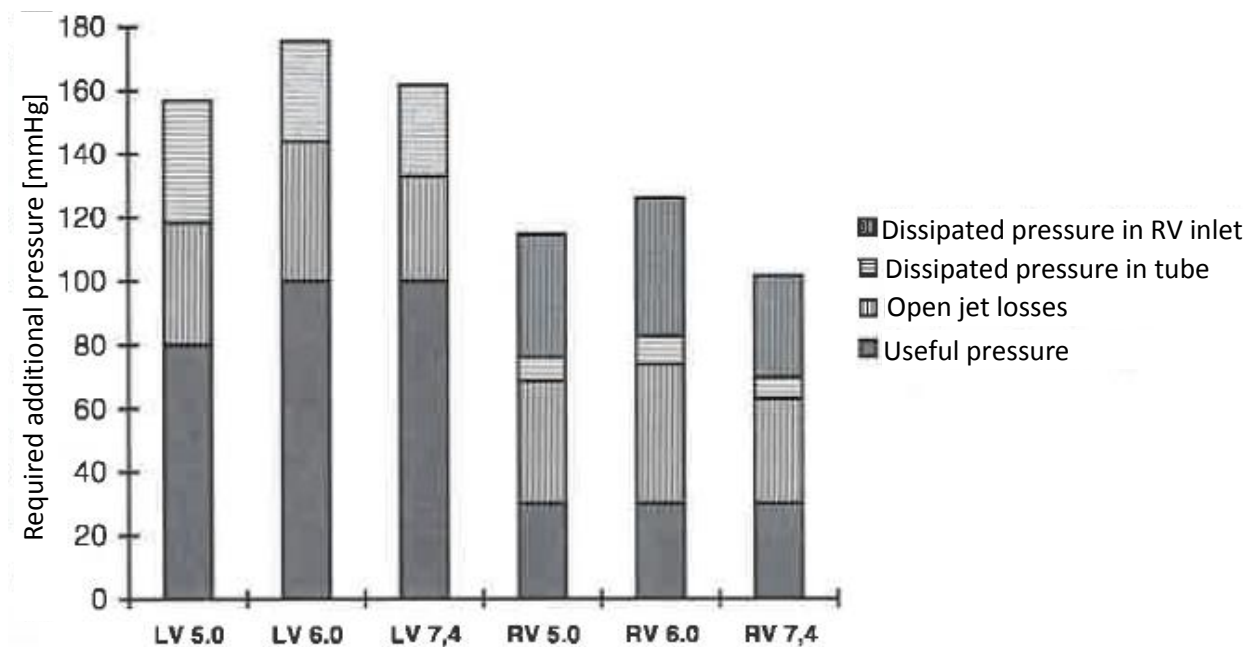


Figure 5.5 Components of the total additional pressure of the pumps

5.5 Assessment of the optimum rotation speed: Cordier vs. cavitation border

The optimum rotation speed is assessed using the experimental data. As a basis, we generally use the Cordier diagram /Gallus 1989/, i.e. the connection of the specific diameter δ_{yM} and the specific rotation

speed σ_{yM} for the best efficiency rate. The specific diameter and the specific rotation speed are defined as follows /Gallus 1986/, page 138:

$$\delta_{yM} = 1,054 \cdot D_B \cdot \frac{y^{1/4}}{\dot{V}^{1/2}} \quad \sigma_{yM} = 2,108 \cdot n \cdot \frac{\dot{V}^{1/2}}{y^{3/4}} \quad \text{with } y = \frac{\Delta p_{\text{Pumpe}}}{\rho} \quad (\text{Equation 5.13 a,b,c})$$

D_B is the diameter, which corresponds to the rotor diameter, n is the rotation speed of the impeller and y is the specific flow work.

According to the design by Cordier, the systems in question generally produce to high rotation speeds, which lead to the peripheral speeds of ≈ 10 m/s, which clearly exceed the peripheral speeds permissible for blood pumps. We can only deduct the design type from this diagram based on the ration of diameter, pressure and volume flow. Thus, pumps with axial flow are located in the best efficiency rate area. The design types of all LV and RV pumps are based on this recommendation.

Consequently, the permissible rotation speed is based on the maximum peripheral speed, which is generally acceptable in terms of hemolysis, as well as the cavitation border, which is mostly the same for the LV pumps. It will be explained below on the example of a 6.0 mm LV pump.

With an impeller diameter of 5.8 mm for a 6.0 mm LV pump, the maximum permissible peripheral speed in the inlet gives us the maximum permissible rotation speed of $n_{\text{max}} = 32,900/\text{min}$, which will now be considered in terms of cavitation.

To calculate the limit rotation speed based on the cavitation border, we must choose the worst imaginable operating state of the pump. It will be done on the basis of a pump with pre-connected suction tube at the operating point $V = 4$ l/min, $n = 33,000/\text{min}$.

As a limit, we will take the rotation speed at which straight cavitation due to a sudden tube blockage is visible in rotor. With this sudden blockage, there is the lowest pressure for a short time before the rotor resulting from all losses in suction tube, plus the maximum delivery head of the pump, as well as an additional dynamic pressure reduction resulting from inertia of the fluid in the tube and of the pump.

At the temperature $\vartheta = 37^\circ\text{C}$, blood has a steam pressure of $p_{\text{Dampf}} = 6,050$ Pa (46 mmHg), so that the available residual working pressure $p_{\text{res-p}}$ corresponds to the atmospheric pressure minus the steam pressure: $p_{\text{res-p}} = p_{\text{atm}} - p_{\text{Dampf}} = 93,950$ Pa (714 mmHg). If the pump suddenly attaches to the ventricle, which can cause a transient total blockage of the suction tube, then the maximum pressure decrease at the blading inlet edge is:

$$\Delta p_{\text{total}} = \Delta p_{\text{Einlauf}} + \Delta p_{\text{Schlauch}} + \Delta p_{C_{\text{max}}} + \Delta p_{\text{Förderhöhe}} + \Delta p_{\text{dyn}} = 102600 \text{ Pa (780 mmHg)}. \quad (\text{Equation 5.4})$$

From the requirement that either the cavitation threshold or the maximum permissible peripheral speed serves as the upper limit for the rotation speed of the pump, we arrive to the limit rotation speed $n_{\text{grenz}} = 30,000/\text{min}$ for the 6.0 LV pump. However, this limit rotation speed can only be determined in an iterative way, since the maximum achievable delivery head for each blading can only be expressly identified during a lab experiment. Reasonable maximum rotation speeds are:

$$n_{\text{max}} [\text{min}^{-1}] = 40000_{\varnothing 5,0 \text{ mm-LV / RV-Pumpe}} / 30000_{\varnothing 6,0 \text{ mm-LV / RV-Pumpe}} / 26000_{\varnothing 7,4 \text{ mm-LV / RV-Pumpe}}$$

5.6 Rotor entrance angle

The angles of the rotor in the entrance plane are calculated in such way that the flow enter the running blade channel as smoothly as possible, i.e. in the relative system of the rotor, the flow lines should run parallel to the blading in the entrance area. Since the flow does not have angular momentum, the absolute speed of the rotor is located in the meridian plane.

If $u_1(r)$ is the peripheral speed of the running blade and $c_1(r)$ is the absolute speed of the flow at the rotor entrance, then the following expression applies to the entrance angle $\beta_1(r)$ according to Figure 5.6:

$$\tan \beta_0 = \frac{c_0}{u_0}; \quad \tan \beta_1 = \frac{c_1}{u_1}.$$

(Equation 5.15 a,b)

Planes 0 and 1 are illustrated in Figure 5.4, where c_1 is bigger than c_0 due to the end blockage by the blading. The peripheral speed $u_1(r)$ can be obtained through the rotation speed n of the rotor and the respective radius r :

$$u_1(r) = 2 \cdot \pi \cdot n \cdot r = \omega \cdot r$$

(Equation 5.16)

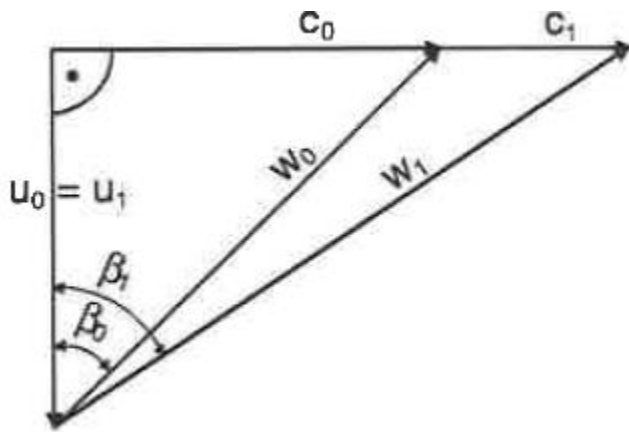


Figure 5.6 Speeds at the rotor entrance

The assessment of the speed profile $c_1(r)$ is a difficult task. Due to the low flow channels, the effect of the border layer is very strong. The assumption of a constant average speed seems to be reasonable only for the RV pumps, since there the flow gets into rotor almost immediately upon entering the pump, so that there is no significant border layer thickness. In absence of exact research of the effect the inlet openings have on the speed profile, the piston profile can be assumed in the first approximation:

$$c_0(r)_{RV-Pump} = \bar{c}_0 = \text{const.}$$

To the contrary, the following considerations apply to the LV pumps. All LV pumps have a pre-connected tube, where a turbulent speed profile is formed. To describe this profile, we can use the research of hydraulically smooth and straight tubes according to /Truckenbrodt 1980/, page 244. According to Figure 5.4, the profile existing at point X is accelerated to point 0 due to the thickness of the hub at the end. Between X and 0, there is a flow in a circle cross-section with a formed speed profile along the external radius, while only a thin border layer can form before the blading inlet edge at the inner radius due to the small inlet length, which is < 2 mm at the hub for all pumps.

According to /Truckenbrodt 1980/, page 244, the approximation over time applies in the tube up to the point X for fully formed turbulent flows in linear, circular tubes:

$$\frac{c}{c_{\max}} = \left(1 - \frac{r}{r_a}\right)^{1/n} \quad \text{mit} \quad \frac{1}{n} = \sqrt{\lambda}. \quad (\text{Equation 5.17 a,b})$$

c_{\max} is the highest speed in the middle of the tube, the exponent $n(\text{Re})$ is a component depending upon the Reynolds number, and can be calculated according to equations 5.7b and 5.17b at $n \approx 5$ for all pump sizes.

The maximum speed is derived from the volume flow as a ratio of the maximum to medium speed for the tube as follows:

$$\dot{V} = \bar{c}_x \cdot \pi \cdot r_a^2 = 2 \cdot \pi \cdot \int_{r=0}^{r=r_a} c(r) \cdot r \cdot dr = 2 \cdot \pi \cdot c_{\max} \cdot \int_{r=0}^{r=r_a} \left(1 - \frac{r}{r_a}\right)^{\frac{1}{n}} \cdot r \cdot dr \quad (\text{Equation 5.18})$$

Substituting $r' = r_a - r$ and $dr' = -dr$, we can solve equation 5.18 as follows:

$$\frac{c_{\max}}{\bar{c}_x} = \frac{(2 \cdot n + 1) \cdot (n + 1)}{2 \cdot n^2} \stackrel{(n=5)}{=} 1,32 \quad (\text{Equation 5.19})$$

In the adjacent circular cross-section from Figure 5.7, between X and 0, the following approximation is used for radius r , which is counted from the middle axis, as it is also done for a tube:

$$\frac{c}{c_{\max}} = \left(1 - \frac{|r - r_m|}{(r_a - r_i)/2}\right)^{\frac{1}{n}} \quad \text{with the middle radius} \quad r_m = \frac{r_a + r_i}{2}. \quad (\text{Equation 5.20 a,b})$$

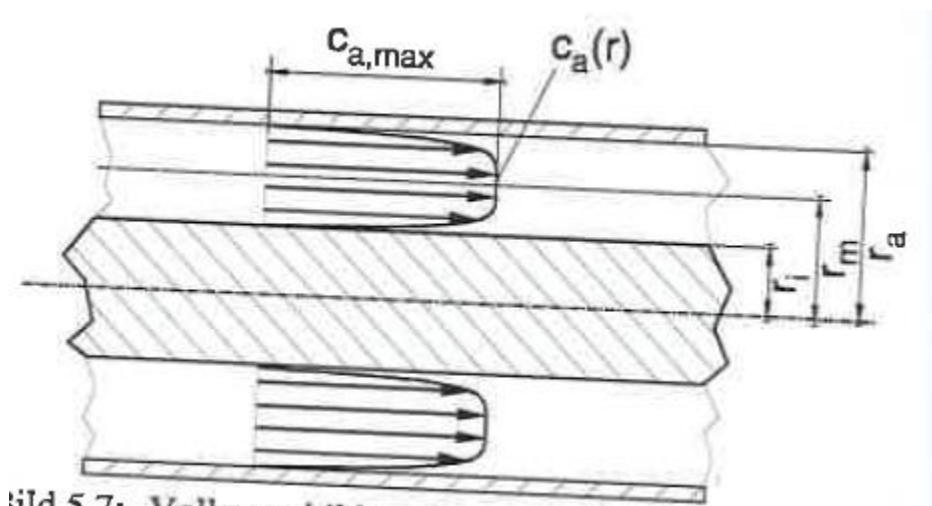


Figure 5.7 Fully formed speed distribution in tubes with circular cross-section

$|r - r_m|$ is the absolute value of the distance of the point in question from the circle with the radius r_m . c_{\max} is calculated from c for the circular section similarly to the tube, by integrating the radial speed

distribution. To take away the absolute value sign in the term for the local speed, the integral must distinguish whether the radius is bigger or smaller than the middle radius:

$$\dot{V} = 2\pi \cdot c_{\max} \cdot \left\{ \int_{r=r_i}^{r_m} \left(1 - \frac{r_m - r}{r_a - r_m}\right)^{1/n} \cdot r \cdot dr + \int_{r=r_m}^{r_a} \left(1 - \frac{r - r_m}{r_a - r_m}\right)^{1/n} \cdot r \cdot dr \right\}. \quad (\text{Equation 5.21})$$

The first integral can be solved by substituting $r' = r - r_i$, i.e. $dr = dr'$ /Bronstein 1985/, and in the second integral the substitution of $r' = r_a - r$ with $dr' = -dr$ brings us to the result. With the following expression:

$$\dot{V} = \pi \cdot (r_a^2 - r_i^2) \cdot \bar{c} = 2 \cdot \pi \cdot r_m \cdot (r_a - r_i) \cdot \bar{c} \quad (\text{Equation 5.22})$$

we arrive to the needed equation for the maximum speed:

$$\frac{c_{\max}}{\bar{c}_0} = \frac{n+1}{n} \stackrel{(n=5)}{=} 1,2. \quad (\text{Equation 5.23})$$

The speed distribution used for the circular cross-section applies to fully formed flows, and thus cannot be applied to the hub with a very short length (≤ 2 mm) between X and 0. Instead, the thickness of the border layer on the hub side is assessed according to /Schlichting 1965/, page 642, as a border layer on a rotating body with a maximum assumed axial extension of the hub up to the impeller entrance of $z_1 = 1.5$ mm till 2.0 mm. Dividing this value by the maximum radius of the hub in the area without blading, we arrive to the following relation:

$$\frac{z_1}{r_{i0,\max} (\equiv r_m)} = 2,0_{\varnothing 5-Pumpe} / 1,7_{\varnothing 6-Pumpe} / 2,0_{\varnothing 7,4-Pumpe}$$

$$\text{with } \lambda_m = \frac{\omega \cdot r_m}{u_m} = 1,5_{\varnothing 5-Pumpe} / 1,2_{\varnothing 6-Pumpe} / 1,1_{\varnothing 7,4-Pumpe} \quad (\text{Equation 5.24 a,b})$$

With these numbers, we can look into the diagram from /Schlichting 1965/, page 642, shown in Figure 5.8, and read the relation from the ordinate axis:

$$\frac{\delta_{2\pi}}{r_{i0,\max}} \cdot 10^3 \approx 1,0_{\varnothing 5; \varnothing 6; \varnothing 7,4}. \quad (\text{Equation 5.25})$$

Due to the short length, the border layer is laminar until the beginning of blading.

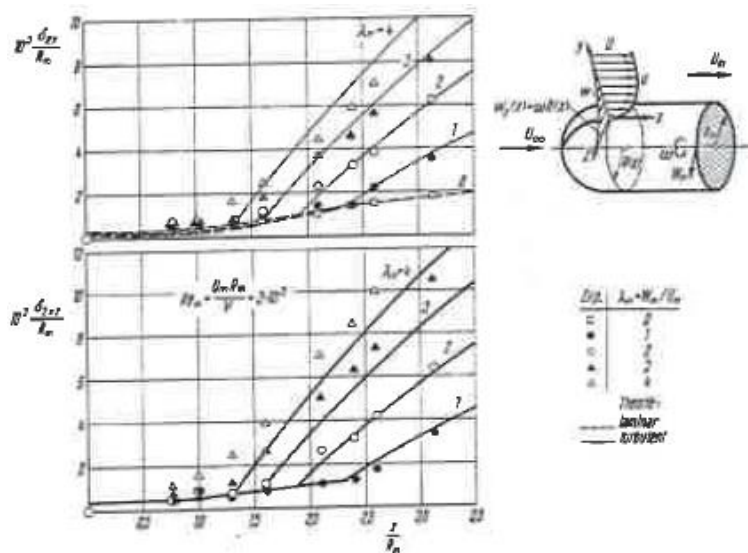


Figure 5.8 Impulse loss thickness δ_{2x} at a rotating body with axial flow /Schlichting 1965/

Here, δ_{2x} is the impulse loss thickness, which is related to the border layer thickness δ_x for ($c / c_{\max} = 0.99$) through the following expression:

$$\frac{\delta_{2x}}{\delta_x} = 0.0972(\text{turb.}) / \text{Truckenbrodt 1980/, volume 2, page 339}; \quad \frac{\delta_{2x}}{\delta_x} = 0.386(\text{lam.}) / \text{Schlichting 1965/, page 122} \quad (\text{Equation 5.26 a,b})$$

For this case, equation 5.26b represents the border layer thickness in the best way. The used diagram from Figure 5.8 applies to the Reynolds number $Re = 3 \cdot 10^5$, so that the results must be adjusted to the available Reynolds numbers:

$$Re = \frac{\bar{c}_0 \cdot r_{i0,\max}}{v} = 580_{\varnothing 5} / 780_{\varnothing 6} / 740_{\varnothing 7,4^*} \quad (\text{Equation 5.27})$$

For laminar border layers the following relation applies in approximation /Schlichting 1965/, page 110/127:

$$\delta'_x \cdot \sqrt{Re'} = \delta''_x \cdot \sqrt{Re''}, \quad (\text{Equation 5.28})$$

so that the border layer thickness at the rotating hub at the impeller entrance for all pump sizes up to $\delta_x \approx 0.05$ mm can be calculated from equations 5.25, 26b, 27 and 28.

The radial speed profile $c_0(r)$ before the area with blading is approximated according to the above said considerations at the pump housing by a potency profile and on the hub side with a border layer thickness of $\delta_x \approx 0.05$ mm.

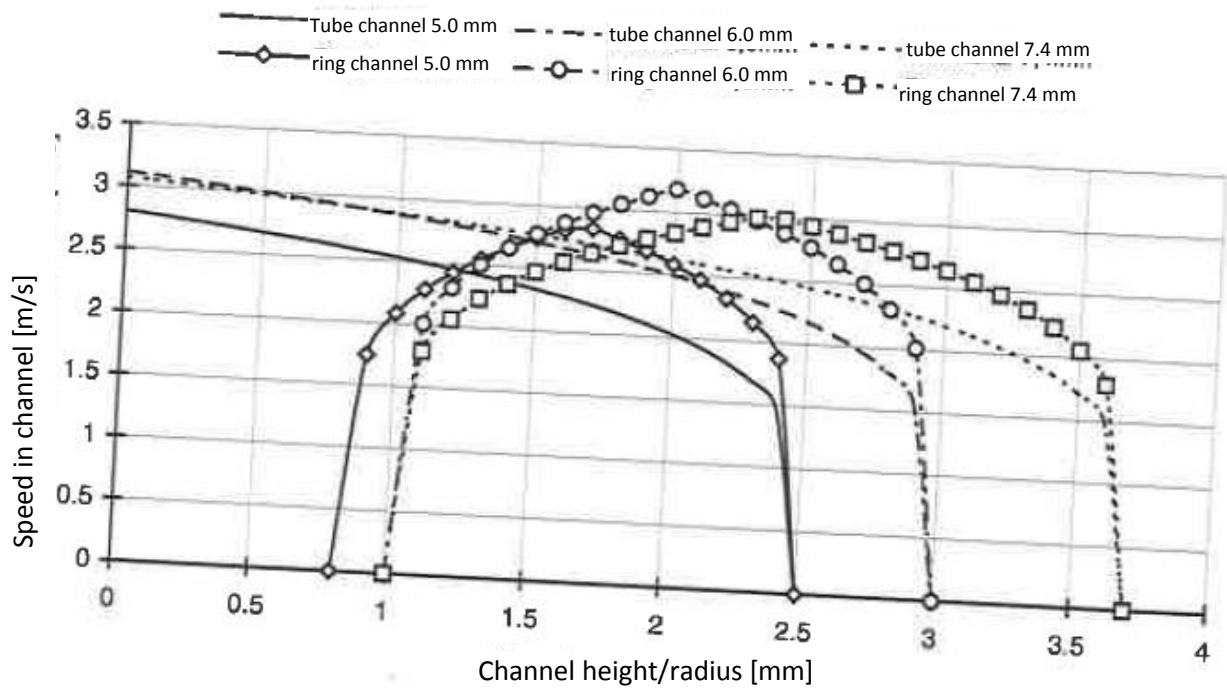


Figure 5.9 Formed speed profiles in tube and ring channel for 5.0 mm, 6.0 mm and 7.4 mm pumps

If we consider the speed profiles of formed flows in tube and ring channel presented in Figure 5.9, which correspond to the geometry of the pump before the hub and immediately before the entrance of the flow in the area with blading at the same volume flow, then it becomes clear, as discussed above, that the genuine speed profile is closer to the tube speed profile than to the ring speed profile. In the hub area with $r = 0.8 \text{ mm} - 1.0 \text{ mm}$, the tube profiles remain flat, so that the central blockage due to the blockage at the end only causes pushing, which increases the profile thickness. At the hub, the speed increases very quickly from 0 (wall adhesion) to c_{\max} with $r = r_i + \delta_z$. From here and up to the external channel limit, the calculated 1/5 profile is assumed according to equation 5.17a with the required proportional thickening. Figure 5.10 illustrates the reported speed profiles, stating the respective profile thickening as percentage.

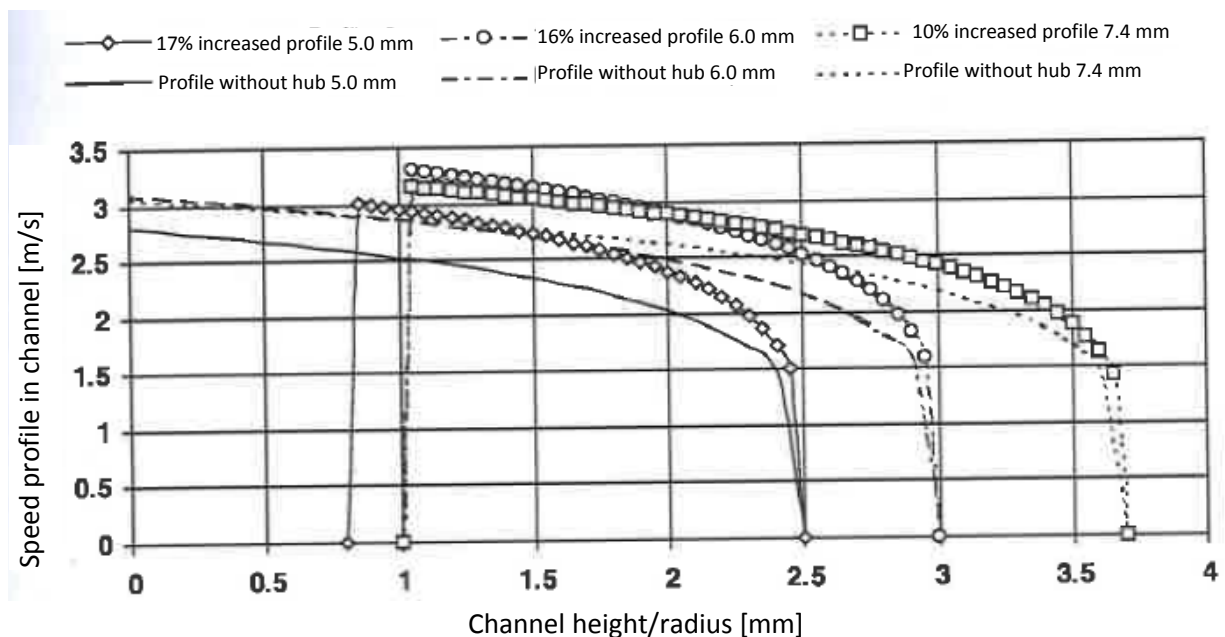


Figure 5.10 Formed, constant flow volume speed profiles $c_0(r)$ in tube channel with and without a hub for 5.0 mm, 6.0 mm and 7.4 mm pumps

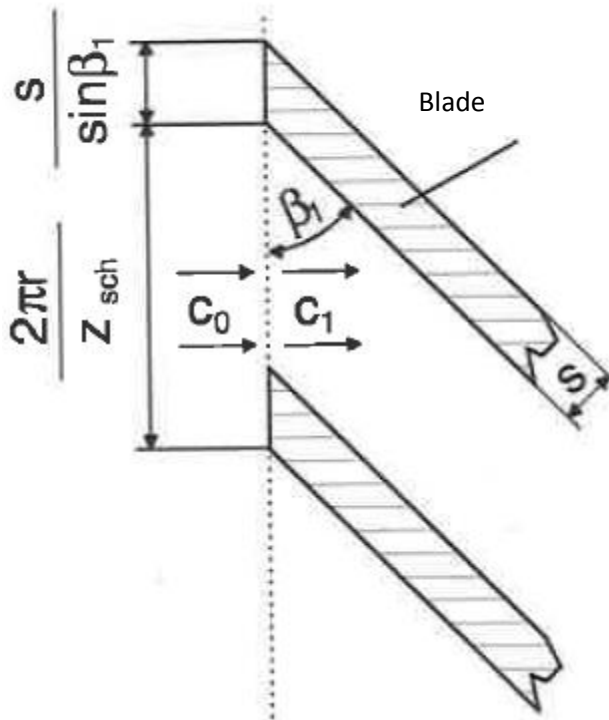


Figure 5.11 Decrease of the flow cross-section in rotor entrance by blade thickness at the end

Through adhesion of the fluid to the rotating hub, the fluid elements in the vicinity of the hub receive, as shown in Figure 5.8, an additional speed component in the peripheral direction. Since the border layer in the rotor entrance plane is still very thin, this effect is neglected for the purposes of the calculation of entrance angle.

The incoming flow can be assumed to be free of angular momentum, which well agrees with the experiments. According to the above considerations, we can now calculate the angle β_0 , which forms the relative speed directly before the running blade channel with the direction of the negative peripheral speed. However, to obtain the respective angle in the running blade channel, it must also be taken into account that the thickness at the end of the rotor blades affects the cross-section reduction, and according to the continuity equation, also the increase of the meridian speed.

For the relation of these speeds shortly before and immediately after the rotor entrance, we obtain the following relation for the specific radius r :

$$\frac{c_1}{c_0}(r) = \frac{2\pi \cdot r / z_{sch}}{2\pi \cdot r / z_{sch} - s / \sin \beta_1}, \quad (\text{Equation 5.29})$$

where z_{sch} is the number of rotor blades, and s is the thickness of a blade perpendicularly to the large chord length of the blade. Since the blade angle β_1 is contained in equation 5.29 for c_1 , the value must be identified in an iterative way.

The number of rotor blades was chosen for all pump sizes and options based on the experimental validation of grid load, blockage and blood damaging in Chapters 7, 8, 9, 10 and 11 as $z_{sch} = 2$; the blade

thickness cannot be less than 0.3 mm for manufacturing reasons, while the blade entrance edge has a radius of $r = \frac{1}{2} \cdot s$, in order to make the blades less sensitive in case of wrong current to detachments triggered by breast or back incidence.

The explicit blade angle β_1 is not explicitly provided for all pump sizes, since they can be easily calculated from equations 5.15b and 5.29, and are unnecessary for understanding the design.

The blade structure angles correspond to the blade angles β_1 plus the breast incidence set at 2° . The latter results from additional thickness pushed out along each blade entrance edge, which causes further increase of the meridian speed.

5.7 Transformation of hub diameter

A purely axial hub design was chosen for the RV pumps in the area with blading, i.e. the hub diameter remains constant across the entire rotor length. An axially accelerated flow in the blading was omitted here for structural reasons, since the fluid flows into the housing from the outside through a gap, and leads a hub, which becomes thicker in the flow direction, to a large hub diameter in the blading exit. This diameter on the exit side must be reduced in the flow direction behind the grid to zero within a very small space, so that a large hub diameter only causes strong delays or detachments. In particular, in the blood pumps these stationary stagnation areas, in which fluid exchange with flowing medium may be low, are critical, since they allow for thrombus formation.

The LV pumps were designed in such way that the hub diameter increases from the rotor entrance to exit. The flow is thus accelerated in the axial direction. This prevents detachment in the rotor blading area, because the border layer of the delay grid in the immediate vicinity of the wall, due to the meridian acceleration, is not so deprived of energy that there would be detachment in the flow direction as the result of raising pressure. Since acceleration should be as uniform as possible in average across the cross-section, a fluid element in rotor is subject to the following requirement:

$$\frac{d\bar{c}_x}{dt} = \text{Constant} \quad ; \quad (\text{Equation 5.30})$$

It is assumed that the flow is quasi-stationary and meridian. Therefore, taken in average over time, the fluid element is subject only to convective acceleration:

$$\frac{d\bar{c}_x}{dt} = \frac{d\bar{c}_x}{dx} \cdot \frac{dx}{dt} = \frac{d\bar{c}_x}{dx} \cdot \bar{c}_x = \frac{d\bar{c}_x}{dA_x} \cdot \frac{dA_x}{dx} \cdot \bar{c}_x = \text{Constant} \quad ; \quad (\text{Equation 5.31})$$

where axial speed gradient can be connected to the cross-section transformation according to equation 5.31. The cross-section perpendicular to the pump axis is denoted A_x , so that dA_x/dx is the sought cross-section transformation.

If we differentiate the continuity equation for incompressible media:

$$\bar{c}_x \cdot A_x = \dot{V} = \text{Constant} \quad ; \quad (\text{Equation 5.32})$$

we obtain the following connection:

$$\frac{d\bar{c}_x}{dA_x} = \text{Constant} \cdot \frac{1}{A_x^2},$$

(Equation 5.33)

If we substitute equation 5.33 into equation 5.31, then, upon transformation and combination of the constants, we arrive at:

$$\frac{dA_x}{A_x^2} = \text{Constant} \cdot \frac{1}{\bar{c}_x} \cdot dx,$$

(Equation 5.34)

If we transform equation 5.32 for speed and substitute this expression into the equation above, then the resulting equation, upon further combination of the constants, can be integrated:

$$\int \frac{dA_x}{A_x^3} = C_1 \cdot \int dx + C_2$$

with C_2 as integration constant.

(Equation 5.35)

The indefinite integral provides the connection:

$$\frac{1}{2 \cdot A_x^2} = C_1 \cdot x + C_2.$$

(Equation 5.36)

Neglecting the blockage by blading, we obtain the following expression for the cross-section area and hub diameter under the assumption of a constant external diameter D_a :

$$A_x(x) = \frac{\pi}{4} \cdot \left\{ D_a^2 - [D_i(x)]^2 \right\},$$

(Equation 5.37)

so that we get the following function for the hub diameter:

$$D_i = D_a \cdot \sqrt{1 - \frac{1}{D_a^2 \cdot \sqrt{C_1' \cdot x + C_2'}}}}$$

(Equation 5.38)

The constants C_1' and C_2' are obtained from the respective boundary conditions.

The considerations on acceleration collision at the beginning of the blading due to the thickness at the end of the blade have shown that levelling off of the collision with even two blades with a material thickness of only 0.3 mm makes the hub thinner in the flow direction. The associated risk of flow displacement at the hub makes this measure unfeasible, so that the acceleration collision is only reduced by horizontal tangent of the hub in the entrance area. The resulting hub transformation in the rotor is split respectively into three portions, so that starting from the beginning of the hub and up to 0.2 mm before the blade entrance edge, the fluid is constantly accelerated according to equation 5.38. In the area from 0.2 mm before till 0.4 mm behind the beginning of the blading, the cylindrical hub part moves with horizontal tangent, and only then joins the further area of constant meridian acceleration according to equation 5.38 until the end of the blading.

The hub diameter remains constant in the whole stator area of all LV pumps, although a meridian acceleration reducing displacement risk is also useful here, due to channels becoming too low, but is no longer practical.

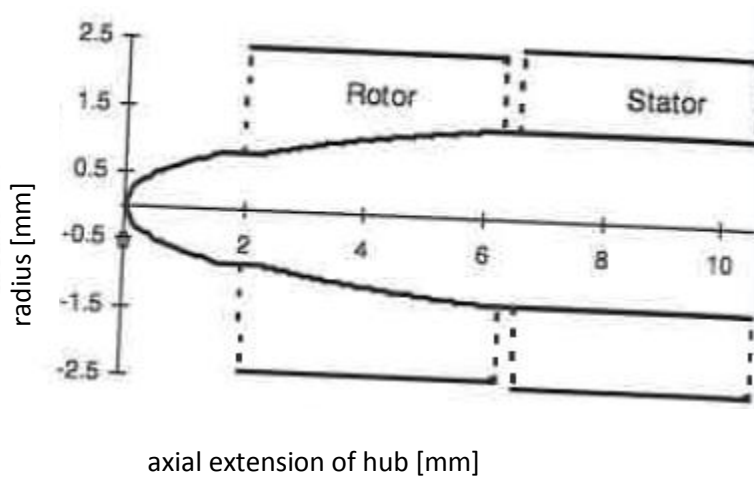


Figure 5.12 Hub contour of a 5 mm LV pump

Figure 5.12 shows an example of a hub transformation in rotor and stator area of a 5 mm pump version.

5.8 Speed distribution and calculation of the angles in the rotor exit

In this section, we will present the considerations on the axial and peripheral speed distributions in the axial gap of the LV pump between rotor and stator, or directly upon exiting the rotor of an RV pump. They will help to determine the blade angles in the rotor exit plane, and for the LV pump also the entrance angles of the stator.

5.8.1 Specific blading work

The flow energy induced in the fluid at the time of passing through the pump is coupled solely through the running blades. The total energy that must be produced for this is defined through the specific blading work, which consists of the total specific flow work plus all dissipation terms:

$$y_{sch} = a = \frac{y}{\eta_{hyd}} = \frac{\Delta p_{Pumpe}}{\rho \cdot \eta_{hyd}} \quad \text{with} \quad a = y_t + j; \quad y_t = y + \frac{1}{2} \cdot (c_a^2 - c_e^2) + g \cdot (z_a - z_e). \quad (\text{Equation 5.39})$$

The hydraulic efficiency rate η_{hyd} used here according to equation 5.1 was obtained from the measurements of the useful pressure Δp_{nutz} on the total system, but without pressure or suction tubes. Therefore, the pressure loss in the tube, which consists of the channel friction and flow profile transformation losses, must be added to the useful pressure in order to obtain a good assessment of the required specific blading work based on the measured efficiency rate. All further pressure losses of the total system, as discussed in Chapter 5.4, are already taken into account in the efficiency rate in question. The required Δp_{Pumpe} results from the useful pressure plus the channel friction losses, as well as the additional entry losses in the tube according to the equations 5.3, 5.6 and 5.7 a,b:

$$\Delta p_{Pumpe} = \Delta p_{nutz} + \Delta p_R + \Delta p_{L(nur \text{ für LV-Pumpe})} \quad \text{with} \quad \Delta p_R = \zeta_R \cdot \frac{\rho}{2} \cdot \bar{c}_x^2; \quad \Delta p_L = (\zeta_L^* - 1) \cdot \frac{\rho}{2} \cdot \bar{c}_x^2$$

(Equation 5.40)

Therefore, the required pressure difference equals to:

$$\Delta p_{\text{Pumpe}} = 13400\text{Pa}(102\text{mmHg})_{\emptyset 5-LV}; 14500\text{Pa}(110\text{mmHg})_{\emptyset 6-LV}; 14000\text{Pa}(106\text{mmHg})_{\emptyset 7,4-LV}; \\ 4950\text{Pa}(37,6\text{mmHg})_{\emptyset 5-RV}; 5100\text{Pa}(39\text{mmHg})_{\emptyset 6-RV}; 4800\text{Pa}(36,5\text{mmHg})_{\emptyset 7,4-RV}.$$

The required total specific blading work with the efficiency rates from Chapter 5.4 comes up to:

$$y_{sch} = 63,3 \frac{\text{m}^2}{\text{s}^2} \emptyset 5-LV; 23,4 \frac{\text{m}^2}{\text{s}^2} \emptyset 5-RV; 45,7 \frac{\text{m}^2}{\text{s}^2} \emptyset 6-LV; 16,0 \frac{\text{m}^2}{\text{s}^2} \emptyset 6-RV; 44,1 \frac{\text{m}^2}{\text{s}^2} \emptyset 7,4-LV; 15,1 \frac{\text{m}^2}{\text{s}^2} \emptyset 7,4-RV.$$

As we can see, the grid load of the 5.0 mm pump is the highest, with the smallest required delivery head due to the smaller efficiency rate of only 20%, compared to all the bigger pump options. With this result, further reduction of pumps is no longer feasible, if it requires significant effort.

This total specific blading work y_{sch} represents the enthalpy, which is added to the liquid by the blades in a unit of time for mass volume:

$$y_{sch} = a = \frac{\dot{H}_{sch}}{\dot{m}}. \quad (\text{Equation 5.41})$$

The specific blading work a generally changes with the radius. For an infinitely small ring, the following expression applies:

$$a(r) = \frac{d\dot{H}(r)}{d\dot{m}(r)}.$$

A different way to write down the specific blading work results from the Euler equation for axial pumps:

$$a(r) = u(r) \cdot \Delta c_{u,0-3}(r) = u(r) \cdot [c_{u,3}(r) - c_{u,0}(r)], \quad (\text{Equation 5.42})$$

where the flow enters the pump without pre-existing angular momentum ($c_{u,0} = 0$):

$$a(r) = u(r) \cdot c_{u,3}(r) = \omega \cdot r \cdot c_{u,3}(r). \quad (\text{Equation 5.43})$$

In this section we will only derive relations for the sizes immediately upon exiting the rotor according to Figure 5.4, which is why index 3 will be left out, if it cannot cause any misunderstandings.

The integral connection among the sizes is as follows:

$$y_{sch} = \frac{1}{\dot{m}} \cdot \int_{r_1}^{r_2} a(r) \cdot d\dot{m} \stackrel{p=\text{Constant}}{=} \frac{1}{\dot{V}} \cdot \int_{r_1}^{r_2} a(r) \cdot d\dot{V} = \frac{1}{\dot{V}} \cdot \int_{r_1}^{r_2} a(r) \cdot c_a(r) \cdot dA. \quad (\text{Equation 5.44})$$

Equation 5.44 already contains the axial outflow speed $c_a(r)$, which changes with the radius and is tied to the peripheral speed $c_u(r)$. A proven method to calculate the axial outflow speed $c_a(r)$ from the angular

momentum distribution $c_u(r)$ is the **method of radial balance**, which can be applied in the axial gap between the rotor and stator, which is free of blading. The constant average axial speed will be calculated as a reasonable starting value for the iterative process, which consists of the choice of a proper angular momentum distribution, calculation of the axial outflow speed distribution, verification that volume flow is constant, and the actually obtained specific blading work according to Figure 5.3:

$$y_{sch} \approx \frac{1}{A} \cdot \int_{r_i}^{r_a} a(r) \cdot dA = \frac{2\pi}{A} \cdot \int_{r_i}^{r_a} a(r) \cdot r \cdot dr \quad \text{with} \quad c_a = c_a(\bar{r}) \quad \text{and} \quad \bar{r} = \sqrt{\frac{r_a^2 + r_i^2}{2}} \quad (\text{Equation 5.45 a,b,c})$$

If upon the calculation of the axial speed distribution with the radial balance method the subsequent calculation results in deviation of the total specific blading work by more than 5%, then a different angular momentum distribution should be chosen.

Since a subsequent calculation should be performed in any case, because the speed distribution is unknown, a good approximation can be achieved by introducing an “average plane radius” \bar{r} according to equation 5.45c, in order to be able to quickly choose various angular momentum distributions, which already to a large extent give the produced blading work (see also equation 5.63a). The average plane radius results from the condition that the flow cross-sections outside and inside the circle with this radius are equal.

Therefore, we use the following relation:

$$y_{sch} = a(\bar{r}) . \quad (\text{Equation 5.46})$$

Subsequent calculations showed a very good correspondence between the exact values and the ones calculated using this approximation.

5.8.2 Method of radial balance

The method of radial balance gives an opportunity to approximate the spatial flow in axial turbomachines /Gallus 1992/, TAM-100, pages 107 – 110.

It can only be applied in blading free cross-sections, such as the axial gap between the rotor and stator mentioned above or behind the rotor of a no-stator pump, since otherwise the interaction between the blade and fluid must be taken into account. The assumptions of this method look as follow:

$c_r = 0$ (no speed in radial direction);

$r_m \rightarrow \infty$ (disregarding the meridian flow line curvature).

c_r is the speed in radial direction, r_m is the curvature radius of the flow line in the meridian plane. Both assumptions are only approximately fulfilled in the pump, which is to be designed. In the LV pumps this automatically results from the hub diameter being variable in the flow direction. However, in purely axially designed RV pumps these conditions are not exactly met either due to the existing secondary flows. At the same time, the flow research in Chapter 7 of explicit particles in the fluid proves that the main volume flow runs concentrically with respect to the middle axis with $c_r = 0$. The spiral turbulence according to Figure 7.6 does not cause any relevant radial speed components in the main flow. In

/Gallus 1992/, page 110 the following condition is stated for sufficiently exact compliance with these assumptions:

$$\frac{\text{blade height}}{\text{grid width}} < 2$$

(Equation 5.47)

which is complied with by all pump options with a blade height from 1.1 mm to 2 mm and a grid width from 4 mm to 8.5 mm.

The differential equation of the radial balance looks as follows according to /Gallus 1992/, TAM-102:

$$\frac{\partial h_t}{\partial r} - T \frac{\partial s}{\partial r} - c_u \frac{\partial c_u}{\partial r} - c_a \frac{\partial c_a}{\partial r} - \frac{c_u^2}{r} = 0.$$

(Equation 5.48)

$h_t = h + c^2/2$ is the specific total enthalpy, $T \frac{\partial s}{\partial r}$ is the change of the specific dissipation energy with the radius for an isothermal adiabatic flow.

The convective acceleration terms $c_u \frac{\partial c_u}{\partial r}$ and $c_a \frac{\partial c_a}{\partial r}$ can be interpreted as radial gradients of the kinetic energy of the fluid elements for the movement in peripheral or axial direction with respect to the

mass of the element. $\frac{c_u^2}{r}$ is the centripetal acceleration of a fluid element along the radius r with the peripheral speed c_u . Since this equation, which is based on the assumption that the flow line curvature is negligible, only contains derivatives by radius, this is a simple differential equation, and the partial derivative $\frac{\partial}{\partial r}$ can be simply substituted with $\frac{d}{dr}$.

We should first consider the case without friction, i.e. of disappearing viscosity of the fluid. In such case, $ds/dr = 0$. The friction effect will be discussed below in Chapter 5.8.4. The simplified differential equation of the radial balance thus becomes:

$$\frac{dh_t}{dr} - c_u \frac{dc_u}{dr} - c_a \frac{dc_a}{dr} - \frac{c_u^2}{r} = 0,$$

(Equation 5.49)

Upon transformation of this equation according to the rules of the differential calculus, we arrive at:

$$\frac{dh_t}{dr} - \frac{d(\frac{c_u^2}{2})}{dr} - \frac{d(\frac{c_a^2}{2})}{dr} = \frac{c_u^2}{r} \Leftrightarrow d(h_t - \frac{c_u^2}{2} - \frac{c_a^2}{2}) = \frac{c_u^2}{r} \cdot dr.$$

(Equation 5.50a,b)

Equation 5.50a can be interpreted as follows. The radial gradient of the total enthalpy, i.e. the increase or decrease of the total enthalpy with the radius, consists of the gradient of the specific kinetic energy and the centripetal acceleration at that point. The centripetal acceleration is the radial gradient of the

static pressure divided by the fluid thickness. If c_u is not zero, then this pressure is always positive, since the pressure must increase from inside outwards in order to keep the fluid element on its concentric path around the middle axis. The centripetal force results as the total force from the pressure forces affecting this fluid element.

The left side of equation 5.50b can be integrated in general, the right side first upon choosing a reasonable radial distribution of peripheral speed or angular momentum distribution according to Chapters 5.8.1 and 5.8.3, assuming steady and differentiable transformation of all sizes of r appearing in the range $r_i < r < r_a$:

$$(h_{t,a} - h_t(r)) - \left(\frac{c_{u,a}^2}{2} - \frac{c_u(r)^2}{2} \right) - \left(\frac{c_{a,a}^2}{2} - \frac{c_a(r)^2}{2} \right) = \int_r^{r_a} \frac{c_u(r)^2}{r} \cdot dr \quad (\text{Equation 5.51})$$

The definite integral is taken from the variable radius r to the external radius r_a . The second index a denotes the respective size on the external radius.

The total enthalpy in question in the axial gap between the rotor and stator on a given radius r consists of the total enthalpy before the rotor and the enthalpy, which is added to the fluid in rotor in the form of the specific blading work on such radius:

$$h_t(r) = h_{t,0}(r) + a(r), \quad (\text{Equation 5.52})$$

The enthalpy before the rotor will be discussed below in Chapter 5.8.3.

5.8.3 Choice of a proper angular momentum distribution

The relative blade angle in the exit plane of the rotor is determined from the following equation:

$$\tan \beta_3(r) = \frac{c_{a,3}(r)}{u(r) - c_{u,3}(r)}, \quad (\text{Equation 5.53})$$

The angle β_2 is determined using the axial speed within the running blade channel:

$$\tan \beta_2(r) = \frac{c_{a,2}(r)}{u(r) - c_{u,2}(r)}, \quad (\text{Equation 5.54})$$

where the speed ratio $c_{a,2}/c_{a,3}$ according to equation 5.29 is no more than 1.08 for all pump versions in the vicinity of the hub with the smallest hub diameter and realistic blade construction angles $\beta_2 \geq 70^\circ$. Therefore, since $c_{a,2} = c_{a,3}$, it can be assumed in good approximation that $\tan \beta_2 \approx \tan \beta_3$.

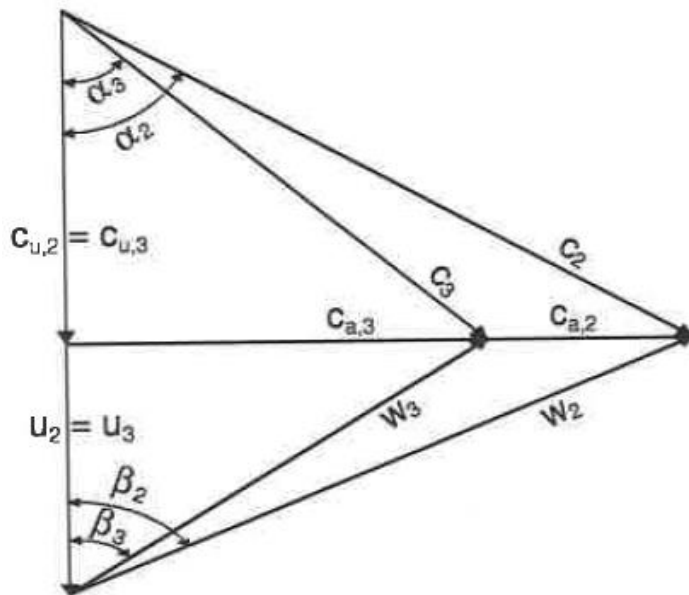


Figure 5.13 Speed ratios at the rotor exit

Below we will discuss various radial angular momentum distributions and the resulting exit angles. A reasonable outcome will be an angular momentum distribution, which most closely approximates a constant angular momentum impact along the radius with the realistic exit angle and production oriented contour. In order to get a specific blading work, which does not change with radius, and which has a constant total enthalpy at the rotor exit in case of approximately constant total enthalpy before the rotor, the peripheral speed would have to be distributed over the radius according to the following equation:

$$c_u(r) = \frac{B}{r}$$

(Equation 5.55)

Here B is a constant, which must be chosen according to the required total blading work. This way equations 5.41 and 5.43 result in the following expression:

$$a = u(r) \cdot c_u(r) = \omega \cdot r \cdot \frac{B}{r} = \omega \cdot B = \text{const.} = y_{sch}$$

(Equation 5.56)

According to equation 5.56, the peripheral speed of the liquid must be highest in the hub area due to the small peripheral speed of the rotor in that area. Therefore, with given blading work, exit angle in the hub area becomes very large, here specifically for the LV blading $\beta_{2,i} > 120^\circ$, which is far too large for all pump sizes according to the research in Chapter 9.2.1. To make the exit angles of the rotor smaller in the hub area and larger outside of it, the fluid must be re-distributed with smaller peripheral speeds in the hub area and the large ones outside, respectively. Then there is a specific blading work $a(r)$ increasing from inside outwards, and thus a total enthalpy $h_t(r)$ changing with radius:

$$h_t(r) = h_{t,0}(r) + \omega \cdot r \cdot c_u(r)$$

(Equation 5.57)

The total enthalpy $h_{t,0}(r)$ before the rotor can be determined as follows:

$$h_{t,0} = u_0 + \frac{p_0}{\rho} + \frac{c_0^2}{2}.$$

(Equation 5.58)

The inner energy u is constant under the assumption of an isothermal flow ($T = \text{const}$). In the incoming flow free of angular momentum, pressure is also constant in good approximation over the radius, i.e. the pressure is applied to the border layer as $p_0 = \text{const}$. Also, since in equation 5.51 it is always only the difference of the total enthalpy values that is included at two points of the cross-section, the values constant over the radius compensate each other. Besides, the speed component disappears on the external radius, so that the difference of the total enthalpy required for equation 5.51 is determined as follows:

$$h_{t,0,a} - h_{t,0}(r) = -1 \cdot \frac{c_0(r)^2}{2}.$$

(Equation 5.59)

Therefore, the total enthalpy distribution results from the speed profile of formed turbulent flows, which depends upon the radius, at the rotor entrance, according to equation 5.17a and Figure 5.9.

In case of the RV pumps, as it has already been discussed, at the rotor entrance there is a block profile $c_0 = \text{const}$. This also renders $h_{t,0}$ constant over the radius. Based on the constant channel height in rotor, equation 5.51 can be solved for the RV pumps without further simplifications with the used angular momentum distribution.

In case of the LV pumps, it is not immediately possible due to the hub getting thicker in the flow direction. Instead, there is a problem of providing the exit radius, which would correspond to the entrance radius. This can be done volumetrically, but requires significant iterative work due to the axial speed at the exit first resulting from the radial balance. To make the calculations, it is rather necessary to use the assumption of circular cross-section at the entrance of the LV pumps according to equation 5.20 a,b with a 1/6 speed distribution and inner diameter D_i , which corresponds to the inner diameter of the hub at the rotor entrance. The resulting total enthalpy difference at the entrance is as follows:

$$\Delta h_{t,0}(r) = h_{t,0,a} - h_{t,0}(r) = -\frac{1}{2} \cdot \left\{ c_{\text{max}} \cdot \left(1 - \frac{|r - r_m|}{(r_a - r_i)/2} \right)^{\frac{1}{n}} \right\}^2.$$

(Equation 5.60)

Substituting it in the integral equation 5.51 of the radial balance, we arrive at:

$$\left\{ \varrho \cdot [r_a \cdot c_u(r_a) - r \cdot c_u(r)] + \Delta h_{t,0}(r) \right\} \cdot \left(\frac{c_{u,a}^2}{2} - \frac{c_u(r)^2}{2} \right) - \left(\frac{c_{a,a}^2}{2} - \frac{c_a(r)^2}{2} \right) = \int_r^{r_a} \frac{c_u(r)^2}{r} \cdot dr. \quad (\text{Equation 5.61})$$

An appropriate angular momentum distribution can only be found iteratively by trying freely chosen starting points and the respective adjustment based on the results. The following criteria must be taken into account:

- As it has already been mentioned in the explanation on constant blading work, the blade angles should not exceed 90° on any radius for the reasons of the flow mechanics.
- For production reasons, the angles across the radius may not differ to the point that there are strongly different wrap angles of the blade over the radius.
- If the peripheral speed of the flow, and thus the blading work, increases outwards too strongly, then the speed profile gets disturbed to the point that the continuity equation no longer complies with the theory of the radial balance. There will then appear flow aspects that negatively affect the pump capacity.

Angular momentum distribution of the LV pumps

As a good overlap of these criteria, which will be discussed further, the linear angular momentum was chosen for the LV pumps in the following form:

$$c_u(r) = C \cdot r + A$$

(Equation 5.62)

C and A are constants, whose equations result from the required blading work y_{sch} (see equations 5.43, 5.45 a,b,c, and 5.46) and the maximum permissible blade construction angle β_2 :

$$a(\bar{r}) = \omega \cdot \bar{r} \cdot (C \cdot \bar{r} + A) = y_{sch}$$

(with radius \bar{r} taken average over plane)

$$u(r_i) \geq c_u(r_i) \Leftrightarrow \omega \cdot r_i \geq C \cdot r_i + A$$

(Equation 5.63 a,b)

The second equation was derived from the condition that the angle between the flow (relative to blade) and the negative peripheral direction cannot exceed 90° in the vicinity of the hub as well. A more detailed consideration of the border angle is provided in Chapter 9.2.1. Solving the system of these two equations for the limit value $\beta_2 = 90^\circ$, we get the required constants and the first angular momentum distribution with which the axial speed distribution can be calculated over the radius according to the radial balance (equations 5.51 and 5.61). Upon integration and separation of the axial speed components, we obtain:

$$c_a(r)^2 - c_{a,a}^2 = 2 \cdot \left\{ -\Delta h_{r,0}(r) + (\omega - C) \cdot C \cdot (r^2 - r_a^2) + (\omega - 3C) \cdot A \cdot (r - r_a) + A^2 \cdot \ln \frac{r_a}{r} \right\} \quad \text{(Equation 5.64)}$$

$$= X(r)$$

Since only positive values make sense for the respective speed quadrants, the following must apply:

$$c_{a,a}^2 \geq -1 \cdot X(r)$$

(Equation 5.65)

For the borderline case on the hub side, $c_a(r = r_i) = c_{a,i} = 0$, we obtain an axial speed in the vicinity of the housing wall, which is clearly not equal to zero. Since the axial speed was obtained from equation 5.65 assuming the fluid viscosity is negligible, the condition of housing wall adhesion cannot be fulfilled. This issue will be discussed in more detail in Chapter 5.8.4.

Angular momentum distributions for the RV pumps

Due to the lower required pump capacity, the rotor exit angles of the RV pumps are in average smaller than the respective angles of the LV pumps. Therefore, two possible angular momentum distributions will be discussed for lower specific blading works:

$$1. \quad c_u(r) = \frac{B}{r} \quad (\equiv y_{sch} \text{ is constant}) \text{ and}$$

$$2. \quad c_u(r) = A + \frac{B}{r}. \quad (\text{Equation 5.66 a,b})$$

If the required pump capacity cannot be reached with these speed distributions in absence of stator, then it appears reasonable to use for the RV pumps the angular momentum distribution according to equation 5.62 with the respective limiting conditions for the maximum permissible blade angles.

$$c_u(r) = \frac{B}{r} ;$$

On item 1.

The specific blading work is constant here over the radius. Constant B can be obtained from the required total blading work:

$$a(r) = \omega \cdot r \cdot c_u(r) = B \cdot \omega = y_{sch} = \text{const.}$$

With $h_{t,o}(r) = \text{const}$ and $\Delta h_{t,o}(r) = 0$, the integrated form of the radial balance according to equation 5.51 looks as follows:

$$c_a(r)^2 - c_{a,a}^2 = B^2 \left(\frac{1}{r_a^2} - \frac{1}{r^2} \right) + 2 \cdot \int_r^{r_a} \frac{B^2}{r^3} \cdot dr = 0,$$

It provides that the distribution of the axial speeds is not affected by the rotation movement. This can be interpreted as follows.

The total enthalpy according to equation 5.58 is constant over the radius at the rotor exit, since both the total enthalpy at the rotor exit and the specific blading work over the radius are constant. From the fact that the static pressure must increase with radius, in order to keep the fluid elements on the curved path, and the kinetic energy of the peripheral speed increases outwards, it can be derived that the sum of these two enthalpies remains constant over the radius. Thus, without the viscosity effect the axial speed distribution at the rotor exit would have a block profile based on the radial balance. However, based on the viscosity effect, the speed distribution at the rotor exit is assumed to be that of a turbulent formed flow according to equation 5.17a. The constant n is chosen here equal to 10, in order to obtain a more complete profile compared to a 1/5 or 1/6 distribution, since based on the small length of the flow no formed profile is available at the hub and housing, if there is no suction tube.

With the speed profile calculated this way, the blade angles at the rotor exit can be immediately calculated based on equations 5.29 and 5.54. The effect of the blade thickness at the end according to

equation 5.29 is required for the generally smaller exit angles of the RV pump. Since the fluid rotation does not affect the speed profile, and it can be chosen already here taking into account the viscosity effects and the permanent volume flow, the final blade angles become clear directly taking into account the angle excess from Chapter 5.8.7.

On item 2. $c_u(r) = A + \frac{B}{r}$:

Taking into account the required specific blading work and the maximum permissible angle in the rotor exit, we can determine constants A and B similarly to the procedure for the LV pumps according to equations 5.63 a,b.

If we integrate the simplified differential equation of the radial balance from equation 5.51, then we obtain the following for the axial speed distribution in the case with $h_{t,o}(r) = \text{const}$ and $\Delta h_{t,o}(r) = 0$:

$$c_a(r)^2 - c_{a,a}^2 = 2 \cdot A \cdot \left[\omega \cdot (r - r_a) + B \left(\frac{1}{r} - \frac{1}{r_a} \right) + A \cdot \ln \frac{r_a}{r} \right].$$

If we take into account that, similarly to the procedure for the LV pumps, only positive values make sense for speed quadrants, we obtain for the borderline case $c_a(r = r_i) = c_{a,i} = 0$ the speed distributions for which clearly non-zero speeds take place in the immediate vicinity of the housing wall. The viscosity effect must be subsequently taken into account in this case as well.

5.8.4 Viscosity effect

The general differential equation of the radial balance looks as follows assuming that the meridian flow curvature is negligible, $c_a^2/R_m \approx 0$, according to equation 5.48:

$$\frac{\partial h_t}{\partial r} - T \frac{\partial s}{\partial r} - c_u \frac{\partial c_u}{\partial r} - c_a \frac{\partial c_a}{\partial r} - \frac{c_u^2}{r} = 0.$$

For calculation of the axial speeds, the expression $T \frac{\partial s}{\partial r}$ had to be disregarded due to unknown radial dissipation terms. Therefore, it was assumed at this point that no energy is transferred into heat in fluid by dissipation. This applies in viscous media, but only for a disappearing radial speed gradient ($\frac{\partial c}{\partial r} \approx 0$), which condition is not even closely met in the largest part of the cross-section. Thus, the condition of wall adhesion must be fulfilled in the vicinity of the channel limits, but a rather high speed gradient can also exist in the middle of the channel, depending upon the angular momentum and channel length.

The effect of the neglected term on the axial speed comes from the above equation with $s \approx \tau$:

$$\frac{\partial s}{\partial r} < 0 : \Rightarrow c_a \uparrow$$

increases (hub border layer);

$$\frac{\partial s}{\partial r} > 0 : \Rightarrow c_a \downarrow$$

decreases (housing border layer).

The thickness of the border layers was assessed according to /Truckenbrodt 1980; Schlichting 1965/. A similar calculation for an even plate resulted in a border layer on the housing side for the LV pumps, which layer is thicker than half the channel height due to the suction tube. In the vicinity of the hub, the length is much shorter. Here it corresponds to the length of the border layer on the housing side for the RV pumps, and are thinner. A rough estimate on the hub side according to /Schlichting 1965/ on rotating bodies results in border layer thicknesses of the order of half the channel height as well, so that the total flow cross-section consists of a border layer. The border layer thickness can be exactly calculated neither on the hub, nor on the housing side, since no final and applicable calculations are available for a turbulent flow with positive pressure gradients in the flow direction. This is even more so, since neither the effect of the secondary spiral whirl in channel together with the gap flow on the border layer on the housing side, nor its effect on the border layer thickness on the hub side can be assessed.

However, in order to approximately take into account the viscosity effect on the axial speed distribution, an indicator $f_a(r)$, which depends upon the radius, is introduced and determined from the turbulent speed distribution in circular gap free of angular momentum, based on equation 5.20 a,b:

$$f_a(r) = \frac{c(r)}{c_{\max}} \bigg|_{c_a=0} = \left(1 - \frac{|r - r_m|}{(r_a - r_i)/2} \right)^{1/n} \quad \text{with the middle radius } r_m = \frac{r_a + r_i}{2} \quad (\text{Equation 5. 67})$$

Due to the pressure increase in rotor, the flow slows down here along all channel limits, and causes the border layers get thicker in the flow direction. However, the rotation movement and secondary flows counteract this thickening of the border layer, similarly to the flow accelerated in the axial direction in the LV pump, according to Chapter 5.7. Therefore, under the assumption of the mutually mostly compensating effects from the beginning of the rotor to the exit in the axial gap, the constant n gets the same value as in the rotor entrance of $n_{LV} = 5-6$. According to the experimental results from Chapter 7, which imply due to constant color detachment qualitatively identical wall shear stress in rotor from the entrance to exit, this assumption looks reasonable, as long as there are no significant detachments.

Due to the small length of flow in the pump (missing suction tube), $n_{RV} = 10$ was chosen in the RV pump. This allows for better description of incompletely formed flow.

This indicator f_a is multiplied by the respective axial speed from Chapter 5.8.3 received from the radial balance. To avoid misunderstandings, these values calculated disregarding viscosity receive the index rGG:

$$\frac{c_a(r)}{\text{const.}} = f_a(r) \cdot c_{a,rGG}(r) \quad (\text{Equation 5.68})$$

The constant in equation 5.68 is calculated from the condition that the volume flow is constant according to Chapter 5.8.5.

5.8.5 Continuity equation

To obtain a meaningful speed distribution, the constant introduced above must be determined in such way that the required volume flow can be transmitted. The volume flow is obtained from the axial speeds with equation 5.68:

$$\dot{V} = 2\pi \cdot \text{const.} \cdot \int_{r_i}^{r_a} f_a(r) \cdot c_{a, rGG}(r) \cdot r \cdot dr.$$

(Equation 5.69)

This integration cannot be performed in a closed way for the existing axial speed distributions. Therefore, we perform summation of partial volume flows through a sufficient number of circles with the number k , in which the speed can be assumed to be constant:

$$\dot{V} = 2\pi \cdot \text{const.} \cdot \sum_{i=0}^k f_a(r) \cdot \bar{c}_{a, rGG}(r) \cdot r \cdot \Delta r.$$

(Equation 5.70)

The required constant designated as “const” can be calculated from equation 5.70, so that we can now determine the final axial speed distribution in the axial gap behind the rotor, or between the rotor and stator. The profile calculated this way should be complete and fill the available channel height in a proper way. If this is not the case with the assumed angular momentum distribution according to Chapter 5.8.3, then an alternative angular momentum distribution needs to be chosen. A complete profile uses the small available channel height in the best way, and causes the highest volume flow at a relatively low dissipation.

We can now finally determine the required relative angles of the flow in the rotor exit according to equation 5.54, so that upon verification of the total specific blading work and taking into account of angle excess, we obtain the blade structure angles of the rotor.

5.8.6 Subsequent calculation of the total specific blading work

Except for the RV pump angular momentum distribution discussed in Chapter 5.8.3, $c_u=B/r$, an additional calculation is required, where the following applies:

$$a(r) = \text{const.} = y_{sch}.$$

In all other cases, the actually transferred blading work must be additionally calculated following the calculation of the axial speed distribution. Similarly to equation 5.44, it results in:

$$y_{sch} = \frac{2\pi}{\dot{V}} \cdot \int_{r_i}^{r_a} a(r) \cdot c_a(r) \cdot r \cdot dr.$$

(Equation 5.71)

Since this integral cannot be solved either, we again perform summation of k partial works:

$$y_{sch} = \frac{2\pi}{\dot{V}} \cdot \sum_{i=0}^k [\bar{a}(r) \cdot \bar{c}_a(r) \cdot r \cdot \Delta r] = \frac{2\pi \cdot \omega}{\dot{V}} \cdot \sum_{i=0}^k [\bar{c}_u(r) \cdot \bar{c}_a(r) \cdot r^2 \cdot \Delta r].$$

(Equation 5.72)

The difference between the total specific blading work calculated this way and the target values from Chapter 5.8.1 should not exceed 5%. Otherwise, it is necessary to choose a new angular momentum distribution according to Chapter 5.8.3.

5.8.7 Angle excess and blade structure angle β_2

Due to the distance at the end of the blades in the peripheral direction, the flow does not exactly follow the blade contour, but experiences slip. For fluid elements in the middle of the blading channel, it becomes particularly strong. To make possible using the calculated flow angles in the pump in average over the perimeter, the blade structure angles β_2 in the rotor exit must be chosen bigger to take into account the expected slip. An assessment of this angle excess is only possible based on potential theoretical connections, disregarding viscosity, so that the actual situation in the pump in question may be reflected in a very inexact way. However, the flow visibility results according to Chapter 7 show a good correlation, which can be best demonstrated using the incidence free stator flow in the LV pumps for the design point.

The angle excess based on the division at the end can be determined according to /Gallus 1992/, pages 36 – 39, TAM-B-61a. The actual angle distribution based on the blade thickness at the end is no longer required, since this effect has already been taken into account in equations 5.53 and 5.54. For z rotor blades and a rotor length L , we obtain the following division relation:

$$\frac{t(r)}{s} = \frac{2 \cdot \pi \cdot r \cdot \sin\left(\frac{\beta_1(r) + \beta_2(r)}{2}\right)}{z \cdot L}$$

(Equation 5.73a)

Together with middle incidence free flow angle:

$$\gamma_{\text{mid}} = \frac{\beta_1(r) + \beta_2(r)}{2}$$

(Equation 5.73b)

we can now obtain the angle excess factor μ from Figure 5.14 and calculate the blade structure angle β_2' with the help of the angle excess δ :

$$\beta_2' = \beta_2 + \delta \quad \text{with} \quad \delta = \frac{1-\mu}{2 \cdot \mu} (\beta_2 - \beta_1)$$

(Equation 5.73 c,d)

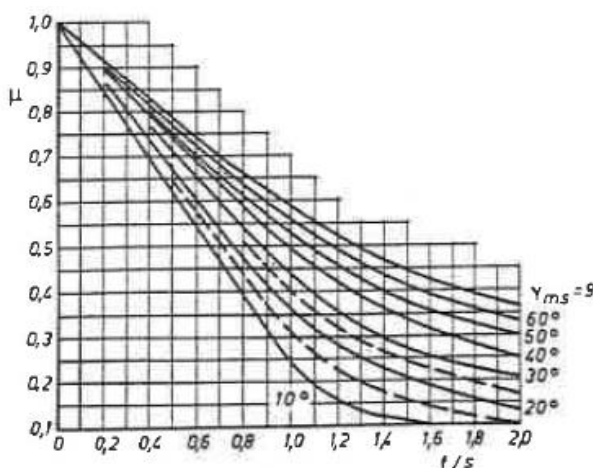


Figure 5.14 Angle excess through division at the end in incident free flow /Gallus 1992/

The dotted line shows here the sought blade structure angle, while the regular line shows the previously calculated flow angle. For the first angle, there is the condition that it cannot exceed 90° according to Chapter 9.2.1.

To calculate β_2' , we will assume, similarly to the radial balance in the LV pumps, that the flow lines are parallel to axis, so that the thickening of the hub is considered here to be negligible. The length L of the rotor was chosen in all pump versions in such way that the separation ratio from equation 5.73a equals $t/s \approx 0.8$. According to Chapter 9.2, this is a good point from the axial enthalpy curve, lengths of the fluid flows along the blading and blockage.

5.9 Calculation of the guide wheel angle

The function of the stator is to transform the kinetic energy of the fluid rotation into additional pressure. In case of the RV pumps, the peripheral speeds are small based on the comparatively low required pump capacity. The possible additional pressure in stator can therefore only be low. It must even be assumed that the losses due to blockage of the guide blade in the highly viscous medium in question are higher than the possible use. Therefore, the RV pumps were constructed without the stator from the very beginning. It is not the subject of this discussion, to which extent to total portion of fluid rotation dissipates or is transferred into additional pressure even without a stator.

To identify the relative pressure portion of the stator in the total pressure, we will determine the reaction degree τ as the ratio between the additional pressure in rotor and the total pressure difference over the pump (with stator):

$$\tau = \frac{P_3 - P_0}{\Delta p_{\text{pump}}} \quad \text{and} \quad \tau \approx 1 - \frac{y_{sch}}{2 \cdot u(\bar{r})^2} \quad (\text{Equation 5.74 a,b})$$

It can be roughly assessed according to equation 5.74b /Pfleiderer and Petermann 1986/, page 53. For the RV pumps, we obtain the following reaction degree:

$$\tau \approx 83\%_{\varnothing 5,0-Pumpe}; 86\%_{\varnothing 6,0-Pumpe}; 87\%_{\varnothing 7,4-Pumpe}$$

and for the LV pumps, correspondingly:

$$\tau \approx 55\%_{\varnothing 5,0-Pumpe}; 60\%_{\varnothing 6,0-Pumpe}; 63\%_{\varnothing 7,4-Pumpe}$$

Already these values demonstrate that the large portion of the additional pressure in the RV pumps is obtained in the rotor. Figure 9.15 gives an idea of the extent to which LV pumps can do without a stator. A final solution can only be obtained from the hydraulic measurements in pulsating environment with physiological pressures.

The entrance angles in stator are calculated for the LV pumps in such way that the flow to the stator blades is incidence free:

$$\tan \alpha_4(r) = \frac{c_{a,4}(r)}{c_{u,4}(r)} \quad \text{with:} \quad c_{u,3}(r) = c_{u,4}(r) \quad \text{and} \quad \frac{c_{a,4}(r)}{c_{u,3}(r)} = \frac{2 \cdot \pi \cdot r / z_{sch}}{2 \cdot \pi \cdot r / z_{sch} - s / \sin \alpha_4(r)} \quad (\text{Equation 5.75 a,b,c})$$

The pressure increase in the guide wheel as the result of removal of the peripheral speed component makes the border layers thicken very quickly already at the beginning of the guide blade channel, since, contrary to the rotor, the border layers are no longer centrifuged by rotation. This additional narrowing

of the flow cross-section makes the axial speed in the entrance of the guide blade channel somewhat higher according to equation 5.75c, taking into account the blade thickness at the end. Therefore, similarly to the entrance of fluid in the rotor, we assumed an additional average breast incidence of 2° .

The exit angle α_5 of the stator always equals 80° - 85° .

The length of the stator in all LV pumps was chosen according to the experimental values and design restrictions between 4 mm and 6 mm.

Summary:

According to the design system described in Chapters 5.3 – 5.9, the blading for the smallest axial and semi-axial flow pumps can be designed with the diameters of 4.8 mm – 7.2 mm for viscosity of the pumped fluids of 3.0 – 4.0 mPa. This completely describes the blading, with the exception of the axial enthalpy distribution according to equation 6.1, and can be combined with the milling manufacturing in Chapter 6.

6. Creation of the blading components

We will omit presentation of the technical production aspects required to manufacture the total system of an intra-vascular micro-axial pump /Rosarius 1994/, and use the computer supported manufacturing of the blading components instead. We will also omit the description of the software used and its features.

The structures described below with dimensions in millimeter order are produced using the precision engineering methods. The production methods of micro technology cannot be used here, because the structures in question are approximately three orders to large.

6.1 Determination of the axial enthalpy distribution and CAD/CAM creation of the blading components

Creation of the blading components is based on the blade structure angles calculated in Chapter 5, meridian grid length L and hub curves. Merely the total wrap angle of the grid and the axial enthalpy distribution are first determined through the grid parametrization over the radius. This should produce the geometries that need to be manufactured.

Basically, the goal is a linear enthalpy distribution, where the rotor entry angle is transformed linearly into the exit angle, with mostly constant curvature according to equation 6.1, depending from the coordinate x, which coincides with the rotation axis:

$$\beta(x) = \frac{\beta_2 - \beta_1}{L} \cdot x + \beta_1 \quad (Equation 6.1)$$

To obtain a straight line entry edge, the wrap angle is set to be zero over the radius at the beginning of the blade. If as the result of the linear enthalpy distribution we obtain at the end of the blade a very difference wrap angle over the radius in excess of 10° , then the enthalpy distribution shall be weighted accordingly in order to obtain at the end a blade, which is not strongly tilted in or against the direction of rotation, seen with respect to the hub, and not twisted in the radial direction.

The geometry of a blade chord plane obtained in this manner is produced by CAD tool. The final thickness of the blade was obtained by a plane projection orthogonal to the chordal plane with a defined offset distance. Since the experiments show that such small pumps require very thin profiles in order not to narrow the flow cross-sections, which are already very small, we do not perform a blade profiling. The constantly thickened chord plane is only rounded at the incoming and outgoing flow edge. Even the rounding between the blade and hub can be omitted, since this automatically happens due to the relative size of the ball nose. The blade produced this way is rotated and duplicated, according to the required number of blades, on the hub designed as a rotation plane, so that we obtain a complete blade channel. The sculptured surfaces of a channel can now be added to the milling manufacturing (CAM).

Figure 6.1 a,b shows the principle of the milling path. Limiting and guiding lines are added here to the blade surface, and between such lines the NC module generates single milling curves in the 2.5 dimensional mode with three tool axes or in the 3 dimensional mode with 4 to 6 axes, taking into account the milling geometry. These tool paths can be immediately used for manufacturing upon preparation for the respective machine control.

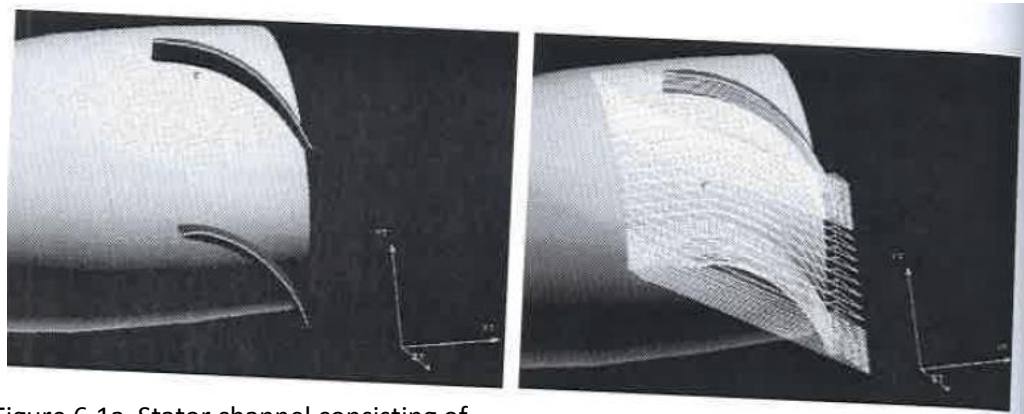


Figure 6.1a Stator channel consisting of two blades and one hub, where the milling area is shown by guiding lines (light) and the limiting lines going beyond them (dark).

Figure 6.1b Stator channel with a roughing tool generated in the milling area. The side offset visible here between the paths provides the rest roughness constant in the area.

6.2 Production aspects and process parameters

The use of milling production as the last metal removing procedure in the production process is the prerequisite for production of small three-dimensional structures of the blading components.

Since the repeated clamping of the structures generated upon the milling production is no longer possible, the rotor or stator blank must already have all the necessary functional connections. They must be designed in such way as to enable an exact position secured against twisting for the milling processing shown in Figure 6.2. This requires joining surfaces on blanks that would allow for position tolerance < 0.01 mm of the blank with respect to acceptance. Securing of the blanks against twisting at acceptance is ensured by a 2 component epoxide glue. Upon the processing, the prepared part is deformed in a thermic way, and the surfaces of the blades are manually prepared with polish from dental accessories.

All blading components were made of brass, since the requirements to the production are simpler. This way the metal cutting can be performed with low rotation speed $n < 5,000$ turns/min, which can be

achieved by most milling spindles, without causing strong displacement or even breakdown of the 1 mm radial mill by the produced forces.

To produce blading components from biocompatible materials, only metals can currently be used due to their thin walls and the possibility of subsequent manual polishing. Production of parts from pure titanium proved to be feasible. However, this requires using of a high frequency spindle with the rotation speed of up to $n = 80,000$ turns/min, since the cutting speeds of > 2 m/s must be achieved.

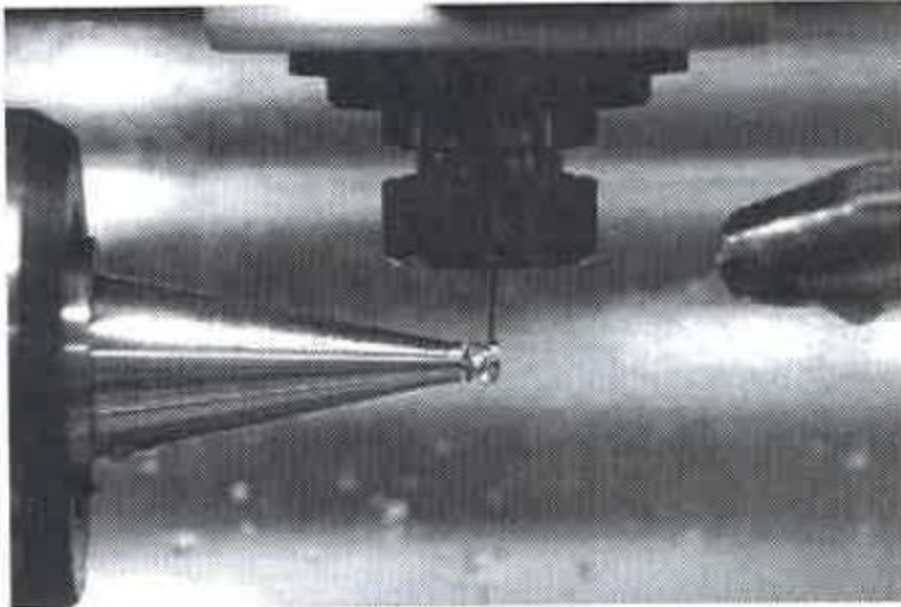


Figure 6.2 Rotor on milling with 1 mm radial mill during production

Figure 6.3 shows a choice of the blading components manufactured so far.

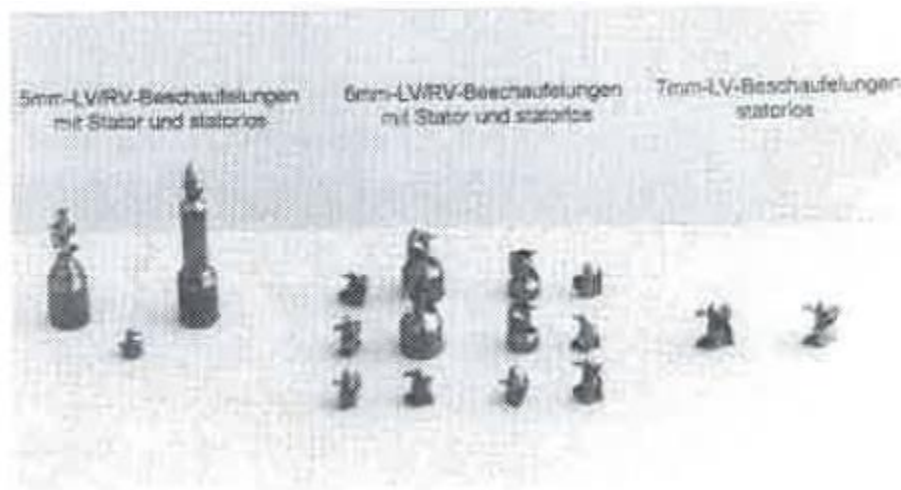


Figure 6.3 Rotors and stators of brass and pure titanium

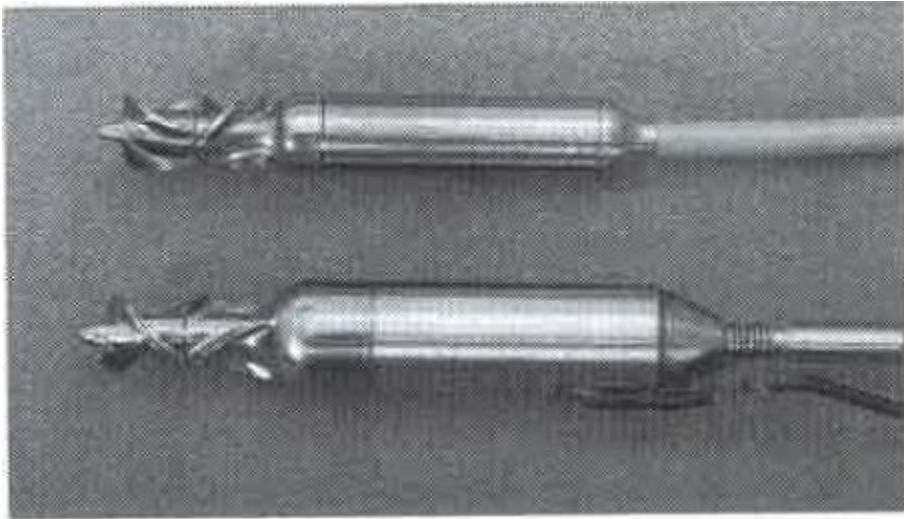


Figure 6.4 6.4 mm drive with blading (above)

8.5 mm drive with blading (below)

Figure 6.4 demonstrates complete 6 mm systems consisting of pump and drive without a pump cover and suction tube.

The 8.5 mm drive shown here corresponds to the modular lab drive shown in Figure 4.8, while the 6.4 mm drive is already reduced to the final dimensions for the first in vivo applications. The motor cables are brought here past the back bearing directly to the inverse guide catheter.

7. Experimental Flow Visualization in Micro-Axial Pump Blade System

Further to the theoretical foundations of the design in Chapter 5 and to the technical realization in Chapter 6, what follows now is a flow analysis by way of select blade system components, assisted by adapted analysis procedures. In Chapter 5, the principal iterative procedure for designing an axial turbo machine was outlined. At this point we can therefore dispense with the interactive processes of experiment, analysis, and new calculation, which are required in the context of flow improvement, in favor of the experimental results and variations according to the design parameters from Ch. 8.2 and Ch. 9.2.

The flow analysis of existing blade system components can in principle be done either experimentally or with computerized support. The latter makes sense only when extensive experimental data are available. Accordingly, in the framework of this project, the flow analysis is done only by means of flow visualization methods which are adjusted specifically to the dimensions of the pumps and the high rotation speeds, and which are meant serve as a foundation for further flow simulations. In this context, the methods used (light section and tracer methods, particle tracking in the rotor by means of high-speed video, washing method, explicit current filament method, color injection) are described, characterized in view of the expected outcomes, and used for the evaluation of an exemplary \varnothing 6 mm blade system.

For hydraulic improvement, apart from flow control within blade system, peripheral flow events such as inflow and outflow are also examined and characterized by means of appropriate methods.

With respect to the blade system, it must be examined in the context of the flow analysis to which extent the flow in the rotor enters free of incidents and follows the contours of rotor and stator blade system without the occurrence of flow separation, and consequently, recirculation regions, and whether the transfer of the flow from the rotor to the stator is free of incident. Moreover, the operational behavior of the examined pumps outside of the operating point must be characterized in flow terms, since the pumps run only periodically in the operating point. Longer-lasting deviations from the operating point may not lead to stationary flow separation inside the pumps, however, since otherwise there would be a risk of a thrombocyte agglomeration in the stationary recirculation regions.

7.1 Experimental Flow Visualization in Micro-Axial Pump Blade Systems

The flow visualization methods described below are discussed only in the context of the field of application and - when necessary for a better understanding, by way of the example of the \varnothing 6 mm LV pump, used throughout this study. The methods are characterized here in terms of their function and their expressiveness, whereby the interfaces between the methods are given specific attention.

7.1.1 Light section and tracer methods

In a light section process, preferably spherical particles of a similar density are added to the fluid, which either strongly reflect the incoming light, or emit energy at a different wavelength within the visible spectrum (fluorescent particles).

The part of the pump that is being examined is lit during operations with a slit lamp at various parallel levels, so that the particles passing through the light slit leave behind tracers which reflect the local flow field from the perspective of a stationary observer.

The analysis of thus-obtained flow measurements shows to which extent the flow follows the calculated pump contours. It can also be shown whether the calculated inflow and outflow angles of rotor and stator blade system correspond to the experimentally obtained results. The length of the tracers for a known exposure time also provides an impression of the speed distribution in the respective light section.

The generation of a light section by means of a pulsed laser in combination with coupled computerized analysis of the particle points is generally referred to as Particle Image Velocimetry (PIV). This method depends on the generation of a clean light section, and can be used in a model enlarged at a scale of 10:1 of a micro-axial pump as described in Ch. 7.3.

However, this method is not suitable for flow visualization in micro-axial pumps in the original size according to Ch. 7.4, since thin light planes cannot be generated cleanly due to the refraction effects on the strongly curved surfaces. Like the pump dimensions, the flow is strongly curved, so that light sections are unsuited for tracing particles which are only briefly present in the light slit. Preliminary attempts to apply the PIV method with a light slit and a pulsed laser failed not only due to the strong curvature of the particle trajectories, but also due to the insufficient ability to assign the particle points. Attempts to filter out refraction and reflection effects by means of the use of fluorescent particles showed that the intensity of the light emitted by the particles when used with a He-Ne laser was insufficient to produce light points or tracers that could be analyzed.

Accordingly, instead of the light section method, the tracer method was used, in which a light source is used to illuminate the entire flow region. When a video camera is used, this method is suitable for evaluating the total flow in a stationary system. However, a computerized analysis is no longer possible due to the lack of depth information from the two-dimensional image with the flow lines crossing each other in the projected image plane. When selecting the particles, it should be observed that the particles be as small as possible (10 - 300 μm in diameter) and globular in shape. The particle movement in the fluid is not only translational but also rotational. Therefore, if globular particles are used, this ensures that any incoming light rays are reflected at all times and in the same intensity.

For usable test results, apart from the right particle selection, their concentration is significant as well. If the concentration is too low, only few flow lines can be traced, resulting in a fragmentary image of the flow. If, on the other hand, the concentration is too high, there will be too much overlap between the individual particle traces, rendering an unambiguous allocation impossible.

With this modified method, there is a possibility to make qualitative statements about the local speeds based on individual particle traces. If a particle moves at a low velocity, it appears brighter on the image than an image with a higher velocity. It must be considered, though, that the brightness of particles also depends on the distance from the hub. Particles closer to the hub tend to be less bright due to the absorption of the light by the fluid.

If the particle traces in the stator show a flow line in relation to the blades, this is not the case in the rotor, due to its rotation. Instead, one can see the absolute flow line, which allows for conclusions on local accelerations. The goal should be an acceleration distributed evenly over the entire rotor, which manifests itself in a harmonic flow with a largely constant curvature of the particle trajectories.

One problem with the application of the tracing method is the slowness of the particles. This fact may distort the results specifically in areas of high acceleration, since in those areas the particles may not be able to follow the flow sufficiently. Despite small component diameters, the fluid is subject to high acceleration especially in the rotor due to the high rotation speeds. This is a reason that the particle size was reduced from 200 - 300 μm originally to 10 - 20 μm . The latter particles do not allow for a representable documentation of the flow field, but

they are only larger by a factor of 1/3 than the erythrocytes, wherefore they may be expected to show a similar flow behavior.

7.1.2 Particle tracking

As compared to the tracing method, the particle tracking method in the form described below allows for first quantitative statements about trajectory curvatures in relation to the rotating rotor blades, as well as first statements about the speed profiles and shear stress values in the rotating channel of the real-size micro-axial pumps. This method is based on the tracing method, except that the rotating blades and the particles are displayed sharply from image to image due to the short exposure times and the high frequencies of the imaging media. If, for instance, a particle is tracked across multiple images, and its position is calculated with respect to the original image, for example, the projected trajectory curve of the particle in relation to the channel is obtained. On the other hand, a comparison of two sequential images allows for determining the local speed of the particle. Depending on the number of particles observed this way, one obtains a speed profile over the entire flow channel. The latter allows for first statements about the development of the Newtonian shear stress, and consequently, about any blood damage that might be expected according to Ch. 8.1 and 8.2.

Due to the light source necessary for illuminating and the only two-dimensional imaging process, this method too lacks depth information. The latter can be determined only inaccurately from measurements of the particle's distance from the hub, or the housing, respectively, or from the resulting particle trajectory curves projected onto enveloping surfaces of varying radii. From thus generated trajectory curves of a single particle onto multiple enveloping surfaces, the probably correct height of a particle in a channel can only be established because intersecting trajectory curves of different particles can be excluded on an enveloping surface, so that in an overall view of the flow field, an approximate allocation is possible.

Imaging media and systems comparison:

The Kodak EktaPro (model 4540) and NAC Ultramac (model RS-501) high-speed video systems were used.

The Kodak EktaPro high-speed video system offers up to 4,500 full images per second with a resolution of 256 x 256, and up to 40,500 partial images per second with a correspondingly lower resolution at apparently random partial image formats. In partial image mode, either 9,000, 13,500, 18,000, 27,000, or 40,500 images per second can be recorded. The exposure time of the images in this case is reciprocal to the partial image frequency. The data generated from the images are stored by the system in a dynamic random access memory (DRAM). This memory can be copied at varying image refresh rates onto a standard S-VHS video tape, with a target resolution of 256 x 256 pixels per image, and where every individual pixel has an 8-bit grayscale depth. A digital output possibility is not provided, so that in case of a demand, a retroactive digitalization of the individual images is required.

The alternatively used NAC Ultramac system is a programmable image convertor camera with per image individually adjustable dark and exposure times.

The high-speed system provides between 8 and 24 individual images at an adjustable recording frequency from 2 kHz to 20 MHz. The pixels of the exposed CCD chip were digitally stored, so that the images are directly available for further analysis by means of image-processing software.

Number of individual images	Resolution
8	390 x 280
12	260 x 280
15	260 x 230
18	260 x 190
24	260 x 140

Table 3: Resolutions of the NAC system

In this system too, the image resolution is linked to the number of images according to the table above. With a CCD total resolution of 1152 x 790, it still amounts to approx. 260 x 140 in the 24 image mode, which corresponds to almost a full image in the EktaPro system. Therefore, while the image frequencies and exposure times are clearly more flexible in the NAC system, the system is limited by its very low number of images.

A direct systems comparison with respect to the present field of application shows that with an operating speed of $n = 30,000$ rpm of the exemplary $\varnothing 6$ mm LV pump blade system used throughout Ch. 7, shutter speeds of $t < 1/18000$ are necessary for obtaining sharp images of the particle and the rotor contours. In the respectively required partial image mode of the EktaPro system, the image section is already so small that due to their size, format, and their reduced resolution, their analysis requires considerable effort.

As can be seen in image 7.1, qualitative statements about the flow can be made because the particles added to the flow are clearly visible. If the "current" image is used for the evaluation of the flow, very good results can be obtained, because the total flow can be monitored almost three-dimensionally. For the purposes of analysis, however, one must depend on human cognitive abilities. A quantitative analysis of the images in view of local speeds and shear stresses cannot be done consistently.

Contrary to the Kodak EktaPro video system, in the NAC system, the exposure time is independent of the image frequency. The exposure and illuminance times are selected so that a flow channel of the rotor in the course of a 24-image sequence passes once through the recording area according to image 7.2. The time and local movement sequence of the flow is exemplary shown in image 7.2 by way of small particles of a size of 10 - 20 μm , in which the numbers indicate the image frequency.

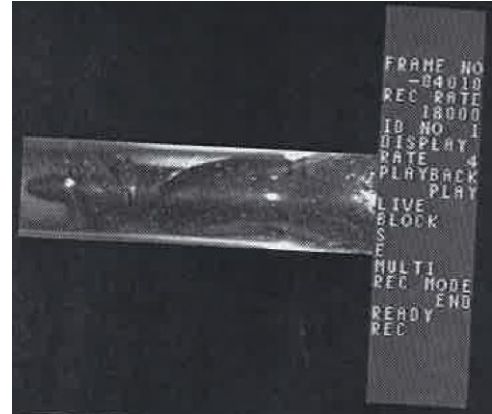


Image 7.1: Flow image recorded by means of a Kodak EktaPro at $t = 18,000/\text{s}$

By tracking and back-transformation to an initially recorded image, based on the underlying and subsequently described enveloping surfaces, it is now possible to establish the trajectory curve of an individual fluid element in the flow, according to Images 7.3 through 7.5.

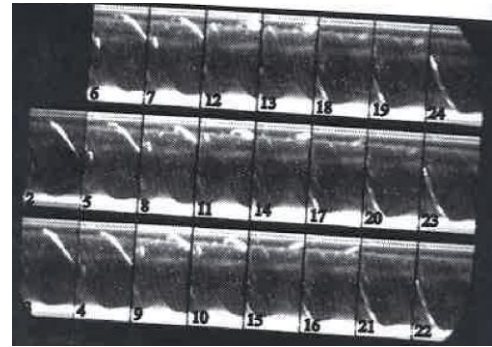


Image 7.2: Image of the rotor of a 6 mm LV pump, recorded by means of a NAC Ultramac; $V = 3.1 \text{ l/min}$; $\Delta p = 100 \text{ mmHg}$; $n = 30,000 \text{ rpm}$

Image analysis method

In order to obtain trajectory lines in a single image, the particle, or respectively, the rotor rotation must be eliminated. For these purposes, templates of enveloping surfaces are needed, into which all positions of a single particle from consecutive images can be entered, so that “rotational trajectory lines” of the flow particles are obtained. The reentry of the particle movement to a moveable coordination system means in practice a back-rotation of the rotor or of the “rotational trajectory lines” of the flow particles by a certain amount, relative to a fixed set reference image. The time interval from image to image of, for instance, $t_{\text{interval}} = 35 \mu\text{s}$ at a rotor speed of $n = 30,000 \text{ rpm}$, due to the rotor movement, leads to a rotation of the particle of 0.0175, multiplied by the periphery on whose radius the particle is located. This leads to an equation for determining the peripheral trajectory s_i by which a particle point of the individual image i must be turned back, in relation to the initial image i_0 :

$$s_i = n \cdot t_{\text{interval}} \cdot 2 \cdot \pi \cdot r_i \cdot (i - i_0) = 0.0175 \cdot 2 \cdot \pi \cdot r_i \cdot (i - i_0) \quad (\text{Equation 7.1})$$

in which r_i is the radius of the circular cross section on which the particle is moving. If on the template one draws a line perpendicular to the pump axis through the point which in image i marks the location of the particle, this line intersects with the flow line delineating the enveloping surface. If a perpendicular line is now drawn from this intersection to the ordinates, the value of r_i can be read.

The required templates represent flow lines for a meridional flow on concentric enveloping surfaces to the rotor axis of the micro-axial pump. Templates are made for near the hub, the middle of the channel, and near the housing, in order to allow for a discussion of the absent depth information according to the description above. Image 7.3 shows an exemplary individual image from Image 7.2, focusing on an enveloping surface near the hub. The determination or calculation of the meridional flow lines of each enveloping surface is done from rotor entry to exit at five explicit positions relative to the rotor axis. The distance between the positions in an axial direction in this case is 1 mm. At the respective locations, the known pump dimensions were used to determine the free flow cross sections. If ideal flow control in the rotor is presumed, a particle which is in the plane-oriented middle of the free channel cross section when entering the rotor must also be there when exiting the rotor, to the extent that no fluid exchange exists orthogonally to the imagined cross section-oriented enveloping surface. This presumption, which is necessary for the analysis, disregards the spiraling channel swirls, which must be considered in principle.

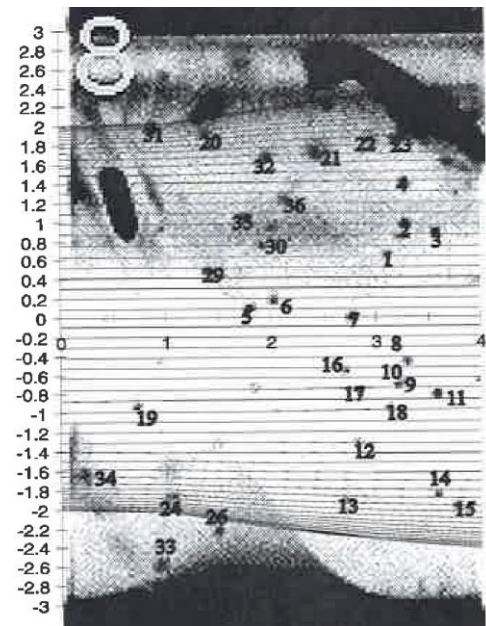


Image 7.3: Eighth image in inverted mode with an enveloping surface near the hub, with numbered particles.

The desired template of the enveloping surface is therefore obtained if the following considerations are implemented, and when the supporting points resulting from the resulting described five positions are connected to form meridional lines:

If, on a half circumference of a circular cross section starting from point $x = 0, z = R$, markings are made at a distances of 0.1 mm, these may be projected into the $y-z$ plane according to image 7.4. The larger the diameter of the circle, the closer to each other are the correspondingly projected points in the range of $z = R$.

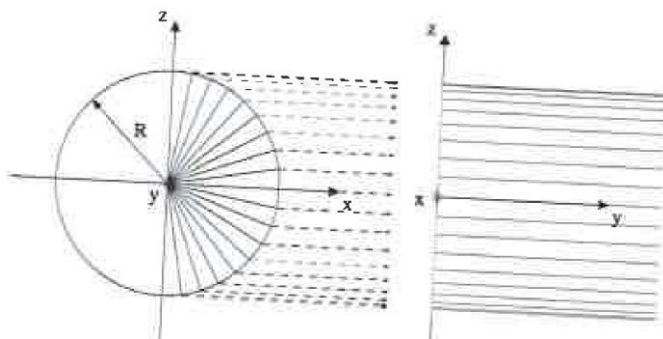


Image 7.4: Projection of markings on the circumference of a circle

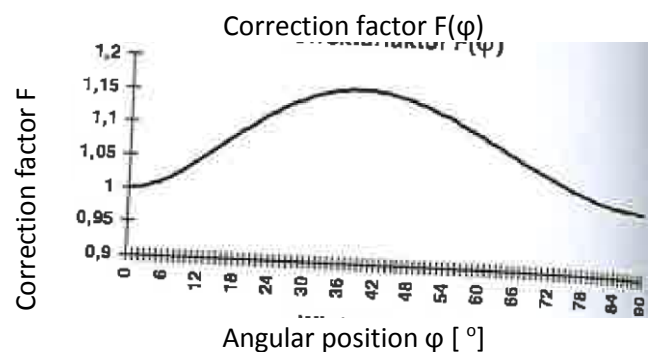


Image 7.5: Correction of the refraction-induced angle distortion

For a correct back-transformation of the particles, a correction of the enveloping templates from Image 7.4 is necessary as well. In the present case, if instead of the rotor a cylinder is built into the test rig of Image 7.15, of which the circumference is marked with equidistant lines, the result is a refraction-induced deviation from the projection in Image 7.4 in the image plane of the video system. This is shown in Image 7.5, and leads to an angle-

dependent correction of the enveloping templates. Clear fixed rotor positions can now be back-transformed after an optical correction of the templates congruent with explicit particles. The results of this process are represented in detail in Ch. 7.4.2.

7.1.3 Washing method

In this process, the parts of the model that are subject to examination are uniformly coated with a high viscosity non-hardening color film that is insoluble in water. Depending on the wall shear stress and the operating time, this color film is washed out to different degrees, so that qualitative statements about the wall shear stress distribution can be made. Correspondingly, this method allows for determining eddy water and recirculation regions as well as flow lines immediately adjacent to the wall, which is important for determining the secondary flow close to the wall in the rotor and the stator according to Image 7.6. This process complements the methods from Ch. 7.1.1 and 7.1.2, which do not provide much information about [the flow] adjacent to the wall.

Likewise, the washing method is suitable for determining the flow contraction, possibly in the event of separation at the inlet, and for characterizing the drain of fluids from the pump along the motor. In blood pumps, due to the risk of formation of blood clots, stationary separation bubbles close to the wall must especially be visualized. This method is specifically suitable for this purpose, since it can be used on all surfaces of the system.

By way of color, a four-component lacquer consisting of line seed oil, oxide black, zinc white, and turpentine, a mixture which must be experimentally adjusted in the pump to the respective flow region in terms of its viscosity due to the strongly different shear stress ranges. High wall shear stresses in the original size, as well as the viscosity of the color, which cannot be set arbitrarily high, produced washing times in the range of 30 seconds to 3 minutes, as opposed to up to 60 minutes in the enlarged model. This required that the operating point was reached quickly during the experiment. Long lead times would have left their own mark on the walls, and hence distorted the results.

7.1.4 Explicit current filament method

While the light section and tracing methods as well as the particle tracking method, only the flow in the channel could be analyzed, and with the washing method only the flows close to the wall, this method leads to result for the transition zone between the wall and the flow channel. Immediately obtained are flow lines in relation to the blade or hub contours, without there being a need for an interim step of back-transformation into an original or a location-fixed coordinates system.

For this method, soft filaments were attached to the rotor blade system and to the hub; these orient themselves according to the local current. In order to obtain qualitatively expressive results, short filaments must be chosen, in order to avoid 'straightening' due to wall shear stress caused by the filament itself. Furthermore, it is essential that the filament be sufficiently thin, and be inserted into the flow in sufficiently small amounts, so that the interaction of the filament with the flow will not have a lasting effect on the latter, which would distort the results. Since these are explicit current filaments, the location which they are to examine must be carefully selected prior to the insertion of the filament into the rotor. In order to make the light-colored filament better recognizable in the original size, the rotor itself is coated in matte black paint (RAL 9005).

When examining the rotors in original size by means of filament, the impact of the centrifugal force of the rapidly rotating pump, as compared to that in the enlarged model, cannot remain unconsidered. In the rotational direction, due to their physical connection with the rotor at the adhesion point, the filament has a higher speed than that of the fluid flowing along the blades. Since the density of the filament is comparable with that of the fluid, they undergo a correspondingly stronger force in a radially outward direction than the fluid. This notwithstanding, this method has proven itself to be effective for making qualitative statements about local flow separations, since despite the centrifugal acceleration, the filament does not show a tendency to be drawn by the gap swirl to the opposing side of the rotor. Rather, the filament usually stays in the compartment in which it is attached.

If the pump in the original size is illuminated by a stroboscope which emits light in short pulses at regular intervals, and if the proper time interval between the light pulses is selected, an image is obtained that suggests a non-rotating or only slowly rotating rotor. This can be easily documented by means of a photo or video camera.

7.1.5 Color injection method

The color injection method serves for characterizing the outflow of the fluid from the pump component past the motor that is positioned behind it. For these purposes, a color bolus is injected into the suction tube while the pump is operating. When exiting the pump, the fluid thusly colored can be easily differentiated from the transparent fluid, so that the free jet can be characterized, depending on the position of the pump in the outflow vessel. In addition to the form of the free jet, when the image frequency of the recording medium is known, the outflow speed can be determined based on the drive as well. This is necessary for the approximate determination of the heat transfer from the drive to the fluid flowing by.

7.1.6 Laser-Doppler anemometry

Laser-Doppler anemometry (LDA) is a very elegant method for quantitative and non-interventional flow analysis, to the extent that it can be implemented. In the present field of application, only a Backscatter LDA System can be used that as a matter of principle allows for low data rates of $f_{backscatter} < 100$ Hz. Furthermore, at the prescribed beam distance and focal length of the available 1 channel system, the resulting dimensions of the hyperboloid measurement volume are a length of $l = 0.76$ mm and a diameter of $d = 0.1$ mm, which makes this system unsuitable for measurements in the original size of a micro-axial pump due to the only integrally recordable speeds. Accordingly, measurements were only done in an enlarged model, in which measurements in a rotating system are also bound to a time- and location-wise triggered LDA window, because the data rate does not allow for a continuous recording of speed despite the rotational speed, which is lower by a factor of 100 as compared to the original size.

7.1.7 Recording media and their suitability for documentation purposes

The aforementioned methods for flow visualization can be subdivided in terms of recording media into moving and static [media]. For the latter, which includes the washing method, documentation by means of a conventional compact camera is suggested due to the achievable image quality and the possibility of exposure series. A film

system, whether high-speed or compact camera, can be used in principle in all other cases as well. However, due to the development time of film material and the frequently resulting need to perform a certain experiment multiple times, this is not a pragmatic choice. In these cases, electronic image conversion systems which allow direct control of the results are recommended. This allows for a significant shortening of the iteration steps, at the expense of image quality. Two high-speed systems based on cutting edge CCD chip technology were already suggested in Ch. 7.1.2, and characterized in terms of their suitability.

Since these systems are not generally available, all ongoing flow visualization experiments were done by means of a 50 Hz CCD video camera, the recordings of which can be retroactively digitized for processing purposes as well. The advantages of the tested video system (Canon EX1-HI) are the satisfactory light sensitivity of the high-resolution chip, the high-speed shutter with exposure times from $t = 1/6$ sec. to $t = 1/10,000$ sec., as well as the choice of lenses. By means of an adapter (CANON EOS VL adapter) and a macro lens with a focal length of 50 mm, of which the image scale with respect to the 24 x 36 mm compact image format is 1:1, objects of 5 x 5 mm can be recorded in a frame-filling manner. This is a condition for resolving small particles of 10-20 μm in original-size rotors.

If fluorescent lamps are used for object illumination, the depth of field and the brightness can be controlled by means of the built-in aperture. When illumination is done by way of a stroboscope as required in the explicit current filament method, a synchronization between the image frequency and the light source would be desirable. Instead, due to the lack of a possibility to achieve such synchronization, the flash frequency is set to a multiple of the image frequency, and the shutter time of the camera is selected so that there are no dark phases between successive images. This way, the number of exposures per video half-frame can be controlled manually.

7.2 Secondary Flows

For a better understanding of the complex flows within the curved rotor and stator channels, insights from the literature on turbo machine construction are provided first, adapted to the presently addressed micro-axial pumps (*Gallus, 1992*).

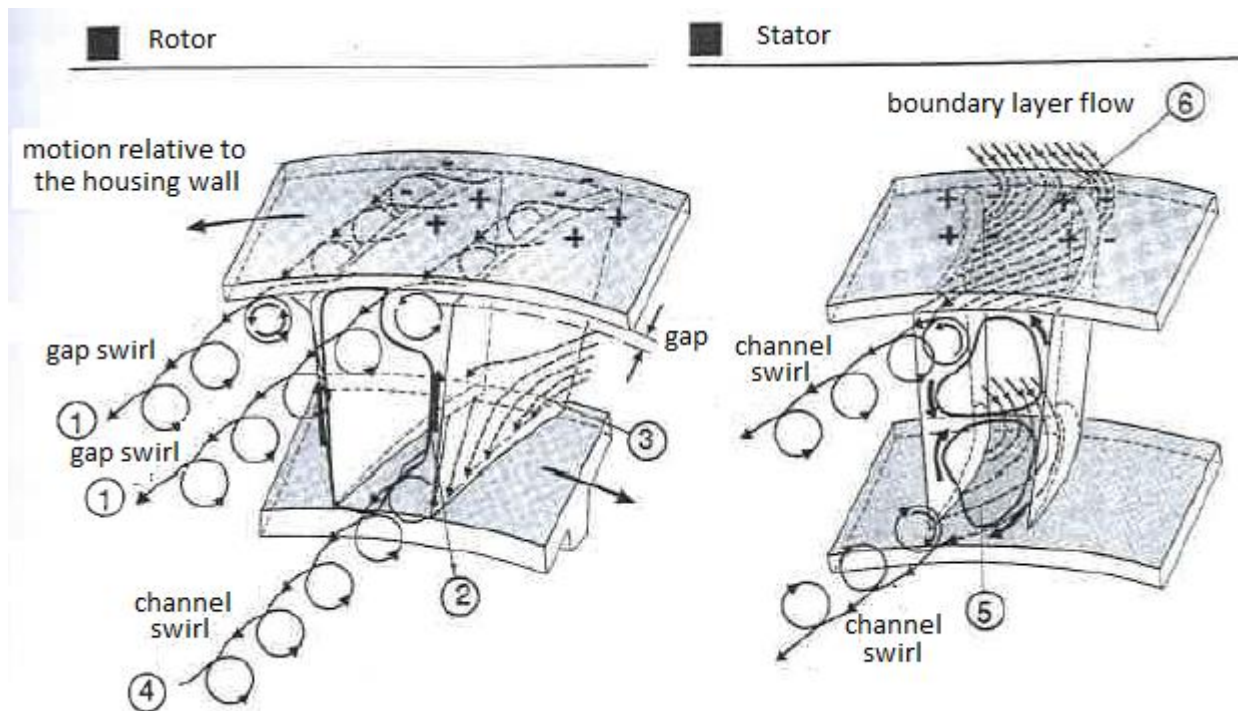


Image 7.6: Secondary currents in axial deceleration grids (*Gallus, 1992*)

As the flow enters into the rotor, a split flow is formed between the rotor and the housing due to the local relative movement there, in consideration of Stoke's wall adhesion and due to the pressure difference between the outlet and the inlet side. This, in turn, induces a split swirl ① on the respective inlet side which, depending on the size of the channel and the viscosity of the fluid, may either be singular as in Image 7.6, or flow directly into a large spiral swirl. The latter may include the entire channel.

In the flow-through direction, a boundary layer is formed on the blade surfaces which loses energy and which may detach as a result of the increased static pressure in the flow direction. The fact that this is not necessarily the case in the rotor is due to the centrifugal acceleration, to which the fluid elements proximate to the blades are particularly exposed, which leads to a situation in which the bigger part of the boundary layer is spun-off outward ②, and moreover, drawn in by the split swirl ①. This interaction makes the rotor less sensitive to separations along the blade system than the stator, given a similar grid load.

The lower axial speed of the fluid elements in the boundary layer close to the hub leads at that location to a wide flow diversion ③. This boundary layer describes a narrower radius, based on the radial equilibrium due to the pressure caused by the channel flow. The associated radial ② and rotational ③ mass transport generates channel swirls ④ which in turn generate narrow flow diversions in the direction of the middle of the channel.

Relative to the micro-axial pump with only two or three blades, a low channel height, a large chord length, and a relatively highly viscous fluid, it must be assumed that not all channel swirls are present locally, but rather, that they combine to form a large spiral swirl, which leads to a wide diversion of the flow near the hub and to a clear narrow diversion near the housing. This narrow diversion is not covered by the narrow diversion resulting from the finite blade division described in Ch. 5.8.7.

In the stator, the low-energy boundary layer generates a wide diversion (radial equilibrium) of the flow near the hub ⑤ and the housing ⑥. To which extent these effects lead to a single large stator channel swirl or to two of them in case of an overlap with the rotor spiral swirl cannot yet be determined definitively. The secondary flow in

the stator channel can be compared with the flow in curved tubes with a rectangular shape according to *Truckenbrodt 1980*. Here too a characteristic double swirl is generated.

7.3 Flow Analysis in an Enlarged 10:1 Model

Due to the small dimensions, the examination of the flow manifestations in LV micro-axial pumps was initially done by way of a model of Component I from Ch. 3.1.3, enlarged at a scale of 10:1.

7.3.1 The test rig and the 10:1 model

The design and the layout of the test rig were done according to the strict specifications in the form of the enlarged pump model, which was laid out according to the theory of similarities.

Initially, the conditions for the similarity between the two systems are found, in order to determine the regularities for the transfer of properties from one system to the other. For reasons of manageability, the index figures within which individual influencing quantities of the system are summarized are stored instead of these influencing quantities themselves. Therefore, also in the present case, all relevant quantities are summarized as known index figures, and the calculation of the model geometries and of the operational parameters is based on these yet to be determined index figures.

In principle, there are two methods for determining the relevant index figures:

- i) A presumption is made that the context subject to the examination can be phrased in terms of physically correct regularities, or in other words, that all relevant quantities are correctly made part of this context, and that not only the numerical values, but also the units of the individual terms are corresponding.
- ii) In order to find the dimensions and the operational parameters that characterize the problem, use can be made of the fact that quantities and reference quantities both use the same measurement units.

In the framework of the dimensions analysis, a set of dimensions and index figures can be derived from the influential quantities that describe the problem which meets the requirement the numerators and denominators or products of powers all consist of quantities with the same dimensions (*Dibelius, 1990*).

According to both methods i) and ii), the system-specific index figures were determined, in consideration of the relevant influencing quantities.

Influencing quantities: $\Delta P \equiv$ Pressure difference over the pump; $\dot{V} \equiv$ volume flow of the pump; $n \equiv$ drive rotation speed; $D \equiv$ pump diameter; $\eta \equiv$ viscosity of the blood or of a replacement fluid; $\rho \equiv$ fluid density; $g \equiv$ gravitational acceleration.

Index figures - In what follows, the Reynolds number (Re), which represents the ratio between the forces of inertia and the frictional forces, will be considered as an essential index quantity [sic] since, as in the present case of small Reynolds numbers (Re: 2000-4000) in contradiction to the values generally found in turbo machines, the impact of friction, and therefore of the boundary layer character of the flow, are immanently important (*Truckenbrodt 1980; Schlichting 1965*). An identical Reynolds number implies similar speed triangles, in other

words, a geometry of the model which is also similar to that of the original, so that the rotor and the stator only have to be enlarged according to the scale.

- The Euler number (Eu) represents the ratio between the pressure compressive forces and the forces of inertia, and allows for making statements about the scale-dependent pressure build-up of the model.
- The Strouhal number (Sr) describes the non-stationarity by way of the characteristic time, or the flow periodicity by means of the frequency, such that the rotational speed of the model can be derived from it (*Krause 1988, Prandtl 1956*).
- The Froude number (Fr) considers the flow-deforming impact of gravity on the flow image when particles are used with a density slightly higher than that of the fluid, which is significant for the enlarged model due to the same magnitude of the angular momentum, axial, and gravity acceleration.

Departing from the index figures, the wanted model data can be determined by means of the requirement “model index figure = original index figure”. Not all index figures can be maintained simultaneously.

In first instance, the Reynolds (Re) equality must be maintained. From it, the maintenance of the Euler number (Eu) and the Strouhal number (Sr) follows without contradiction. The Froude number (Fr) is contradictory, however, so that it can only be considered globally due to the fact that the pump model is operated vertically.

The model parameters thus determined in the design point for operating the model of a Ø 6 mm LV pump with the blade system examined throughout Ch. 7 are represented in the following table:

Scale (M)	1:1	10:1	10:1
Fluid	Blood / blood replacement substance	Water	Blood replacement substance
Mean viscosity (η)	$3.6 \cdot 10^{-3} \text{ Pa} \cdot \text{s}$	$10^{-3} \text{ Pa} \cdot \text{s}$	$3.6 \cdot 10^{-3} \text{ Pa} \cdot \text{s}$
Mean density (ρ)	1059 kg/m ³	1000 kg/m ³	1059 kg/m ³
Internal diameter (D)	6 mm	60 mm	60 mm
Feed length (s_L)	200 mm	300 mm	300 mm
Volume flow (\dot{V})	3 liter/min	8.825 liter/min	30 liter/min
Pressure difference (Δp)	18400 Pa 138.3 mmHg 1877 mm H ₂ O	15.04 Pa 0.113 mmHg 1.534 mm H ₂ O	184 Pa 1.383 mmHg 18.77 mm H ₂ O
Rotational speed (n)	30000 l/min	88.25 l/min	300 l/min

Table 4: model parameters

With respect to the flow-through regions, it was ensured that the enlargement from the original was true to scale. An essential construction feature of the test rig according to Fig. 7.7 is the receptacle above the actual pumping unit, which was made to resemble the actual aorta conditions for stationary operation for as much as possible. On the one hand, a diagonal outflow was implemented in a cylinder enlarged according to the aortal cross-section (Reservoir 2), and on the other hand, the flow conditions were made to resemble those in the aorta.

This includes the large eddy at the outflow of the pump, and the nearly axial outflow of the fluid from the container through several overflow slits around the perimeter of Reservoir 2. Due to the fact that the fluid level in the outflow drain is below that of the container, it is further ensured that the external pump as well as the outflow to it do not have a negative impact on the flow image in the container (no overlap between the source flow of the pump with the sink associated with the outflow with the corresponding deformation of the outflow from the pump itself). These sufficiently reconstructed outflow conditions, as well as the transparent implementation of the container and its good accessibility, ensure that the flow is recorded in this location as well.

The problem of the optical refraction and the resulting cylindrical pump casing is solved by means of planar surfaces, which are realized by means of a rectangular “aquarium” filled with water that is put over the casing. Image 7.7 illustrates the integration of the pump model in a suitable test rig which allows for the low pressure build-up of the model, the vertical installation position, as well as the necessary feed length s_L . The driving force for the volume flow through the pump model is the geodetic height difference Δh between Reservoirs 1 and 2.

The external pump only serves here for the compensation of the flow losses in the flow meter and in the recirculation tubes, and in order to set the value of Δh . The advantage of this arrangement is an extensive decoupling of the external pump, of which the dosing fluctuations in the large Reservoir 1 have only an insignificant effect on the geodetic height.

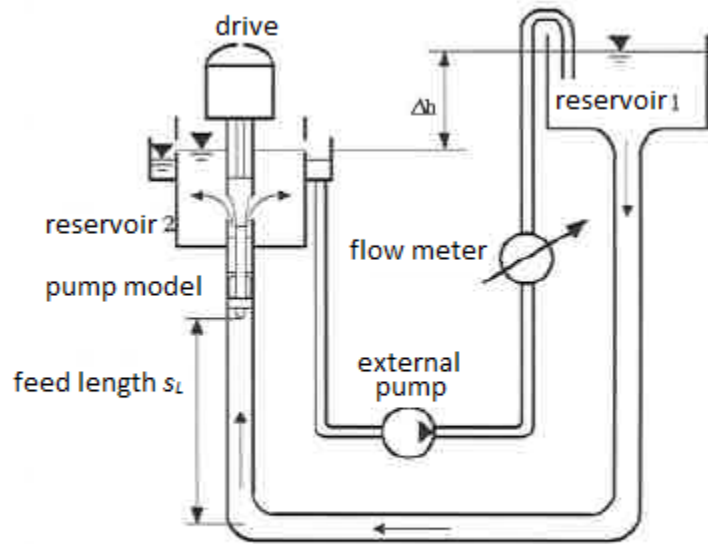


Image 7.7: test rig design with pump model

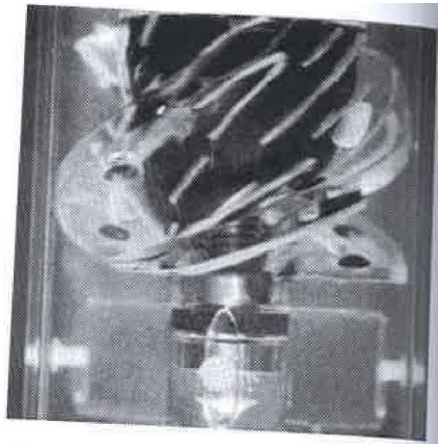
7.3.2 Flow results in the enlarged model

Even though extensive flow testing was done in the upstream pipe, the intake funnel with its profiles, on the rotor, on the stator, and at the outflow along the diagonal shaft end, only the rotor and the stator are exemplarily examined here. The intake funnel, supported by three profiles, only results from the discontinued Component I from Ch. 3.1.3, so that those results are irrelevant for the continued blade system development. The speed measurements performed in the tube by means of the LDA backscatter did not lead to productive insights beyond the discussion on the speed profiles immediately before the hub head and before the beginning of the rotor blades according to Images 5.9 and 5.10, so that a presentation of the measurement results can be dispensed with. It is

worth noting, though, that as early as 35 mm before the beginning of the hub, or respectively, 3.5 mm in the original size, a significant speed reduction can be measured in the center of the tube. The displacement of the flow due to the high viscosity clearly starts upstream from the contour. The resulting delay leads to a slightly thicker boundary layer near the hub. For lack of exact measurement methods in the original size, the thickness of the boundary layer as determined in Ch. 5.6 of $\delta_x = 0.05$ mm immediately near the blades can be sustained despite this understanding.

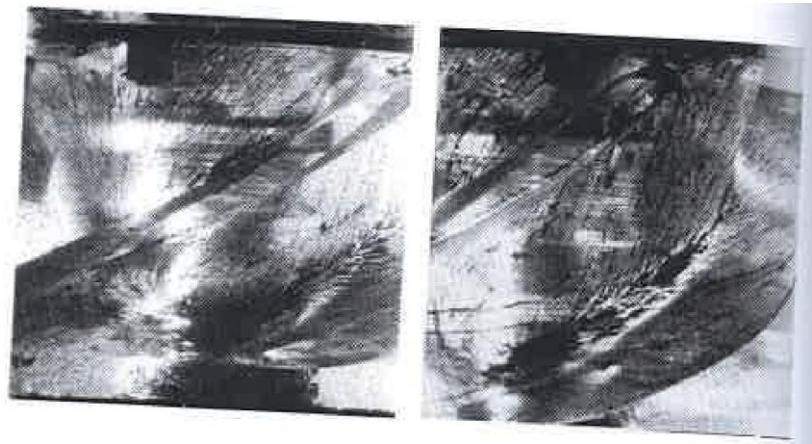
The flow in the rotor:

As previously mentioned, the light section method does not allow for an allocation of the flow lines to the blade system contours, since this is a rotating frame of reference. With this method one can only obtain an impression of the course of the flow through the rotor region against an absolute frame of reference (for comparison, cf. Images 7.10 through 7.12). Images of the flow along the blade contours, on the other hand, can be obtained by means of the current filament and washing methods.



Fluid: blood replacement
Exposure time: 1/1000 seconds
Aperture: 4

Image 7.8: Rotor



Fluid: blood replacement
Operation time: 60 minutes

Image 7.9a, b: Rotor

In Image 7.8, filaments of natural silk of various lengths can be seen on the blades and on the hub, which represent explicit flow lines in the boundary layer adjacent to the wall. The blade current adjacent to the wall thus visualized does not follow the blade contours from the intake to the output side in a parallel manner, but proceeds from the hub with an outward slant due to the spun-away boundary layer near the blades. Near the hub, a strong flow redirection of the current can be clearly observed on the intake side. This is even clearer in Image 7.9b due to the current which is adjacent to the wall in its entirety, as compared to Image 7.8, in which the filaments already slightly reach into the channel as per Ch. 7.1.4. This strong flow redirection on the hub side is the result of a radial equilibrium, as a result of which the slow fluid elements near the hub have a smaller radius than the blade curvature, due to the pressure gradient between the intake and the output side. The aforementioned secondary currents, in combination with the gap and channel swirls and with the lesser flow redirection which increases in strength with the radius, results in a strong spiral swirl. In Images 7.9a and b, a local horseshoe swirl caused by the boundary adjacent to the hub can be observed on the output side at the beginning of the rotor blade. This causes the washing at the hub with a strong flow redirection, which reaches from the base of the blade into the

channel. Moreover, due to its finite thickness, this swirl leads to the less washed-out regions according to Image 7.9b that can be seen downstream from the blade in the base of the blade. Otherwise, the washings at the hub and at the intake and output side of the blade are very homogenous, so that one can presume a uniform wall shear stress distribution in these regions. Moreover, no recirculation areas, swirls, and in particular no eddy regions can be observed.

The flow in the stator

For these purposes, the light section method was used, among other things. The flows were examined in three planes parallel to the pump axis. Each plane was illuminated with a light slit with a width of approx. 3 mm. In each case, only the flow within the light slit of the selected plane was examined. This produced depth information which does no longer exist in the tracer method done on the original size:

Plane 1: flow at the hub, including the boundary layer current

Plane 2: flow at the middle blade level

Plane 3: flow along the blade head, or respectively, near the housing wall.

The images of the rotor in the left half of the images and of the stator in the right half explain how a rotation-free current can acquire momentum between the beginning and the end of the rotor, which is subsequently lost in the stator.

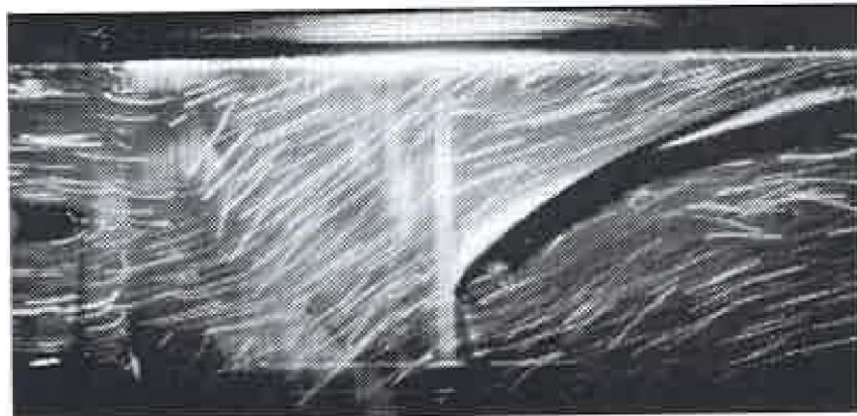


Image 7.10:

Rotor + stator in Plane 1

Fluid: blood replacement

Exposure time: 1.30 sec.; aperture: 2.8



Image 7.11:

Rotor + stator in Plane 2
Fluid: blood replacement
Exposure time: 1.30 sec.; aperture: 2.8



Image 7.12:

Rotor + stator in Plane 3
Fluid: blood replacement
Exposure time: 1.30 sec.; aperture: 2.8

Image 7.10 shows the flow at the hub. On the intake side of the stator, which is visible here, an early flow separation occurs due to the breast incidence caused by the strong flow redirection in the rotor on the side of the hub, but which joins the blade contours again along the intake side. On the output side, the current follows the stator contours. Here too, analogous to the rotor, at the beginning of the blade, signs of a horseshoe swirl beginning at the blade base can be seen.

The more strongly diverted flow lines reaching from half the elevation of the blade on the output side into the channel and the resulting seemingly uncontrolled channel flow are signs of an overlap of a spiral-shaped double channel swirl in the stator according to Ch. 7.2 with the rotor spiral swirl flowing in the opposite direction at the hub. The boundary layer flow near the hub is explicitly described by way of the wash Image 7.13 in the stator.

Image 7.11 shows the main current at half the elevation of the blade. As compared to Image 7.10, the separations on the intake side are no longer visible. Rather, for the design point, the flow is directed at the stator factually incident-free. The irregularity caused in Image 7.10 by the channel and horseshoe swirls almost doesn't exist in the main current here, which leads to the conclusion that the channel swirl does not significantly affect the main current. In contrast, it is noteworthy that elements of the strong flow redirection at the hub can still be observed in the middle of the channel.

Image 7.12 documents the flow adjacent to the housing wall. A clearly visible incidence of recirculation, which follows from the lesser flow redirection based on the finite division, leads to a visible separation on the intake side. In the flow direction as of half of the blade elevation, it settles again. While in an overall view, due to the lesser flow redirection in the rotor, the current flows at a smaller angle than that of the blade construction of the stator, there is a region with flow lines along a diagonal line starting above the blade entry and reaching into the channel, which has an even larger angle. This is an example of the unsteady flow inside the stator, which behaves cyclically due to the finite blade division in the rotor and due to the rotor movement. While the flow close to the rotor blade undergoes a stronger redirection, the flow in the middle of the channel undergoes a lesser redirection. Consequently, the flow along the diagonal line is a region which previously extended along the rotor blade. Complementary to Ch. 7.1.1 and 7.1.3, it now becomes clear that the light section or tracing methods always show only a snapshot of the flow, whereas the washing method shows a flow image averaged over time.

In summary, it can be said that the fluid flows well through the stator, but leaves it with a remnant of momentum. The main current is directed at the stator incident-free, without this leading to major separation incidents. The swirls in the boundary layers have only a minor impact on the main current, because they do not reach significantly into the channel.

Image 7.13 shows the washing traces of the stator after approx. 60 minutes of operating time. It is a global flow line progression of the boundary layer on the hub side straight across the flow channel with stronger local curving radii visible than that of the respective blade contour according to Ch. 7.2. This progression is interrupted by a region with fewer washes, which extends from the beginning of the output side to the upper end of the intake side. While the current enters into the stator, the previously mentioned horseshoe current is generated due to the surface boundary layer near the hub. This means that the current close to the surface on the blade side dives down inward from the middle of the channel toward the hub, creating a swirl or a tunnel. This flow channel extends from the output side at the stator entry to the intake side at the stator exit, without, however, significantly affecting the main current. Due to the generated flow channel, the boundary layer on the side of the hub is drawn away. The horseshoe current is directed exactly at the stator exit on the intake side, and is able to suppress local eddies which are primarily generated in the separation-prone region on the intake side, so that this secondary current effect, which is unavoidable to begin with, can be positively evaluated in the end effect.

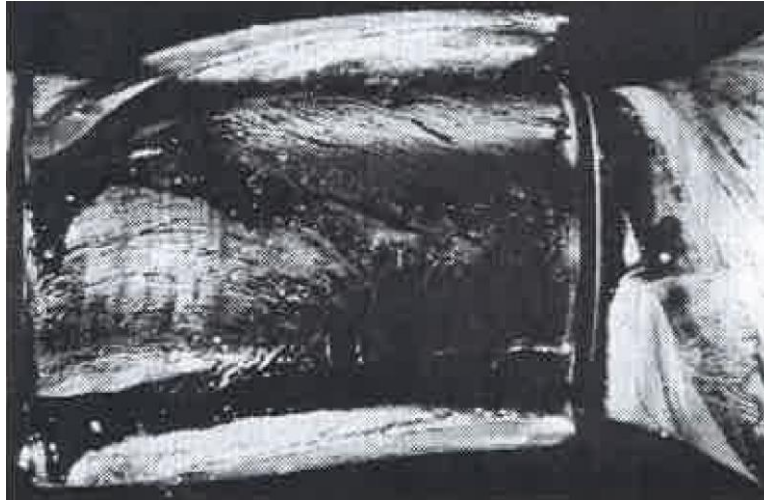


Image 7.13:

Stator

Fluid: blood replacement

Operation time: 60 minutes

7.3.3 Discussion of the informative value of the enlarged model

The results with the enlarged model show a very harmonious flow through the rotor and the stator without significant separations in the design point. The fact, however, that the original blade system in the original size reaches only half the volume at the design point, shows that there must be considerable differences between the model and the original size, which are not reflected in the enlarged model.

While in principle, a similarity of the speed profiles can be presumed due to the identity of the Reynolds number of the model and the original, the impulse losses in viscous media due to turbulent shear stress and the resulting eddy lengths cannot be magnified correspondingly. Furthermore, even in the enlarged model, secondary currents reaching far into the channel can be observed, whose performance-reducing effect can only be evaluated in the original in the form of a quantified lower hydraulic capacity.

All these performance-reducing influences cannot be obtained from the enlarged model, since based on the negligible pressure build-up according to Ch. 7.3.1. and Image 7.7, the model does not pump itself, but receives the flow volume at the design point from outside.

However, if the volume flow at the design point in the original size is set at the design speed and at a low delivery pressure, the flow results of the original will be very similar to those of the model, so that in this case, the results for the enlarged model can continue to be used. The achievable high local flow resolution suggests this anyway.

If, on the other hand, it is possible to document the flow in the original size sufficiently, a flow visualization of the original should always be preferred, since this does not only allow for an evaluation of the flow at the design point, but also allows for an analysis of other operating points. The latter is of great importance for a system operating in a pulsatile environment.

Therefore, flow changes, among other things, can be studied based on different counter-pressures and definition of the cavitation limit only in the original.

7.4 Flow Analysis in the Original Size

In what follows, flow analysis will be done in $\varnothing 6$ mm LV pump blade system, of which the geometry is similar to that of the enlarged model to such extent that comparisons between the model appear to be permissible. There is an essential difference in the used lab model. While the blade system of the enlarged model is integrated into Concept I from Ch. 3.1.3 with the infeed star wheel and the rotating shaft at the outlet side, the blade system in the original size belongs to Concept IV from Ch. 3.2.2. The latter essentially differentiates itself by the spinner which is integrated in the rotor, and by the diagonal exit region with its integrated replacement diffuser. Image 7.14 shows the blade system of the enlarged model with the similar blade system of the original size, integrated in Concept IV (Sieß 1995).

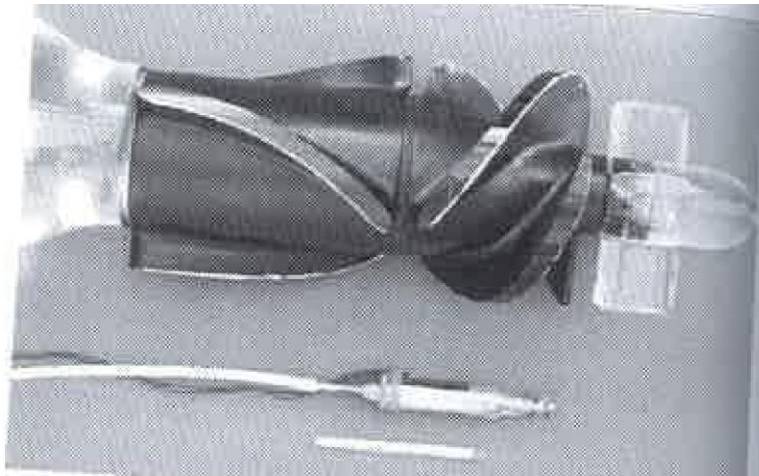


Image 7.14: Blade system of the 10:1 model and in the original size

For the flow examinations in the original size of $\varnothing 6$ mm with $n = 30,000$ rpm, the classical methods such as light section and washing had to be modified, and specifically developed methods as per Ch. 7.1 had to be reexamined for suitability.

7.4.1 Test construction for flow visualization

For the purpose of flow visualization, the pump was integrated into a test construction comparable to that of Image 9.1a. The synthetic PMMA pump casing used here is bounded on the outside by four planes positioned vertical to each other. The flow can typically be observed through one of these planes with negligible optical distortion. That relevant distortions may nevertheless occur which might have a significant impact on the results was already discussed in Ch. 7.1.2 and Image 7.5. However, when there is no need for the flow visualization results to be displayed geometrically exactly on a template, as with the particle tracking method, they can be analyzed without retroactive corrections.

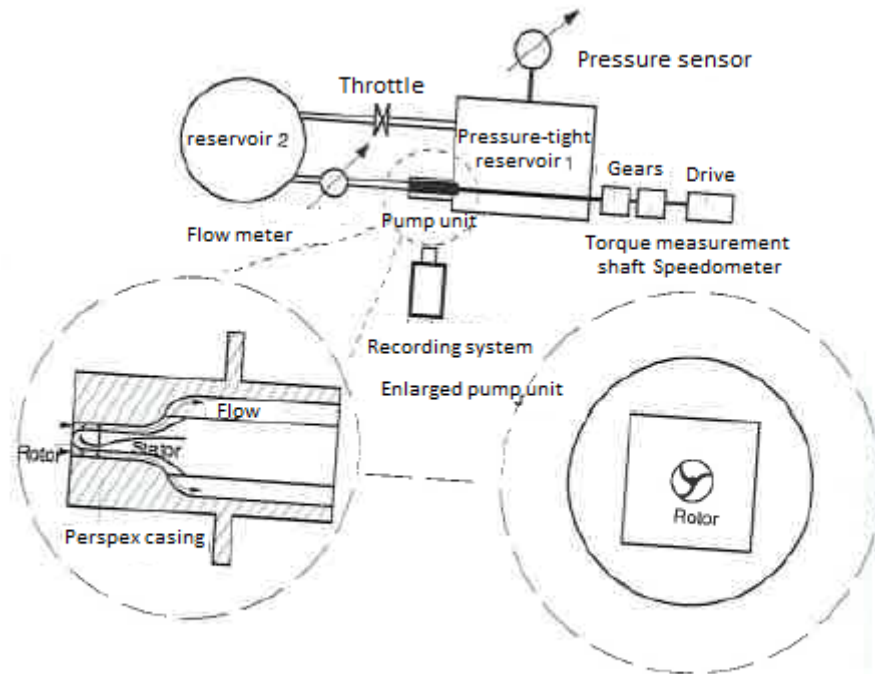


Image 7.15: Flow visualization construction in the original size

7.4.2 Test construction for flow visualization

Image 7.16 shows the wash-outs on the rotor at a counter-pressure of 100 mmHg and $n = 30,000$ rpm. On the intake side of the blade, the radial speed component of the flow adjacent to the wall is clearly visible. Due to the strong reflection from the polished surfaces, the lines on the outlet side, which are radially outward-directed as well, are harder to see.

Like in the enlarged model, the traces in the flow channel indicate a flow from the outlet to the intake side, so that the outflow angle in the lower part of the channel cross-section is larger than that of the blade contour. The reason is the previously mentioned large spiral swirl which results from channel and gap swirls and from fluid inertia, in combination with the strong redirection caused by the radial equilibrium.

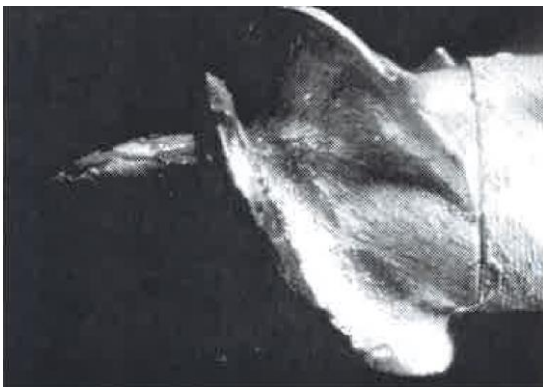


Image 7.16:
The rotor at a counter-pressure of 100 mmHg



Image 7.17:
The stator at a counter-pressure of 100 mmHg

In Image 7.17, which shows the stator at a counter-pressure of 100 mmHg, two things can be seen. The first is that here too, a flow adjacent to the wall can be observed from the outlet side to the intake side. This results from the radial equilibrium for boundary layer flows in curved channels, which has already been mentioned several times, in combination with the horseshow swirl starting from the beginning of the blade. However, the zone of reduced diagonal washing from the beginning of the outlet side to the end of the intake side is clearly less pronounced than in the enlarged model. Noteworthy are also the very different wall shear stresses in the stator. Despite the use of different viscous colors along the outlet and intake sides, the intake side still showed only a reduced washout rate. This is an indication of a thick boundary layer with only small speeds at the wall, and with correspondingly low speed gradients based on the current entering into the stator with breast incidence. This wrong current does not allow for observing a temporally invariant separation along the intake side, however. The washout, in Images 7.16 and 7.17 comparable in strength after an identical operating time, as reached through coatings of different viscosity. The color used in the rotor was about 10 times as viscous as that in the stator, so that without exactly quantifying the wall shear stresses at this location, the wall shear stresses in the rotor are approximately 10 times stronger than those in the stator. A plausible explanation for this significant difference cannot be found in the actual flow through the curved channels of the rotor and the stator, since the flow goes through both regions at similar speeds due to the continuity condition, given comparable surface areas. Instead, the rotation and the resulting boundary layer flows near the wall, together with the internal leakage of which a quantification attempt was made in Ch. 8.1.2, is significantly responsible for the wall shear stresses, which are high, as compared to those in the stator. This system, with its boundary layer spun away along the rotor blades and its gap swirl, leads to high wall shear stresses on the one hand, but supports the washing of all the surfaces, which is extremely important for blood pumps, so that in terms of thrombogenicity, the rotor can be deemed to be less critical than the stator, as long as it does not result in a rotating stall.

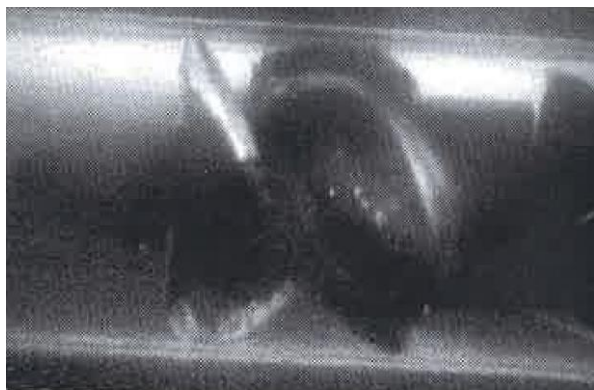


Image 7.18:
The rotor at a counter-pressure of 100 mmHg.
Compartment with three filaments



Image 7.19:
The rotor at a counter-pressure of 100 mmHg.
Filaments on the outlet side moved by the gap
current

Images 7.18 and 7.19 show the same rotor at a counter-pressure of 100 mmHg with the method of explicit current filaments. Connected to it via small adhesion points are three thin filaments, the position of which relative to the blade is visualized during operation through illumination by stroboscope by means of a 50 Hz video camera. Apart from the clearly visible filament on the intake side, two additional filaments can be seen on Image 7.18: one in the rear one-third of the compartment base, and the other on the outlet side of the middle blade. The latter filament begins just behind the brass-colored part of the blade, and ends even before the end of the blade.

In this image it can be seen that the filaments connected to the blade walls follow the contours of the blades, and are diverted along the hub analogous to the washing results. Even after the end of the blade, the filaments retain their flow angle. Furthermore, the filaments split only slightly at their ends, which indicates a low degree of swirling in the trailing range. These are indicators for good flow control at the surface at the rotor, as is also documented by the washing method in Image 7.16. Image 7.19, on the other hand, illustrates a potential disadvantage of this method, which was already discussed in Ch. 7.14. A filament is gripped here by the gap stream, and is pulled from the outlet side of the blade to its intake side. After this point, however, it perfectly follows the flow along the intake side again. A supercritical elongation of the filaments cannot be observed in any of the images.

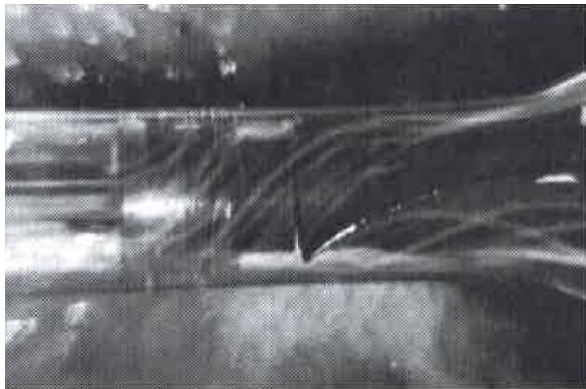


Image 7.20:

Rotor + stator at 100 mmHg; $\dot{V} = 2.5$ l/min

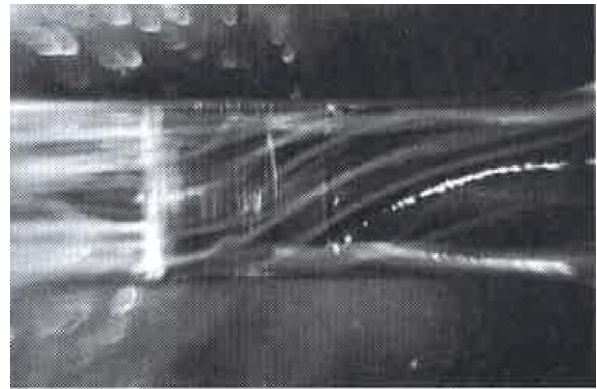


Image 7.21:

Rotor + stator at 60 mmHg; $\dot{V} = 3.2$ l/min

Image 7.20 shows the entire micro-axial pump at a counter-pressure of 100 mmHg and a flow rate of 2.5 l/min in the tracing method. It can be seen that the individual particles of 200 to 300 μm are uniformly accelerated in the rotor in the rotational direction. This is shown by the constant curve radii of each of the particles. Furthermore, the distance of the particles from the hub is responsible for the size of the curve radius, and therefore for the degree of acceleration.

After the particles have left the rotor, they enter into the stator at a large flow angle. The result is the separation of the flow already in the front region of the blade, which correlates with the small washing on the intake side in Image 7.17. No visible recirculation region is generated, however.

In the stator one can often find intersecting particle traces. These indicate different speeds across the channel height. For instance, the particle near the hub which was initially flowing along the outlet side of the blade, before bending downward. This flow correlates with the results of the washing experiment in Image 7.17. The result in the enlarged model, according to which the impact of the boundary layer on the main current in the stator is small, cannot be confirmed based on the number of the stronger curved particle traces that are being observed. Rather, the assumption suggests itself that the entire flow consists of a single boundary layer.

If one looks at the rotor entry, a particle trace can be seen above the hub, which appears to be clearly lighter at one point, which may be explained by a briefly lower axial speed. This observation shows the weakness of this analyzing method with the large particles used here, which is that the inertia of the particles leads to a distortion of the results. A fluid particle which is infinitesimally small in comparison flows around the rotor, initially without colliding with the beginning of the blade. This is a reason why in the course of the study, significantly smaller particles were used. Due to the small differences in contrast, however, their particle tracers are no longer easy to record, which is why larger particles are used for documentation purposes.

Image 7.21 shows the same system at a counter-pressure of 60 mmHg. The lower pressure, at a rotational speed of 30,000 rpm, leads to a flow of 3.2 l/min, which involves an increase of the meridional speed. In the rotor, the redirection is smaller than would have been the case at 100 mmHg. The resulting smaller flow angle at the stator leads to a very good flow. The current follows the intake side without separating, and on the outlet side no breast incidence is observed. In total, these recordings document a very harmonic flow which is very similar to that of the enlarged model.

Knowing about the internal losses as a function of the channel height according to Ch. 9.2.2, in a first iteration step for the blade system studied here, the hub was made smaller, and thereby the channel height was increased, while the geometry of the blades was retained. With this modified blade system, flow results could now be obtained at 100 mmHg which correspond to those of 60 mmHg as shown in Image 7.21 due to the increased volume.

A presentation of the flow analysis results by means of the Kodak EktaPro and NAC UltranaC high-speed video systems cannot be given comprehensively here, but only in excerpts. The emphasis will be placed on the required analytical methods, complementing Ch. 7.1.2.

The Kodak EktaPro system is used in order to determine the fluid entry with respect to the boundary layer form along the blade entry edges with the respective wall shear stresses according to Ch. 8.1.2 viii.

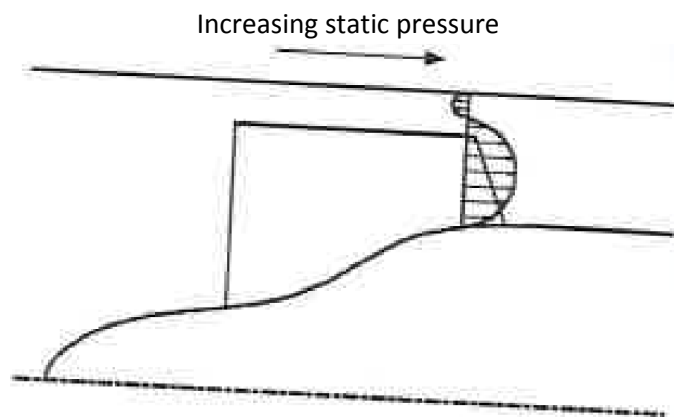


Image 7.22: Recirculation near the casing wall

Furthermore, this system allows for a dynamic viewing of the flow over an extended period ($t < 1s$), so that even cyclical flow manifestations can be observed, which includes periodic separations. During the analysis of the available image material at the design point, no eddies or recirculation regions were observed. In analogy to Image 7.22, however, some particles were observed that were traveling against the primary direction of the current due to the gap heights of 0.2 to 0.3 mm in the model between the outer rotor blade edge and the casing. It can therefore be presumed that the counter-pressure at the rotor exit has more impact than the blade system. In order to avoid such leakages as well as intolerably high shear stresses, the gap must have exactly the target measure of 0.1 mm.

Flow analysis with the particle tracking method

As previously explained in Ch. 7.1.2, the flow images created with the help of the two-dimensional UltranaC system as show in Image 7.2 do not provide direct information about the distance of the individual particles to the hub or to the casing wall, respectively. Relative depth information (because it is comparative) becomes possible,

however, when a trajectory of a particle is determined in all three templates, so that a respective progress of an “inner” flow line close to the hub, an “outer” flow line close to the casing wall, or a “median” flow line at the free channel level can be discussed. For these purposes, the following criteria have proven useful, cf. Images 7.23 through 7.25:

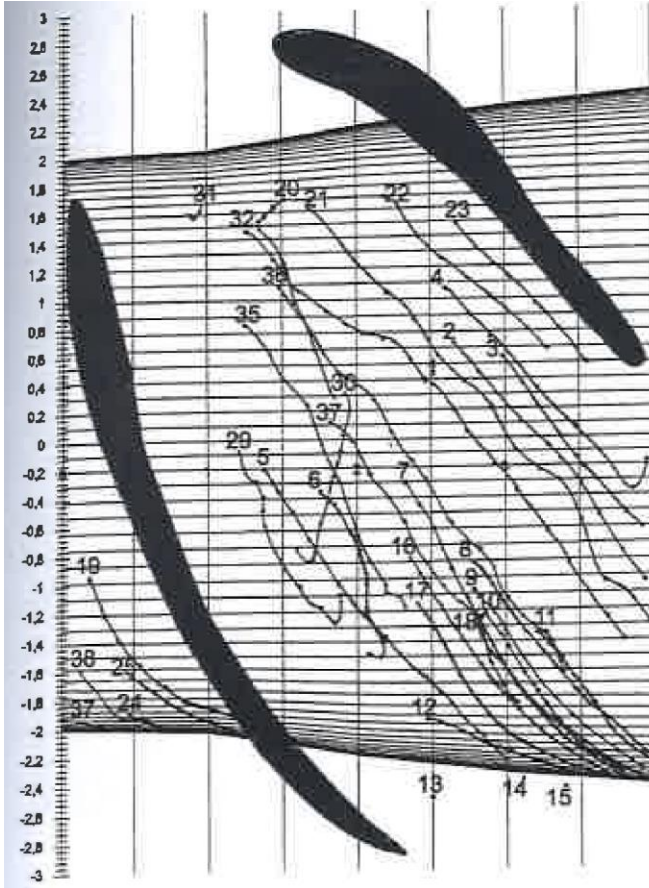


Image 7.23: Particle trajectories for an “inner flow line” adjacent to the hub

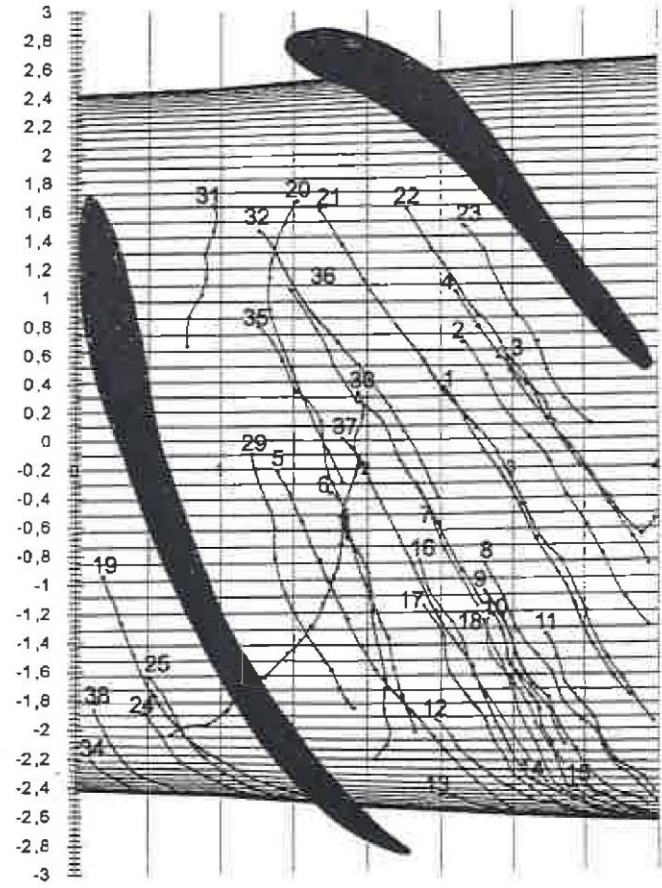


Image 7.24: Particle trajectories with 50% of the flow volume inside and outside of the “median flow line”, respectively

- If a fluid particle one on of the recorded images moves beyond the edges of the template used, it will certainly not be moving on the corresponding enveloping surface. Rather, the next “larger” template, that is, a flow line at a greater distance from the rotor hub, must now be used. This allows for determining that, for instance, Particles 13, 14, and 15 are no longer moving along a flow line close to the hub, and that Particles 26 and 33 are flowing through the rotor close to the casing wall.
- Spatially intersecting trajectories on an enveloping surface can be excluded due to the short time interval of only 0.84 ms for the 24 recordings. For these purposes, also compare Particle 20 in Image 7.25 to Particles 32 and 35.
- Particle trajectories with a largely constant curving and a sudden bends downward can be excluded based on the harmonious and bend-free particle trajectories in a locally fixed coordinates system according to Images 7.10 through 7.12 and Images 7.20 and 7.21. They result merely from the projection of the particle onto the wrong template. Also compare Particles 4, 6, 20, 29, and 30 in Image 7.23.

- Particles progressing at specific locations with respect to the rotor must also do this geometrically after a successful transformation to the original image. This includes measureable distances, the progression of the particle from the outlet to the intake side (Particle 30), etc.

Based on the particles marked with numbers “4”, “6”, “19”, “29”, and “30”, exemplary results are discussed below, by way of which the possibility of an approximate depth estimation can be visualized. No attempt is made, however, to characterize particles more in detail, other than by the categories of close to the hub, to the middle of the channel, or to the casing:

As can be seen in Image 7.25, fluid particle “30” does not follow the main current, but is drawn from the outlet side of the rotor blade to its intake side. The observable jump of the particle over the blade results from the split stream that built up between the outside edges of the rotor blade and the pump casing, or respectively, between the outlet and the intake side. In other words, the particle is moving adjacent to the casing wall, where the counter-pressure at the rotor outlet has a stronger impact on the fluid particle than the blade system, which is also what is responsible for the backward movement of the particle (cf. results EktaPro, Image 7.22).

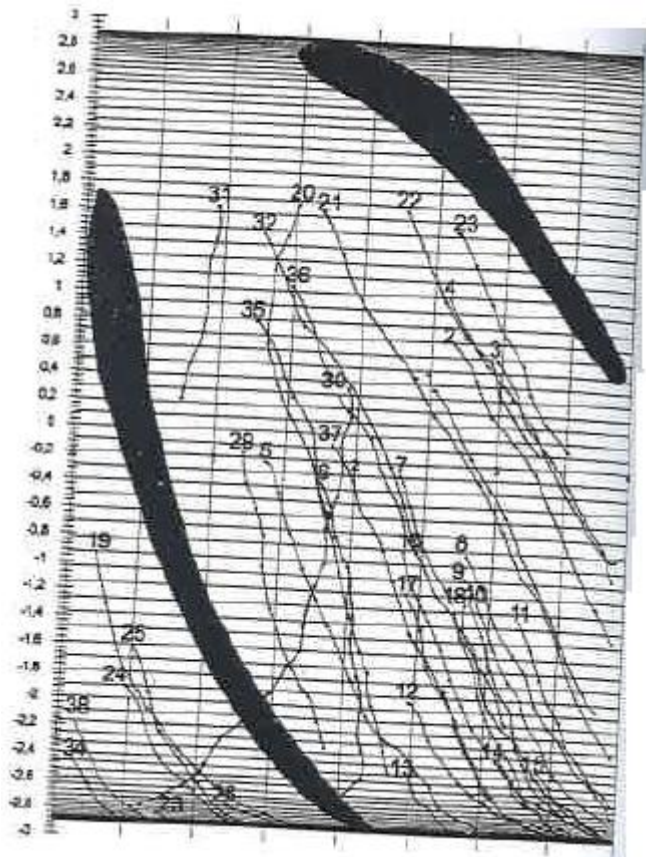


Image 7.25: Particle trajectories for an “outer flow line” adjacent to the casing wall

The trajectory of Particle “6” in Images 7.24 and 7.25 is interesting as well, in that it shows a lesser redirection in the direction of the blade intake side. The reason for this lesser redirection is the resulting channel swirl, which has already been described several times before. This channel swirl clearly leads to a strong redirection at the hub and, as in the case of Particle 6, to an equally strong lesser redirection near the casing.

When looking at Particles “4” and “29” on a flow line close to the hub (Image 7.23), towards the end of the trajectory curve, a certain movement forward of the particles in the rotational direction can be observed. This may be caused by the sudden impact of the secondary current near the hub, which induces a strong redirection. On the other hand, there may be an incorrect assumption about the progression of the flow line, with respect to the assumed channel height. In the case of these two particles, the latter may be presumed, since a sudden change of the particle directory can be excluded according to the aforementioned considerations. With the increased distance from the rotor hub, the examined trajectory lines do not show any movement contrary to the principal direction of the current (cf. Images 7.24 and 7.25).

In Image 7.23, Particle “19” wanders from the intake side of the rotor blade against a higher pressure to its outlet side, whereas when the “outer” template is examined, a flow line along the blade contour as in Image 7.25 can be observed, which is more “sensible” in view of the pressure situation.

The aforementioned examples of individual particles show that a principal depth assignment is possible. Nevertheless, there are some particles which, despite the knowledge about general manifestation of flows, cannot be assigned unambiguously.

The flow recordings made with the Ultracac system offer the further possibility of obtaining not only qualitative, but also approximate quantitative information about speeds in the rotor channel. This knowledge serves as a basis for first estimates of the rotor-induced blood damage in such micro-axial pumps, according to Ch. 8.1. This allows for determining Newton's shear stress progression by way of a speed profile. The process needed in order to this is described below:

In all three templates, at respectively the same locations of the rotor blade system (here: "A" after half of the channel length, and "B" the last third of the channel length), the respective speed profiles were calculated in orthogonal sections in absolute terms to the blade contour. With the knowledge about the followed trajectory between two particle positions of a trajectory line and of the time needed in the event of a neglected local acceleration, a mean speed can be determined for each particle. An analyzable speed profile of the entire current can only be obtained, however, when the smoothened curve of the thus determined speeds is drawn, which may still vary due to incorrect depth assignments to particles. All speed distributions are also characterized by Stoke's adhesion principle, so that the flow speed at a rotor blade is set to zero.

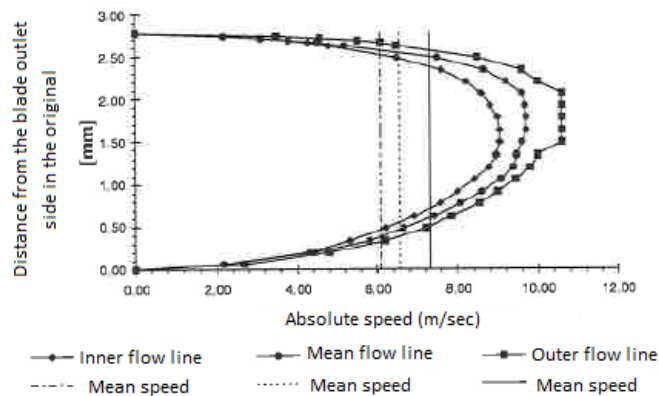


Image 7.26: Speed profiles at Position "A"

$\dot{V} = 3.1 \text{ l/min}$ at $\Delta p = 100 \text{ mmHg}$

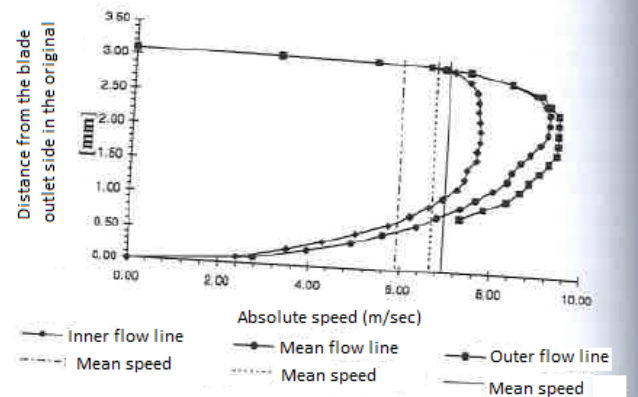


Image 7.27: Speed profiles at Position "B"

$\dot{V} = 3.1 \text{ l/min}$ at $\Delta p = 100 \text{ mmHg}$

Images 7.26 and 7.27 show that on the blade intake side, flow speeds are stronger than on the outlet side. According to Bernoulli's equation, the static pressure on the concave side of the blade is therefore higher than on the convex side, which confirms the theory of the flow around the blade with an outlet and an intake side. The speed profiles describe the form of a parabola which is fuller on the intake side, which must be ascribed primarily to the impact of turbulent boundary layers in the region of high speeds. Correspondingly, the du/dy gradient immediately adjacent to the wall is big.

Compared to the laminary flow, there is a significantly larger impulse exchange perpendicular to the principal current direction. As a result, the mean speed profile over time is fuller, and wall shear stresses increase. A differentiation between individual boundary layers is not possible, due to the extremely small channel size. Rather,

it can be learned from the events that there is one large boundary layer in the entire channel, which confirms the assumption from Ch. 5 that there is no unaffected central flow.

If the three speed profiles for the region close to the hub, close to the housing wall, and midway between these two elevations are superimposed, as is done in Images 7.26 and 7.27, one recognizes that the highest absolute speeds occur near the housing wall. The maximum speeds resulting from all the profiles are in the range of 7.7 to 10.6 m/sec., whereas the mean speeds are in the range of 5.9 to 7.3 m/sec.

The speed profiles thus determined can be used in order to determine Newton's shear stress progression. For that purpose, tangential lines are drawn at the respective points on the speed profiles, the inclination of which corresponds to the speed gradient du/dy . The values thus obtained, multiplied with the dynamic viscosity of blood ($\eta = 3.6 \text{ mPa} \cdot \text{s}$) results in the local Newton's shear stress:

$$\tau \left[\text{N/m}^2 \right] = \eta \cdot \left| \frac{du}{dy} \right| \approx \eta \cdot \left| \frac{\Delta u}{\Delta y} \right|.$$

(Equation 7.2)

The resulting shear stress distributions are shown in Images 7.28 and 7.29. Turbulent shear stresses, which in some occasions may be higher than Newton's shear stress, cannot be calculated due to the locally unresolvable variation and frequency. To which extent these are relevant for blood damage is beyond the scope of our discussion here. However, it is worth noting that the classical turbulence models as a matter of principle always overestimate the Reynolds turbulence in blood, since the turbo-elastic, and therefore moderating, effect of the large amount (approx. 40% in volume) of erythrocytes on the eddy length cannot be registered. The impact of the turbulence on the blood damage is accordingly usually overestimated.

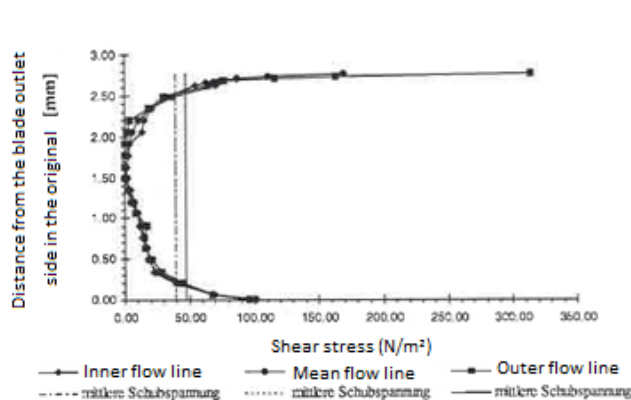


Image 7.28: Shear stress distribution at Position "A"

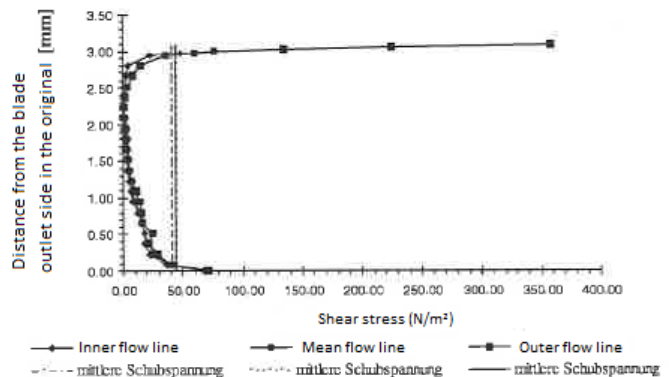


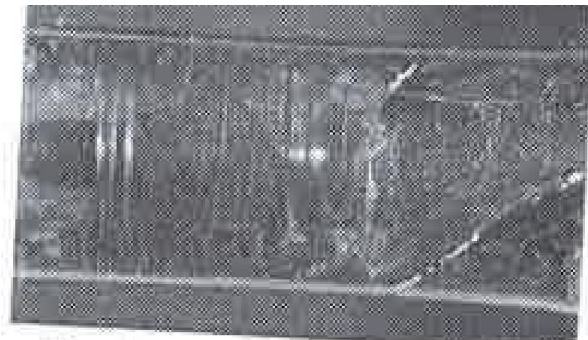
Image 7.29: Shear stress distribution at Position "B"

Evaluation of the method:

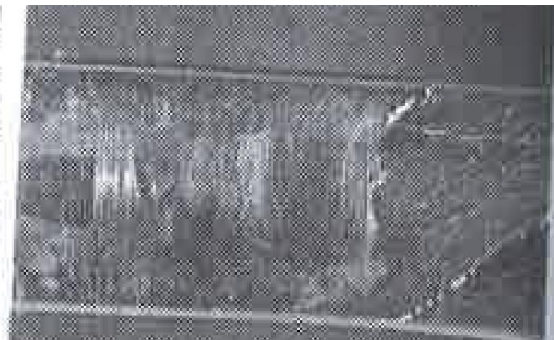
The results of the particle tracking method shown here have a principal error that cannot be specified exactly due to the lack of calibration methods. However, this is the first method that offers the possibility of quantifying speeds at all, inside such small and rapidly rotating pumps.

Visualization of the cavitation in the blade area:

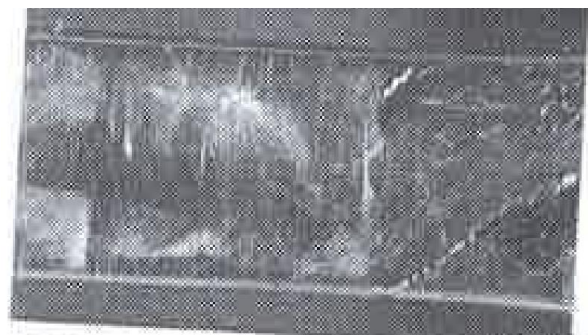
With the flow visualization setup from Image 7.15 it is also possible to determine the boundary rotation speed according to Ch. 5.5, which is based on the cavitation limit of the system in case of a sudden occluding intake. The sequence in Image 7.30 shows the development over time of a cavitation event at 25 images per second, which may also occur *in vivo* in case of a suddenly suctioning pump. The first image shows the pump at the beginning of the stall based on the fully occluding intake, so that now the entire capacity of this powerful blade system is a power-reducing initial load in the intake region. The first cavitation bubbles become visible only 40 ms after sealing. They increasingly grow between exposures, and either collapse or exit the pump after the intake region is opened.



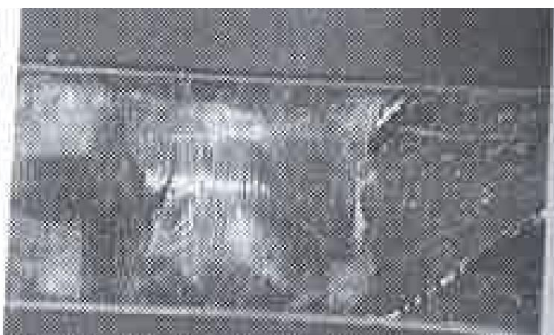
a: seal



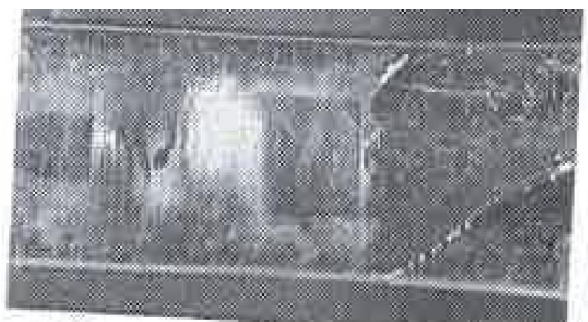
b: first bubbles in hub area



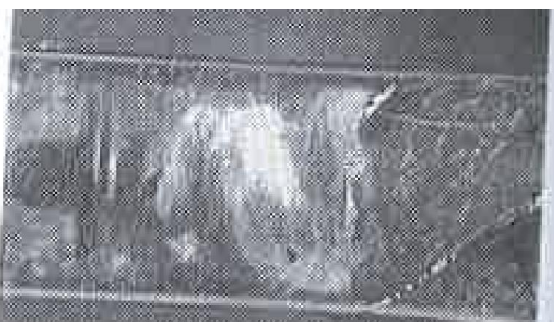
c: bubble growth



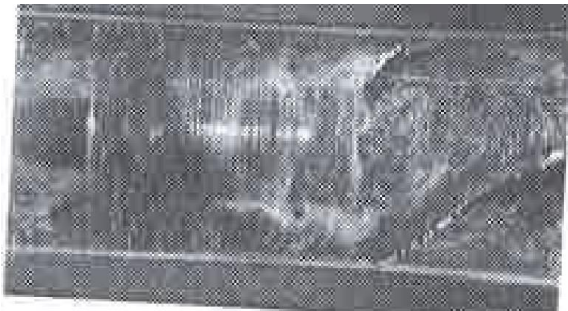
d: further bubble growth



e: opening of the suction tube



f: washing out the bubbles



g: collapsing and washing out



h: end of the event

Image 7:30: Cavitation event

To which extent the cavitation bubbles leave the pump depends on the respective life span.

While the steam cavitation bubbles collapse immediately, in cases of lasting occlusion, gas bubbles out of gases physically dissolved in the fluid (in this case: primarily nitrogen) may be generated as well. Their life expectancy can be multiple times higher than that of the steam bubbles, so that gas bubble embolisms as a result of cavitation events cannot be ruled out. Cavitation is therefore not only damaging to blood, but it may also cause long-term damage to an organism, which is why it should be avoided by all means in medical applications of these fast-operating axial pumps. If this cannot be done by means of a correspondingly selected rotational speed due to the required hydraulic performance, the static pressure in the suction tube of the LV pumps must be controlled in real time according to Ch. 10.4, and the pump must be operated regularly.

Visualization of the outflow region:

Images 7.31 and 7.32 show the outflow behavior of the 6 mm LV micro-axial pump within a Perspex tube which, at $\varnothing 24$ mm, has a diameter comparable to that of an average aorta. The pump is integrated here in a device for surface temperature registration, in which the pump position corresponds to the *in vivo* position of the pump when the aortic valve is closed.

In Image 7.31, the pump, consisting of rotor and stator, can be seen in the right margin. The motor with its total length of 30 mm is located in the middle of the picture, where at time $t = 0$ no contrasting dye is visible. In Image 7.32, which comes immediately after Image 7.31 without a significant dark phase and which was exposed for $t = 1/25$ sec., an asymmetrical free jet reaching from the pump outlet behind the motor, can be seen in the upper half of the image. Based on the absent coloring information, the contrast dye (potassium permanganate) can only be seen as it looks like a shadow. The reason for the observed asymmetry is the three-fold outflow of the fluids from the three-leaf stator.

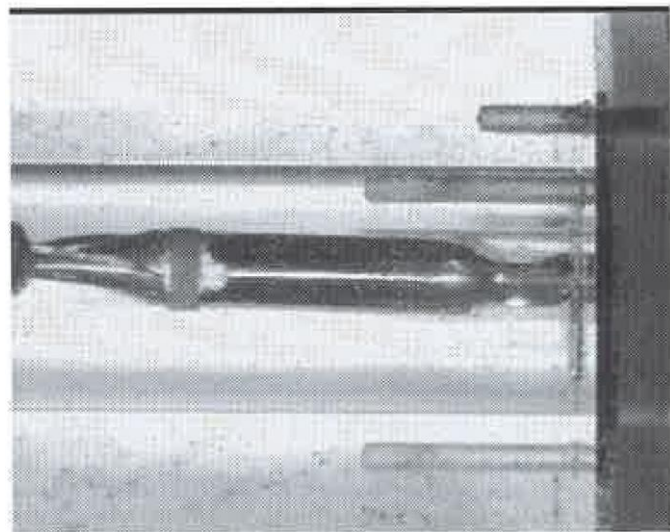


Image 7.31: The outflow behavior of Lab III at $t = 0$

Departing from these two images, the free jet may be assigned a mean speed $V_{free\ jet} = 1.0\text{ m/s}$ with a starting speed of $V_{stator} = 3.1\text{ m/s}$, which is necessary for the calculation of the surface temperature in Ch. 4.2.2.

It can be learned from Image 7.32 that the free jet from the beginning of the stator to the end of the pump hugs the surface, so that convective heat dissipation is guaranteed.

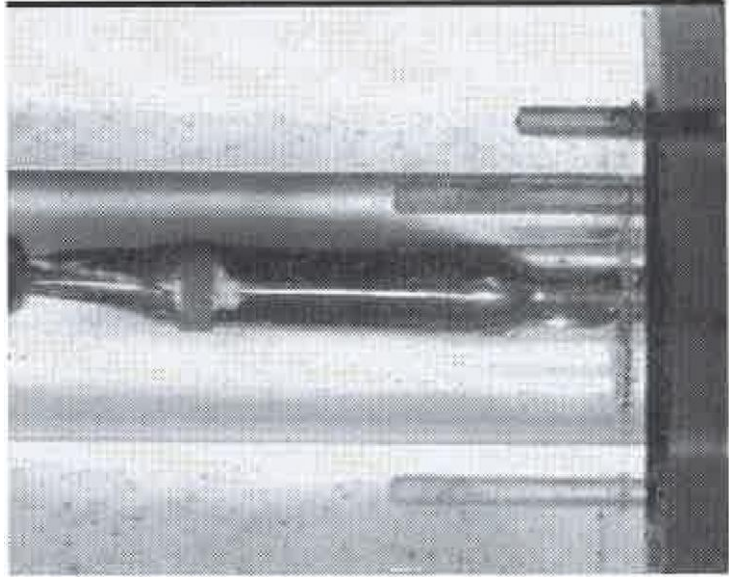


Image 7.32: The outflow behavior of Lab III at $t = 1/25\text{ sec}$

7.4.3 Analysis of the results and evaluation of the methods

The results of the flow visualization process have already been described in the previous chapter, and extensively analyzed by means of the exemplary illustrations. Important for the evaluation of the various analysis methods used is, however, that all these methods are proven not to contradict each other. Rather, it is only a cumulative review of the all the results specific to a certain method that offers a profound understanding of the current in general. The respective informational values of the methods used can be found in Ch. 7.1, 7.3.2 - 7.3.3, and 7.4.2. In what follows, we will provide a brief analysis of the results in the context of the examined pumping system. At a counter-pressure of 60 mmHg, the 6 mm LV micro-axial pump that was extensively examined here proves to have a very good flow which correlates with the results of the enlarged model based on similar flow volumes and rotational speeds:

In the tracing method, the rotor shows a uniform redirection of the individual particles, so that the flow may be referred to as an orderly flow. This can be confirmed by the results of the particle tracking method. While these results were obtained at a counter-pressure of 100 mmHg, but they produce a flow volume similar to that at 60 mmHg due to the expanded channel cross section at that place, wherefore the results are similar. Based on the harmonic bend-free and constant curvature of the particle traces, the rotor proves to have an almost linear enthalpy development, which corresponds to the geometrically realized enthalpy distribution of Ch. 6. Consequently, the wall shear stresses as a determinant reason for blood damage are homogenous through the entire rotor. This is confirmed by the uniform removal of the color in the washing method. Avoidable shear stresses due to local swirls could not be observed in any of the methods used.

In the stator, the flow closely followed the blades. This is confirmed by the results of the washing and tracing methods. Based on the viscosity of the wall coating in the stator, which is smaller by a factor of 10 as compared to that in the rotor, which leads to comparable washing results at identical operating times,

it can be expected that in comparison, in this region there is a considerably smaller amount of blood damage.

In total, it can be expected that relevant blood damage can be traced mainly to high shear stresses in the rotor, especially close to the wall and in the gap between the outer edge of the blade and the housing. This aspect will be more closely examined in the next chapter.

For the design point of a counter-pressure of 100 mmHg, a high degree of blood damage can be predicted, since at comparable wall shear stresses in the rotor, the flow volume is reduced due to the higher pressure alone. The retention time is therefore higher than at a counter-pressure of 60 mmHg:

The results of the tracing method and the washing method attest an orderly flow in the rotor at 100 mmHg as well.

The sharp angle of the blade at the entry into the stator leads to the observed separation manifestations at the intake side.

Conclusion and consequences for the remainder of the process:

Based on the results in the enlarged model as well as in the original size, it can be concluded that while for the design point of 60 mmHg at a design rotation speed of $n = 30,000$ rpm, the 10:1 model provides similar information, this is information without added value, so that a parallel production of modified blade systems at a scale of 10:1 can be dispensed with. For the further development, only flow examinations in the original model in the scale of 1:1 are done, since these can be performed without significant loss of informativeness. Further examinations by means of the tracing method for analysis purposes are only done with particles in the range of 10 to 20 μm , in order to minimize the distorting impact of the particle size on the flow results. These particles are only larger than the human erythrocytes by approx. a factor of three.

Image 7.33, like Images 7.30a through h, show flow recordings with particles of 10 to 20 μm . It shows the difficulty previously described in Ch. 7.1.7 of dissolving particles that are so small in relation to the flow channel, and of documenting them.

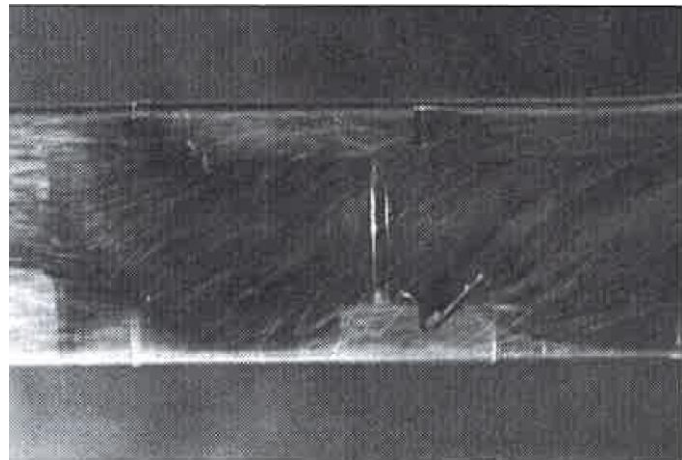


Image 7.33: Blade system with small particles of 10 to 20 μm in the fluid

8. Method for Examining Pump-Induced Blood Damage

Based on the experimental flow examination in Ch. 7, a method for the quantitative assessment of the blood damage will be proposed in this chapter, and subsequently implemented in the exemplary $\varnothing 6$ mm blade system

components that were already extensively reviewed in Ch. 7. In addition, the impact of the design parameters relevant for small fast micro-axial pumps on blood damage will be discussed.

8.1 Assessment of Pump-Induced Hemolysis

Based on the results presented in Ch. 7.3.2 and 7.4.2, an assessment is made of the rotor-induced hemolysis (= destruction of the red blood cells and release of hemoglobin). The result is then juxtaposed with the hemolysis as measured *in vitro*, and discussed.

In the literature, various experimental (*Blackshear 1965, 1972; Bleifeld, 1973; Kramer, 1970; Sallam, 1976*) as well as mathematical-numerical (*Bludszuweit, 1994, 1995a, b; Pinotti, 1995; Yeleswarapu, 1995*) models for the quantification of component-specific hemolysis are described. In these, either the generally measureable blood damage is correlated with a shear stress at a corresponding retention time, or the experimental results are used in order to exercise a time-variant load of individual erythrocytes along a trajectory curve in numerical models. The latter method is based on Lagrange's examination of a co-moving coordinates system. Furthermore, the examined flow field must be described at every point in terms of local pressure and speed. In order to reach relevant results with respect to blood damage based on Lagrange's examination, an arbitrary large number of particles must be launched for averaging purposes at identical, and for the entire flow field, at sufficiently proximate starting points, and subsequently be weighted and integrated for a description of the cumulative damage. The description of this method alone emphasizes the rather theoretical character of this method, for which, moreover, no validation is available at this point.

Alternatively, there is Euler's examination method with a locally fixed coordinate system. With respect to the present field of application, this leads to an integral examination of the fluid at the end of the blade channel, in which only damage due to a speed profile and a corresponding stress field oriented in the direction of the flow is considered. Any internal blood damage resulting from internal leakages and rotor-specific secondary currents are not included, which leads to a significant underestimation of the actual hemolysis. In order to compensate for this disadvantage of Euler's method, internal hemolysis source terms are determined, which are superposed in a volume flow-weighted manner with the blood damage result obtained via Euler's method. Such source terms follow from the boundary layers adjacent to the wall, with respective directions deviating significantly from the primary direction of the current, and from the gap flow, which can be described as an internal leakage with rotor-specific load level, retention period, and volume flow.

The following calculation of a rotor-induced hemolysis should be phenomenologically understood. It is a first attempt to derive a hemolysis that is comparable with the experimental results in terms of magnitude from a punctually described and very complex flow field. Apart from the damage index thus calculated, a comparative description of local hemolysis is important, as this demonstrates the design-relevant criteria or "hotspots" that may be considered in the design process.

8.1.1 Method and simplifying assumptions for determining pump-induced blood damage

- i. A speed profile in the channel is generated based on the measurement results obtained by means of the NAC UltranaC and the particle tracking method according to Images 7.26 and 7.27.
- ii. Based on this speed profile, a shear stress field is determined. In the region adjacent to the housing wall, this field is overlaid with a shear stress resulting from the relative speed in the rotational direction.
- iii. From the shear stresses thus determined, a relevant local load size for the erythrocytes is determined.

- iv. The local load time can be calculated based on the local speed vector (quantity and direction) in combination with the characteristic run length.
- v. The local damage can be determined by way of a suitable model describing the blood damage as a function of retention period and shear stress.
- vi. This local damage is then normalized with the local volume flow, integrated or summarized for the entire channel, respectively, and then divided by the measured resulting volume flow of the pump. The damage index thus determined describes the blood damage occurring in the channel after one passage, if all internal leakages and source terms are disregarded.
- vii. The internal leakages in the gap flow are determined. A damage rate may be assigned to this flow of fluids as well.
- viii. Boundary layers close to the blade have a direction significantly deviating from the main current, so that fluid is spun off along the blades which then ends up in the gap swirls or in the resulting channel swirls. Furthermore, locally increased wall shear stresses due to boundary layer formation can be expected at the beginning of the blade. In this respect too, resulting volume flows with blade-specific damage rates can be determined.
- ix. The source terms calculated in **vii.** and **viii.** are superposed with the result of **vi.**, resulting in an integral quantity in the form of 'blood damage per passage', which can now be compared with the results of the hemolysis measurements performed *in vitro*.

This principal process is based on essential simplifications which are necessary in order to calculate any blood damage rate based on the available measurements. They include:

- For lack of suitable mathematical models, the blood-damaging impact of the surface roughness of the material used, which naturally generates a hemolysis as compared to the body's own tissue in its own right, is not considered (*Blackshear 1967, 1971; Wurzinger 1991*).
- For lack of quantification options, turbulent shear stresses are not accounted for.
- The blood damage in the stator following the rotor is not considered here, because due to the Newton's wall shear stresses, which according to Ch. 7.4.2 (cf. Images 7.16 and 7.17) are smaller by a factor of 10, and, according to *Giersiepen 1990*, at similar retention period, as compared to [the blood damage in] the rotor is smaller by a factor of $\tau^{2.416} \approx 10^{2.416} = 140$. If the stator-induced hemolysis would be lower than that in the rotor by a mere factor of ten, it's being disregarded in the framework of this primary evaluation could already be justified.
- The blood damage in the free jets is disregarded. According to *Steegers 1997*, this is permissible due to the results of the leak jet-induced hemolysis of mechanical heart valves. In that study, leakage jets with speeds of up to 3.5 m/sec were examined in *in vitro* hemolysis experiments, in which the resulting hemolysis was smaller than the best measurement with micro-axial pumps by a magnitude of approximately 10. The speeds of the free jets at the pump exits are comparable with the leakage jets of the heart valves in terms of the maximum speeds, but they differentiate themselves less from the immediately surrounding fluid, so that in the large jets of the pumps an even smaller degree of blood damage can be expected.
- For the calculation of the hemolysis generated in the channel, the geometry of the rotor is simplified such that an average channel height according to Position "B" in Image 7.27 is assumed, rather than a height decreasing from the beginning of the blade until its end, with a continuous speed profile.
- It is assumed that the channel is singly bent in the flow direction, rather than doubly, as it is in reality due to the hub, so that in an orthogonal section from the outflow to the intake side, one can observe a rectangular channel as in Image 8.1. This geometrical simplification has no material impact on the result, but it considerably simplifies the calculation as there is no need for a coordinate's transformation.

8.1.2 Execution of the method

On i.:

In order to determine a characteristic speed profile which, when simplified as required, still represents the general speed in a channel of the three-leaf LV rotor with sufficient accuracy, a mean channel height for the mean radius r

$$r = 1 / (Z_n - Z_{i=0}) \cdot \sum_{i=0}^n [r(Z_i) \cdot (Z_i - Z_{i-1})] \stackrel{\text{here}}{=} 1.6 \text{ mm} \quad (\text{Equation 8.1})$$

is determined as $\bar{h} = 1.4 \text{ mm}$. Furthermore, the speeds relevant for this channel height at position “B” from Image 7.27 are used. By way of relevant channel length S_L , which corresponds to the mean run length of all fluid particles conforming to the channel contours, the chord length of a blade is taken of $S_L = 9.0 \text{ mm}$. From here follows a speed distribution in the channel according to Image 8.1, in which the rotational direction of the fluid particles flowing close to the housing relative to the housing wall has not yet been considered. The relative channel height of $h = 1.6 \text{ mm}$ refers to the hub here, whereas $h = 3.0 \text{ mm}$ refers to the housing wall.

If at a distance of $a_D = 0$ one looks at the outflow side, the maximum distance of $a_D = 3.6 \text{ mm}$ refers to the intake side of the channel.

A look at the speed profile clearly shows that the speed gradient in the proximity of the housing wall is significantly higher than close to the hub.

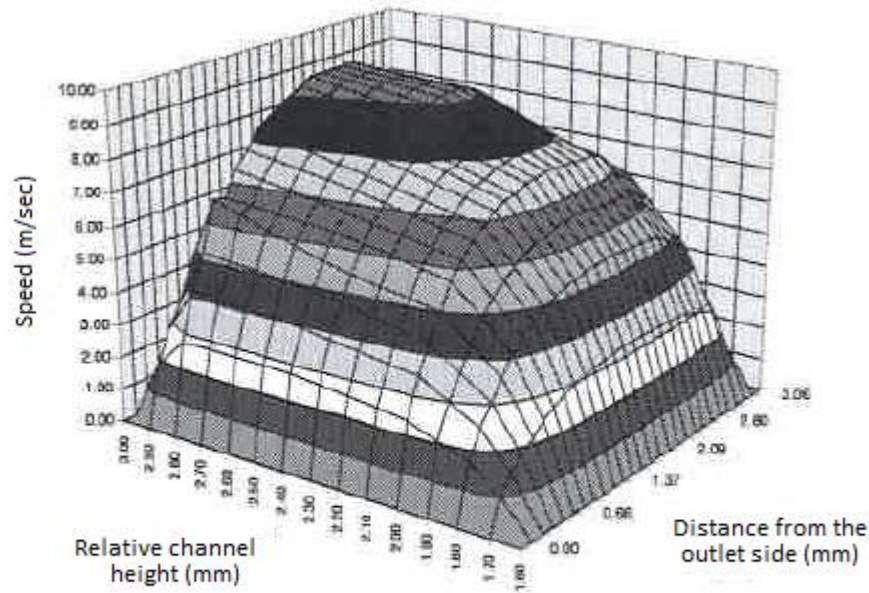


Image 8.1: Speed profile in the channel.

In order to test the validity of the underlying speed profile, the resulting volume flow is compared with the total volume flow as measured:

$$\dot{V} = \int_{a_D=0}^{a_D=3.06} \int_{h=1.6}^{h=3.0} v(a_D, h) \cdot da_D \cdot dh \stackrel{\text{here}}{=} 1.6 \text{ mm} \quad (\text{Equation 8.2})$$

A deviation of only 12% of the calculated volume flow value from the measured value indicates a good correspondence.

On ii.:

Based on the speed distribution in Image 8.1 and the relative speed of the rotor with respect to the housing, a resulting shear stress field is determined according to Equation 7.2. The resulting values are based on the locally relevant erythrocyte load in **iii.**

In order to determine the relative speed, multiple recordings were evaluated analogous to Image 7.21 for traces of particles adjacent to the wall, whereby the mean diversion of the particles in the rotational direction was determined based on the momentum-free current at an angle of 25 to 30 degrees at t (C_{mm}) in the form of a lesser flow redirection, as compared to the mean blade construction angle at the wall, when by way of a meridional speed the mean speed C_{mm} is used, which follows from the mean channel height $\bar{h} = 1.4$ mm. This significant lesser flow redirection cannot be confirmed by the particle tracking results in the channel. However, if the absolute speed C of the particles adjacent to the wall is applied to the meridional projection of the mean speed in the channel, adjacent to the wall as well, from Image 7.27, with $C_{mD} = 4$ m/sec as compared to $C_{mm} = 2.55$ m/sec, the flow according to Image 8.2 will actually conform to the contours, despite all the simplifications.

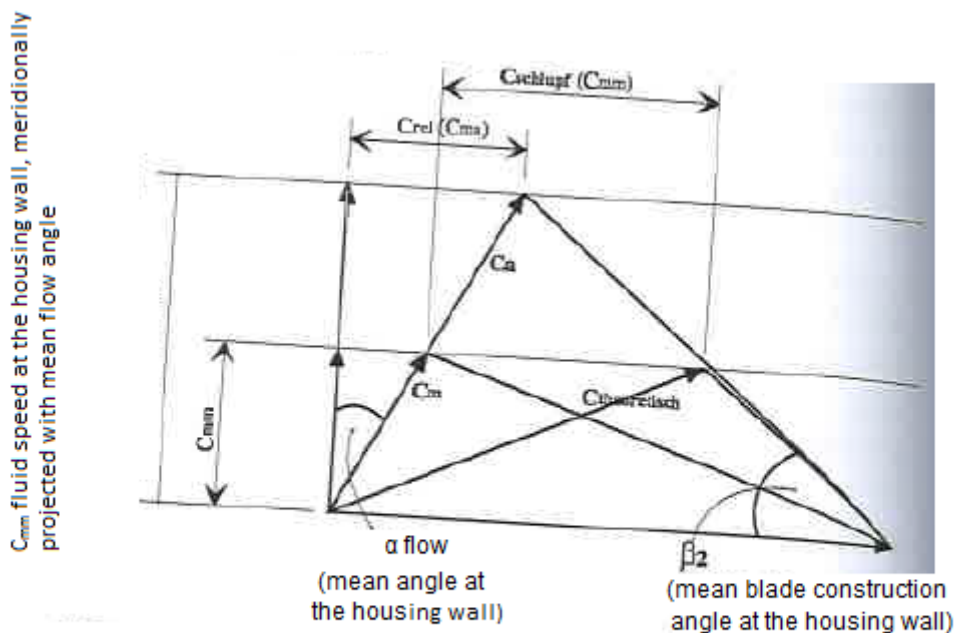


Image 8.2: Scaled speed triangles in the channel adjacent to the housing wall

The mean relative speed thus calculated amounts to $C_{rel} = 2.1$ m/sec, and is considered, in addition to the speed profile from Image 8.1, for determining the resulting local shear stress for fluid layers immediately adjacent to the housing wall with a distance of 0.1 to 0.2 mm from the surface.

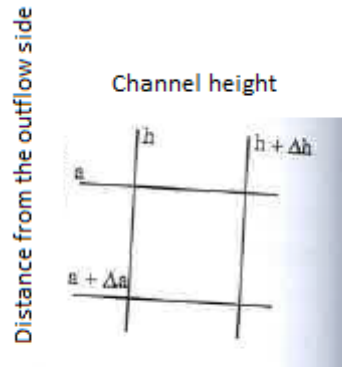


Image 8.3: Data net in an orthogonal channel section

The determination of the resulting shear stress field as well as of the respective local speed is done by way of averaging analogous to Image 8.3 and Equations 8.3, where every shear stress in Equation 8.3a should already be understood as a resulting load according to the considerations from iii. According to Equations 8.6a and b:

$$\tau_{h+\Delta h/2; a+\Delta a/2} = \frac{\tau_{h;a} + \tau_{h+\Delta h;a} + \tau_{h;a+\Delta a} + \tau_{h+\Delta h;a+\Delta a}}{4}$$

(Equations 8.3a, b)

$$u_{h+\Delta h/2; a+\Delta a/2} = \frac{u_{h;a} + u_{h+\Delta h;a} + u_{h;a+\Delta a} + u_{h+\Delta h;a+\Delta a}}{4}$$

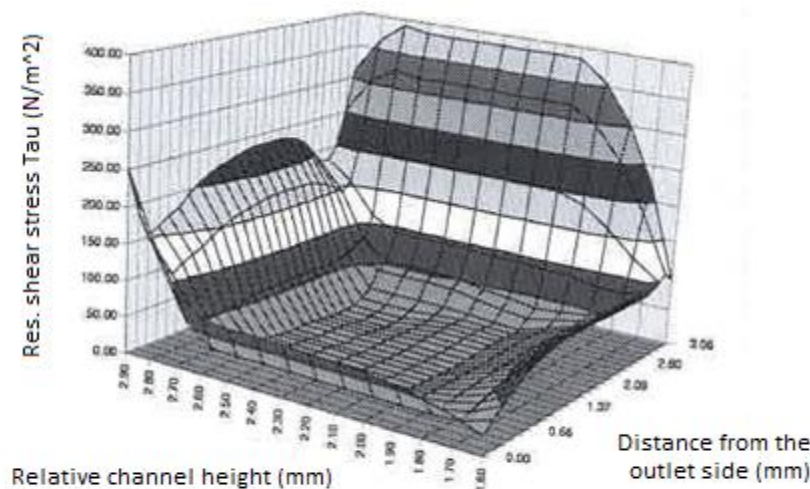


Image 8.4: Averaged resulting shear stress development

The shear stress thus determined is shown in Image 8.4, which makes it clear that the strongest load exists close to the wall, and in particular immediately near the intake side. Shear stresses with peak values of approx. 400 N/m² are generally deemed to be very high in the context of blood-transporting systems, and definitely result in

significant blood damage. The reason for the fact that the resulting blood damage is still tolerable, especially along the blade contours, even though they feature the highest stress values as well as the principally longest retention period due to the slow speeds at the wall, will be discussed in **iv.** to **vi.**

On iii.:

In addition to establishing the resulting stress, establishing a damage model is also determinant for establishing rotor-induced blood damage. The former is done in a manner analogous to the description of stress in “rigid bodies”, whereas in analogy to a “rigid body”, in this case an infinitesimally small fluid element is meant (*Prandtl, 1956*). The internal stress therefore results from the sum of all applicable forces, specifically pressure and thrust forces, and for the flow profile according to Image 8.5 it can be described by way of the stress tensor $\bar{\bar{s}}$:

$$\bar{\bar{s}} = \begin{pmatrix} \sigma_x & \tau_{xy} & \tau_{xz} \\ \tau_{yx} & \sigma_y & \tau_{yz} \\ \tau_{zx} & \tau_{zy} & \sigma_z \end{pmatrix}$$

whereas based on the principle of the equality of shear stresses according to *Adomeit, 1986*,

$$\tau_{xy} = \tau_{yx}; \tau_{xz} = \tau_{zx}; \tau_{yz} = \tau_{zy}$$

(Equations 8.4a, b)

The tri-axial stress is already described when three shear stresses and three normal stresses are known. The latter cannot be derived from the speed profile, but only be learned from local static pressure. However, the normal stresses are immaterial for determining the relevant load that leads to the damaging of the thrombocytes as well as the erythrocytes, in which we are primarily interested here. According to *Blackshear, Bernstein, 1967*, significant excess pressures and even negative pressures can be oscillatingly applied to full blood until immediately above the vapor pressure without relevant blood damage being observable, which may be due to the incompressibility of the cell interior, which is sufficient for our purposes. There is therefore no critical load for the membrane, which would have led to a lysis.

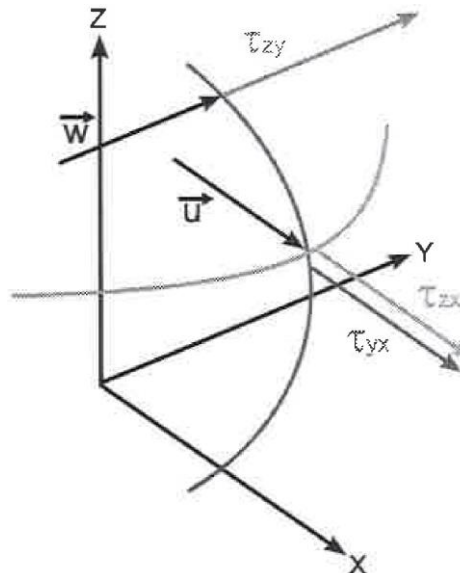


Image 8.5: Scheme of the shear stresses in the speed profile of the channel

With respect to shear stresses, the membrane of the erythrocyte, like that of the thrombocytes, is considerably more sensitive, which, according to the example of the erythrocyte membrane, can be attributed to the double lipid layer, which is unable to absorb shear stresses (*Stryer, 1975; Evans, 1977*).

The marginal values for tolerable shear stress that are mentioned in the literature, or alternatively, damage rates as a function of shear stress and retention period, strongly diverge due to the large scattering range of the biological material and due to different testing equipment and methods, not to mention the different questions that are formulated. For the presently attempted calculation of a blood damage estimate, the descriptions by *Heuser, 1980*, and *Giersiepen, 1990*, suggest themselves, since in both cases, the lysis of the blood corpuscles was examined as a function of the retention time and the shear stress, for only short stress durations. To which extent this allows for a correct quantification at retention times of only a few milliseconds and maximum shear stresses of approx. 400 N/m², is beyond the scope of the present discussion. *Giersiepen, 1990*, offers function contexts for blood damage, but for the present subject of the rapidly operating micro-axial pumps these are only available in an extrapolated form. Further research that was not feasible in the framework of the present study is therefore necessary in order to obtain reliable blood damage rates for whole blood, specifically in cases of extremely short stress durations and high shear stress. When results of such studies should become available in the future, they can be considered at that time.

The following contexts describe the release percentages of corpuscular ingredients, which are a measureable and reliable indicator for respective cell damage (*Giersiepen, 1990, Wurzinger, 1991*):

$$\frac{\Delta Hb}{Hb}(\%) = 3,62 \cdot 10^{-5} \cdot t_{exp}^{0,785} \cdot \tau_{res}^{2,416} \quad (\text{for erythrocytes})$$

$$\frac{\Delta LDH}{LDH}(\%) = 3,31 \cdot 10^{-6} \cdot t_{exp}^{0,77} \cdot \tau_{res}^{3,075} \quad \text{mit: } t_{exp} [s]; \tau_{res} \left[\frac{N}{m^2} \right] \quad \text{for thrombocytes} \quad (\text{Equations 8.5a, b})$$

In light of the resulting stress values, the required flow parameters can be taken from Image 8.5. Two shear stress components result from the speed profile in the channel, and three shear stress components result from it immediately at the housing wall due to the relative speed there, which are positioned at a right angle to each other. From this tri-axial stress situation, disregarding the normal stresses, the resulting shear stress in Image 8.4 can be calculated without a replacement stress as follows:

$$\tau_{res} = \sqrt{\tau_{xy}^2 + \tau_{xz}^2} \quad (\text{in the channel;}) \quad \tau_{res} = \sqrt{\tau_{xy}^2 + \tau_{xz}^2 + \tau_{yz}^2} \quad (\text{at the housing wall}) \quad (\text{Equation 8.6a, b})$$

On iv.:

Beyond that, Equations 8.5a and b also requires the time of exposure to stress t_{exp} . This time can be derived from the local speed which is defined per location and stress, so that the retention time can be determined based on the respective run length and the local speed.

For all regions in the channel, the chord length of the grid is used as a characteristic run length. Immediately at the blade, a redirection takes place due to the significantly different local flow direction with a significant speed component in the radial direction. If, for the characterization of this secondary current, the washing images 7.9a and b and 7.16 are observed for the area immediately near the blade with mean angles of 45 degrees along the blades, as well as Images 7.8, 7.18, and 7.19 of the explicit current filaments for the boundary layers at the wall, it can be observed that even at a small distance from the wall of approx. 0.1 mm, the angle drops to 30 degrees from the main flow direction, and that the impact of the secondary current does not reach beyond approx 0.2 mm. into the channel. Accordingly, the blood corpuscles located within 0.2 mm from the blade remain only briefly

within that high shear zone before they are either drawn into the gap flow by the centrifugal acceleration force, or end up in the large resulting channel swirl.

This also answers the question that follows from Image 8.4 as to the blood damage that can be expected based on the high shear stress at the wall, in combination with the supposedly long retention times based on the lower local speeds in the channel.

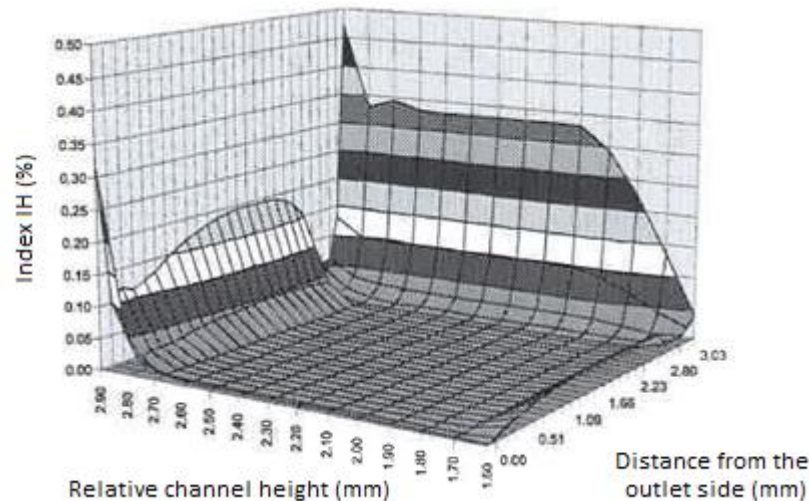


Image 8.6: Damage percentage to the erythrocytes after one run, according to *Giersiepen, 1990*

Based on the results of the flow visualization, the characteristic length for the boundary layers adjacent to the housing wall can only be based on the mean run length of the fluid within the boundary layer, according to the equation:

$$L = \bar{h} \cdot \sin^{-1} 45^\circ \stackrel{\text{here}}{=} 1.98 \text{ mm} \quad (\text{Equation 8.7})$$

For the remaining distance along the blades on the outflow as well as on the intake side, the source terms are indicated according to **viii**.

On v. and vi.:

According to Equation 8.5a, the erythrocytes in the channel shown in Image 8.6 are damaged as a result. It is noteworthy that damage close to the hub is considerable despite the low run lengths, especially along the intake side, and is only put into perspective by the actual volume flow along these zones. However, if Image 8.6 is compared with the mean damage weighted for volume flow as per Image 8.7, it becomes clear that local hemolysis only becomes significant when a large volume flow takes place through these regions. Accordingly, in Image 8.7, we don't find the highest hemolysis along the intake side of the blade, but in the region where the channel borders on the housing, with its additional relative speed and the highest flow speeds along the wall in the direction of the flow.

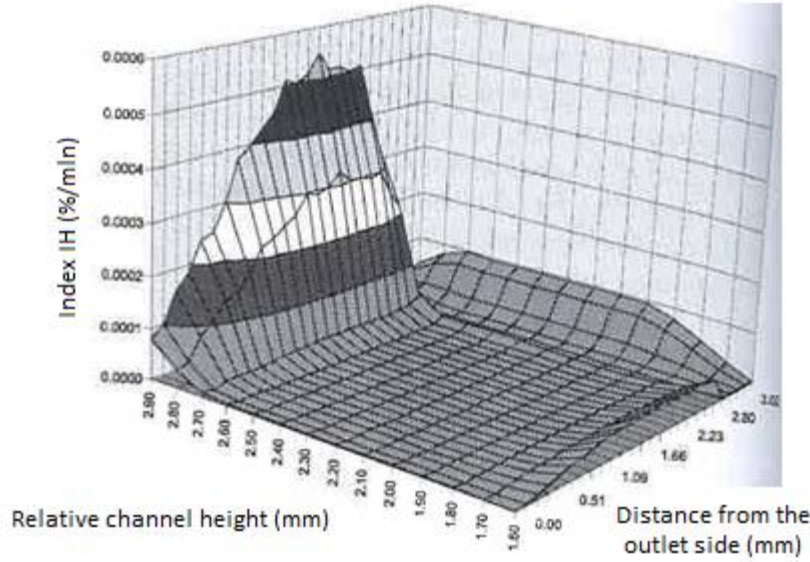


Image 8.7: Damage to the erythrocytes weighted for volume flow percentage after one run

The volume flow-specific hemolysis in Image 8.7 can now be added up for the channel and multiplied for the number of channels, and will thus result in the blood hemolysis after a single passage of the blood through the pump, disregarding all source terms that will be addressed below in **vii.** and **viii.**:

$$IH_{Channel} [\%] = \frac{1}{V_{Res}} \sum_{i=1}^{N_{res}} Z_{Channel} (here = 3) \cdot IH_i [\%] \cdot V_i = 0.01089\% \text{ per passage} \quad (\text{Equation 8.8})$$

On vii.:

The method of superposing locally occurring blood damage which is disregarded in Euler's approach via separate source terms with the results of Euler's approach according to Equation 8.8 is based on the assumption that there is no previous history for the hemolysis presently examined. This presumes that there is no accumulation of damage, and that the damage for each passage through the pump is so small that the starting conditions for whole blood returning to the pump for additional passages remains sufficiently [close to] constant over a period of hours. This presumption is the result of the *in vitro* hemolysis experiments in Ch. 11, in which over a total testing period of 6 hours, a linear increase of plasma hemoglobin could be measured, which is indicative of a degree of blood damage which is constant from passage to passage.

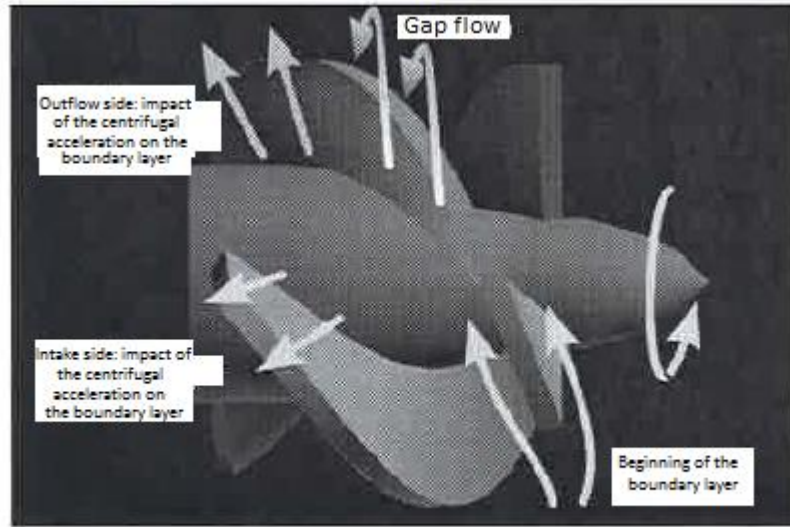


Image 8.8: Schematic illustration of the internal damage terms

In Image 8.8, the various pump-internal damage locations, to each of which a designated hemolysis index is added, are shown schematically:

In the flow direction, a boundary layer is formed in the blade intake side, so that in principle a higher wall shear stress should be expected than in the channel. Moreover, the boundary layer is spun off along all the blade surfaces due to the rotational movement described, so that for each part of fluid that ends up in the channel or gap swirl and does not reach the rotor exit, an internal hemolysis index must be specified. An additional important factor of internal blood damage is the gap swirl, in which high volume flows as well as high shear stresses are encountered. For a characterization of the resulting blood damage, the flow in the gap swirl must be described in terms of the shear stresses, retention times, and volume flows. The latter is done by way of example with regard to fluid particles which, analogous to Particle 30 in Image 7.25, pass along the outside edge of the blade from the outflow to the intake side, as well as by means of a calculation, in order to underpin the results of the few particles that could be evaluated by means of the particle tracking method. The particles pass by the blade, which has a width of 0.3 mm, mostly normally with respect to the blade edge, within $t = 35 \mu\text{s}$, which leads to a speed of $V_{\text{particle}} = 8.57 \text{ m/s}$, which approaches the rotational speed of the blade system of $V_{\text{blade}} = 9.1 \text{ m/s}$ at the design point. If this particle speed is used for determining the leakage, and if the chord length of the blade projected onto the meridional section, the gap height, and the number of blades are taken as relevant leakage gap length, we obtain a volume flow of

$$\dot{Q}_s = V_{\text{particle}} \cdot Z_{\text{blade}} \cdot l_{\text{projected chord}} \cdot h_{\text{gap}} \stackrel{\text{here}}{=} 0.66 \text{ l/min} \quad (\text{Equation 8.9})$$

This leakage flow has a magnitude of 20% of the actually delivered volume flow, and at first appears to be very high. Therefore, the latter is tested by means of a calculation, which poses the problem that the pressure gap between the outflow and the intake sides is not immediately available, as shown in Image 8.9, but must first be obtained by induction from the rotor torque by approximation. From the measurements and from the respective definition of the underlying hydraulic efficiency, in combination with the specific hydraulic performance according to Image 9.3b, the necessary torque at the rotor can be established as:

$$M_{\text{required}} = \frac{\Delta p_{\text{hyd}} \cdot \dot{V}_{\text{hyd}}}{2 \cdot \pi \cdot n \cdot \eta_{\text{hyd}}} \stackrel{\text{here}}{=} 0.56 \text{ Nmm} \quad (\text{Equation 8.10})$$

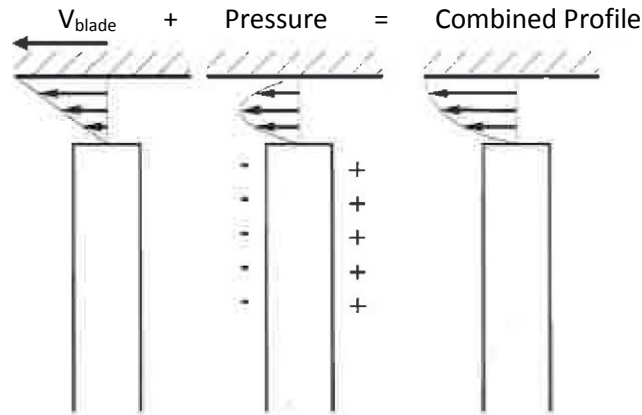


Image 8.9: Schematic representation of the resulting speed profile in the gap flow

The required torque measurable at the shaft results, in turn, from the pressure difference at the blades, multiplied by the meridional projection surface of the blades, since only forces that are applied at a right angle to the rotational axis are relevant to the torque. Every other surface segment contributes to the rotor's axial thrust, but has no impact on the torque applied to the rotor shaft. Therefore, the relevant surface and the radius needed for converting torque into force are derived from the dimensions of the rotor, and calculated from the mean geometrical values:

$$\bar{p} = \frac{F}{A_{proj.-blade}} = \frac{M_{required}}{\bar{r}} \cdot \frac{1}{A_{proj.-blade}} = \frac{M_{required}}{\bar{r} \cdot z_{blade} \cdot l_{proj. chord} \cdot \bar{h}} \quad \text{here } 14260 \text{ Pa (108.4 mmHg)}$$

$$\text{whereas } \bar{r} = \frac{Da_{blade}}{2} - \frac{\bar{h}}{2}$$

(Equations 8.11a, b)

With the mean pressure over the entire blade thus calculated, the gap leakage flow Q_s is now calculated for a gap with a height of h and a mean width of \bar{d} , which results from the to- and from- flow angles at the housing in combination with the blade thickness. The illustration in Image 8.10 shows the context of the individual run parameters and quantities by way of a rectangular blade cross section. P_1 indicates the pressure on the outflow side, and P_2 the corresponding pressure on the intake side. The differential pressure resulting from those two corresponds to the mean pressure \bar{p} over the entire blade as calculated above.

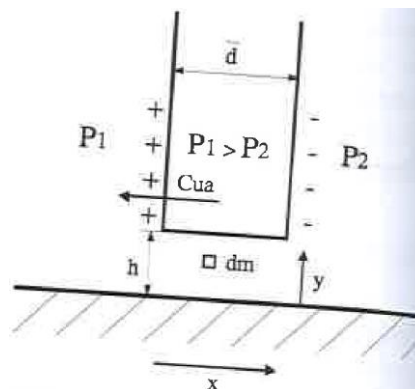


Image 8.10: Schematic illustration of the cross section of a blade end

For the calculation of the leakage volume flow, the retention equations are simplified in the sense that due to the ratio between the rotational width \bar{d} to the height h of the gap, a creeping flow is assumed of which the frictional force is much larger than the force of inertia. In the present case, this leads to the equation:

$$\frac{dp}{dx} = \eta \cdot \frac{\partial^2 u}{\partial y^2} \quad (\text{Equation 8.12})$$

Due to the small gap height, the pressure in the y direction and the speed u in the x direction can be assumed to be constant by a fair approximation, so that in this case, the partials can be replaced by differentials. The double integration in Equation 8.12 for the y coordinate provides the following for the speed u :

$$u(y) = \frac{1}{\eta} \cdot \frac{dp}{dx} \cdot \frac{1}{2} \cdot y^2 + C_1 \cdot y + C_2 \quad (\text{Equation 8.13})$$

The constants can be determined based on the marginal conditions:

$$y=0; u=0 \Rightarrow C_2=0 \quad \text{and} \quad y=h; u=-c_{ua} \Rightarrow C_1 = -\frac{c_{ua}}{h} - \frac{1}{2 \cdot \eta} \cdot \frac{dp}{dx} \cdot h \quad (\text{Equation 8.14})$$

For determining the leakage volume flow, the speed $u(y)$ is now integrated over the entire gap height and multiplied by the projected chord length. The absolute coordinate system underlying the integration must be considered:

$$\dot{Q}_s = l_s \cdot \int_{y=0}^{y=h} (u(y) + c_{ua}) dy = l_s \cdot \left(\frac{1}{12} \cdot \frac{\Delta p}{\eta \cdot \bar{d}} \cdot h^3 + \frac{1}{2} \cdot c_{ua} \cdot h \right)$$

$$\text{whereas: } \frac{dp}{dx} \approx \frac{p_2 - p_1}{\bar{d}} = \frac{-\Delta p}{\bar{d}}; \bar{d} = \frac{s}{\sin((\beta_{1a} + \beta_{2a})/2)} \quad (\text{Equation 8.15})$$

In the present tri-blade example, with an underlying differential pressure according to Equation 8.11a, the resulting leakage is $Q_s = 0.72$ l/min. This is congruent with the results obtained for specific observed particles in the gap flow not only in terms of order of magnitude, but is actually almost identical to it, wherefore a mutual confirmation of the methods may be presumed.

Based on the mean leakage speed and the geometry of the gap, the resulting shear stress and retention time are calculated, such that with Equation 8.5.a, an erythrocyte damage rate per passage results for the gap flow of 0.017%, with $Q_s = 0.72$ l/min. The blood damage in the gap is therefore slightly above that in the channel, and is considered according to Equation 8.16 as a first source term in addition to the channel-specific damage.

On viii.:

Based on the insights on the flow at the blade, for the calculation of the channel-specific damage discussed in **iv.**, only the final part that actually leaves the rotor is considered. For the remainder of the run along the blades, the blood damage occurring near the blades is described by means of separate source terms according to the extent of the damage and the volume flow, which in turn are differentiated by the outflow and the intake side.

For these purposes, for a wall distance of 0 to 0.1 mm, a flow at a flow angle of 45 degrees to the rotational axis is assumed, and for the adjacent boundary layers at a wall distance of 0.1 to 0.2 mm, a flow angle of 30 degrees.

Applied to the mean channel height \bar{h} , the corresponding run lengths of the flow in the direction of the channel can be determined to be $S_{45 \text{ deg}} = 1.98 \text{ mm}$ and $S_{30} = 2.8 \text{ mm}$. In order to describe the entire flow at the blade, these run lengths are considered x times, with $x = S_L / S_{45 \text{ deg}/30 \text{ deg}} - 1$ per blade surface. This, in turn, allows for determining the resulting retention times and the local shear stresses, based on the measured speeds in the flow direction according to Image 8.1, so that all the values necessary for the description of the blood damage along the remaining trajectories close to the blades are now available.

As shown in Image 8.8, based on the boundary layer formation along the blade entry edges, increased shear stresses should be expected as compared to the further progression of the blades. For these purposes, high-speed images were evaluated that were made with the Kodak EktaPro system in subframe mode with $t = 1/40,500 \text{ sec.}$ at the design point of the pump analogous to Image 7.1. Without going into the details of this method, which in principle is very similar to the described particle tracking method, no wall shear stresses were determined for any of the particles near the wall that would be significantly higher than the maximum values in Image 8.4. The highest stress here, which is $t \approx 425 \text{ N/m}^2$, is only slightly higher than the values that can be determined in the channel on the intake side, whereas the mean value of all the particles, which is $t \approx 389 \text{ N/m}^2$, is even slightly lower. This insight can be traced to the limited resolution in time and in place of the analysis system, so that local maximum stresses are simply underestimated.

If one follows the particles observed here in the direction of the flow, with the criterion for the consideration of a particle being its direct proximity to the blade along the blade entry edges, it is noticeable that the particles remain only for a maximum period of $t_{exp} = 0.4$ milliseconds within the range of very high wall shear stresses, before they move away from the wall due to the formation of boundary layers and their resulting displacement. The smallest distance from the blade of the particles as they enter the channel was determined to be $s = 0.08 \text{ mm}$. A displacement thickness-specific distancing of the particles from the wall was observed in all cases to be from the initial distance of $s = 0.08 \text{ mm}$ to $s = 0.25 \text{ mm}$. The impact of particle size and the related mass inertia on the subsequent behavior of the particles was already pointed out in Ch. 7.1.1. For the initially used particles with sizes within the range of 200 to 300 μm , there certainly have been observations of particles that impacted into the surfaces as they entered the blade region. For the presently studied particles in the range of 10 to 20 μm , however, this has not happened. On the contrary: not a single particle was observed that got closer to the blade than the aforementioned minimum distance of $s = 0.08 \text{ mm}$.

Based on the explanations above, no further source terms are given for the fluid entry into the blade region and for the associated formation of boundary layers along the blades, due to the absence of methods that allow for a closer quantification of the locally operating shear stresses. All the damage terms operating locally in the pump in addition besides the channel flow are listed below for the present example:

<u>Source term - type</u>	<u>Volume flow (l/min)</u>	<u>hemolysis (%)</u>
1 - gap flow	0.72	0.014
2.1 - 45° outlet side of blade	0.09	0.002
2.2 - 45° intake side of blade	0.26	0.023
2.3 - 30° outlet side of blade	0.21	0.001
2.4 - 30° intake side of blade	0.19	0.001

Therefore, the rotor-induced hemolysis can now be calculated with a good degree of approximation:

$$IH(\%) = 1/(\dot{V}_{\text{mean volume flow}} \cdot \sum_i IH_i \cdot \dot{V}_i^{\text{here}} = 0.0167\% / \text{passage} \quad (\text{Equation 8.16})$$

If this value is compared with the results of the *in vitro* experiments performed so far as per Ch. 11, the calculated value even falls inside the interval of the experiments, which was not necessarily what was to be expected, due to all the simplifications and the damage model used:

$$IH_{exp.}^{(n=5)} = [0,0038; 0,0187]$$

Conclusion:

More essential than the correspondence in terms of magnitude between calculated and measured hemolysis is the quantified statement, which was never previously made, about the damage percentages that can be associated with the gap swirl and the boundary layer close to the blade, as opposed to the channel. Based on the considerations above, the damage to the thrombocytes can now be determined as well, using Equation 8.5b. With a resulting total thrombolysis of $IT = 0.0626\%$ per passage, this turns out to be high as compared to hemolysis when identical parameters are used. Even if this time too we are not primarily interested in absolute values, the qualitative comparison between thrombolysis and hemolysis with an approximately 4 times higher thrombolysis is significant. This result may in principle explain the drastic reduction of thrombocytes often observed with the hemo pump in patients during otherwise generally tolerable hemolysis (*Aboul-Hosn, 1995*).

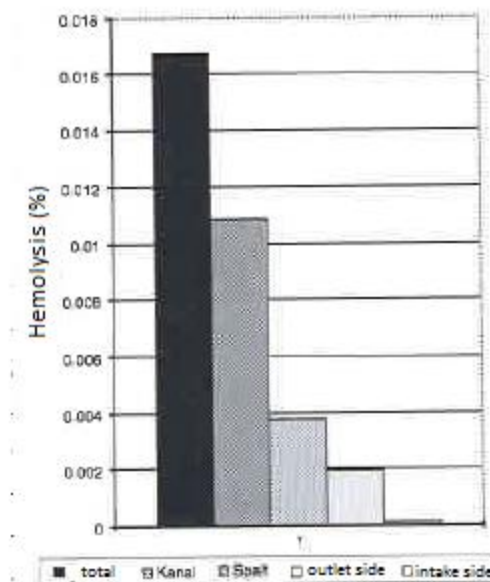


Image 8.11a: Total hemolysis and diversification of the percentages

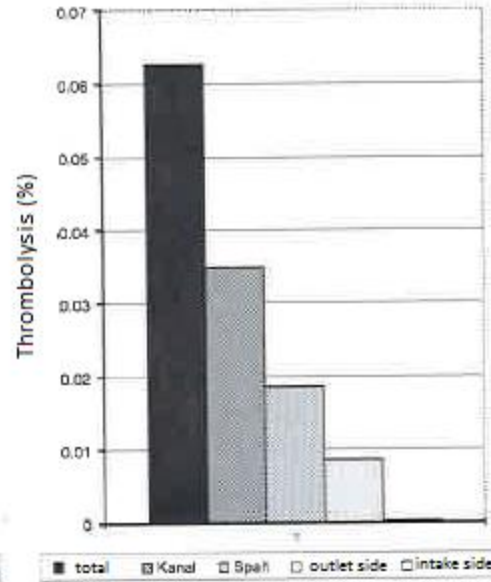


Image 8.11b: Total thrombolysis and diversification of the percentages

8.2 Impact of the Design Parameter on Blood Damage

In the framework of this chapter, some of the various design parameters and operational descriptions will be discussed in terms of the blood damage that can be expected. The purpose is to clarify that despite the few parameters examined, there is a great number of possible variations which jointly have a significant impact on the expected blood damage, and would typically have to be evaluated through tests.

Based on the discussion of blood damage in Ch. 8.1, blade system parameters and system parameters are discussed with the purpose of indicating meaningful limits for pumps in the dimensions examined here, with respect to blood traumatization.

At this point it should be stated again that the following calculated values should not be discussed in absolute terms, but only in relation to one another, since all results are based on the underlying critically examined damage model of *Wurzinger and Giersiepen, 1990*. Independent of the absolute amount of damage, this allows for a good approximation of a blood traumatization tendency as a function of the parameters listed below, wherein a distinction is made between design parameters and operational parameters.

For the basic parameters and settings, the tri-blade rotor grid described in Ch. 8.1 is used, with its chord length of 9 mm and its gap height of 0.1 mm at the design point at a volume flow of 3.1 l/min, a discharge head of 100 mmHg, and a design rotational speed of $n = 30,000$ rpm. The design parameters that vary while the other parameters remain constant include the gap height between the housing and the blade, the chord length of the blades, as well as the number of blades.

By way of a sole operational parameter, a geometrically constant blade system is incrementally reduced by the other parameters, assuming a linearly increasing static pressure in the grid in the flow direction. The resulting grid load leads to volume flow specifically strongly diverging leakage flows, shear stresses, and retention times in the gap and in the channel.

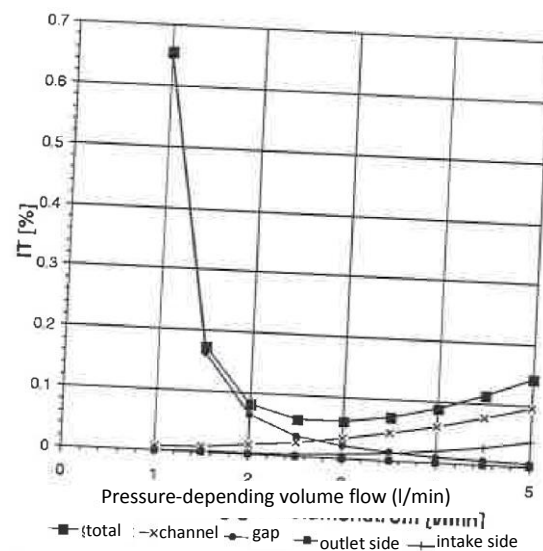


Bild 8.12a: Thrombolysis bei Druckerhöhung

Image 8.12a: Thrombolysis with a reduction of the pump at geometrical basic parameters

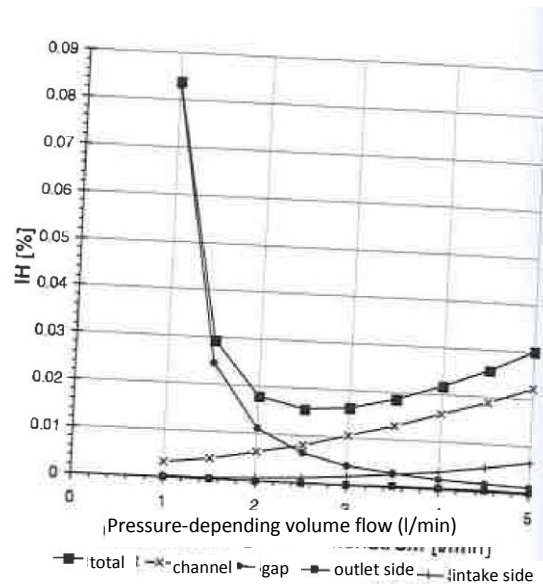


Image 8.12b: Hemolysis with a reduction of the pump at geometrical basic parameters

As one can see in Images 8.12a and b, at strongly reduced operations, most of the damage takes place in the gap and in the large volume flow in the channel itself. This qualitative development corresponds with the *in vitro* hemolysis results from Ch. 11, where blade systems designed for maximum volume flows also generate a higher hemolysis than moderately delivering blade systems of up to 4 l/min at the measured operation point.

In Images 8.13a through e, the impact of the design parameters on the blood damage is summarized (*Schima 1993*):

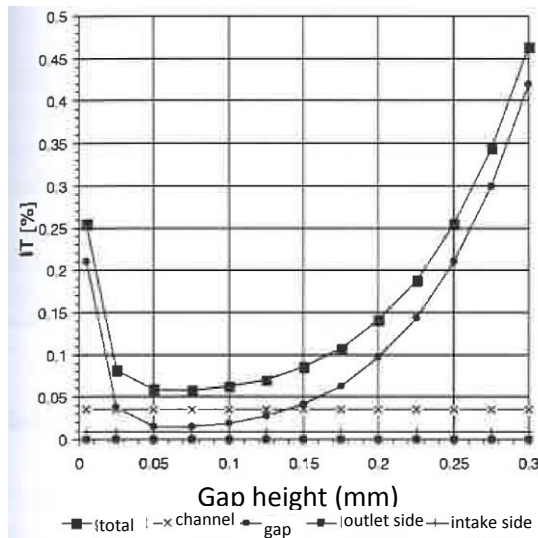


Image 8.13a: Thrombolysis as a function of gap height

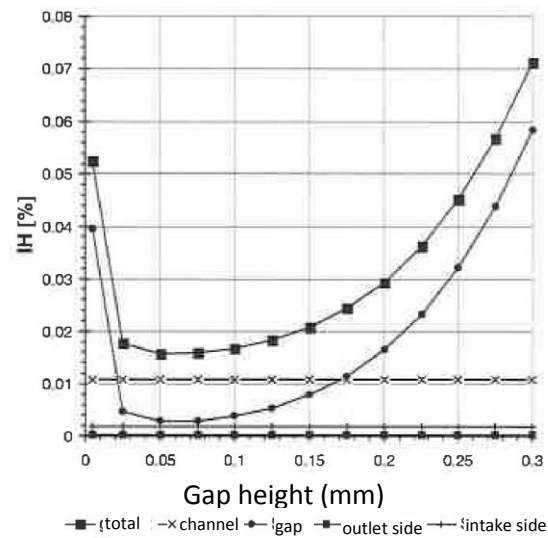


Image 8.13a: Hemolysis as a function of gap height

According to Images 8.13a and b, the gap height of 0.1 mm that was so far realized in all pumps is the best compromise between blood traumatization and manufacturing requirements with respect to form and position tolerances. It becomes clear that gap heights of up to 0.05 mm are useful, so that rotors can be allowed a correspondingly high eccentricity without a disproportional increase in blood traumatization.

This has consequences in terms of manufacturing as well, since such a position tolerance value can still be reached with conventional production means, which has a cost-reducing effect on the manufacturing of the pump.

For the calculation of blood traumatization, which was based on a given chord length, a constant rate of blade system activity was presumed, so that for longer blade system times, the grid load is reduced, analogous to the explanations in Ch. 9.2.1 and Image 9.6. According to Images 8.13c and d, despite the increased gap lengths, this leads to a gap-related reduction to the calculated blood damage. In contrast, the channel-induced blood damage increases proportionally due to the shorter retention times of the fluid in the shear zone, so that the damage resulting from an increase in channel length, taking into account the damage at the outflow and intake sides close to the blade, even increases disproportionately.

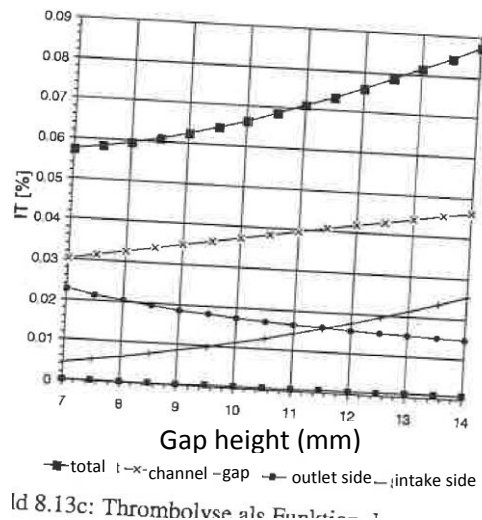


Image 8.13c: Thrombolysis as a function of chord length

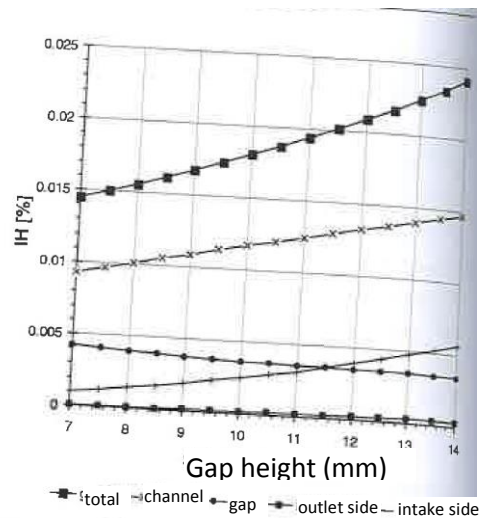


Image 8.13d: Hemolysis as a function of chord length

The impact of the number of blades on the traumatization rate can be derived quantitatively from Image 8.13e. Even though at this time we will not go into a quantitative analysis of these data, it can be established that in principle, a two-blade system induces less blood damage.

Since nothing in the explanations of Ch. 9.2.1 and Image 9.7 points to disadvantages in hydraulic terms, future rotors for use in the relevant application areas should in principle be constructed with two blades.

Finally, if one compares hemolysis with thrombolysis, the higher degree of damage to thrombocytes established earlier in Ch. 8.1 and in Images 8.11a and b is confirmed here as well.

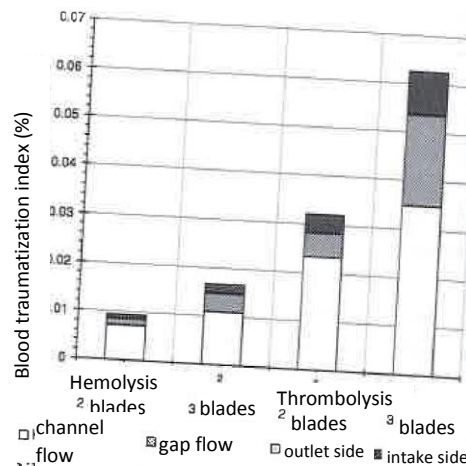


Image 8.13e: Blood traumatization for two- and three-blade rotor grids

If one makes a worst-case assumption that the actual damage rates are within the order of magnitude calculated here, a medium-term use of the pumps should lead to a presumption of an almost complete destruction of a body's thrombocytes. Due to their short lifetime of a maximum of 10 days only, however, their number returns to the physiological level within days of acute pumping.

During and briefly after the use of pumps, a patient's blood levels should be monitored more closely than usual.

9. Hydraulic and Mechanical *In-Vitro* Tests on Lab Samples

While in Chapters 7 and 8 the micro-axial pumps were examined in terms of their impact on flow and the resulting blood traumatization, Chapter 9 examines and analyses the test rigs, selected results related to blade system, and the impact of essential design parameters on the achievable hydraulic performance, efficiency rates, and pump characteristics.

In conclusion, mechanical studies of the lab sample of Version IV are shown with respect to the system in its entirety, in order to experimentally prove the feasibility of this concept.

9.1 Hydraulic Properties of the Blade System Components

The subject of the examinations are results of selected blade systems, which are reviewed not only at the design point or with respect to the design rotation rate with a design volume flow at random capacity levels, but also at their actual field of operation.

9.1.1 Test structure and measuring technology

All blade system components were initially operated in a non-pulsatile test rig, where they were hydraulically characterized. The purpose was to realize a simple structure which can be described by just a few parameters, so that equal test conditions can be used in all subsequent measurements, which is a condition for the reproducibility and verifiability of the results. The structure used here is schematically shown in Image 9.1a, and it is similar to the test rig for flow visualization in Image 7.15, except that in this case the PMMA cover was replaced with a polished metal pump cover, and the pump is taking in fluid from a small cavity here, rather than from a tube.

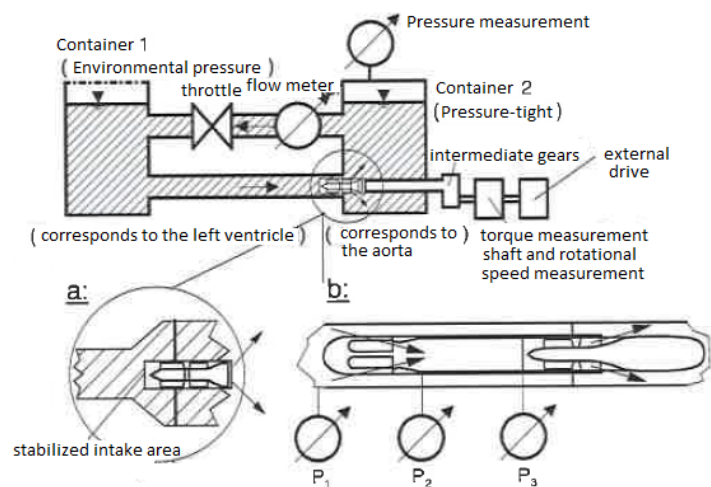


Image 9.1: Schematic Representation of the *in-vitro* measurement structure for hydraulic measurements:

a: of the pump

b: losses at intake and in the pipeline

The pump therefore takes in the fluid from a stable region, which is closer to the actual situation in the ventricle, and also registers the actual intake losses more accurately. For these purposes, Image 9.2 contrasts the hydraulic results of three intake variants in order to clarify how big the impact of the pump position is on the measured hydraulic performance. For these purposes, the blade system was integrated in a housing used for hemolysis measurement, which features tube connections on either side and features a rounded intake. The blade system was then first hydraulically measured with the housing in the tube according to Image 9.1b, and subsequently in the position according to Image 9.1a, first with the hemolysis housing, and finally with a sharp-edged pump cover of its own and without a housing. The results clearly show the impacts of the inflow and outflow losses on the ultimate measureable capacity, and confirm that the standard structure best represents the losses.

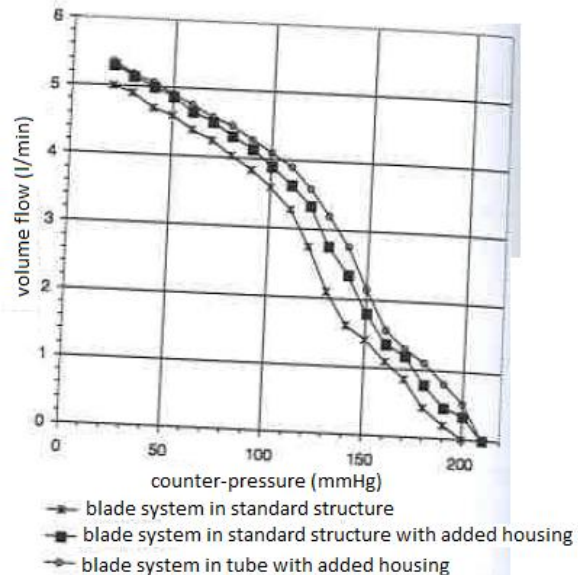


Image 9.2: Identical blade system in different measurement structures at $n = 30,000$ rpm

The entire testing structure in Image 9.1a corresponds, in a simplified form, to the systemic blood circulation, in which peripheral resistance is implemented by means of the choke. Container 1 simulates the left ventricle. When the pump function is entirely taken over by the LVAD as in the present case, the container assumes the function of a reservoir, characterized by an environmental pressure which is both the hydrostatic pressure of the water column and the intake pressure for the pump unit positioned in Container 2. The latter is sealed from the two containers by means of a punctured rubber disk as shown in Image 9.1a, so that no undesired pressure equalization will occur along the pump cover during stationary operation.

As a result, the pump is operating against the hydrodynamically set simulated aortic pressure in Container 2. This pressure is kept sufficiently constant by means of an air cushion in the upper part of the container, where it is measured (Hg manometer; Cobe pressure sensors), so that a stationary operation of the pump at regular operating points can be ensured. The produced volume flow is measured at the outflow from, and, respectively, at the inflow to Container 1, or alternatively, directly before the pump, by means of a flow meter (electromagnetic: Zepeda; ultrasound: Transonic). The pressure in Container 2 is reduced by recirculation via the adjustable throttling of the environmental pressure of Container 1. If the levels of the two containers remain at the same level during measurements, and if the intake to the pump has sufficiently large dimensions for the hydraulic losses in the intake to be negligible, the pressure measured in Container 2 suffices for characterizing the discharge head or the differential pressure via the pump.

A filter integrated in the inlet to the pump for stopping dust particles in particular is essential for the quality of the measurements as well, as these accumulate in front of the rotor blades and significantly reduce the hydraulic performance of the pumps.

While the testing structure described above features the required simplicity of construction, but it has the disadvantage that the ventricle representative by Container 1 is purely passive, so that the characteristic parameters of the blade system are limited to positive pressures and to a single quadrant. *In vivo*, however, the ventricle builds up pressures that may even be higher than those of the aorta, in systolic terms, so that for this period, the pumps see a positive filling pressure which practically helps them with the blood delivery. Such a negative value for the pressure parameter cannot be covered by this simple structure.

When an external drive is used, the measurement technology implemented here does not only include the measurement of the basic hydraulic values of the blade system, but also the recording of the rotational speed and of the rotational torque of the blade system (torque measurement shaft: Dr. Staiger Mohilo + Co. GmbH, Schorndorf; type: IT; version: W). The latter can be derived from a differential measurement of the torque of the blade system with and without fluid at a constant rotational speed. However, if the blade system is measured with an already integrated drive, there is no direct measurement of the hydraulically required performance, since only the rotational speed of the motor and the motor's electrical performance can be measured. Due to the inability to determine the exact electrical efficiency of a drive, which depends to a significant extent on the respective required performance, the hydraulically required performance can no longer be determined based on the motor's electrical performance.

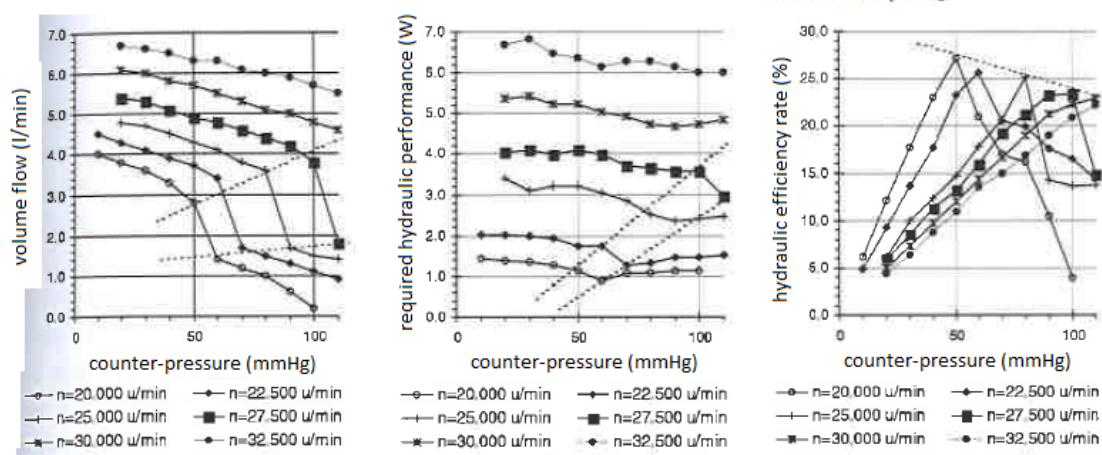
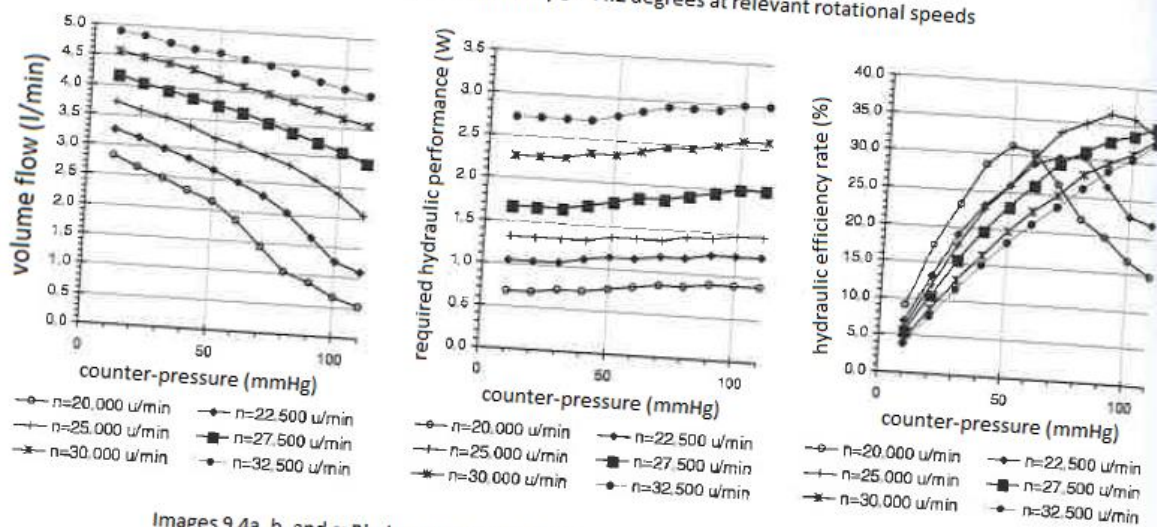
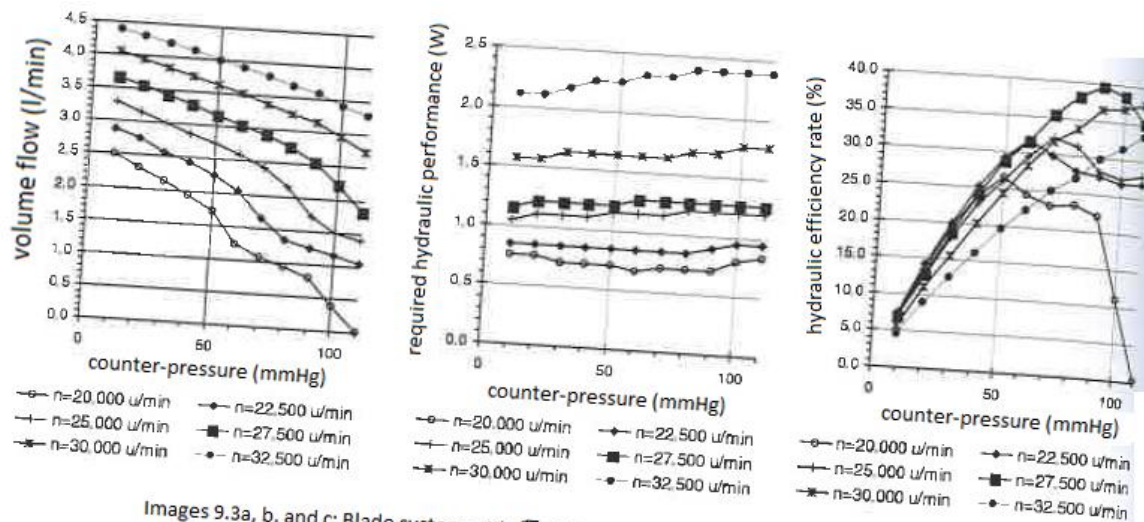
9.1.2 Results for select blade systems

In the framework of this chapter, not all realized blade systems are described. Instead, some representative blade systems with different output densities are introduced.

Images 9.3 through 9.5 respectively characterize in hydraulic terms such blade systems in the rotor and stator that were attested by flow visualization to have a clean flow field around the design point, so that the different hydraulic performances can be ascribed in first instance to the respective designs and the corresponding choice of angle, momentum and enthalpy distribution, without this being attributable to hydraulic deficits. The respective blade systems are characterized analogous to the following Chapter 9.2.1 by the mean rotor outflow angle as a measure for induced performance.

If we now compare the blade systems in Images 9.3 to 9.5 in terms of the hydraulic performance, the disproportional increase of mechanical performance that is required for increasing hydraulic performance stands out. This becomes even more clear when we look at the achievable hydraulic efficiency rates, which decrease with increased pump performance despite the significant increase in hydraulic performance. Even within a blade system, it turns out that the maximum efficiency rate is not at the design point, but usually at a lower rotational speed. If we compare these results with the examinations of internal loss in Ch. 9.2.2, the conclusions overlap: Based on the disproportionally increasing pressure loss in the channels as the volume flow increases, if the flow cross section of the various blade systems is constant, the efficiency rate of achieving a higher hydraulic performance can only go down, since the internal losses are increasing disproportionally.

It must therefore be established that a blade system in our present order of magnitude can either be designed to be highly effective with a low hydraulic performance, or to have a high hydraulic performance with necessarily a low efficiency rate. That certain performance limits should not be exceeded in this case either can be learned from Images 9.5a, b, and c, 9.8. and 9.9.



As explained in detail in Ch. 9.2.1, the blade system causes separation at the rear end of the rotor blades at the intake side, depending on the respective rotational speed and on the counter-pressure, which is reflected in the significant performance losses and in the efficiency rate. These areas are marked by interrupted lines, and clearly correlate with each other. A blade system such as the one shown in Image 9.5 can only be operated with great effort, and moreover, with 5.5 W, it requires so much capacity at the design rotational speed that while operation through a micro-motor is still possible, such a motor does not have any capacity reserves, so that various failure possibilities such as an increased capacity upon the entry of blood into the system can no longer be covered.

9.2 Impact of the Design Parameters on Performance, Efficiency Rates, and Pump Characteristics

In the framework of this chapter, the impact of various design parameters on the hydraulic capacity, the internal losses, and the achievable efficiency rates will be discussed, as well as the related pump characteristics of the blade systems.

Based on the results of the experiments in Ch. 7 and the insights about blood damage in Ch. 8, blade parameters and system parameters, including the intake and outflow regions, are discussed with the purpose of indicating meaningful limits for the pumps in the order of magnitude relevant to our purposes. For reasons of transparency, only 6 mm LV blade systems will be reviewed below. They may provide useful mid-range values between those for the smaller 5 mm pumps and those of the larger 7.4 mm pumps. Moreover, these include more variants, allowing for a sufficiently broad discussion of the design parameters.

In conclusion, a comparison will be made between blade systems with and without a stator, and from this comparison the various delivery characteristics and the counter-pressure stability specifically associated with it can be derived.

9.2.1 Impact of the induced total enthalpy on the performance characteristics

Induced total enthalpy here means the required specific flow effort according to Equation 5.39, divided by the experimentally determined efficiency rates. Depending on the underlying volume flow, according to Ch. 5, the intake and outflow angles of the blade system components can be determined. In what follows, the blade systems are only differentiated by way of the mean outflow angle of the rotor blade construction angle [sic] and the mean distribution ratio, in order to obtain a simple quantification of the induced total enthalpy with otherwise identical channel heights and rotational speeds. The presently examined fractional ratio of t/s according to Equation 5.73a described the impact of the blades on the fluid. The smaller this ratio is, the better the flow will follow the blade contours, but the larger will be the impact of the boundary layer and of the viscosity on the flowthrough volume, as experimentally proven in Ch. 9.2.2 by means of explicit stators. The mean rotor outflow angle, on the other hand, is a measure of the induced speed in the rotational direction, with the lesser flow redirection in turn being determined by the fractional ratio.

The fractional ratio is defined by the grid length, the number of blades, and the wrap. If these parameters are reviewed in the context of the available blade systems, a differentiation by length, respective wrap, and number of blades can be made:

The blade parameters, intake angles, and specifically the mean outflow angle must be kept consistent when determining the impact of the rotor length on the hydraulic capacity in order not to obscure the impact of the rotor length. In Image 9.6., two-blade systems with a rotational speed of $n = 30,000$ rpm are compared to each other in hydraulic terms. A requirement of identical mean blade construction angles and even wrap angles is given with a blade length of 6.2 mm, $\bar{\beta}_1 = 22.8$ degrees, $\bar{\beta}_2 = 65.2$ degrees, $\bar{\gamma} = 174.5$ degrees with a blade length of 8 mm, $\bar{\beta}_1 = 23.6$ degrees, $\bar{\beta}_2 = 70.0$ degrees, $\bar{\gamma} = 176.7$ degrees. The shorter blade system has a higher fractional ratio

here, which is ultimately caused by the shorter blade length. When counter-pressures are small, the longer blade system reaches an overall higher volume flow due to the mean outflow angle, which is larger by 4.8 degrees. However, at higher pressures in the volume flow, it decreases more sharply than the shorter blade system. With the given blade construction angles, these different delivery characteristics cannot be attributed to the only slightly larger mean outflow angle in the longer blade system. Rather, it results from the longer blades and the respective boundary layers, which are thickened as a result of the longer blade. Furthermore, the separations and the resulting blockage of the blade channels in the longer blade version become significantly higher than in the shorter blade version as the differential pressures increase.

In Image 9.7, two geometrically identical blade systems are compared in hydraulic terms, with two and three-blades in the rotor, respectively. This comparison shows the impact that two additional boundary layers along the third rotor blade have on the hydraulic capacity. The additional rotor blade with a wall strength of only 0.3 mm nominally only leads to a blockage of 2.5%. Based on the blockage resulting from the blade thickness and the boundary layer, the three-blade variant generates a volume flow that is smaller by 8%, so that in summary, for small pumps with blade system diameters of approx. 6.0 mm, and at the given viscosities, the number of blades in the rotor should be limited to two at the most.

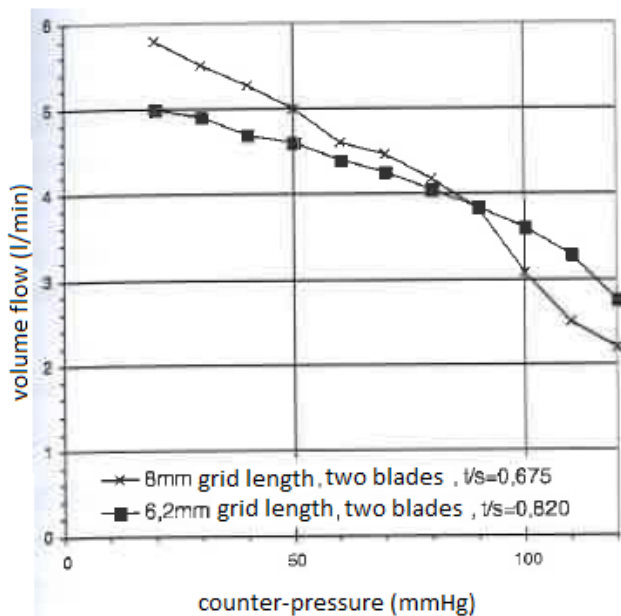


Image 9.6: Impact of grid length on hydraulic capacity

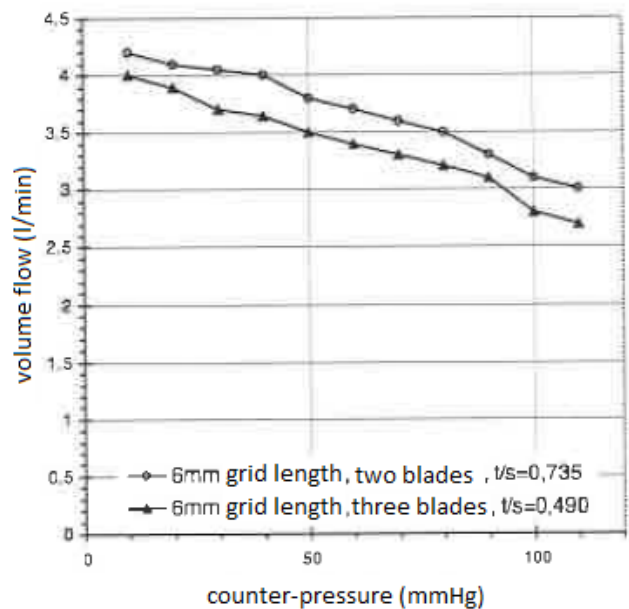


Image 9.7: Impact of number of blades on hydraulic capacity

A further reduction of the number of blades may appear to be advantageous for hydraulic reasons, but is inefficient due to the resulting imbalance in the rotor.

For a definitive assessment of the desirable grid length in the rotor, additional tests are necessary, including, specifically, for hemolytic aspects. It may be stated here, though, that the desired diameter/length ratio is in the range from 0.7 to 1.1. When blades are very short, three-blade rotors are actually slightly superior to two-blade ones in hydraulic terms, so that the most efficient range for the t/s ratio of $\varnothing 6$ mm pumps can be specified as $0.7 < t/s \leq 0.95$.

If the blade system is further characterized by the mean rotor outflow angle in order to obtain from it a measure for the reduced enthalpy in the rotor, an efficient angle range can be determined. Instead of stating an interval for the mean outflow angle, however, it makes more sense to state a critical angle, since depending on application,

the delivered volume flow may be smaller than the maximum possible, so that any angle smaller than the critical angle are efficient in terms of flow.

From Image 9.8, the fundamental relationship between the mean rotor outflow angle and the hydraulic capacity can be derived. For smaller discharge heads, the theory corresponds with the experimental results, so that the blade system with the highest energy density is also the one that generates the highest volume flow.

The example of a blade system designed for maximum performance, with $\bar{\beta}_2 = 94.5$ degrees, with 110 degrees realized at the hub and 88 degrees on the outside, demonstrates that when the discharge head is small, the maximum flowthrough is obtained at the expense of discontinuous pump characteristics, including high differential pressures. In the physiologically still relevant pressure range from 100 to 110 mmHg there is a decrease of the volume flow by 1.75 l/min. Such a pump characteristic is unsuitable for use in a pulsatile environment, since for reasons of volume flow control according to Ch. 10.4, stiff pressure-resistant blade systems are required.

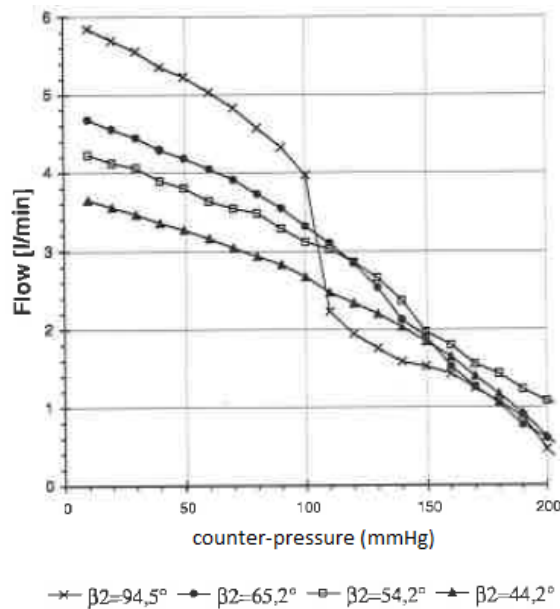


Image 9.8: Impact of the mean outflow angle β_2 on the hydraulic capacity, with $n = 30,000$ rpm

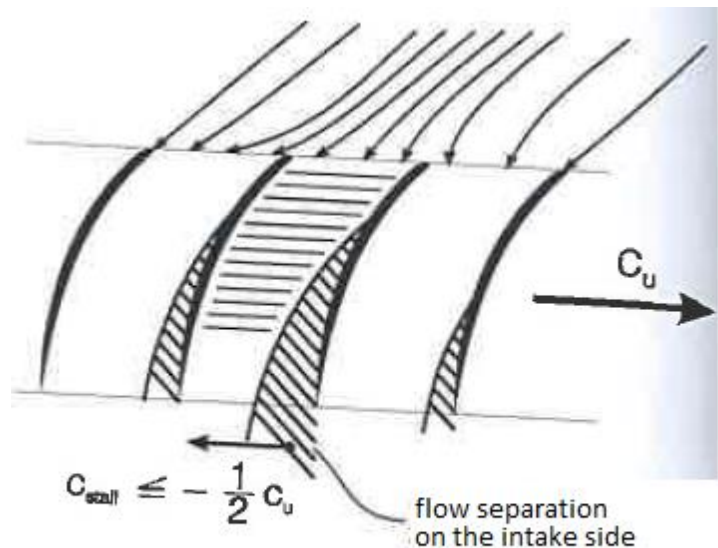


Image 9.9: Principle of "rotating stalls"

As rotor outflow angles become smaller, the throttling of the pumps is so harmonious, however, all the way until the stalling range, that by way of a critical angle, a mean blade construction angle at the outflow of $\bar{\beta}_2 = 80$ degrees can be specified. With increasing differential pressure, no abrupt separation is observed in the blade system on the intake side below this critical angle that would lead to a sudden blockage of the channel.

Flow examinations by means of the tracing method have confirmed that all blade systems listed in Image 9.8 have a rotating stall according to Image 9.9, which engages as of a discharge head of 90 mmHg at a rotational speed of $n = 30,000$ rpm. In pumps with low outflow angles this leads to small cyclical separations close to the blade at the intake side which reach only slightly into the channel, whereas at extreme angles the separation covers a big part of the channel and does not cyclically release it. In this case, the separation is constant over time.

9.2.2 Impact of the channel height on internal losses

For double-curved channels in the present form with channel heights that are low in relation to their width and length, the literature has not indicated any pressure losses as a function of wall coarseness, viscosity, or volume flow that can be compared with what is measured in our case. Attempts to describe the loss of pressure in the channel as an elbow with a rectangular cross-section according to *Miller 1990* would lead to a significant underestimation of the losses. This also applies to the description of the channels as an annular cross section. A more suitable approach is that of *Schlichting 1965; Truckenbrodt 1980; Backé 1988*, which describes the resulting losses as:

$$p_R = \lambda \cdot \frac{L}{D_H} \cdot \frac{\rho}{2} \cdot v_m^2 \quad \text{with:} \quad v_m = \frac{4 \cdot \dot{V}}{\pi \cdot D_H^2} \quad \text{or} \quad \frac{\dot{V}}{A_{real}}; \quad D_H = \frac{4 \times \text{flow area (A)}}{\text{sum of all rotations (U)}} \quad (\text{Equation 9.1a, b, c})$$

λ is described here for a rectangular cross section as $\lambda = C / \text{Re}$ in the laminary range, and as $\lambda = A \cdot 0.316 \cdot \text{Re}^{-1/4}$ in the turbulent range, in analogy to Blasius. The constants A and C are form constants which describe the height to width ration of the rectangular channel according to *Schlichting 1965; Truckenbrodt 1980*, so that the calculation of the pressure loss is based again on the equivalent hydraulic diameter with an annular cross section. For the calculation of the Reynolds number from the real flow cross section, the resulting mean speed is based on the underlying volume flow, whereas for the calculation of the pressure loss, the mean speed is based on the equivalent hydraulic diameter.

Considerations for $\lambda = \text{constant}$ and $V' - v_m \cdot D_H^2$ indicate a dependence of pressure loss on the hydraulic diameter, and with respect to the channel height, which is significant here in the form of $p_R \sim 1/D_H^5$. This demonstrates how important the channel height is, and that maximum possible channel heights must be attempted in order to keep the system-specific inner losses as low as possible.

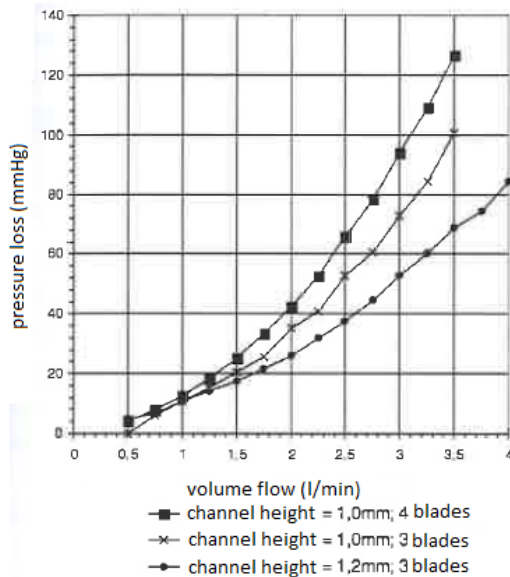


Image 9.10: measured pressure loss
for $\eta = 3.0 \text{ mPa} \cdot \text{s}$

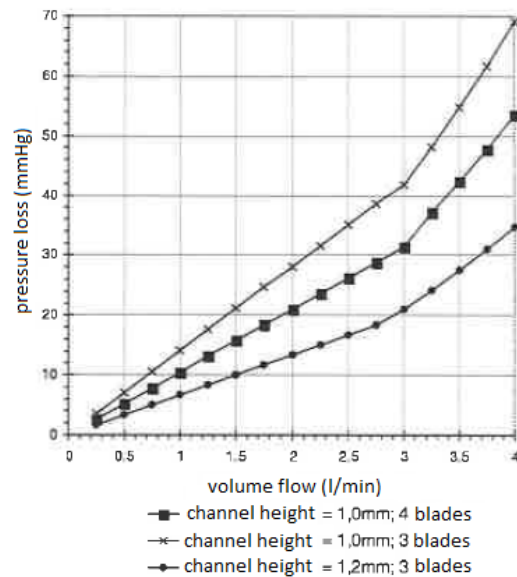


Image 9.11: calculated pressure loss
for $\eta = 3.0 \text{ mPa} \cdot \text{s}$

In view of the multiple assumptions and simplifications that were made for the purpose of calculating channel losses, the following experimental validation was done: The calculation of the losses is necessarily unprecise, since based on the preliminary flow visualization tests in Ch. 7, the impact of all the secondary flows in rotational and axial direction resulting from the double curve cannot be registered.

For the purpose of experimental validation, three stators identical in terms of blade geometry but with different numbers of blades and channel heights were integrated into a suitable testing rig, such that the through-flow of the stators changes from $\alpha_2 = 90$ degrees at the outflow to a mean $\alpha_1 = 45$ degrees at the intake in order to allow for an incident-free intake. Based on the cylindrical hub in the stator region, it can be predicted with a fair degree of approximation that the channel losses thus measured are similar to those when the system is operated with a rotor with incident-free intake. Only the swirling outflow in the experiment with its scarp at the edge of the rotor hub may cause all the measured values to be higher.

Comparative studies of [the impact of] the number of blades and of channel height on pressure loss can be done independently, so that their impact on internal losses on such small pumps can be quantified here for the first time ever based on examples.

It is impossible to perform similar tests at either the intake or the outflow of existing standing rotors due to blade construction angles deviating sharply from 90 degrees.

By means of the example studies here of stators with flow directions reversed from those in the description above, it was already possible to demonstrate that an impulsive intake at a volume flow of 3 l/min leads to additional pressure losses of approx. 24 mmHg.

In view of the geometrically identical pressure measuring points before and after the stator, the difference measured can be categorized as a pressure loss. The stator pressure losses thusly measured and adjusted for system-specific losses between the pressure measuring points are documented in Image 9.10. A comparison with the calculated pressure losses according to Image 9.11 shows that the latter are lower than the measured values in absolute terms by a factor of two. Whereas the channel height-specific pressure loss still correlated with the measurements according to Image 9.12, the calculation no longer includes the boundary layer influx in cases of three to four blades. This error results from the hydraulic equivalence diameter according to Equation 9.1c, which undervalues the channel of the four-blade stator based on its rather quadratic profile, as compared to the three-blade stator with an identical channel height and a larger width, in terms of pressure loss.

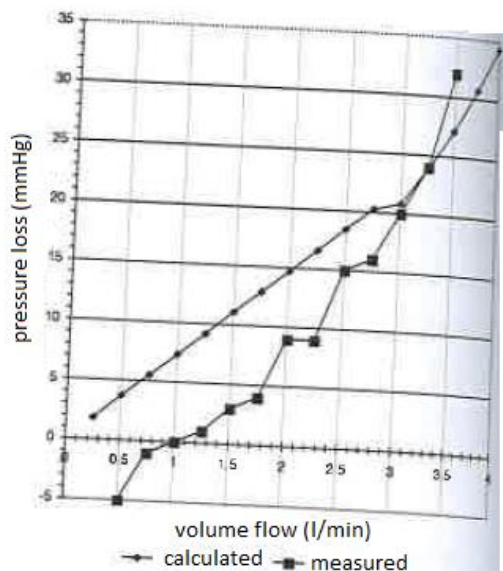


Image 9.12: Pressure loss difference in the stator for $\Delta h = 0.2$ mm, with $\eta = 3.0$ mPa · s

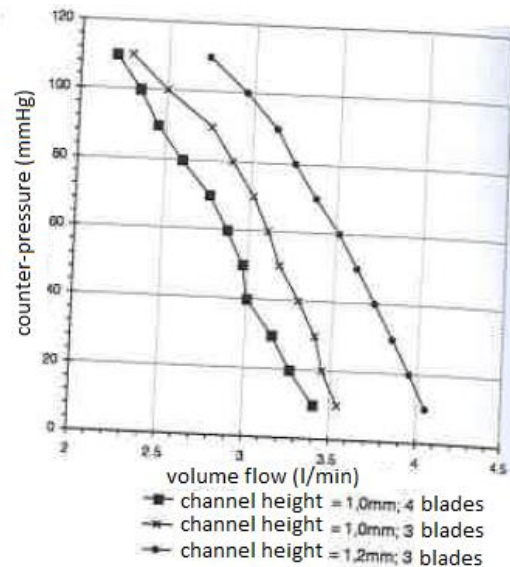


Image 9.13: Stator characteristics with corresponding rotors for $n = 30,000$ rpm, with $\eta = 3.2 - 3.6$ mPa · s

The pressure losses measured according to Image 9.10 correlate with a fair degree of approximation with the corresponding pump characteristics in Image 9.13, if we disregard the counter-pressure characteristics of the pumps which depend on internal losses, as described in Ch. 9.2.3. They have been recorded with geometrically

identical rotors which fit the respective stators in terms of channel height. If one compares the discharged head as measurable from the outside at identical volume flows, the pressure difference between the pump versions is on average higher than that of the separately measured stators. This is a result of the additional internal losses that can be allocated to the rotors. Without going into a detailed evaluation of the measurements, which are error-prone due to the measurement tools and methods, it can be stated that the internal losses in the relevant volume flow region between 2 and 4 l/min are significant. If, for instance, for a Ø6 mm LV pump, the internal losses, of which the order of magnitudes known, are added to the intake, tube, and free jet losses, a blade system must build up a total pressure of 250 mmHg at an externally measurable discharge head of 100 mmHg at 3.5 l/min. According to Ch. 9.1.2, measurements of the externally measurable hydraulic capacity with respect to the mechanic capacity of the rotor lead to hydraulic efficiency rates of 15% to 30%. The efficiency rates, which are very low compared to those of large pump systems, can be easily explained by the internal losses, as well as by the not yet considered gap flows according to Ch. 8.1.2 vii in the rotor. When the loss components are more closely analyzed, it becomes clear that the efficiency rate of the pumps cannot be arbitrarily increased. Rather, most losses are caused by the high viscosity of the fluid.

If, alternatively, the hydraulic efficiency rate is calculated by taking into consideration the entire pressure, and if even internal leakages are considered as an additional volume flow, the rotor-specific efficiency rate can be determined as

$$\eta_{\text{rotor}} (\%) = \frac{V'_{\text{external} + \text{internal}} \cdot \Delta p_{\text{total}}}{P_{\text{mech}}} \cdot 100 \stackrel{\text{here}}{=} 45\% - 90\%$$

Accordingly, the conversion losses resulting from [the conversion of] mechanic into hydraulic energy as well as the flow losses caused by reasons of geometry is relatively small. The hydraulic efficiency rate can therefore only be increased to a limited extent by way of larger channel cross sections, which in cases of limited dimensions can only be accomplished by way of a reduction of the blade surface and the hub size.

Alternatively, in Ch. 9.2.3, hydraulic characteristics of stator-less systems are contrasted with those of systems with stators in order to answer the question of whether a stator in the hydraulic capacity range discussed here is needed. In view of the internal losses in the stator and the response rate according to Ch. 5, a stator-less system may certainly be equivalent or even advantageous, in hydraulic terms, for production quantities up to the presently relevant level.

9.2.3 Impact of the internal losses on the pump characteristics

Based on the considerations on internal losses in Ch. 9.2.2, which include tube and intake losses in case of an integration of an intake or pressure tube, a first qualitative analysis of the pumps can now be made, and in this case specifically, of the counter-pressure characteristics.

If the blade system is considered to be an ideal voltage source, the pump as a whole can be described as an ideal voltage source with internal resistances, and the installation as an external resistance which causes the measurable hydraulic capacity to decrease.

With an ideal voltage source without internal resistance, this simple equivalent electrical circuit diagram according to Image 9.14a leads to a vertical in the I - U diagram as in Image 9.14b, and the analogy to the V' - Δp diagram in Image 9.15 is given. In this idealized case, even a small external resistance or a small change in such a resistance will lead to a strong impact on the flow. Image 9.14b shows the change of the external resistance at explicit data points on the curve. The resistance varies from point to point in the given diagram by 5 Ω , between a starting value of 20 Ω and an end value of 100 Ω . In the context of pumps, this load-dependent behavior is referred to as pressure-sensitive. Only when the drawn internal resistances are considered, the load behavior at the external resistance changes, such that as the internal resistance increases, the vertical becomes more diagonal.

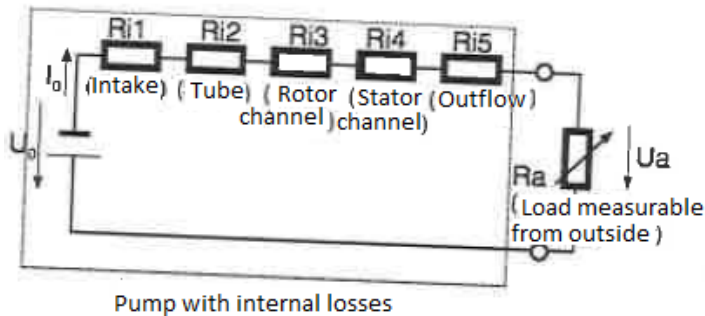


Image 9.14a: Idealized equivalent electrical circuit diagram of a pump with quasi stationary operation

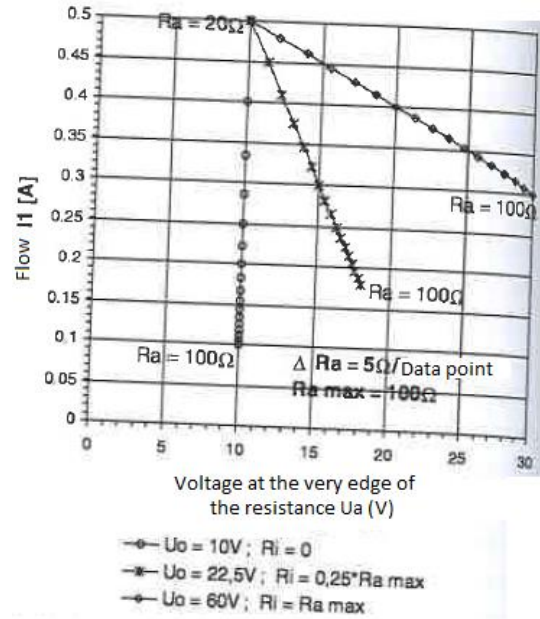


Image 9.14b: Exemplary flow development as a function of the adjustable external resistance and internal losses

Accordingly, the flow that is measurable now appears to belong not only to one voltage, but in case of a large internal voltage and a small external one it may even appear to be independent of resistance, and therefore as an ideal current source of which the current is independent of externally applied resistance. This situation would correspond to an extremely stiff pump.

The example shown in Image 9.14b is based on voltage sources adjusted for the respective internal resistance, in order arrive at the same starting conditions of $R_a = 20 \Omega$. With the voltage source being constant, the increase of the internal losses leads in practice to an analogous decrease of the sensitivity to load, but at the same time also to an overall lower capacity that is available on the outside. This can be observed in Image 9.15. Here, an identical rotor was hydraulically characterized in a respectively identical testing rig, with the internal resistance R_{i2} (tube) and R_{i4} (stator) were successively removed, analogous to Image 9.14a. If one proceeds to compare the pump behavior visible here with the considerations above, the analogy is obvious. The pump with the lowest internal resistance delivers the most at low loads, but is correspondingly load-dependent in terms of production characteristics. Conversely, a higher degree of counter-pressure stability is obtained here in exchange for an overall lower volume flow at a lower counter-pressure due to the higher internal losses.

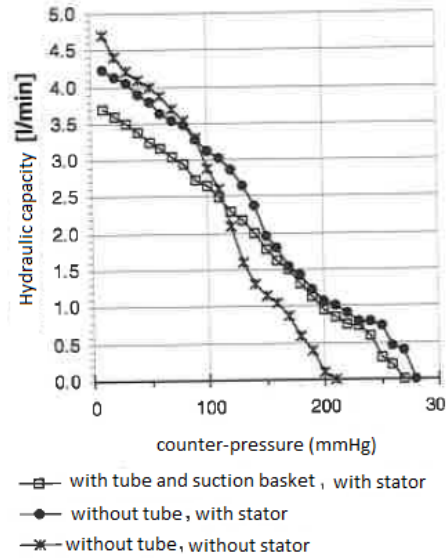


Image 9.15: Rotor with $\beta_2 = 54.2$ degrees
 in various configurations,
 $n = 30,000$ rpm

In Image 9.15, the flow-mechanical impact of the stator is superimposed on these basic explanations on production characteristics, specifically for higher production heights of > 120 mmHg. Consequently, the stator systems can ultimately achieve a higher counter-pressure than stator-free blade systems. Depending on the indication and on the ultimately required production, a stator-less system may be advantageous for physiological use despite the associated increased sensitivity to load, due to the higher maximum flows that can be achieved. The example in Image 9.15 makes it clear that up to an exploitable production level of 90 mmHg, the stator-less system has a higher hydraulic capacity than the corresponding stator system. If the tube losses of approx. 10 to 20 mmHg are subtracted from this production level, the remaining production level is 70 to 80 mmHg, up until which level a stator-free system is to be preferred. Accordingly, the assumption in Ch. 5 of making only stator-free RV pumps is correct. Even for LV pumps, a stator-free system can be advantageous when the average production level measured over the heart cycle is not significantly higher than 70 mmHg.

In stator-free cases, the same design limits apply to rotor blade systems, as counter pressure-dependent flow separations are even more obvious than in corresponding stator-driven systems. For the blade system characterized in Image 9.5, this leads to a maximum volume flow of 7 l/min without counter-pressure at $n = 30,000$ rpm, which is therefore almost one liter above the corresponding design point in the stator. For increased production levels, without stator, separation occurs 20 mmHg earlier, however, and leads to considerable blockages. From 90 to 100 mmHg, the volume flow drops here by the unacceptable amount of 3.4 l/min, as opposed to 2.1 l/min.

If a pump is used with a maximum externally available capacity, the principle of capacity adjustment, known from

electronics, can be used. In this case, an external resistance, $(R_i = \sum_{k=1}^5 R_{i,k})$ is applied to the external resistance R_o according to Image 9.14a in order to access the maximum capacity at the external resistance at a constant voltage U_0 of the ideal voltage source. This leads to an external capacity P_a as follows:

$$P_a = U_a \cdot I_0 = I_0^2 \cdot R_a = U_0^2 \cdot \frac{R_a}{(R_i + R_a)^2} \quad (\text{Equation 9.2})$$

If a first derivative is made of Equation 9.2, and set to zero, the result is:

$$\frac{d(P_a)}{dR_a} = U_0^2 \cdot \frac{R_i - R_a}{(R_i + R_a)^3} = 0 \Rightarrow R_i = R_a \quad (\text{Equation 9.3})$$

For this result, in turn, the second derivative is negative. Therefore, in case of an identical internal and external resistance, the maximum external capacity can be accessed. If the description of the utilizable pressure is compared with that of the dissipated pressure in the pumps according to Image 5.5, it turns out that the requirement for similarly large resistances in analogy to the dissipated capacity has been met. According to this view, to a degree, internal losses are even necessary for maintaining a pump with exploitable pump characteristics.

This one-dimensional view should not tempt us, however, to integrate artificial resistances in the pump systems reviewed here. Based on the requirement of a high hydraulic capacity within an extremely limited space, the internal losses, which are unavoidable anyway, must still be reduced to the extent that this appears to be possible. This is the closest one can get to meeting the requirement of a high internal loss capacity similar to the externally exploitable capacity.

Conclusion:

According to Equation 9.3, the maximum externally exploitable hydraulic capacity is limited to 50% of the overall capacity brought into the system. Correspondingly, an efficiency level measured according to Equation 5.1 of a maximum of 40% in Image 9.3c is already close to the achievable optimum of 50%.

9.3 Flow Control on the Intake and Outlet Sides of the Pump Under Operating Conditions

A discussion of the intake and outlet sides is important because these fields cause significant system (pressure) losses which must be produced by the pumps according to Image 5.5 in addition to the exploitable pressure.

Intake side

The intake side is subject not only to hydraulic requirements, but in first line to physiological requirements as well. On the one hand, intake losses should be small, on the other hand, the limited diameter and the requirement of a maximum hydraulic cross-section do not allow for a geometrically rounded intake opening in the intake tube. Moreover, the intake must be shaped such that the suction of the endocardium by the opening and its subsequent adhesion to it can be securely avoided, even given the smallest ventricle cavity. As a result, the intake may not feature a large central opening that might suck in the endocardium and cause it to attach itself to the opening. Moreover, despite minimal wall strengths, the intake opening may not appear to have sharp edges on the outside, since it must pass through the aortic and pulmonary valves with them in a retrograde manner, and no damage to the thin valve leaves can be tolerated. One of the few practical solutions therefore envisions an intake opening with a basket, of which the lateral openings must have a length of approx. 15 mm in order to securely avoid the sucking in by the basket in apex position, despite the smoothing of the biological material (trabeculae). On the other hand, the flexibility of the biological material might cause the endocardium to press closely to the basket, and consequently, the total obstruction of the lateral openings.

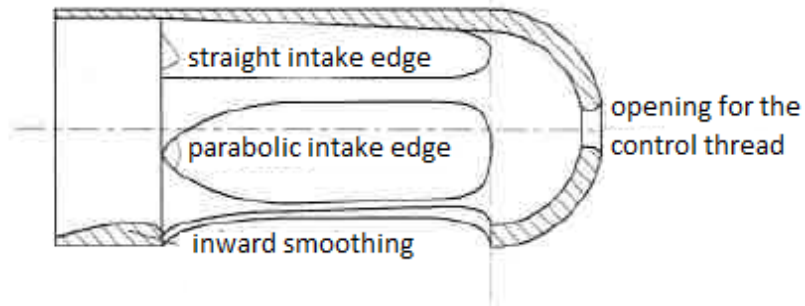


Image 9.16: Basket at the intake side of the intake tube

In Image 9.16, such a basket is shown, with possible inlet geometries. The clearly visible domed structure and the lateral openings, separated by a total of three to five ridges, are shaped such that when it is inserted, injury to the valve system can be safely avoided. The transition to the intake tube is directly near the lateral intake openings. This transition is characterized by a pronounced beam contraction at the edges. The unavoidable separation area immediately near the edges provided the impulse for geometrically exploiting this region and to move the smoothing inward into the dead space. The result is an improved washing behavior, while the intake losses remain at the level of a geometrically sharp-edged intake.

A further approach is based on the underlying thought that the size of the beam contraction is functionally linked with the flow speed along the intake edge. If it is possible to increase the effective length of the intake edge by means of a corresponding geometric design, the resulting intake speed of the flow would be reduced while the general volume flow is constant, and losses would be reduced. This artificial extension of the effective length of the intake edges was exemplarily accomplished by means of an annular and a parabolic profile of the intake edge between the ridges. As compared to a straight edge, this allowed for a length increase of approx. 48%.

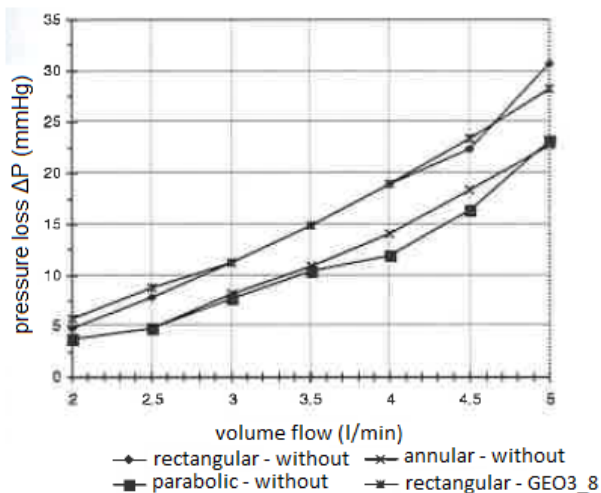


Image 9.17a: Pressure losses for the various basket geometries

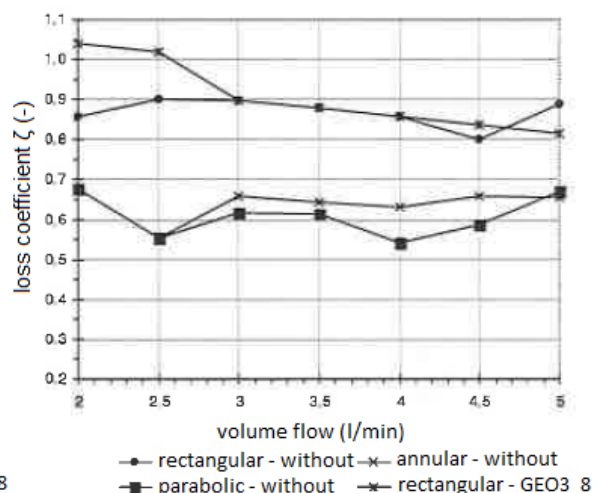


Image 9.17b: Pressure loss coefficients for the various basket geometries

Measurements of the reduction of the intake losses thus achievable prove that this approach is effective. The parabolic intake leads to a lightly lower pressure loss than the annular intake. This can be explained by the good washing behavior without visible color residue immediately after the intake edge. The pressure loss coefficient shown in Image 9.17b can be calculated per the definition that follows:

$$\zeta_v = \frac{\Delta p_v}{p / 2 \cdot v_2^2} \quad \text{with: } \Delta p_v = p_1 - p_2 - \Delta p_{\text{Bernoulli } 1-2} \text{ and } \Delta p_{\text{Bernoulli } 1-2} = \frac{8 \cdot \rho}{\pi^2} \cdot \dot{V}^2 \cdot \left(\frac{1}{D_2^4} - \frac{1}{D_1^4} \right) \quad (\text{Equation 9.4})$$

Here, p_1 and p_2 are static pressures measured immediately before the basket at a diameter of D_1 , and in the intake tube immediately after the basket at a diameter of D_2 . According to equation 9.4, the lost pressure Δp_v is adjusted for its dynamic share, so that even a simplified structure according to Image 9.1b can be used, with a measurement section inside the tube segment.

Measurement of pressure losses in cases in which the basket region gets its intake from a large and still reservoir have not confirmed the results from Images 9.17a and b. The parabolic, annular, and rectangular intake edges are similar in terms of losses, so that under these conditions, only the improved washing speaks for an artificially elongated intake line.

Outflow side

In hydraulic terms, the outflow side is an annular gap which is delineated on its inside by a diagonal hub, and on its outside by the rear edge of the pump casing. According to the calculations in Ch. 5.4, it must be presumed that the entire kinetic energy is dissipated in the free jet, especially since in the outflow region there is no room for a diagonally shaped diffusor, which could significantly slow down the flow. Instead, care should be taken that the annular channel does not operate as a screen. Experiments with a constant channel diameter calculated based on the orthogonal radii to the delimited surfaces showed maximum throughflows at lower production levels that were measurably worse than those of widened channels. Only after an approx. 30% expansion of the outflow diameters as compared to the channel diameters in the blade region, a lower outflow-induced capacity of the pumps was no longer measurable, and as a result, the impact of the beam contraction along the outflow edges was compensated.

The outflow side of the pump is further characterized by the functional link to the drive positioned behind it, due to which the outflow is diagonal, as described. Based on electro-mechanic principles and the extremely small dimensions, at an electrical effectiveness rate of below 30% when fully loaded ($P_{\text{mech}} = 5 \text{ W}$), this drive dissipates up to 11.6 W of energy, which must be transferred via the housing surface to the blood, as the surrounding medium. Due to the small motor surface and the marginal temperature of 41 °C to 42 °C in the blood, heat dissipation must be done convectively, as described in Ch. 4.4.2. For these purposes, the blood flowing out of the pump with its free jets should flow as completely as possible along the surface of the motor, as shown in Image 7.31 and 7.32, and should not separate immediately after the outflow due to its remaining momentum and the diagonal redirection. This tendency is pronounced especially in stator-less LV pump variants. To which extent this may lead to thermal problems on the motor surface can only be analyzed in future *in vivo* experiments.

9.4 Mechanical Testing of the Pump with Integrated Drive

After the successful synthesis of pump and drive, a first mechanical system analysis is needed in order to prove whether an intravascular micro-axial pump with an integrated drive is a feasible concept.

While proof of the drive capacity was already provided in Ch. 4, and the principal proof of the feasibility of the friction seal integrated into Concept IV was provided in Ch. 3, the system has to be subjected in conclusion to a first long-term test.

Initial long-term tests:

The extensive field of material testing is specifically excluded from the present scope, even though the question of materials used for a technical system applied in a biological environment has a high priority. For example, all adhesive connections between the individual assemblies must meet the highest safety standards, and due to the different material pairings these will be resolved in very different ways. However, in the framework of a mostly

structural systems analysis, this complex of themes cannot be dealt with comprehensively, so that we will suffice here by indicating its importance.

In the framework of a structural analysis, only the validity of the concept is examined, including the robustness, reliability, and durability of the first laboratory sample according to Concept IV from Ch. 3.2.2 with a polymer friction seal.

This pump concept has been used in ongoing *in vitro* tests, and examined here explicitly for its durability. The parts of the pump with an integrated motor that are principally subject to wear and tear include the bearings and the seals, whereas failure criteria also include the rupture of the energy cable or the blocking of the drive as a result of strong corrosion of the motor magnet.

With respect to the durability of the bearings, we will dispense here with the manufacturer's respective calculations, which guarantee a minimum lifetime of several months for all used bearings under optimal climatic conditions. For pumps that will be used for a maximum period of one week, this is a satisfactory safety guarantee. Under actual operating conditions, the bearings are exposed to a corrosive medium with a 0.9% NaCl component, and they operate free of grease or oil at relatively high rotational speeds and at changing axial loads due to the pulsatile pump environment. Accordingly, it was examined whether a system consisting of a rearward miniature bearing balls system and combined radial sliding bearings with seals can be operational for more than just a few hours. A first test of such a pump in water at $n = 30,000$ rpm and a differential pressure of 100 mmHg in a non-pulsatile environment was terminated after 144 hours (6 days) since until that point, the system has operated with a constant engine run and without visible leakages.

The subsequent analysis of the component assemblies showed a 0.2 ml leak in the pump mechanics due to clearly visible wear and tear of the shaft. At a circumference of approx. 120° , the TiN film of the shaft was already so worn out that the basis material of the axis was visible. Due to the leakage, the motor magnet, made of NdFeB, which is a corrosive material anyway, was clearly affected by pitting corrosion, but not yet to such a degree that it would have led to an increase of the pump's operating momentum. The combination of radial bearing and seal did not feature more than a single initial mark of wear. The rearward ball bearings of corrosion-resistant steel had suffered from a small degree of corrosion as well, but continued to operate mechanically without flaw. Based on the low degree of wear and tear, the system was reassembled without modification and tested on a 6 hour *in vitro* blood environment, in which, due to the expected seal failure, it was rinsed with a 10% glucose solution similar to a hemopump system. After this period, only the axis showed even stronger wear, whereas the bearings specifically did not suffer further damage.

This experiment as well as individual tests, partially in pulsatile environments, which at this point add up to a cumulative operating time of such pumps of approx. 500 operating hours, did not produce any structural weak points that would require a fundamental new construction. Only the recurring wear of the shaft in the seal region will have to be reduced by an appropriate hardening treatment, since leakages in the pump mechanics were always preceded by significant wear of the shafts.

In conclusion, this system, which will usually be operational for only a few hours, can be attested as having sufficient robustness and operational security, which, however, are yet to be confirmed in extensive *in vivo* experiments. In this respect, a failure analysis exceeding the scope of the present principal functional analysis will be required, which is not within the scope of the present principal functional analysis. In Ch. 12, the principles of the function of the entire system in the organism will be shown in the framework of initial experiments, as these will conclusively prove the principal validity of an intravascular blood pump with an integrated drive for heart support.

10. Pump-ventricle interaction and pump function control

The existing research of the pumps has always been performed in non-pulsating environment and, therefore, provides insufficient description of how the pumps function in the real situation in pulsating environment, which always exists when there is remaining heart activity.

The clinical part of this study, which serves as the basis of the in vitro results /Siess 1996/ provided in detail below, was performed by Prof. W. Flameng and Prof. B. Meyns at the Leuven Catholic University in Belgium /Meyns 1996/.

Sternotomy Hemopumps Hp31 were used for this type of research, since they were easily available in the clinical work, and could also be better used in vitro due to the used measurement technique. Specifically, the used electromagnetic flowmeters by Zepeda Instruments, which could be directly integrated into suction tubes of the pumps with their inner diameters of 6 mm and 7 mm, did not allow for application of the systems with integrated micro motor discussed in this work, since the rotating magnet field in the motor stator affected the measuring heads so strongly that the measurement signal was covered by noise.

This problem did not present itself for obvious reasons with the Hp31 driven by a flexible shaft. Besides, it does not matter for the description of pumps, which pump system is used, since they work according to the same principle, and are even hydraulically similar, so that all results can be immediately re-applied.

The important question here is to which extent the current pump flow of a micro-axial pump can be determined in pulsating environment from statically registered indicators, and how it is possible to present the pump flow on-line. This would provide reliable information to the surgeons on the current pump function, which has not been provided so far by the Hemopump applications /Kunst 1991; Mees 1991; Meyns 1996; Waldenberger 1994/.

10.1 Test set-up

Two experimental stands based on each other were developed for this research, with the main point being reproducing of a pulsating environment.

A pump sucks fluid, similarly to a non-pulsating testing stand shown in Figure 9.1a, from a straight tube with calmed suction area, as shown in Figure 10.1a. At the intake of the pump, a pulsating actuator is integrated directly over a T-connection, which represents a deformed ventricle together with a bio prosthetic on the inlet side, the tube area and the pump on the outlet side.

The analysis of the results obtained on this testing stand has a hysteresis curve of the pump even stronger than the ones shown in Figures 10.2 through 10.3, since the effect of inertia of the fluid volume located in such a deformed and stiff ventricle on the pump characteristics is strong. After that, the pump is largely disconnected from the testing stand by integration of a silicon ventricle, as shown in Figure 10.1b, so that now almost realistic suction conditions of the pump from a “passively pulsating” ventricle are possible. In this structure, the suction tube of the pump is led through a further bio prosthetic into aortic position in the ventricle, so that systolic fluid outside can flow past the pump. In diastolic terms, the flexible leaflets of the valve fit so well to the suction tube, that no measurable regurgitation from the high pressure area into the ventricle activity could be observed even in vitro. As before, the exact characterization of the pump volume flows is ensured due to the flow measuring head integrated directly into the suction tube of the pump.

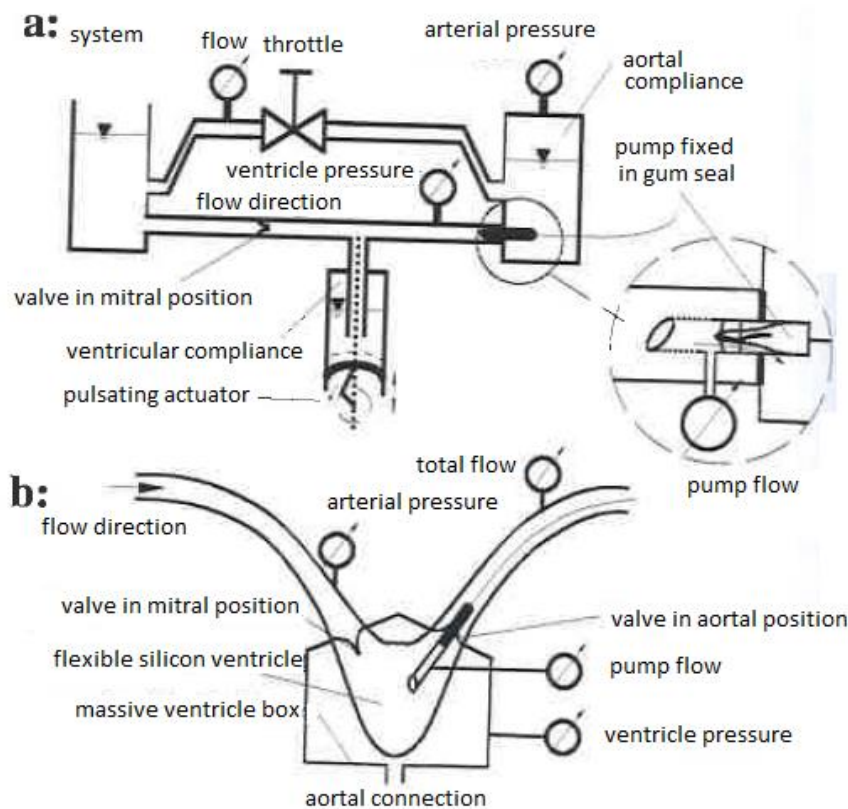


Figure 10.1 Pulsating test set-up

a: with rigid ventricle

b: with flexible silicon ventricle

By implementing the pulsating actuator in the form of a sinusoidal piston motion with a membrane, which can move freely with respect to the piston, we ensure free diastolic filling of the silicon ventricle. In case of inhibited ventricle filling, this can even help to simulate the in vivo measurable suction of the pump to the ventricle. If the silicon ventricle is still not stretched in enddiastolic way, then according to Figure 10.1b, it is enough to have a pressure meter in the stiff ventricle box in order to measure the fluid pressure in the ventricle itself, since the thin silicon wall of the ventricle in absence of pressure does not have any effect preventing correct pressure measurement.

10.2 Pump characteristics in pulsating environment

Despite its own high frequency with the rotating speed of about 20,000 turns/min till 28,000 turns/min, the pump has a clear hysteresis around the corresponding non-pulsating registered curve. Figure 10.2 shows a typical curve for a pulsating cycle.

Since the measurement data were taken with a constant rate, and each measurement point is assigned a circle on the diagram, we can distinguish the fast cycle phases from the slow ones.

The hysteresis loop starts clockwise with the closing of the aortic valve and the opening of the mitral valve, which is followed by the diastolic filling phase with digressive speed. It ends with the closing of the mitral valve, upon which the quasi isovolumetric contraction phase starts. It is no longer genuinely isovolumetric due to the pump function, but we will not be changing its name due to the existing convention.

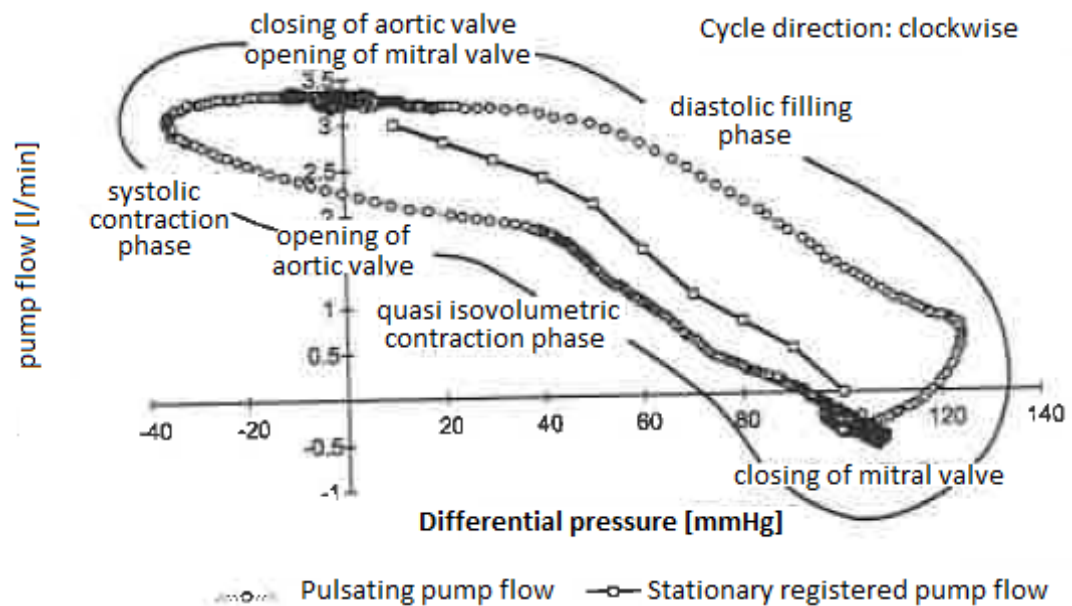


Figure 10.2 Comparison of pulsating and non-pulsating pump flow

Up to the negative pressures, the aortic valve opens without visible pressure surge, and the systolic contraction phase begins. It ends again with the closing of the aortic valve, upon which a new cycle starts.

We can clearly see that the volume flow differs from the curve registered in a stationary way most strongly in those places where the pressure changes and the associated volume flow changes happen at the highest speed. On the other hand, the observed hysteresis is lowest in those places where the stationary curve of the pump in the $\Delta p - \dot{V}$

diagram increasingly goes horizontally, as it is the case up to the high rotation speeds. This situation, which qualitatively corresponds to the in vivo results, is shown in Figure 10.3. As a cause for the constantly observed hysteresis, the flow effects in the blading can only play a secondary role, since the physiological pressure changes function in a quasi-stationary way for the blading. The significant lag of the pump with too high diastolic and too low systolic volume flows is rather a sign of inertia effects in the system, which in the first approximation are only attributable to the fluid amount in the pump and here specifically to the amount located in the suction tube.

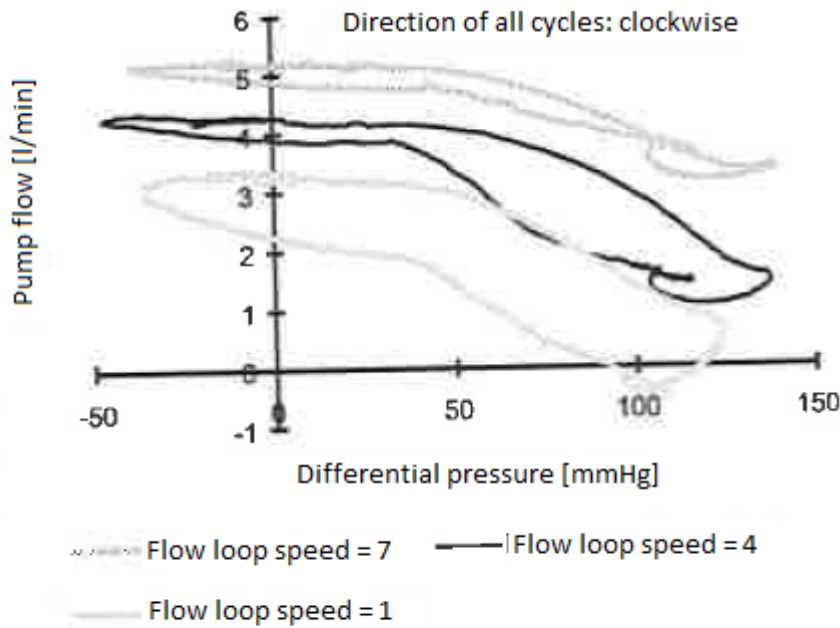


Figure 10.3 Pulsating Hp31 pump flow at the speed of 1, 4 and 7

In equation 10.1b, it gives a pump specific dynamic counter-pressure $\Delta p'$ affecting the blading in the ultimate form $\Delta p_{res} = \Delta p - \Delta p'$:

$$F = \frac{d}{dt}(m \times v) = \frac{\partial m}{\partial t} \cdot v + \frac{\partial v}{\partial t} \cdot m \stackrel{m = \text{const.}}{=} \frac{dv}{dt} \cdot m \quad (\text{Equation 10.1 a,b})$$

$$\Delta p' = \frac{F}{A} = \frac{1}{A} \cdot \frac{dv}{dt} \cdot m = L \cdot \frac{\rho}{A} \cdot \frac{d\dot{V}}{dt} \equiv L \cdot \frac{\rho}{A} \cdot \frac{\dot{V}(t_i + \Delta t) - \dot{V}(t_i)}{\Delta t}$$

where L is the length and A is the cross-section of the suction tube. Figure 10.4 shows a comparison example for speed 4 of Hp31 of the hysteresis curve based on the differential pressures, curve registered in a non-pulsating way and a hysteresis curve based on the adjusted difference pressure Δp_{res} .

Taking into account inertia of the fluid in the suction tube significantly reduces hysteresis in the area of fast volume flow changes. It is only in the area of the obvious sharp bend of the curve registered in a non-pulsating way that there is no exact diagram. This is again the result of the flow parameters in the blading, which, similarly to the blading described in Figures 9.5 a-c, is getting strongly detached on the suction side starting from a certain differential pressure.

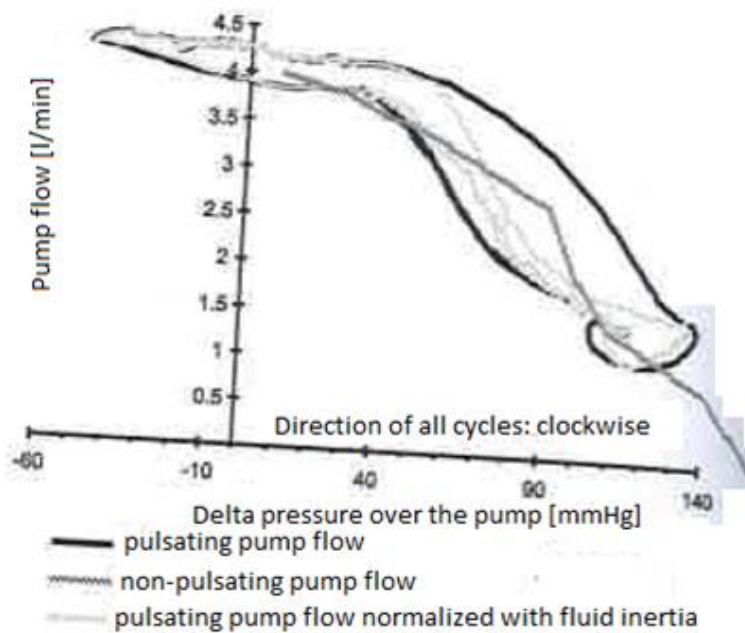


Figure 10.4 Hysteresis reduction by taking into account fluid inertia

Detachment as well as cure effects as such also result in hysteresis, since the pump diagram will look differently depending upon the direction. The non-pulsating diagram shown in Figure 10.4 was registered with increasing differential pressure, so that the pronounced bend is moved to a pressure about 10 mmHg higher than that for falling differential pressure. In absence of the relevant basis, it is impossible to obtain dynamics of the static diagram in the detachment area, and it is also superfluous in view of the actual problem of the pump flow at a given time point.

The description of the pump flow at a given time point is provided here as an example for speed 4 of Hp31. It is done with the pump flow of the curve registered in a static way as a function of the measurable differential pressure being mathematically approximated as shown in Figure 10.5. The pump flow, which is calculated based on the measured differential pressure of the aortic pressure (p_{ao}) minus the ventricular pressure (p_{vi}), is shown in Figure 10.6 with the concurrently measured pump flow. Both volume flows are in excellent agreement, although as described, the pump circles the static curve clockwise in a hysteresis. The resulting deviation is only visible at the steep edges of the differential pressure with high dynamics. Similarly good results have also been achieved with all other pump rotation speeds, which is why we chose to omit those graphs.

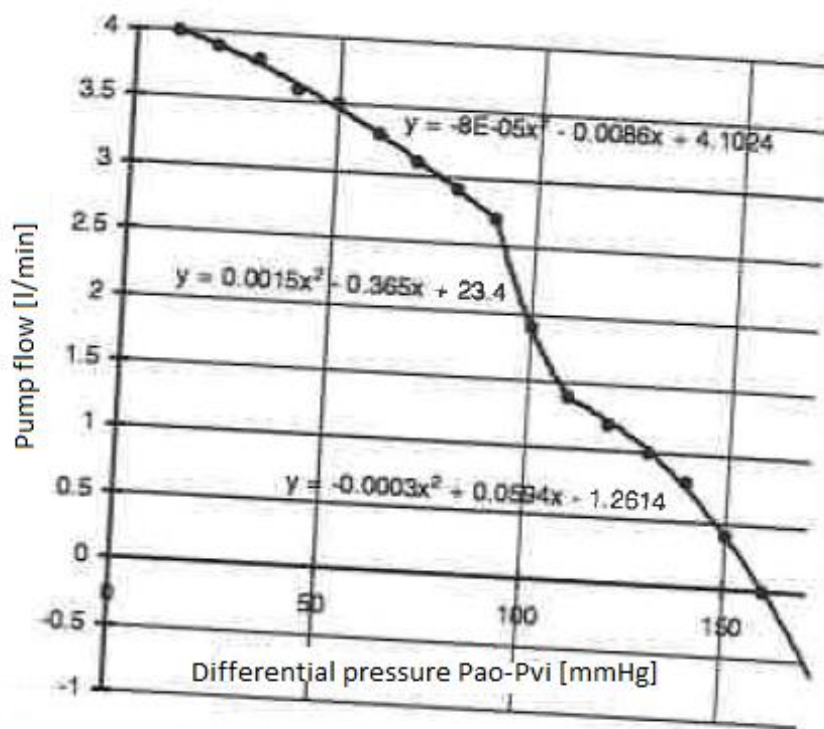


Figure 10.5 Partial approximation of the curve registered in a static way of Hp31 at speed 4

With respect to the concurrent in vivo experiments /Meyns 1996/, it can be concluded that hysteresis registered there at every rotation speed significantly exceeds that registered at the in vitro test stand according to Figure 10.1b, and is rather comparable to the hysteresis generated at the test stand shown in Figure 10.1a. To register the pump flow in vivo, the pump was moved to the aortic by-pass, which strongly increased the pump specific fluid mass compared to that located in the suction tube. This explains the much higher hysteresis. We omit the exact modelling of the in vivo results, since the by-pass is only test specific, and in clinical application the pump is used in the position similar to that shown in Figure 10.1b.

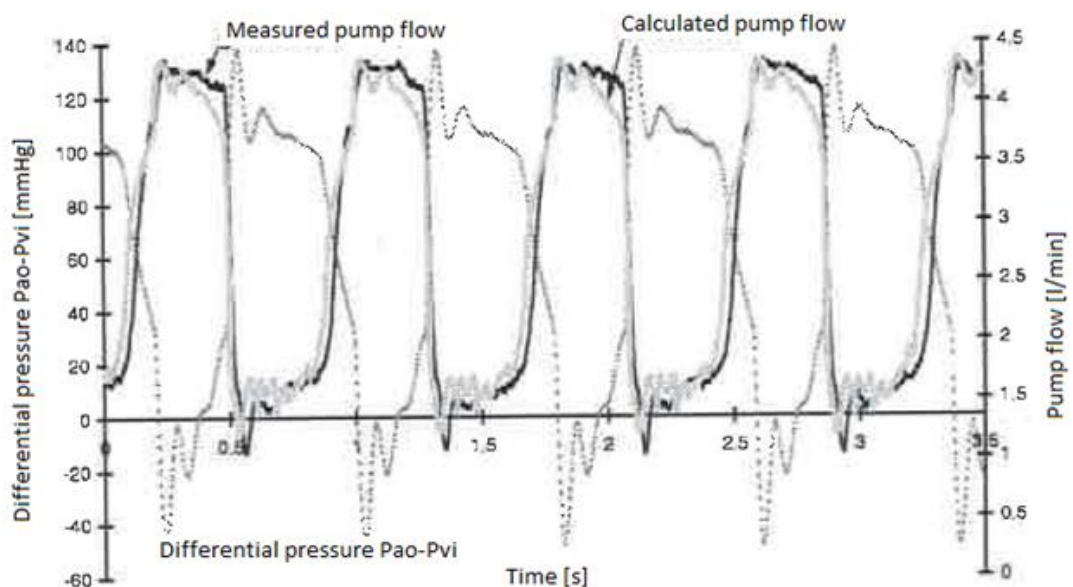


Figure 10.6 Comparison of the measured and the calculated pump flow at speed 4

10.3 Volume unloading of the ventricle and risk of suction

The use of a micro-axial pump in parallel to the ventricle causes a constant volume unloading of the ventricle, since fluid is constantly removed from it. With the respective pump capacity, the unloading causes significant reduction of enddiastolic ventricular activity, which, depending upon the position of the suction end of the pump in the ventricle, can cause temporary suction of the pump to the endocardium with the associated arrhythmia and cavitation in the blading. Furthermore, the substrate flow from the atrium in the ventricle can be inhibited to the point that the transportation capacity reduces despite the increased pump capacity /Meyns 1996; Siess 1996/.

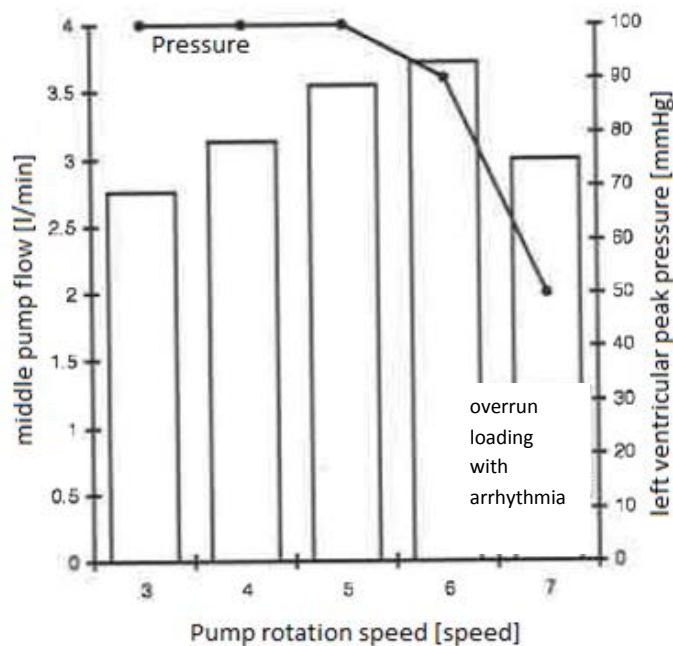


Figure 10.7 Pump flow and left ventricular peak pressures in a 67 kg male sheep with Hemopump

This situation is illustrated in Figure 10.7, where the transportation capacity increases with the increasing rotation speed, and falls significantly at the maximum pump pressure due to the described effects.

Already at the second highest pump rotation speed, which is speed 6, the ventricular peak pressure falls from the constant 100 mmHg to 91 mmHg, which tells that the pump transports already at this point the total heart minute volume, and the ventricle does not release at any point of time in the cycle more blood into the aorta by-passing the pump.

The very fact that the pump capacity clearly depends upon the ventricle activity makes the regulated pump activity necessary for a targeted heart unloading.

According to Prof. B. Meyns, the current survival rate of all patients supported by Hemopump with hypertrophic ventricles /Meyns 1995/, which show low cavity with high muscle mass, is zero, because the available hemodynamics is insufficient for recovery.

This can be caused by unregulated Hemopump operation with insufficient knowledge of the actual transported amounts, so that the pumps may be operated at too high speeds in expectation of the maximum amounts to be transported.

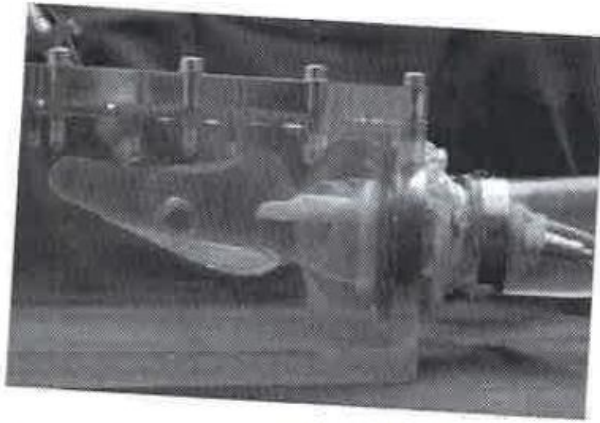


Figure 10.8a Enddiastolic normal size of the silicon ventricle

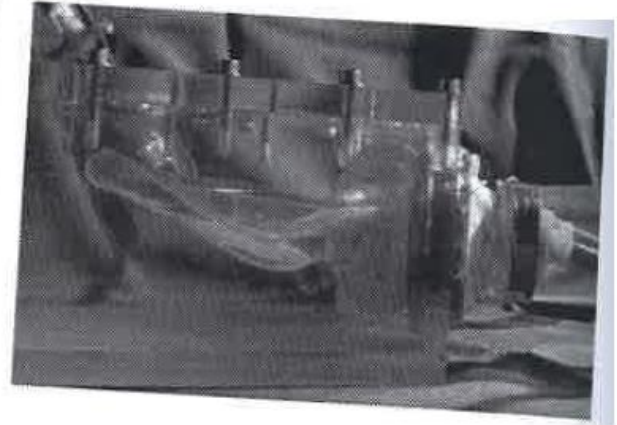


Figure 10.8b Enddiastolic size of the collapsed silicon ventricle

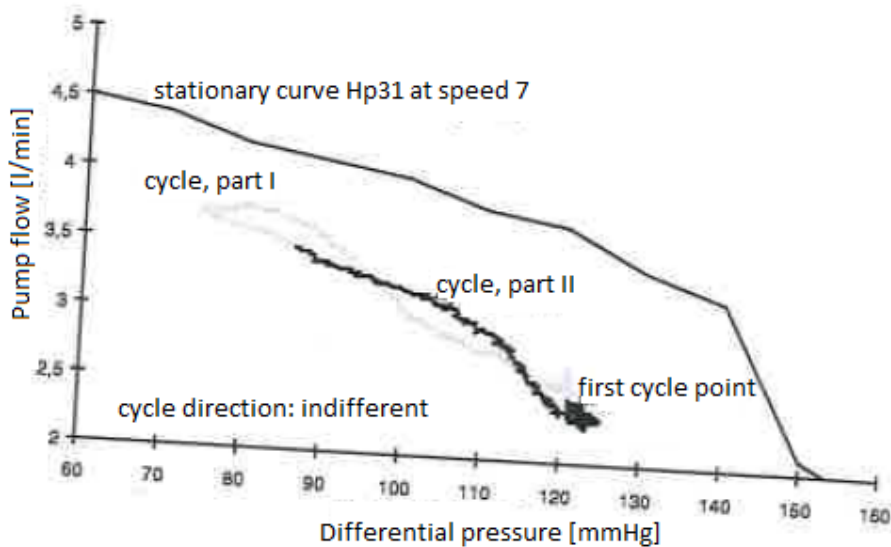


Figure 10.9 Pulsating cycle of Hp31 at speed 7 in collapsed silicon ventricle

To assess this situation better, in vitro experiments were performed on collapsed ventricles based on the in vivo experiments on sheep. Figures 10.8 a,b compare a collapsed ventricle to an enddiastolic ventricle in normal size, in order to clarify to which extent the cavity must be reduced in vitro to achieve approximately the same flow diagrams as in vivo that would correspond to Figure 10.7 at speed 7. The minimum capacity of the pump resulting from the collapsed ventricle only becomes clear at the maximum rotation speed, at which the hysteresis loop observed in Chapter 10.2 clockwise not only falls below the curve registered in a static way, but also degrades to a lying eight shown in Figure 10.9. Suction of the pump to endocardium can only be observed more vividly /Meyns 1996/ in the cases when the pump flow collapses in a systolic way and falls below the diastolic level. The suction in vivo is so obvious that the lying eight in vitro with the crossing sides in vivo even degrades to a counterclockwise cycle.

Suction:

Suction to the ventricle is simulated in vitro, as shown in Figure 10.10, by reduction of the enddiastolic ventricle size from cycle to cycle. A hysteresis loop similar to in vivo, where the pump flow collapses in a systolic way due to suction, can only be achieved by further reduction of the ventricle volume below that shown in Figure 10.8b. This results in a counterclockwise cycle in vitro as well. However, this causes strong and non-physiological negative differential pressures resulting from the test set-up. Contrary to

in vivo, where the collapsed ventricle cannot contract beyond its endsystolic volume, the sinusoidal actuator of the silicon ventricle can be pressed together to a zero systolic rest volume, and even compress air in the ventricular compliance according to Figure 10.1b.

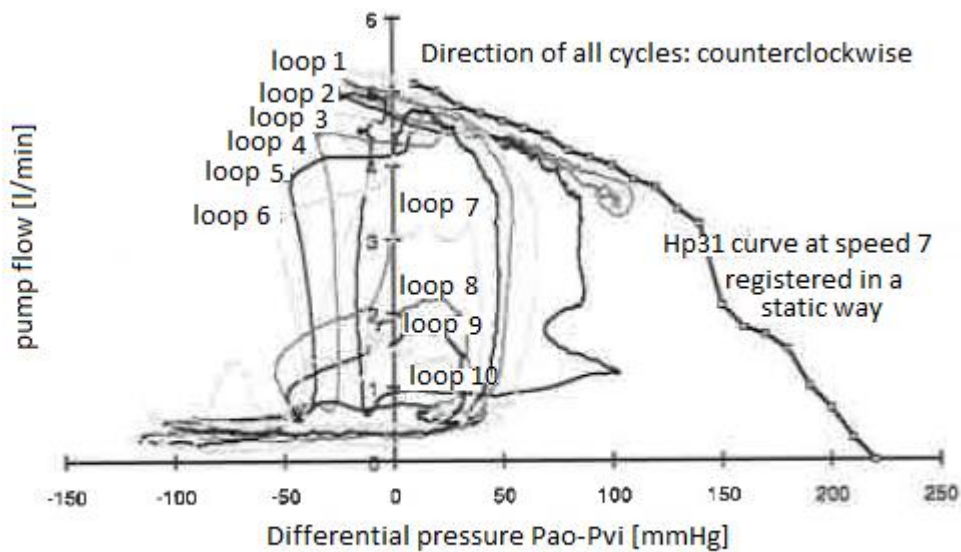


Figure 10.10 Pulsating cycle of Hp31 at speed 7 with the gradually collapsing ventricle from loop 1 to loop 10

10.4 Volume flow calculation and avoidance of suction phases

If we calculate, similarly to Figure 10.6, the volume flow of the pump for the above case of an increasingly collapsing ventricle, we will see that the discrepancy between the measured and the calculated pump flow keeps increasing with the suction phases getting longer and more persistent. In Figure 10.11, the calculated volume flow even increases due to the strong, non-physiological negative differential pressure.

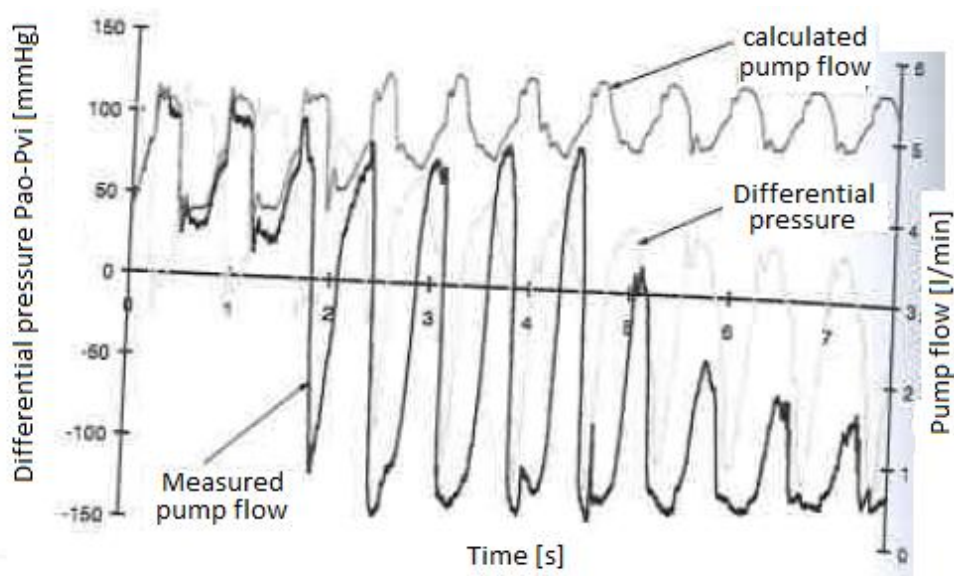


Figure 10.11 Comparison of the measured and calculated pump pressure of Hp31 in an increasingly collapsing ventricle

Therefore, while a very good correlation could be achieved with sufficient substrate amount according to Figure 10.6, it is no longer the case based on the differential pressure $p_{ao} - p_{vi}$ on the example of the collapsed ventricle. To take into account the local suction, which cannot be registered beyond the

pressure P_{vi} measured in the ventricle, it is necessary to integrate a miniature pressure meter immediately in the suction tube. A pressure sensor in the immediate vicinity of the blading can even measure additional tube losses due to stronger curvature or bend and take them into account for the volume flow calculations.

Integration of a pressure sensor instead of a volume flow sensor brings along a further benefit, in addition to its very small size, that high negative pressures in the tube, which no longer result from the dynamic pressure reduction plus tube losses, can immediately be attributed to a suction sequence.

Based on these considerations, we can build, according to Figure 10.12, a volume flow registration and suction control, which have been tested for basic functions in the lab size.

The principle of a regulated pump operation presented in Figure 10.12 is based on the statically determined curve, which is sufficiently identical for pumps of identical design with similar fluid viscosity. Based on the rotation speed of the motor control together with the pressures measured according to the above considerations ($p_{schl.}$ and p_{ao}), the real volume flow of the pump can be determined with an error $<15\%$. It can be identified as a volume flow at a given time point and/or as an average, in order to describe the pump function in more detail. This supports such options as choosing for volume flow with variable rotation speed or a constant pump rotation speed with variable volume flow.

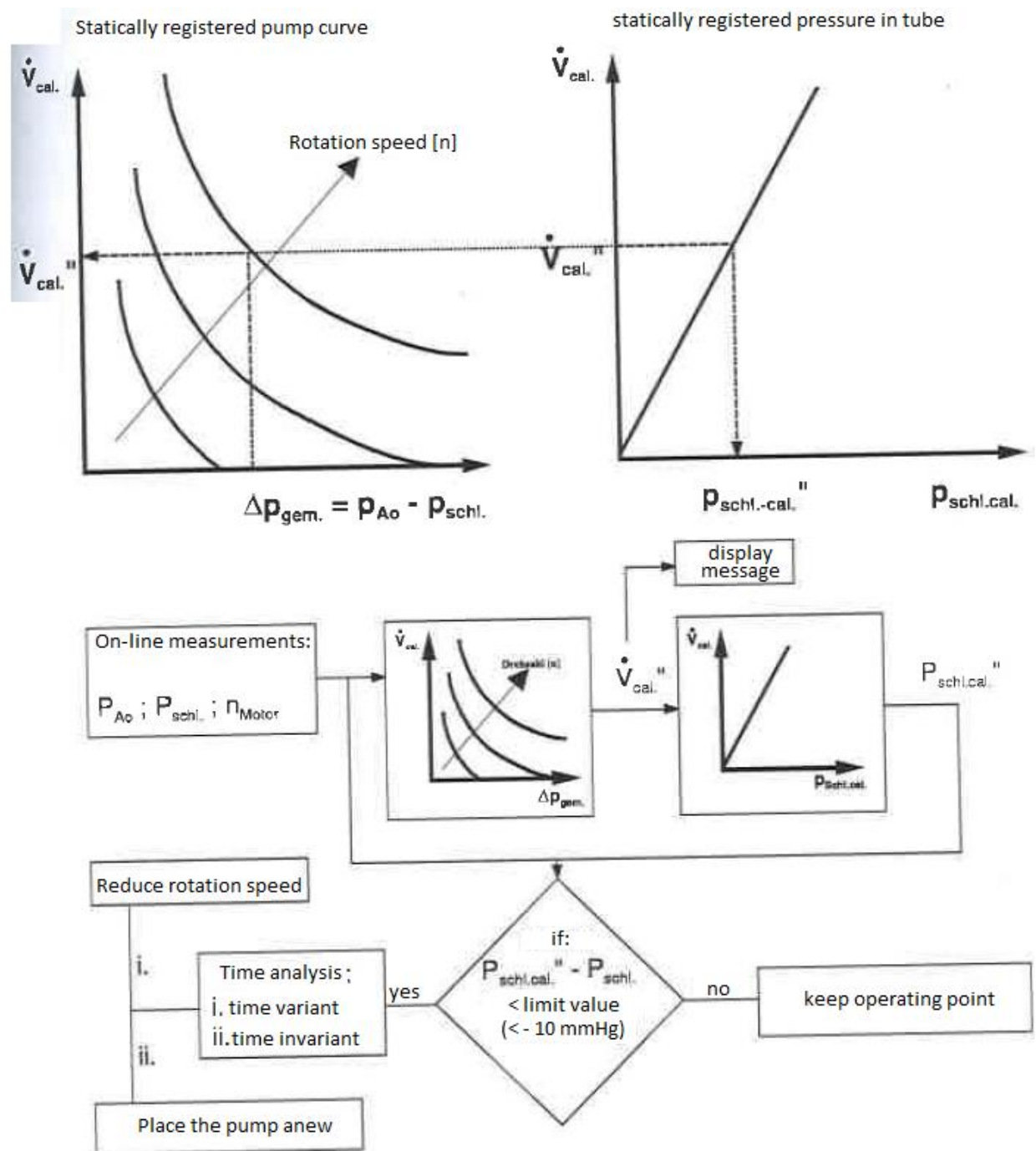


Figure 10.12 Principle of a controlled pump operation

Furthermore, from the calculated volume flow and a curve of the volume flow dependent pressure also registered in a static way, we can determine the pressure to be expected on the tube side pressure sensor for the suction free operation of the pump with a straight suction tube. If this calculated value $p_{schl.cal}$ strongly deviates from the measured value of $p_{schl.}$, then this can be attributed to either a bend in the tube, if the deviation is constant, or a temporary suction sequence, if the deviation is temporary. In the first case, an alarm should be triggered and the pump placed anew, while in the other case the rotation speed should be reduced, until the display message is no longer shown.

11. Experimental in vitro research of blood damages

All considerations on pump design from Chapter 5, qualitative research of hemolysis based on flow research in Chapters 7 and 8, and measurements of the surface temperature of the electric drive in Chapter 4 will be supported in this chapter by research of blood compatibility of the pump.

To this end, in vitro blood experiments were performed based in their structure and protocol on Chapter 11.2; however, they result in insufficient statements with respect to thrombogenicity. If no thrombi appear in the course of research, then this is a necessary, but not a sufficient criterion, since blood must be almost fully anticoagulated for experimental purposes.

Therefore, ultimate thrombogenicity results can only be reported in vivo, as long as there is no adequate in vitro protocol /Schima 1993, 1995; Wurzinger 1991/. The research described in Chapter 12 provides the first results in this respect.

11.1 Blood compatibility of the pump

In this context, blood compatibility means any form of interaction between a pump and a medium. This includes not only the effect of the material, its surface qualities and the effect of the geometrical and operational aspects of the pump on pure blood, but also effect of blood on mechanical components of the system.

For example, a small leak of blood into mechanics of the pump may not immediately cause the system breakdown. On the other hand, the pump induced blood damage cannot exceed certain limit values. Shear stress, stagnant area and water induced thrombi may not appear, if possible, in flow and temperature critical areas, which include the border point between the rotating and stationary component with integrated seal.

Blood damages also cover morphological changes taking place beyond physiological extent or destruction of corpuscular blood particles. For this form of blood damage there is no standard description, but it can be roughly split into osmotic, chemical and physical damages.

With respect to the blood pumps researched in this work, physical damages are particularly relevant. They can, in their turn, be split into physicochemical damages, which result from surface qualities of plastic materials, according to their roughness, tension and chemical structure /Glasmacher 1982, 1991/, and purely physical damages. The latter mostly cover laminar, turbulent shear stress, pressure tensions from pressure gradient in flow field or due to cavitation and temperature effects.

While most of the described damage causes are uncritical for the blood plasma with the macromolecules suspended in it, proteins (albumin, globulin, fibrinogen etc.) can be damaged when temperature exceeds 42°C.

If the peak temperatures also exceed 50°C, as it can happen in the seal area, then they affect adhesion and aggregation of fibrin monomers transformed from fibrinogen /Renardy 1993/ on metallic or ceramic surfaces /Yamazaki 1995/.

The resulting quasi polymerized fibrin aggregates can cause breakdown of seals and bearings due to the narrow gaps and low tolerances inherent to the system. The breakdown avalanche begins with the transformation of fibrinogens into fibrin monomers and the following initial aggregation phase in narrow and dynamic gaps, resulting in increased dissipation with rising local temperature. This causes further increase in the aggregation propensity and solidification of clusters, so that finally the dissipation capacity of integrated drives becomes too high and/or the components become dysfunctional. The quasi

polymerized fibrin aggregates resulting from this process, which can be embedded in thrombocytes and erythrocytes, are very hard and adhere strongly to plastic surfaces.

The described breakdown principle can also be applied in modified form to a micro motor integrated into a pump system. If due to lack of convection on a part of the motor surface the temperatures rise and fibrin monomers display adhesion, then this causes deterioration of the α value and further temperature increase and adhesion, until the system finally breaks down due to excessive winding temperatures.

According to the above considerations, it becomes clear how multifaceted the concept of blood compatibility can be. Therefore, only certain aspects of blood compatibility can be treated in Chapter 11.2, and the ability to perform significantly affects the used test protocol.

11.2 In vitro blood compatibility research

11.2.1 Test parameters and limit values

In connection with the blood damage, we will specifically study the plasma hemoglobin concentration as a readily available parameter of the lysis of erythrocytes, which comprise the largest corpuscular portion of volume in pure blood. To this end, an isolated blood volume will be repeatedly pumped by the researched system under exactly specified hydraulic parameters (volume flow, delivery head and rotation speed). Plasma hemoglobin concentration is measured at regular intervals; as the result of the hemolytic effect of the pump, it increases in the course of the test and can be used to obtain a pump specific hemolysis index. Unfortunately, there are still no standardized indices for blood pumps with the related standardized test set-ups and identical protocols, so that it is still difficult to compare the results of different work groups. It is even difficult to compare identical tests due to different blood lots, even though the index provided below already takes into account and normalizes certain blood differences, which depend on lots. Finally, the stability distribution of the cell membrane varies so significantly for different bloods, that the pumps with high shear tensions can generate very different indices for different tests with identical protocols. Therefore, hemolytic characterization requires at least about 10 tests, which is impossible to do in this work in absence of sufficient number of available pumps. Instead, various geometries and materials were tested in the course of a few tests to find at least a general direction of optimization. We must also mention that all results presented in Chapter 11.2.3 must be treated with caution and may not be deemed representative, because all of them represent single occurrences.

The modified index according to /Müller 1993 and Westphal 1994/ used here includes hematocrit, which depends upon the lot, and the total hemoglobin concentration, so that ultimately only the membrane resistance /Schima 1993/, which has so far remained unmeasured, remains here as an important hemolysis parameter not yet taken into consideration. This lets us compare the tendencies of the results of different tests. To classify a pump exactly, it is necessary, just as previously, to test different systems against each other with the same blood within one test.

As a reference for the systems developed here we use the clinically used sternotomy Hemopump Hp31, which is available as an intravascular micro-axial system. The generated hemolysis is classified for this system as clinically acceptable /Aboul-Hosn 1995, Wampler 1993/.

$$IH^* = \frac{V \cdot (1-Hk) \cdot \Delta Hb_{Plasma} \cdot 10^3}{\dot{V} \cdot t \cdot HB_{ges.}}$$

Hemolysis index (Equation 11.1)

with

V	\equiv	pure blood volume in circulation [l];
Hk	\equiv	hematocrit between 0 and 1 [-];
$\Delta HB_{\text{Pharma}}$	\equiv	plasma hemoglobin concentration between the start and end of the test [mg/100ml serum];
\dot{V}	\equiv	pump volume flow [l/min];
t	\equiv	total pump duration [min];
$\Delta HB_{\text{ges.}}$	\equiv	total hemoglobin [g/100ml pure blood].

The test protocol provides, in addition to a constant operation point of the pump, fixed blood temperature of 37°C for the test duration, so that the temperature effect of the micro motor surface and the seal lip area on fibrinogen can be researched concurrently.

As a limit value for the pump induced hemolysis, a released hemoglobin amount of 10 g/day is provided as clinically acceptable. This amount applies as a limit value of what a “healthy” organism can break down and restore in erythrocytes daily /Butler 1992; Gross 1984/. Beyond this value, there is a risk of anemia, if the pump is used regularly.

For this physiological limit value, the index described in equation 11.1 does not provide any general limit value, since the index includes volume flow as a description of the pump quality.

What is important for an organism though is solely the absolute plasma hemoglobin concentration, and even regardless of the volume flow of the pump. In view of compatibility, a pump, which only transports one liter and causes a 6-fold higher hemolysis than another pump with 6 liter volume flow, is equally compatible with the organism as the other pump. Therefore, the limit value must be stated with the reference to the operating point, as it is done in Figure 11.1. For the results described below in Chapter 11.2.3, the index does properly reflect the quality of pumps compared to each other, but even there the acceptable limit value is stated for each pump depending upon the operating point.

If, however, the pumps in question are only used for a short time, up to several hours, then the index for such an indication may even exceed the respective limit value.

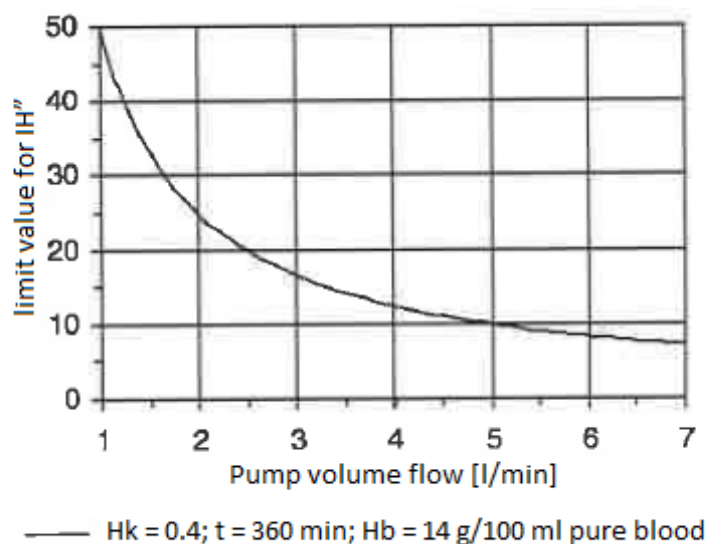


Figure 11.1 Index of hemolysis IH'' depending upon operating point

The limit value for the thromogenicity of the system is defined in a relatively simple way. There may be no flow or temperature induced deposits of fibrin with embedded thrombocytes and erythrocytes either in the pump or on the motor surface. Even the seal area, which includes the gap between the rotating and stationary component, as well as the friction area between the seal lip and the shaft, must be free of adhesive blood particles. Optical control suffices.

Thrombi, which have left the pump in the course of the test, are located upon recirculation either on the entrance edge of the rotor blade or in the filter of the blood bag, where they also can be detected.

No blood should get into the pump mechanics through the seal during the test. If this is still the case, then the pump should not break down immediately. The increasing required capacity can be deduced from the motor flow at the constant rotation speed, so that when the limit value is exceeded, an alarm can be triggered in addition to Chapter 10.4.

11.2.2 Test set-up and performance

The test set-up must be as simple as permitted by the protocol. Therefore, the set-up shown in Figure 11.2 consists solely of a blood bag tempered in water and a connected by-pass containing the pump, pressure sensors (Cobe, Lakewood, CO, USA), possibly on both sides of the pumps, and a connected resistance in the form of an added tube clamp. The pump volume flow is registered by an ultrasound flow meter attachable to the tube (model HT109, Transonic Systems Inc., Ithaca, NY, USA).

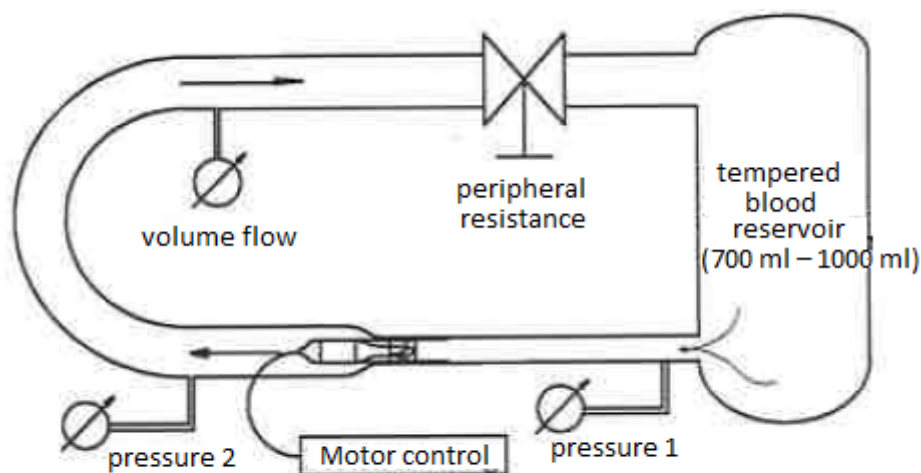


Figure 11.2 In vitro hemolysis test set-up

The tube connections are arranged on the blood bag in such way that the blood discharging connection is located at the point lowest in geodetic terms, while the intake is located high. This can prevent suction of air into the pump, which is essential for a realistic hemolysis.

If fine dispersed bubbles appear in the pump due to air sucked into the pump, they cause significant blood damage and corrupt the results.

Since the test pumps are intravascular systems, which only have suction, but no pressure connections, the pumps must be integrated either with a seal between the pressure and suction side directly in the tube, or into a respective housing according to Figure 11.2. The integration according to Figure 11.2 is better than with a tube, because a tube can be integrated on the suction side in the dimensions of the suction cannula, which is used later on, without causing stagnant areas filled with blood.

Test performance:

The pig blood used in the test is obtained immediately prior to the beginning of the test from the slaughterhouse. The blood is collected there, upon a pig heart incision, from the middle open jet into a container already provided with anticoagulants (Citrate, Heparin, EDTA, CPDA-1) and antibiotics.

If more blood is required, depending upon the number of pumps, than can be obtained from one animal, then blood of several animals can be pooled, unlike human blood. Immediately upon collection, the blood bag is filled and transported from the slaughterhouse to the hemolysis lab in an isolated container to avoid excessive cooling.

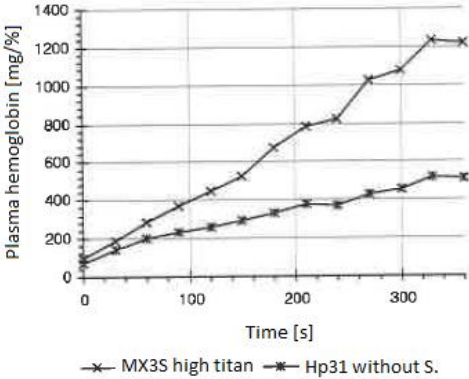
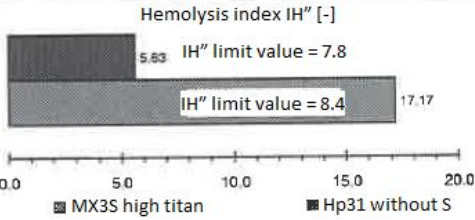
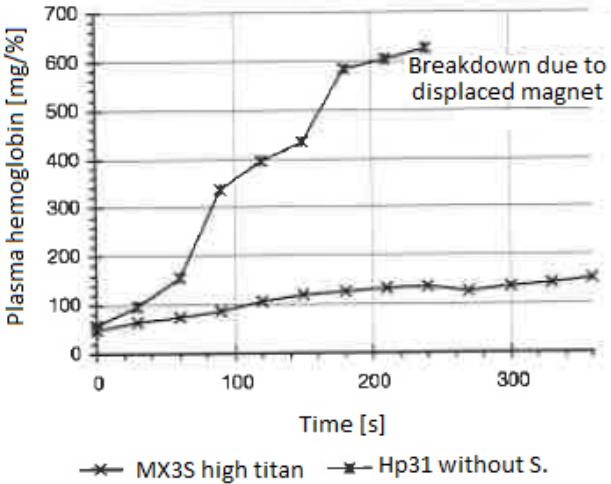
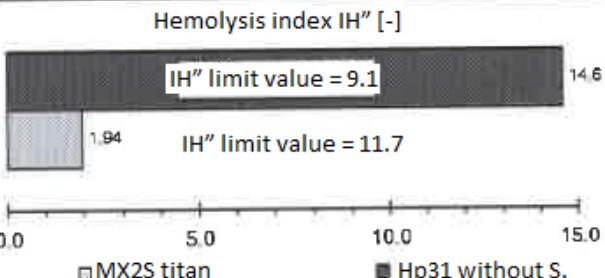
Immediately upon integration of the bag into the previously prepared test stands and air exhaust, the operating points are fixed. The duration of the test starts at this point, and every 30 minutes two 1.5 ml pure blood tests are taken for redundant extinction values and limitation of measurement errors.

These tests are centrifuged at $n = 6,000$ turns/min for 10 minutes, and the supernatant plasma is provided with the reaction solution for hemoglobin determination (Merck 9405) to create a stable color complex. The plasma hemoglobin concentration is determined from the extinction values, upon which the index is calculated from the reported blood values.

Once the test is over, the test stand is inspected for released thrombi, the pump is taken apart, and the blading, seal, bearing and motor surface are visually inspected for blood deposits.

11.2.3 Results

The comparative hemolysis research presented below shows that the systems developed here can generate hemolysis values in the area of Hemopump 31 and below. Since clinical compatibility has been demonstrated for Hemopump, it can also be assumed for these systems, although a subsequent in vivo evaluation is indispensable.

<p>Short description</p> <p>I. Blood (of pig, pooled): Composition: Hk = 0.39; Hb = 14.2; anticoagulant EDTA Hemolysis: blood with average resistance MX3S high titan: Blading with: $\beta_2=94.5^\circ$; t/s = 0.79 L = 5.27 mm; 3 blades; rotor and stator of titan; Teflon seal against the TIN shaft Operating point: n = 30,000 turns/min; $\Delta p = 80$ mmHg; V = 5.81 l/min Hemolysis: high hemolysis, in particular, since the rotor moves to pump cover with local wall contact Hp31 without S. (without suction tube): Operating point: n = speed7; $\Delta p = 80$ mmHg; V = 6.31 l/min Hemolysis: lowest hemolysis so far, which was measured with an Hp31 during this research</p>	<p>Plasma hemoglobin concentration, IH''</p>  <p>Hemolysis index IH'' [-]</p>  <table border="1"><thead><tr><th>System</th><th>IH'' [-]</th><th>IH'' limit value [-]</th></tr></thead><tbody><tr><td>MX3S high titan</td><td>5.53</td><td>7.8</td></tr><tr><td>Hp31 without S.</td><td>17.17</td><td>8.4</td></tr></tbody></table>	System	IH'' [-]	IH'' limit value [-]	MX3S high titan	5.53	7.8	Hp31 without S.	17.17	8.4
System	IH'' [-]	IH'' limit value [-]								
MX3S high titan	5.53	7.8								
Hp31 without S.	17.17	8.4								
<p>II. Blood (of pig, pooled): Composition: Hk = 0.40; Hb = 14.46; anticoagulant EDTA Hemolysis: blood with above average resistance MX2S titan: Blading with: $\beta_2=54.2^\circ$; t/s = 0.73 L = 6.0 mm; 2 blades; rotor and stator of titan; Teflon seal against the TIN shaft Operating point: n = 30,000 turns/min; $\Delta p = 80$ mmHg; V = 4.1 l/min Hemolysis: lowest index of all micro-axial pumps measured so far Hp31 without S. (without suction tube): Operating point: n = 25,500 turns/min; $\Delta p = 80$ mmHg; V = 5.31 l/min; Hp31 blading combined with micro motor; Teflon seal against uncovered unhardened shaft Hemolysis: high hemolysis, in particular, since the rotor moves to pump cover with local wall contact</p>	 <p>Breakdown due to displaced magnet</p> <p>Hemolysis index IH'' [-]</p>  <table border="1"><thead><tr><th>System</th><th>IH'' [-]</th><th>IH'' limit value [-]</th></tr></thead><tbody><tr><td>MX2S titan</td><td>1.94</td><td>9.1</td></tr><tr><td>Hp31 without S.</td><td>14.6</td><td>11.7</td></tr></tbody></table>	System	IH'' [-]	IH'' limit value [-]	MX2S titan	1.94	9.1	Hp31 without S.	14.6	11.7
System	IH'' [-]	IH'' limit value [-]								
MX2S titan	1.94	9.1								
Hp31 without S.	14.6	11.7								

III. Blood (of pig, pooled):

Composition: Hk = 0.40; Hb = 11.96;

anticoagulant EDTA

Hemolysis: blood with average resistance

MX2S brass/titan:

Blading with: $\beta_2 = 54.2^\circ$; $t/s = 0.73$

L = 6.0 mm; 2 blades; rotor of brass and stator

of titan; Teflon seal against the TIN shaft

Operating point: $n = 30,000$ turns/min; $\Delta p =$

80 mmHg; $V = 4.1$ l/min

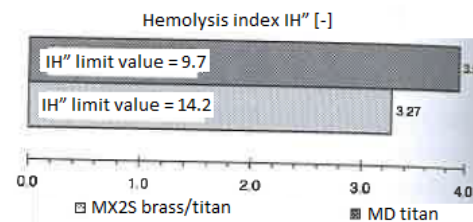
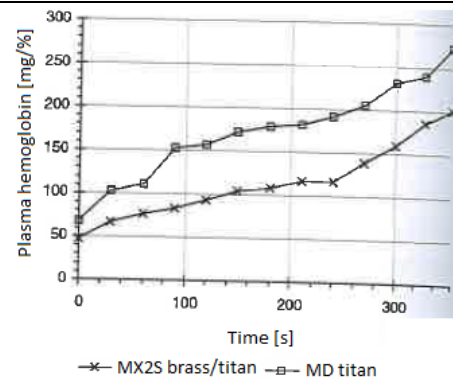
Hemolysis: clearly under the limit value, about one index higher than with identical titan rotor from II.

MD titan (micro diagonal pump as reference):

Operating point: $n = 7,000$ turns/min; $\Delta p =$

100 mmHg; $V = 6.01$ l/min

Hemolysis: middle index for this pump



IV. Blood (of pig, non-pooled):

Composition: Hk = 0.34; Hb = 12.35;

anticoagulant CPDA-1

Hemolysis: clearly too high in all pumps, since blood has low resistance

MX2S high titan:

Blading with: $\beta_2 = 94.1^\circ$; $t/s = 1.0$

L = 6.0 mm; 2 blades; rotor and stator of titan;

Teflon seal against the TIN shaft

Operating point: $n = 30,000$ turns/min; $\Delta p =$

80 mmHg; $V = 5.0$ l/min

Hemolysis: clearly over the limit value, in particular, since the stator does not optimally fit to rotor (too strong back incidence)

MX3S brass:

Blading with: $\beta_2 = 44.2^\circ$; $t/s = 0.56$

L = 4.2 mm; 3 blades; rotor and stator of brass;

ferric fluid seal

Operating point: $n = 30,000$ turns/min; $\Delta p =$

80 mmHg; $V = 2.5$ l/min

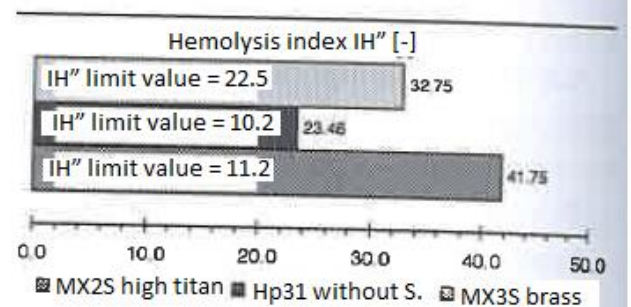
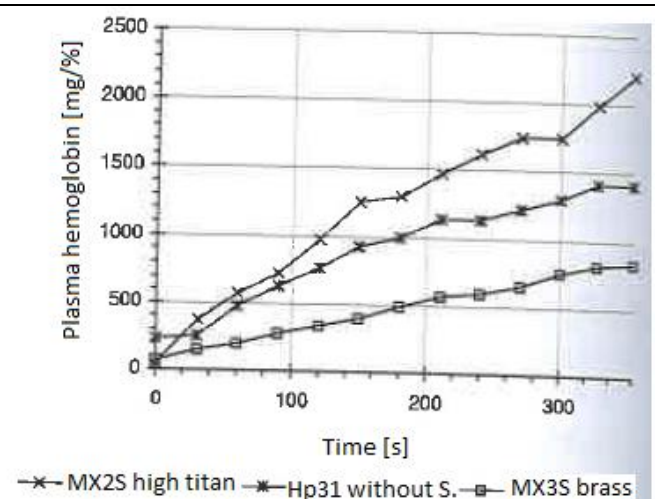
Hemolysis: over the limit value, in particular, since rotor runs strongly excentrically to the pump housing with a large radial gap

Hp31 without S. (suction tube):

Operating point: $n = \text{speed7}$; $\Delta p = 80$ mmHg;

$V = 5.5$ l/min;

Hemolysis: lowest index, but clearly over the limit value



Effect of geometry and operating points on hemolysis:

Even though the hemolysis research conducted in this work can only be applied to a limited extent as such, due to its limited scope, certain tendencies can still be derived from them, when considered together with the geometry effect on hemolysis from Chapter 8.2.

The dependence of hemolysis on the gap height presented in Figures 8.13 a, b is fully confirmed by the experiments. In all cases, where the rotor blade edge was definitely coming into local contact with the pump cover (I: MX3S high titan; II: Hp31 without S.), or the gap was varying between 0.05 and 0.4 mm due to eccentricity (IV: MX3S brass), the measured hemolysis is high.

Furthermore, similarly to Figure 8.13e, the lowest hemolysis values are achieved with two blade pumps (II: MX2S titan; III: MX2S brass/titan).

All systems are operated at their design points, which at the same time correspond to the permissible rotation speed with the highest local shear tensions. For these points, the hemolytically most favorable volume flow of about 4 l/min can be determined for the geometrically limited flow cross-sections of the 6 mm pumps based on the reduction in Figures 8.12 a,b. (Hemopump 31 must be taken aside at this point, since its diameter is about 1 mm too big). Up to the smaller volume flows (< 4 l/min), the hemolysis increases significantly due to the longer staying times compared with the small reduction of shear tension, since the latter strongly depends upon the rotation speed in the direction of small volume flows, which are always fixed here at $n = 30,000$ turns/min.

On the other hand, up to larger volume flows (> 4 l/min), the hemolytic effect increases the shear stress overproportionally compared to the achieved reduction of the staying time, which also causes increased blood damages.

Effect of the materials on hemolysis:

The moderate systems MX2S titan and MX2S brass/titan considered in tests II and III are geometrically identical, so that the only difference between them is the rotor material. Therefore, with reservations, the material effect of the brass on hemolysis can be set at $\Delta IH' = 1$. This corresponds well to the results from test III with respect to the micro diagonal pump MD titan for constant heart support, which we will not be considering further. This titan system produces in average a hemolysis $IH' = 3$. The identical system of brass produces, on the other hand, an index $IH' = 5$, so that the effect of the material can be set at $IH' = 2$ for much larger surfaces.

Thrombogenicity:

Based on the considerations from Chapter 12 on limited applicability of the existing in vitro blood research with respect to thrombogenicity, we can state at this point that neither thrombi in the blading and blood bag, nor blood deposits on the motor surface or in the seal could be observed in the course of the tests conducted in this work. It was merely at the place affected by the frictional connection of the seal that a thin and hard blood film (fibrin cluster) could be observed in many experiments.

The actual thrombogenicity of the system will only be demonstrated by in vivo experiments.

Robustness:

Despite the system being not tight in test I: MX3S high titan and test II: Hp31 without S due to strong shaft wear, the pumps did not break down when friction increased slightly due to blood getting into the mechanics. Even the miniature ball bearings could be re-used for further experiments upon being cleaned.

On the other side, it cannot be ruled out at this point that with the increased winding temperature as the result of poor heat transport mechanism blood will coagulate stronger in the gap between the magnet and winding, so that the system can still break down for this reason in several minutes.

12. First in vivo experiments

First in vivo experiments provide the most valuable information and show the actual development better than any others, when a pump is developed to primarily fit the physiological conditions, which cannot be clearly identified. The success or failure of the experiments depends, in addition to the pump, in particular on the total system, which consists of the suction tube with a wire basket in the front, pump with drive and inverse guide catheter.

Such aspects as attachment places between plastic and metal, rigidity of the suction tube and the actual location options of the system play an increasing role.

12.1 Animal model

The first in vivo experiments were conducted in the animal model of grown sheep (65 kg – 75 kg) in acute, non-sterile environment to research the functionality of the developed complete system in terms of placement options and the possible hemodynamics.

With respect to the placement options, this means that the pump must be placeable through the periphery, retrogradely through the aortic arch and with the suction cannula through and beyond the aortic valve.

In a sheep it means, furthermore, that the femoral artery (leg artery) must be first dissected and exposed, and then further dissected in the direction of larger vessels until the vessel diameter in the order size of the human femoral artery is found.

In sheep, this requires dissecting of the second largest iliac, which precedes the femoral artery in the heart direction, or even the abdominal aorta, which involves access to the stomach area of the animal.

Upon being inserted successfully, the system is pushed forward and placed by the inverse guide catheter, and the correct position can be checked by feeling the aorta on an open animal or by X-rays.

The suction tube of the placed pump cannot be thrown out of the animal, even if it is standing, due to the ventricle activity, which was frequently the case with Hemopump 21 with its curved and soft suction tube.

The heart unloading can be assessed with the working pump from the ventricle and aortal pressures together with the respective ventricle size, since the integration of sensors in the pump for online volume flow calculation is not provided for in the system for the initial function testing.

12.2 Test performance and results

For the initial function testing of the total system, three acute tests on animals were conducted by Prof. Flameng and Prof. Meyns at the Catholic University of Leuven, Belgium, according to the guidelines for keeping and use of lab animals of the US Department of Health.

A micro-axial pump was used for functional analysis, as described in the first experiment below. This 6.4 mm pump is shown in Figure 12.1 together with the inverse guide catheter.

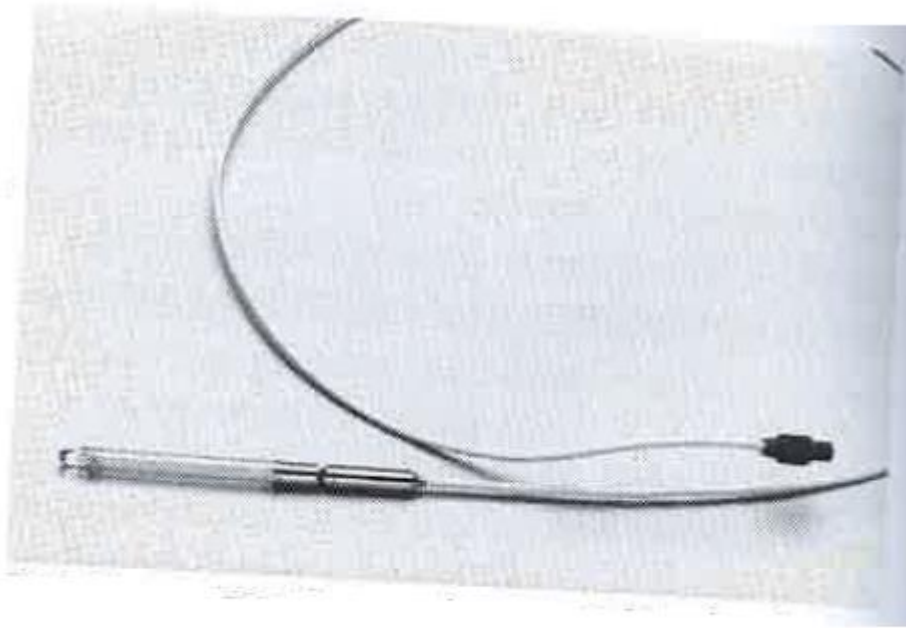


Figure 12.1 6.4 mm pump with suction tube on silicon basis and basket, version I

1st experiment (male sheep, 65 kg)

- Pump:** moderate blading MX2S titan from Chapter 11.2.3 on 6.4 mm motor with spiral reinforced suction tube on the silicon basis, suction basket version I and guide catheter from the human sector.
- Insertion:** Insertion was first performed through graft attached to iliac as a port. The vessel and the graft radius proved to be too small for insertion. The attempt to insert the system without graft failed as well due to the depth of the insertion point and the resulting small radius. Subsequently, the stomach area was opened and the abdominal aorta, which has the size of a human femoral artery, was dissected and exposed. The system could now be inserted without complications.
- Placement:** The pump could be pushed through the aortic arch without problems. A proper placement of the pump was achieved by pushing it into the ventricle with the suction tube. Then the pump was pulled back until the motor and the rigid pump part could be clearly felt through the aorta ascendens.
- Hemodynamics:** The pump rotation speed was gradually increased from $n = 10,000$ turns/min to $n = 35,000$ turns/min. No effect of the pump on the ventricle could be observed. Instead, the pump broke down at the maximum rotation speed.
- Analysis:** The subsequent research showed that attachment of the suction tube to the pump cover was too unstable (loss of the tube during removal). Also, a piece of collagenous tissue was located in the gap between the rotor and stator, which was proved to belong to the valve apparatus. Therefore, it must be assumed that the very flexible suction tube was thrown out of the ventricle after several heart cycles, and the pump attached to the valve apparatus. The sharp front entrance edge of the version I suction basket damaged the valve apparatus at suction pressures of up to 400 mmHg. Repeating of the described procedure for a number of times confirmed the results.

2nd experiment (female sheep, 75 kg)

- Pump:** moderate blading MX2S titan from Chapter 11.2.3 on 6.4 mm motor with spiral reinforced suction tube on the silicon basis, suction basket version I and guide catheter from the human sector, improved adhesion between the suction tube and pump covering.
- Insertion:** Insertion was first performed on this large animal directly through the iliac without graft.
- Placement:** Placement was also performed from the first attempt.
- Hemodynamics:** The pump rotation speed was gradually increased from $n = 10,000$ turns/min to $n = 35,000$ turns/min. Again, no effect of the pump on the ventricle could be observed.
- Suction tube:** In addition to the pump, a parallel suction tube could be felt in the aorta, so that within several cycles the tube was relocated due to strong heart activity. After that the suction tube was replaced with a spiral reinforced suction tube with thicker walls on silicon basis. However, no permanent position could be found for the tube head in the ventricle. Instead, the tube bent in the higher bending torque area at the connection place between the tube and pump housing.
- Analysis:** The pump function could not be researched in this experiment either, since the suction tube was too sensitive to bends to achieve a secure position in the transfer from the tube to the rigid pump covering. Furthermore, the following attempts should be performed with X-rays in order to better observe the retrograde passage of the aortic valve, as well as the position and the tube movement.

3rd experiment (male sheep, 68 kg)

- Pump:** moderate blading MX2S titan from Chapter 11.2.3 on 6.4 mm motor with spiral reinforced suction tube on the silicon basis, suction basket version II and guide catheter from the human sector.
- The suction tube is now equipped with an integral rigidity gradient. While in the basket area it is as flexible, as the tubes from the previous experiments, at the back end it is much more rigid and less sensitive to bends due to a different choice of material and constant wall thickness.
- Insertion:** Insertion was performed on this animal directly through iliac without graft, although the insertion point was as deep as in the first animal.
- Figure 12.2 shows the pump in the exposed and dissected iliac area. The basket together with a part of the tube is already located in the vessel, while the rigid unit with the guiding catheter is still visible. The small curvature radius resulting from the deep insertion place, specific to this animal, is hardly visible, but makes it possible to insert the pump applying significant pressure through the guidance catheter. In the human sector, the insertion is much easier, since the femoral arteries are better accessible. Upon the third insertion, the suction tube was damaged due to the small radii, which is most clearly visible in Figures 12.8 and 12.9 compared to Figure 12.7.



Figure 12.2 Deep insertion area in the iliac artery

X-rays: The pump is well visible in all areas due to the metallic parts. Figure 12.3 shows an X-ray of the pump compared to a hemostat. Due to the spiral in the suction tube and reinforcement in the guide catheter, these areas are also visible.

Particularly visible is the suction basket of version II, which is equipped with a spherical dome and only one small central opening for the guide catheter, according to Figure 12.10, to avoid damage to valves and vessels.

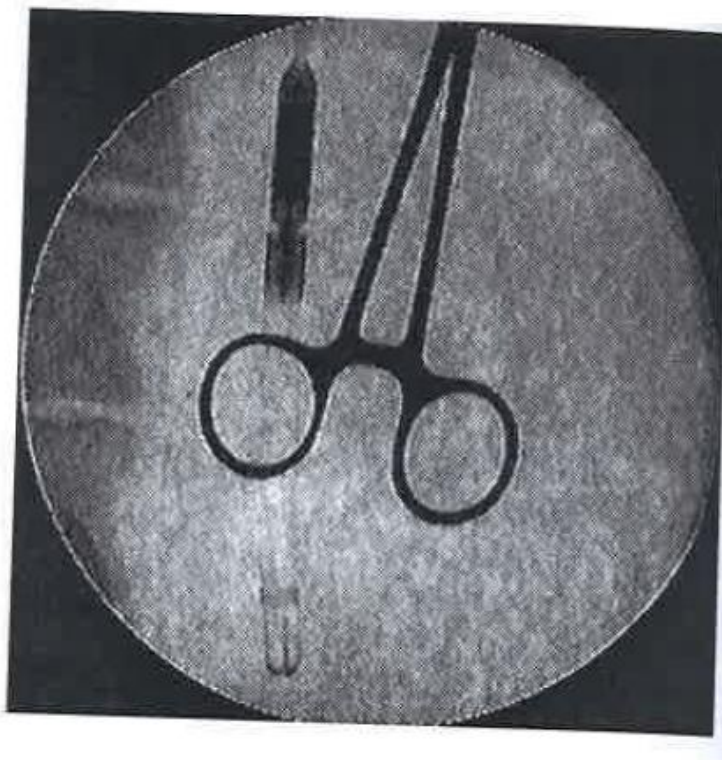


Figure 12.3 Large image of the pump under X-rays

Placement: The pump could be placed here, similarly to the first and second experiment, under X-rays, so that the procedure of the retrograde passage of the aortic valve could be observed in all details.

The placement sequence visible in Figures 12.4 – 12.7 was confirmed in all experiments with the flexible suction head.

In Figure 12.4, the system is lying unpowered in the aorta. The basket is located immediately before the aortic valve. The tube and the pump head are in the aortic arch, while the drive and a part of the guide catheter are located in the aorta descendens.

At this point, an axial thrust is engaged through the guide catheter, so that the system increasingly pushes against the external wall of the aorta, and the suction tube bends, initially at the stiff connection place between the tube and pump housing and, as intended, immediately above the basket.

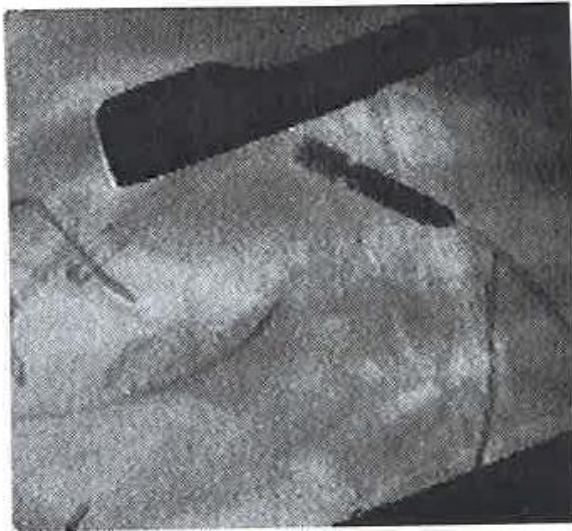


Figure 12.4 Pump in aorta descendens; basket immediately before the aortic valve

In Figure 12.5 the axial thrust is lifted to the point that the pump already disappears behind the thoracic spreader. The tube makes in the vicinity of the basket an arch $> 90^\circ$, which extends in the direction of the middle of the valve.



Figure 12.5 With the tip of the basket in sinus, the suction tube bends in the valve area by more than 90°

In the next figure, i.e. Figure 12.6, which follows the previous one by $t = 1/25$ s, the suction tube already passed the valve. The pump has moved far into the ventricle, due to the energy saved in the guide catheter, and is now lying in the suction basket in the

apex. Therefore, at the end of the valve passage the entire system must be put back into the position according to Figure 12.7. This can be done either as in this case by X-ray control, or by a pressure sensor placed on the pump before the blading and immediately behind the outlet.

Thus, the pressure sensors integrated at a later point of time can be used not only for determination of the pump volume flow, but also for the placement, since the pressures in the ventricle and aorta are sufficiently different, so as to allow for exact identification on the pump position.

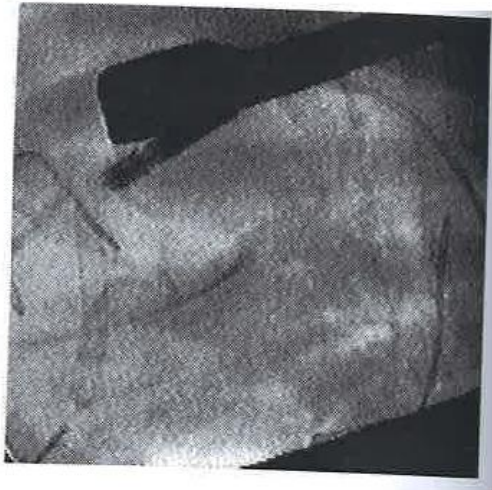
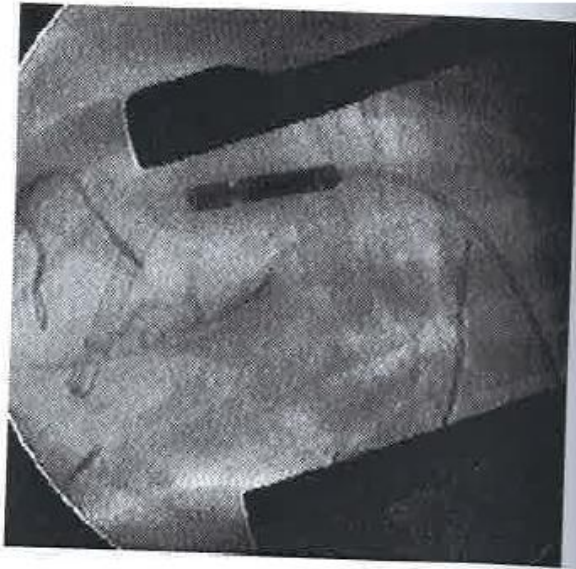


Figure 12.6 The suction tube starts bending under pressure

The pump was placed several times, repeating the described procedure. In all cases, the basket did not pass directly through the valve, but the passage first went through the tube bent in the direction of the middle of the valve.

The pump movements were researched with the pump in the position shown in Figure 12.7, where the rigid pump part is lying in the aortic arch. For this purpose the system was left twice without functioning in this position for 20 minutes each time. With the stiff suction tube, tube was not thrown out of the ventricle, as it was observed in the first and second experiments.



Pump in a proper position

Hemodynamics: The pump rotation speed was again gradually increased from $n = 10,000$ turns/min to $n = 40,000$ turns/min. With the proper pump position shown in Figure 12.7, the total heart minute volume of about 4.5 l/min could now be pumped at the maximum rotation speed, despite the damaged and strongly bending suction tube.

With the increasing pump rotation speed, the ventricular peak pressure decreased, while the aortic pressure became increasingly non-pulsating. At the speed of $n = 40,000$ turns/min the ventricle pressure no longer reached the level of aortic pressure, so that it could be assumed that the valve did not open at any time point of the cycle more than was necessary for the suction tube. Therefore, it was ensured that under these conditions the entire left ventricular blood was transported by the pump.

Figures 12.8 and 12.9 represent contrast pictures of the situation without pump support and at $n = 40,000$ turns/min enddiastolically and endsystolically.

In case of complete volume unloading and takeover by the pump it can be clearly seen that the ventricle does not exceed the systolic size even in the filling phase, since the pump transports the incoming substrate all the time.

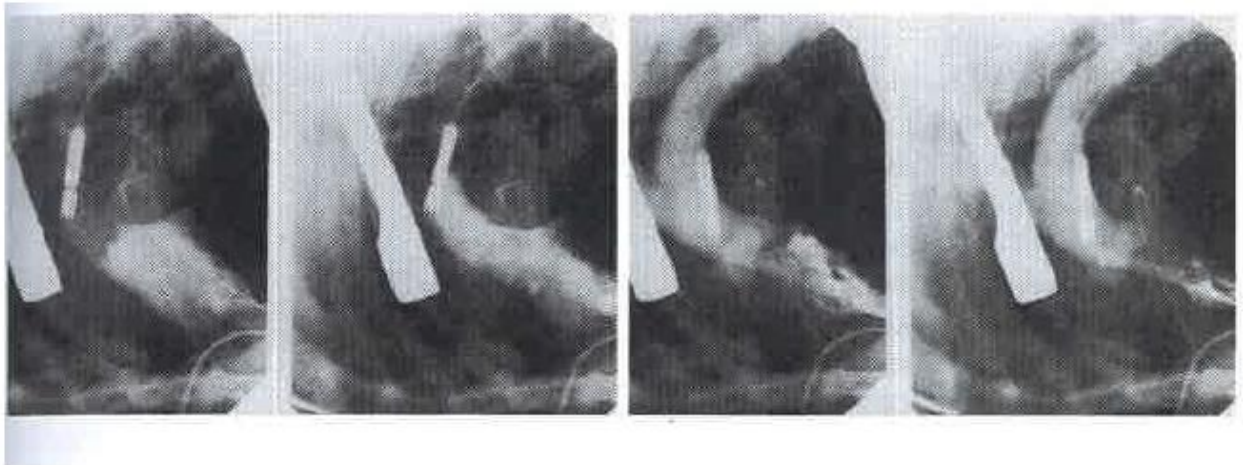


Figure 12.8 X-ray contrast picture with placed pump without unloading; left: diastolic; right: systolic

Figure 12.9 X-ray contrast picture with placed pump and maximum unloading; left: diastolic; right: systolic

Summary:

During the first three in vivo experiments, the problems, which all result from the system periphery and not from the pump, were recognized and resolved to the extent that a first hydraulic function check became possible. This way the measurable in vitro capacity of the pump was also confirmed in vivo.

A 6 mm micro-axial pump can even fully take over the left side heart support under maximum load for a short time.

No pump specific problems were observed during the experiments, which at this time lasted at $n = 30,000$ for the total of 3.5 hours, of which 1.5 hours continuously during the third experiment.

The pump related thrombogenicity, which could only be briefly treated in Chapter 11, has been confirmed in vivo for short time use. No thrombi were found in the first three experiments in the blading, which would also originate there.

On one occasion a thrombus was found in the rotor before the blading entrance edge from the version I suction basket, which was specifically and repeatedly blocked in the central opening. The way the thrombus got into the blading area is clearly similar to that of the caught swimming dust particle from in vitro experiments, so that growth at that place can be virtually ruled out.

Blood deposits were not found either on the motor surface, or in the seal area, despite the undefined position of the pump in the vessel. This confirms the surface temperature research from Chapter 4.2.2 performed on the 8.5 mm motors instead the 6.4 mm motors used here. It is only in the area affected by the sealing lip on the shaft that a thin and hard blood film was observed on the shaft side upon taking equipment apart, similarly to the in vitro research from Chapter 11.2.3. In all cases, it did not cause for short term use any leakage of blood into the pump mechanics. Therefore, to the extent these three experiments are representative, compatibility of the pump for short term use according to the definition from Chapter 11.1 has been tentatively confirmed.

The nearly unusable suction basket of version I could be significantly improved with respect to its valve compatibility, suction propensity and thrombogenicity. Figure 12.10 shows all baskets used so far.

The suction tube developed in the meanwhile with gradual rigidity has significantly improved not only the placeability, but also the stability of the tube in the ventricle.

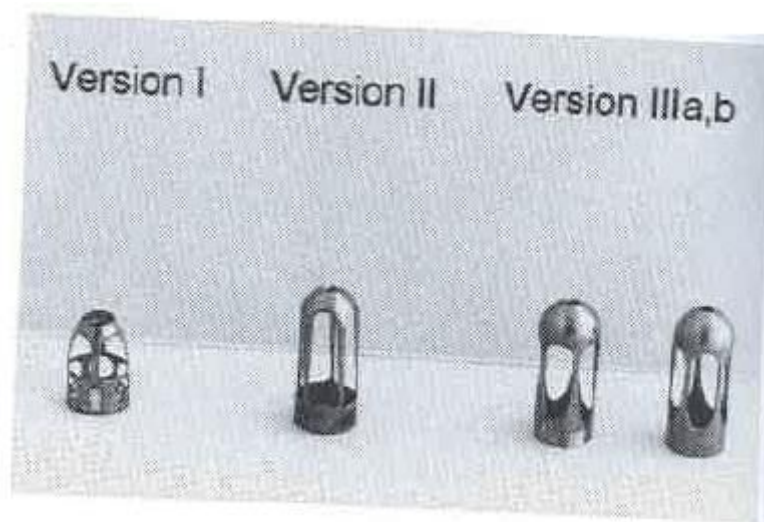


Figure 12.10 Used suction baskets

13. Perspectives

There is further improvement potential in the areas of flow control, the associated hydraulic capacity and blood damage, mechanical long term stability of the pump, clinical application and sensor based pump management.

This work covered at this point exclusively research with the flow visualization methods; with respect to further improvement of flow mechanics of the blading components, it would be pertinent to obtain images on a relevant 3D flow simulation platform. Once this adjustment step is made, the flow will be better shown in time and space as opposed to the very limited methods of experimental flow visualization. More exact information can be expected about the locally high shear tension, so that a computer supported iteration process may result in further increase of hydraulic capacity and reduction of the pump induced blood damage. A parallel comparison of the simulated and visualized flow is still required.

Based on the existing information, it is necessary to test the intravascular blood pumps with integrated drive in extensive experiments for days in a row, in order to obtain definitive conclusions on long term stability of the polymer seal integrated in the pump and thrombogenicity of the entire system.

It can be expected that the flow control will have to be improved on the outlet side for no-stator LV impeller pumps for long term use, in order to avoid temperature induced thrombi, so as to ensure a sufficiently good flow around the drive.

This work covered insertion of the system through peripheral vessels in vivo, but it is also necessary to develop a percutaneous insertion system for a generally applicable concept, which is to be clinically relevant in cardiology as well. A special outlet tube must also be developed for the right heart use, where the pump is supposed to be inserted through peripheral vessels, which allows for pushing and simple placement of the pump.

The sensors discussed in this work and specifically their long term stability and integration in the existing pumps without significant increase of the total diameter represent another important development aspect.

The pump system can only be securely placed and monitored for system functions with integrated sensors. The sensors also allow, based on the calculated pump flow, for a controlled adjustment of circulation and, in case of two-sided heart support, a fluid balance.

14. Summary

Intravascular blood pumps represent a promising concept of temporary heart support, if the benefit of simple and minimally invasive placeability does not come at the price of low hydraulic capacity. For example, the intra-aortal balloon pumps (IABP), the first clinically available intravascular heart support system working according to the displacement principle, can only unload the left heart by some 10%.

The concept of an intravascular blood pump according to the rotary pump principle pursued in this work with capacity of up to 100% of heart activity is clearly more efficient and based on the Hemopump system, which has already been used clinically.

The pump head of the Hemopump placed in the vicinity of heart is driven by an external drive through a flexible shaft, which is as long as the catheter required for the pump placement. The resulting drawbacks, which include breakdowns of the flexible shaft and start-up times of up to 30 minutes due to the required shaft oiling time, are avoided in this work by integration of a miniature drive in the immediate vicinity of the pump head. Besides, systematic research of hydraulic capacity and transportation parameters has been performed to improve the pump capacity.

The most important logical and development steps, as well as the solutions and assessments can be summarized as follows.

Helmholtz axial pump:

Based on the clinical experience with Hemopump system and the above described restrictions inherent to the system of all Hemopump systems developed so far, Helmholtz Institute for Biomedical Technology is developing intravascular rotary blood pumps with integrated drives.

By integration of a proximal drive in the immediate vicinity of the pump, the flexible shaft, which has been discussed as an important conceptual drawback of the Hemopump system, can be eliminated. Furthermore, no active flushing of the seal is performed, so that the system can be used directly, without a start-up period.

Due to the dependence of the respective pump capacity on the pump size, the 6.4 mm and 5.4 mm pumps for percutaneous use and an 8.0 mm system for intraoperative use on open thorax have been developed in this work.

Based on the 6.4 mm system, extensive research was performed on the implemented blading using chosen and adjusted methods of flow visualization. This allowed for gradual and significant improvement of the hydraulic capacity of the blading with the following results.

The hydraulic capacity currently obtainable with realistic transportation parameters constitutes for the 5.4 mm system 2 – 2.5 l/min, for the 6.4 mm system 2.5 – 4 l/min, and for the 8.0 mm system 5 – 7 l/min. This data is based on physiological pressures with short and hydraulically beneficial suction tubes.

In addition to a qualitative description of the flow, the latter was also described quantitatively within the chosen blading with the flow visualization methods, in order to obtain the first assessment of the pump induced blood damage. Based on this research, it became possible to describe the design parameters, which affect the transportation capacity and pump characteristics, as well as the expected blood damage.

Concurrently with the blading development, we assessed the mechanical capacity required for the most important 6.4 mm system to operate the blading. The drive concepts were then developed based on such assessment.

A no-sensor synchronous machine was adjusted to the specific requirements and developed in cooperation with Ecole Polytechnique Federale de Lausanne (Prof. Jufer'); the mechanical capacity achievable with a nominal diameter of 6.5 mm equals up to 6.0 W at $n = 30,000$ turns/min.

At this point, electrical drives for a pump system with 6.4 mm and 5.4 mm diameters have been created and integrated into the total system with a pump sealed with frictional connection with the drive according to concept IV, and extensively tested in vitro in blood and blood substitute. Both pump sizes result in secure operation of the blading components even beyond the design point, with the measured surface temperatures of the drive remaining below the critical temperature due to the convective heat transport to the pumped medium.

Finally, the 6.4 mm pump could be tested on sheep as a total system consisting of the front suction tube, pump, drive and guide catheter in the first in vivo experiments. During these experiments, the suction tube and the suction basket were improved to the point that the system could be inserted without problems peripherally and retrograde through the native valve apparatus. Due to the short and sufficiently rigid suction tube, the system stayed with its suction tip in the ventricle and was not thrown out due to the heart activity.

Using all capacity reserves, the heart minute volume that had to be transported (sheep 68 kg, HZV = 4 – 5 l/min) could even be completely taken over by the pump for a short period of time.

In view of the documented problems with application of Hemopump resulting from uncontrolled operation, a sensor concept for capacity registration and control of the integrated pump system was tested in vitro, consisting of a pressure sensor preceding the blading and another sensor behind the outlet opening on the pressure side. With this arrangement the volume flow of the pump could be determined based on the measured differential pressure, rotor rotation speed and pump curve, even in pulsating environment with an error below 15%.

Therefore, a functioning concept of an intravascular rotary pump with integrated drive was developed and implemented in this work, and it can be used as a platform for the development of similar systems, which target specific indications.

A concept development, as well as the concept synthesis and system validation of an effective intravascular pump with integrated drive was performed successfully.

List of references

- W. Aboul-Hosn, R. Wampler**
The Hemopump: Clinical Results and Future Applications
Assisted Circulation 4, Springer-Verlag Berlin Heidelberg New York, 1995
- G. Adomeit**
Mechanik für Ingenieure: Festigkeitslehre Band 1+2
Vorlesungsumdruck 1986
Lehrstuhl und Institut für Allgemeine Mechanik
- H. J. Althoff**
Ein Elektromechanisches Herzunterstützungssystem
Entwicklung eines Konzepts und Überprüfung seiner
Realisierbarkeit
Dissertation an der RWTH Aachen 1987
- Anatomischer Atlas des Menschen, zsgest. von J. P. Schädé
7. Aufl., Stuttgart: Fischer, 1991
- W. Backé**
Grundlagen der Ölhydraulik
Vorlesungsumdruck, 7. Auflage 1988
Institut für hydraulische und pneumatische Antriebe und Steuerungen
der RWTH Aachen
- A. Benninghoff**
Makroskopische und mikroskopische Anatomie des Menschen
(Hrsg. Kurt Fleischhauer), Band 2: Kreislauf und Eingeweide, 13./14. Aufl., Verlag Urban &
Schwarzenberg, München, 1985
- E. Bernstein, P. Blackshear, K. Keller**
Factor influencing erythrocyte-destruction in artificial organs
Am. J. Surg., Vol. 114, 126, 1967
- P. Blackshear, F. Dorman, J. Steinbach**
Some mechanical effects that influence hemolysis
Trans. ASAIO 11, S. 112, 1965
- P. Blackshear, R. Forstrom, F. Dorman, G. Voss**
Effect of flow on cells near walls
Federation Proceedings Vol. 30, No.5, 1971

P. Blackshear

Mechanical hemolysis in flowing blood

Chemistry of Biosurfaces, Ed.: Y.C. Fung, Vol. 2, chapter 11, New York, 1972

C. Blutszuweit

A theoretical approach to the prediction of hemolysis in centrifugal blood pumps

Ph.D. Thesis, University of Strathclyde, Glasgow, 1994

C. Blutszuweit

Model for a general mechanical blood damage prediction,

Artif. Organs., Vol. 19, No. 7, S. 583-589, 1995a

C. Blutszuweit

Three dimensional numerical simulation of stress loading of blood particles in a centrifugal pump

Artif. Organs., Vol. 19, No. 7, S. 590-596, 1995b

I. N. Bronstein

Taschenbuch der Mathematik

22. Aufl., Thun, Frankfurt/Main: Verlag Harri Deutsch, 1985

K. C. Butler

Recent Advances in Cardiac Prothesis

Proceedings of the Annual Intern. Conference of the IEEE Engineering in Med., and

Bio. Soc., 1988: 68-69

K. C. Butler, R. K. Wampler

Development Of An Implantable Axial Flow LVAS

Nimbus Medical Inc., Rancho Cordova

K. Butler, T. Maher, H. Borovetz, R. Kormos, J. Antaki, M. Kameneva,

B. Griffith, T. Zerbe, F. Schaffer

Development of an Axial Flow Blood Pumpd LVAS

ASAIO Journal 1992

G. M. Deeb, S. F. Bolling, J. Nicklas, R. S. Walsh, C. N. Steimle, M. J. Shea,

J. S. Meagher

Clinical Experience with the Nimbus Pump

ASAIO-Transactions 1990;36:M632-M636

G. Dibelius

Ähnlichkeitsprobleme im Maschinenbau

Vorlesungsumdruck 1990

Institut für Dampf- und Gasturbinen der RWTH Aachen

J. M. Duncan, O. H. Frazier, B. Radovanecvic, V. Velebit
Implantation Techniques of the Hemopump
Ann.Thorac.Surg. 1989;48:733-735

R. Eppler
Strömungs- und Wärmegrenzschichten
Manuskript zur Vorlesung an der Universität Stuttgart, 1991

R. Eppler
Strömungsmechanik
Manuskript zur Vorlesung an der Universität Stuttgart, 1987

E. Evans, R. Hochmuth
A solid-liquid composite model of the erythrocyte membrane
J. Membrane Biol. 30, 351, 1977

Ferrofluidics Corporation
Catalog of Standard and Replacement Ferrofluidic Feedthroughs

H. R. Figulla
Circulatory Support Devices in Clinical Cardiology
Cardiology 1994;84:149-155

W. Flameng
Indications for the use of the Hemopump
Steinkopff Verlag Darmstadt/Springer-Verlag New York, 1991: 73-77

O. H. Frazier
Investigational Trials of the Hemopump at the Texas Heart Institute: practical issues
Temporary Cardiac Assist with an Axial Pump System (W.Flameng)
Steinkopff Verlag Darmstadt/Springer-Verlag New York, 1991: 47-50

O. H. Frazier, R. K. Wampler, J. M. Duncan, W. E. Dear, M. P. Macris, S. M. Parnis, J. M. Fuqua
First Human Use of the Hemopump, a Catheter Mounted Ventricular Assist Device
Temporary Cardiac Assist with an Axial Pump System (W.Flameng)
Ann Thorac Surg 1990a, 49:299-304 und
Steinkopff Verlag Darmstadt/Springer-Verlag New York, 1991

O. H. Frazier, M. P. Macris, R. K. Wampler, J. M. Duncan, M. S. Sweeney, J. M. Fuqua
Treatment of Cardiac Allograft Failure by Use of an Intraaortic Axial Flow Pump
J. Heart Transplant 1990b;9:408-414 und

H. E. Gallus

Wärme- Kraft- und Arbeitsmaschinen, Teil: Turbomaschinen
Manuskript zur Vorlesung an der RWTH Aachen, 1988

H. E. Gallus

Turboarbeitsmaschinen-Berechnung
Manuskript zur Vorlesung an der RWTH Aachen, 1992

O. H. Gauer, K. Kramer, R. Jung

Physiologie des Menschen, Band 3: Herz und Kreislauf
Verlag Urban & Schwarzenberg, München, 1972

M. Giersiepen, L. J. Wurzinger, R. Opitz, H. Reul

Estimation of shear stress-related blood damage in heart valve prostheses - in vitro
comparison of 25 aortic valves
International Journal of Artificial Organs /Vol. 13/no.5, 1990/pp.300-305

B. Glasmacher

Werkstoffe in der Medizintechnik
Diplomarbeit RWTH-Aachen, Helmholtz-Institut, 1982

B. Glasmacher

Kalzifizierung von Polyurethan-Biowerkstoffen im kardiovaskulären System
Dissertation RWTH-Aachen, Helmholtz-Institut, 1991

H. Groß

Vergleichende Hämolyseuntersuchungen an Blutpumpen,
Medizinische Dissertation der Freien Universität Berlin, 1984

G. Heuser, R. Opitz

A Couette Viscometer For Short Time Shearing Of Blood
Bioreology Vol. 17, pp. 17-24, 1980

O. Jegaden

Clinical results of Hemopump support in surgical cases
Hôpital Vasculaire Louis Pradel, Lyon, France
Proceedings of the international Workshop of rotary blood pumps, Vienna 1991 und
Steinkopff Verlag Darmstadt/Springer-Verlag New York, 1991: 61-66

O. Jegaden, O. Bastien, C. Girard

Temporary left ventricular assistance with a Hemopump assist device during acute myocardial
infarction
Journal of Thorac. and Cardvasc. Surg. Vol. 100, no.2:311-312, 1990

Johnson & Johnson Interventional Systems Co., 1988
Compendium of Technical and Scientific Information for the
Hemopump Temporary Cardiac Assist System

Johnson & Johnson Interventional Systems Co., 1994
Hemopump Cardiac Assist System: Directions For Use

I. Karassik

Pump Handbook

2. Auflage, McGraw-Hill Book Company, New York 1985

B. Knierbein

Konstruktion, Fertigung und Test von pneumatisch
angetriebenen Membranpumpen zur Herzunterstützung
Dissertation an der RWTH Aachen 1990

C. Kramer

Studies of flow induced mechanical haemolysis
AGARD Conf. Proc. 65, S. 5, 1970

E. Krause

Strömungslehre II

Vorlesungsumdruck 1988

Lehrstuhl für Strömungslehre der RWTH Aachen

E. Kunst, J. van Alste

Dynamic Pumping Characteristic of the Hemopump - a Small Intraventricular Bloodpump
Proceedings of the international Workshop of rotary blood pumps, Vienna 1991

Lambert

Zusammenfassung der Vorlesung Strömungsfragen der Medizin I
an der RWTH Aachen, 1989

D. Y. Loisanee

Development And Technological Evolution Of The Hemopump;
Experience with The Hemopump;

Summary of discussion

Concerted Action HEART: Intraventricular Blood Pumps (D.Y. Loisanee)
Proceedings of the Expert meeting held in Paris, March 31, 1990, s.5-12

D. Y. Loisanee, J. L. Dubois-Randé, P. Deleuze, J. Okude, O. Rosenval, H. Geschwind
Prophylactic intraventricular pumping in high-risk coronary angioplasty
Lancet, 1990a; 335:438-440

D. Y. Loisanze, P. Deleuze, J. L. Dubois-Randé, J. Okude, N. Shiiya, F. Wan, H. Geschwind
Hemopump Ventricular Support for Patients Undergoing High Risk Coronary Angioplasty
ASAIO Transactions 1990b; 36: M623-M626

U. Lönn, J. Wulff, K. Keck, B. Wranne, P. Ask, B. Peterzen, H. Casimir-Ahn
Flow Characteristics of the Hemopump: An Experimental In Vitro Study
Ann Thorac Surg, 1997; 63:162-166

Magnetic-Fluid Seals (Magfluid Seals) US Pat.Re32573
NSK Nippon Seiko

U. Mees, P. Sergeant, W. Daenen, W. Flameng
Success and failure of the Hemopump; a critical analysis
Temporary Cardiac Assist with an Axial Pump System (W.Flameng)
Steinkopff Verlag Darmstadt/Springer-Verlag New York, 1991:51-60

M. E. Merhige, R. W. Smalling, D. Cassidy, R. Barrett, G. Wise, J. Short, R. K. Wampler
Effect of the Hemopump left ventricular assist device on regional myocardial perfusion and function: Reduction of ischemia during coronary occlusion
Circulation 1989;80 (suppl III):158-166

B. Meyns, P. Sergeant, W. Daenen, W. Flameng
Left Ventricular Assistance With the Transthoracic 24F Hemopump for Recovery of the Failing Heart
Ann Thorac Surg 1995; 60:392-397

B. Meyns, T. Sieß, S. Laycock, H. Reul, G. Rau, W. Flameng
The Heart-Hemopump Interaction: A Study of Hemopump Flow as a Function of Cardiac Activity.
Artificial Organs, 20(6):641-649, 1996

W. Michaeli
Einführung in die Kunststoffverarbeitung
Carl Hanser Verlag München Wien 1992

D. S. Miller
Internal Flow Systems
BHRA, 1990

M. Müller

In vitro hematological testing of rotary pumps: remarks on standardization and data interpretation
Artificial Organs, Vol.17, No.2, pp 103-110, 1993

G. V. A. van Ommen

Hemopump Versus Intra-Aortic Balloon Pump (IABP)
Concerted Action HEART: Intraventricular Blood Pumps (D.Y. Loisanse)
Proceedings of the Expert meeting held in Paris, March 31, 1990, s.13-18

H. Petermann

Einführung in die Strömungsmaschinen
3. Aufl. Berlin, Heidelberg, New York: Springer-Verlag, 1988

M. Pinotti, E. Rosa

Computational prediction of hemolysis in a centrifugal ventricular assist device
Artif. Organs, Vol. 19, No. 3. S. 267-273, 1995

C. Pfeleiderer, H. Petermann

Strömungsmaschinen
5. Aufl., Berlin, Heidelberg, New York: Springer-Verlag, 1986

C. Pfeleiderer

Kreiselpumpen
Berlin, Heidelberg, New York: Springer-Verlag, 1924

L. Prandtl

Führer durch die Strömungslehre
4. Aufl., Vieweg & Sohn, Braunschweig, 1956

M. Renardy, H. Planck

Untersuchung der Biokompatibilität von medizinischen Kunststoffen
Kunststoffe und Elastomere in der Medizin, Stuttgart, Kohlhammer Verlag 1993

U. Renz

Grundlagen der Wärmeübertragung
Vorlesungsumdruck der RWTH-Aachen, 1990

N. Rosarius T. Sieß, H. Reul, G. Rau

Concept, Realization, and First In Vitro Testing of an Intraarterial Microaxial Blood Pump with an Integrated Drive Unit
Artificial Organs, 18(7):512-516, 1994

R. E. Rosensweig

Ferrohydrodynamics

Cambridge Monographs on Mechanics and Applied Mathematics;
Cambridge University Press, 1985

P. M. Rutan, W. D. Rountree, K. K. Myers, L. E. Barker

Initial Experience with the Hemopump

Critical Care Nursing Clinics of North America-Vol.1, No.3, Sept. 1989

I. Sallam, A. Shaw, W. Bain

Experimental evaluation of mechanical haemolysis with Starr-Edwards, Kay-Shiley, Björk-Shiley valves

Scand J Thor Cardiovasc Surg, Vol.. S. 117-122, 1976

H. Schima, G. Wiesenthaler

Mechanically Introduced Blood Trauma: Are the Relevant Questions already solved, or is it still an Important Field to be Investigated

Artificial Organs, 19(7):563-564, 1995

H. Schima, H. Siegl, S. Mohammad, L. Huber, M. Müller, U. Losert, H. Thoma, E. Wolner

In Vitro Investigation of Thrombogenesis in Rotary Blood Pumps

Artificial Organs, 17(7):605-608, 1993

H. Schima, M. Müller, D. Papantonis, C. Schlusche, L. Huber, C. Schmidt, W. Trubel, H. Thoma, U. Losert, E. Wolner

Minimization of hemolysis in centrifugal blood pumps: influence of different geometries

The International Journal of Artificial Organs Vol.16, no.7, 1993

H. Schima, M. Müller, S. Tsangaris, G. Gheiseler, C. Schlusche, U. Losert, H. Thoma, E. Wolner

Mechanical Blood Traumatization by Tubing and Throttles in In Vitro Tests: Experimental Results and Implications for Hemolysis Theory

Artificial Organs, 17(3): 164-170, 1993

H. Schlichting

Grenzschicht-Theorie

5. Aufl., G. Braun, Karlsruhe, 1965

R. F. Schmidt, G. Thews

Physiologie des Menschen

19. Aufl., Berlin, Heidelberg, New York: Springer-Verlag, 1977

K. H. Scholz, J. P. Hering, T. Schröder, P. Uhlig, U. Tebbe, H. Kreuzer, G. Hellige
Effect of the Hemopump in cardiogenic shock and in the early stage of regional myocardial ischemia

In: Temporary Cardiac Assist with an Axial Pump System (W.Flameng), s.17-26
Steinkopff Verlag Darmstadt/Springer-Verlag New York, 1991

K. Scholz, H. Figulla, F. Schweda, R. Smalling, G. Hellige, H. Kreuzer, W. Aboul-Hosn, R. Wampler

Mechanical left ventricular unloading during high-risk coronary angioplasty: first use of a new percutaneous transvalvular left ventricular assist device
Cathet Cardiovasc Diagn 31(61):61-69, 1994a

K. Scholz, J. Hering, T. Schröder, P. Uhlig, H. Kreuzer, G. Hellige

Left-Ventricular Unloading by Transvalvular Axial Flow Pumping in Experimental Cardiogenic Shock and during Regional Myocardial Ischemia
Cardiology, 1994b;84:202-210

K. Scholz, U. Tebbe, M. Chemnitius, H. Kreuzer, T. Schröder, J. P. Hering, P. Uhlig, G. Hellige, H. J. Grönc, R. Autschbach, B. Schorn, W. Ruschewski, H. Dalichau
Transfemoral Placement of the Left Ventricular Assist Device „Hemopump“ During Mechanical Resuscitation

Thorac. cardiovasc. Surgn. 38 (1990): 69-72

H. Schulz

Die Pumpen

13. Aufl., Berlin, Heidelberg, New York: Springer-Verlag, 1977

T. Sieß, B. Meyns, K. Spielvogel, H. Reul, G. Rau, W. Flameng

Hemodynamic System Analysis of Intraarterial Microaxial Pumps In Vitro and In Vivo
Artificial Organs, 20(6):641-649, 1996

T. Sieß, H. Reul, G. Rau

Concept, Realization, and First In Vitro Testing of an Intraarterial Microaxial Blood Pump

Artificial Organs, 19(7):644-652, 1995

T. Sieß, H. Reul, G. Rau

Hydraulic refinement of an intraarterial microaxial blood pump

The International Society of Artificial Organs, Vol. 18, no. 5:273-285, 1995

S. Silbernagl, A. Despopoulos

Taschenatlas der Physiologie

3. Aufl., G. Thieme Verlag, 1988

H. Skudelny

Elektrische Antriebe und Steuerungen

Vorlesungsumdruck der RWTH-Aachen, 1989

R. W. Smalling, D. B. Cassidy, R. Barrett, B. Lachterman, P. Felli, J. Amirian

Improved Regional Myokardial Blood Flow, Left Ventricular Unloading, and Infarct Salvage Using an Axial-Flow, Transvalvular Left Ventricular Assist Device

Circulation 1992, Vol. 85; No.3:1152-1159

J. Sobotta (Hrsg.)

Atlas der Anatomie des Menschen, Band 2: Brust, Bauch, Becken, untere Extremität

19. Aufl., München, Wien, Baltimore: Urban & Schwarzenberg, 1988

A. Steegers

Die Leckage an künstlichen Herzklappenprothesen als potentielle Ursache der Bluttraumatisierung

Dissertation an der RWTH Aachen 1997

O. Stemme, P. Wolf

Wirkungsweise und Eigenschaften hochdynamischer Gleichstrom-Kleinstmotoren

Maxon Motor, 1994

L. Stryer

Biochemistry

Freeman, San Francisco, 1975

G. Thews, E. Mutschler, P. Vaupel

Anatomie, Physiologie und Pathophysiologie des Menschen

3. Aufl., 1988

Thyssen AG

Dauermagnetische Kupplungen und Bremsen für die Antriebstechnik

Thyssen Edelstahlwerke AG, 1992

E. Truckenbrodt

Fluidmechanik, Band 1 und 2

2. Aufl., Berlin, Heidelberg, New York: Springer-Verlag, 1980

K. Trutnovsky, K. Komotori

Berührungsfreie Dichtungen

VDI-Verlag GmbH - Düsseldorf, 1981

VDI-Wärmeatlas

7. Auflage VDI-Verlag, 1994

G. Vetter

Verdichter Teil I: Kompressoren; Teil II: Vakuumpumpen
Vulkan Verlag Essen, 1990

F. R. Waldenberger, P. Wouters, A. Wiebalck, W. Flameng

Use of the Left-Ventricular Assist with the Hemopump in Cardiac Surgery
Cardiology 1994;84:211-215

R. K. Wampler, J. C. Moise, O. H. Frazier, D. B. Olsen

In Vivo Evaluation of the Peripheral Vascular Access Axial Flow Blood Pump
ASAIO Transactions 1988; 34:450-454

R. K. Wampler, B. A. Baker, W. M. Wright

Circulatory support of Cardiac Interventional Procedures with the Hemopump Cardiac Assist System
Cardiology 1994;84:194-201

R. K. Wampler, O. H. Frazier, A. M. Lansing, R. W. Smalling, J. M. Nicklas, S. J. Phillips, R. A. Guyton, L. A. R. Golding

Treatment of Cardiogenic Shock with the Hemopump Left Ventricular Assist Device
Ann Thorac Surg 1991a;52:506-513

R. K. Wampler

Investigational trials of the Hemopump
Im: Temporary Cardiac Assist with an Axial Pump System (W.Flameng), s.39-46
Steinkopff Verlag Darmstadt/Springer-Verlag New York, 1991b

R. K. Wampler, W. Aboul-Hosn, M. Cleary, M. Saunders

The Sternotomy Hemopump: A Second Generation Intraarterial Ventricular Assist Device
ASAIO Journal 1993 M218-223

D. Westphal

Entwicklung einer Zentrifugalpumpe zur Blutförderung
Dissertation RWTH-Aachen, Helmholtz-Institut, 1994

P. F. Wouters

Effects of left-ventricular assist using a co-axial flow pump on organ blood flow during experimental cardiogenic shock
Im: Temporary Cardiac Assist with an Axial Pump System (W.Flameng), s.27-38
Steinkopff Verlag Darmstadt/Springer-Verlag New York, 1991

L. J. Wurzinger, R. Opitz

Hematological Principles Of Hemolysis And Thrombosis With Special Reference to Rotary Blood Pumps

Proceedings of the International Workshop on Rotary Blood Pumps, 1991

L. J. Wurzinger et al.

Platelet and coagulation parameters following millisecond exposure to laminar shear stress

Thromb. Haemost. 1985; 54; 381-386

K. Yamazaki, M. Kameneva, W. Wagner, J. Antaki, J. Tatka, J. Kerrigan,

P. Litwak, H. Konishi, M. Macha, J. Tomczak, Z. Yang, H. Borovetz, R. Kormos

Bearing Seizure in a Rotational Blood Pump - Mechanism and Potential Solutions

Abstract ASAIO 1995

K. Yeleswarapu, J. Antaki, M. Kameneva, K. Rajagopal

A mathematical model for shear-induced hemolysis

Artif. Organs, Vol. 19, No. 7, S. 576-582, 1995

Nicht zitierte, relevante Studien- und Diplomarbeiten

- D. Chihos** : Entwicklung und Beurteilung eines hydraulischen Antriebskonzepts zum Betrieb einer intravasalen Mikroaxialpumpe. Studienarbeit 1995
- M. Ben Khemis** : Einsatz eines Einkanal-LDA-Meßsystems zur Geschwindigkeitserfassung im vergrößerten Modell einer Micro-Axialpumpe zur temporären Herzunterstützung. Studienarbeit 1993
- M. Eisen** : Sytemanalyse und Modifikation des hydraulischen Antriebs einer Mikroaxialpumpe. Studienarbeit 1995
- J. Forsthövel** : Konstruktion, Fertigung und Beurteilung eines hydraulischen Antriebskonzepts zum Betrieb einer Mikroaxialpumpe. Studienarbeit 1994
- D. Friedrich** : Konstruktive Auslegung und Entwicklung von 5mm-Mikroaxialpumpen zur Rechts- und Linksherzunterstützung. Diplomarbeit 1994
- T. Hövekamp** : Strömungsuntersuchungen an Diagonal- und Mikroaxialpumpen in Originalgröße. Studienarbeit 1993
- T. Sieß** : Konstruktive Auslegung und Entwicklung eines 10fach vergrößerten Modells einer Microaxialblutpumpe zur Strömungsuntersuchung sowie dessen Integration in einen geeigneten Prüfstand. Studienarbeit 1992

- T. Sieß** : Fertigungsentwicklung, Montage und erste in vitro-Tests einer Mikro-Axialpumpe zur temporären Herzunterstützung. Diplomarbeit 1992
- H. Tenfelde** : Experimentelle Strömungsuntersuchungen an einem 10fach vergrößerten Modell einer Mikroaxialpumpe zur temporären Herzunterstützung. Studienarbeit 1993
- T. Thelen** : Systemanalyse und Bewertung von High-Speed-Video-Systemen zur Strömungsanalyse im Rotor einer Mikroaxialpumpe. Studienarbeit 1994
- M. Zikorsky** : Entwicklung und Bewertung von Dichtkonzepten zwischen Rotor und Stator für Diagonal- und Mikroaxialblutpumpen. Studienarbeit 1994

Lebenslauf

Personalien: Thorsten Sieß
geboren am 4. August 1965 in Bielefeld
verheiratet, zwei Kinder

Schul Ausbildung:

1972-76 Bültmannshof-Grundschule in Bielefeld
1976-83 Hans-Ehrenberg-Gymnasium in Bielefeld-Sennestadt
1983-84 Auslandsaufenthalt als AFS-Austauschschüler in einem
einjährigen Programm in den USA
Besuch der Lamoille Union Highschool in Hyde Park, Vermont, USA
Abschluß: Highschool Diploma
1984-86 Hans-Ehrenberg-Gymnasium in Bielefeld-Sennestadt
Abschluß: Hochschulreife

Grundwehrdienst:

1986-87 Grundwehrdienst in Delmenhorst und Neumünster

Studium:

1987-92 Studium des Maschinenbaus an der RWTH Aachen
Studienrichtung: allgemeines Maschinenwesen
1986-90 Praktika (insgesamt ½ Jahr)
1992 Diplom

Berufstätigkeit:

1992-1997 Wissenschaftlicher Mitarbeiter am Helmholtz-Institut
für Biomedizinische Technik an der RWTH Aachen in der
Arbeitsgruppe: Biomechanik
Arbeitsbereich: Entwicklung axialer und diagonalen Rotations-
pumpen zur kurz- bis langfristigen Herzunterstützung
Juni 1998 Promotion
seit Anfang 1998 Mitbegründer und Mitarbeiter der Firma
Impella Cardiotechnik GmbH in Aachen in der Funktion des
Leiters Technologie